University of Vigo
Department of Electronics Technology

Dissertation submitted for the degree of
International Doctor of
Philosophy at the University of Vigo

Analysis of Time and Space Harmonics in Symmetrical Multiphase Induction Motor Drives by Means of Vector Space Decomposition

Author: Jano Malvar Álvarez

Directors: Jesús Doval Gandoy and Óscar López Sánchez

Vigo, Date: November 2015

Vita

Jano Malvar Álvarez was born in Bueu, Pontevedra, Spain, in 1981. He received the M.Sc. degree in Electrical Engineering from the University of Vigo, Spain, in 2007. In 2008 he worked as a research and development engineer in Soteco S.L. in A Coruña, Spain. From September 2008 he works in the Department of Electronics Technology of the University of Vigo as a research engineer. He started his PhD in 2010 in the Electronics Technology Department of the University of Vigo. From February to April 2014, he joined the Newcastle University Centre for Advanced Electrical Drives in the United Kingdom for a research stay. His research focuses on power electronics, multiphase systems, electric motors and harmonics. He has been a member of the IEEE Industrial Electronics Society and IEEE Power Electronics Society since 2005 and he is a member of the APET Research Group. He has authored more than 30 published technical papers in the field of power electronics [1–40]. Thirteen of them are published in JCR-indexed journal [1–6, 8, 11, 24–26, 29, 32, 34].

Analysis of Time and Space Harmonics in Symmetrical Multiphase Induction Motor Drives by Means of Vector Space Decomposition

Jano Malvar Álvarez

(Abstract)

The use of multiphase motor drives, i.e., with a phase number higher than three, is an increasingly important trend nowadays. The common procedure to analyze or to design the control algorithm for multiphase motors is to use a decoupling transformation method that transforms the model from the original phase-variable reference frame, where the electrical variables are cross-coupled, into a model decoupled in orthogonal subspaces. One such transformation is the vector space decomposition (VSD), in which each variable is represented by a complex number called spatial vector. When the multiphase induction motor model is decoupled by means of the VSD, different types of subspaces are obtained. The main type of subspace is the one where there is coupling between the rotor and the stator, i.e., where the electromechanical energy conversion happens. There are other types of subspaces in which there is no coupling between the stator and the rotor; these planes do not produce electromechanical energy conversion and their impedance can be very high (in case of homopolar components with isolated neutral points) or low.

In multiphase machines, as happens in three-phase ones, some non-ideal characteristics give rise to harmonics that can lead to undesirable effects such as torque ripple and electrical losses. They can be produced by the converter deadtime, the pulse-width modulation (PWM), flux saturation, the non-perfectly sinusoidal distribution of the windings, non-uniform airgap and some other non-linearities. The characterization of such harmonics in the decoupled motor model and the estimation of the spatial vector of each harmonic is interesting from the point of view of understanding the motor and control. One of the main reasons for identifying the subspace where each current component maps and its spatial vector rotation (SVR) speed is that it is necessary for setting up the controllers. Knowing the subspace where some specific current components map and their SVR speed is essential for sensorless speed measurement algorithms and machine current signature analysis (MCSA). Moreover, the subspace where each current component maps and its SVR speed predict if such a component is going to contribute to the overall motor torque, produce torque ripple or generate losses. Therefore, from the standpoint of the motor performance analysis, the characterization by using the VSD of the current harmonics is also important.

Most of the previous works about multiphase drive harmonics are focused only on machines with a specific number of phases, such as five-, six- and seven-phase motors and they deal only with odd order harmonics, which are the most common low order ones. Furthermore, some studies about series-connected multimotor drives have suggested

that the plane where some current harmonics map depends not only on the harmonic frequency, but also on the phase arrangement in the stator windings connection. As far as the author knows, there are no previous studies about how the phase connection order changes affect the harmonic mapping or studies about how harmonics map in series-connected multimotor drives.

Regarding the topic of spatial harmonics modeling, it has been extensively researched in the three-phase machines field, from the thorough analyses focused on one specific spatial harmonic origin to the more general studies that include the more common causes of spatial harmonics, such as the healthy MCSA. Some spatial harmonic proposals in multiphase motors are directly adapted from three-phase cases and do not take into account the different motor subspaces. Other multiphase spatial harmonic studies, although taking into account the motor subspace decomposition, analyze only particular spatial harmonic causes or are focused just on motors with a specific phase number. The particular case of MCSA for machine status monitoring is also a broadly researched topic in the three-phase field and most of the methods proposed for multiphase motors are based on the adaptation of the three-phase ones, such as the classic MCSA approximation that categorizes the current harmonics according to their frequencies only. However, the study of the motor current harmonics by means of the subspace and the SVR-speed provides more degrees of freedom for classifying such current components than the methods based only on the current harmonic amplitudes and frequencies. Furthermore, the additional subspaces that a multiphase motor has in comparison with the three-phase counterpart provides more levels of classification. Therefore, a MCSA method designed to take advantage of the additional classification variables and the extra subspaces obtains more information about the harmonics origins and avoids some cases of symptoms overlapping in the phase current spectrum. There are some previous works that use the analysis of the currents in the decomposed model of the motor for specific fault detection, such as open-phase or broken bar MCSA, but its application for the identification of faults such as static, dynamic and mixed eccentricity is still to be done.

This thesis presents the study and characterization, by means of the VSD, of the stator current and voltage components due to time and spatial harmonics in a n-phase motor with a symmetrical arrangement of phases. First, an analysis of the stator voltage and current harmonics in a multiphase induction motor, by means of the VSD, that includes the effects of each time harmonic and the phase sequence is developed. As a result it is proposed a very simple time harmonic mapping method valid to predict the subspace where each time harmonic maps and its SVR speed (frequency and direction) in symmetrical multiphase induction motor drives of any phase number and in series-connected multimotor drives. Then, equations to study the subspace mapping and SVR speed of the current harmonics produced for some non-ideal characteristics of a squirrel cage motor such as non-perfect sinusoidal winding distributions, rotor bars, airgap variations due to the stator and rotor slots and magnetic saturation are obtained. These equations are used to study the current signature of healthy multiphase induction motors by means of the VSD. Finally, the model is extended for covering also the static and dynamic eccentricities and, based on it, a VSD MCSA method to detect pure-static, pure-dynamic and mixed eccentricity in multiphase induction motors is proposed.

Contributions of this dissertation have been published in one JCR-indexed journal paper and presented at two international conferences.

Acknowledgments

First of all, I would like to thank my advisor, Dr. Jesús Doval for his trust, guidance and support. He introduced me to the interesting field of power electronics and gave me this opportunity.

Secondly, I would like to express my gratitude to my other supervisor, Dr. Óscar López, for his continuous support, for his ideas and for all his patience and help during these years. This dissertation would have not been possible without his support.

Also, I am very grateful to Dr. Alejandro G. Yepes, for all his help and constructive comments, which have undoubtedly made an impact on the quality of this work.

I would also like to show my appreciation to Dr. Ana Vidal and Dr. Francisco D. Freijedo for their help.

I would like to express my gratitude to Prof. Barrie Mecrow for giving me the opportunity to be at the Centre for Advanced Electrical Drives of the Newcastle University. I also wish to thank Dr. Steve McDonald for all his help and his support during the research stay.

I would like to express my appreciation to all my colleagues of the Applied Power Electronics Technology research group, because of their continuous support and the good moments we have shared. In particular, I would like to thank Ortiz, Pablo, Moisés, Fernando, Diego, Miguel, Jose Miguel, Felipe, Javi, Alex, Guede and Toni.

I would like to express my gratitude to the members of the Ph.D. Committee for their unselfish collaboration in the evaluation of my work.

I would like to thank my parents and my brother for everything that they have done for me.

Finally, I would like to dedicate this dissertation to Seila, for her love, unconditional support and continued encouragement.

A Seila,
a mi familia
y a mis amigos

Contents

List of Figures

List of Tables

List of Abbreviations and Acronyms

1D	one-dimensional
2D	two-dimensional
3D	three-dimensional
AC	alternating current
ADC	analog-to-digital converter
AMD	Advanced Micro Devices
CFFT	complex fast Fourier transformation
CSA	current sheet analysis
DC	direct current
DFT	discrete Fourier transformation
DSP	digital signal processor
DTC	direct torque control
EMF	electro-motive force
FFT	fast Fourier transformation
FOC	field oriented control
GTEM	general theory of electric machines
IEEE	Institute of Electrical and Electronics Engineers
IGBT	insulated-gate bipolar transistor
LEM	Liaisons Electroniques-Mecaniques
MCSA	machine current signature analysis
MMF	magneto-motive force
PI	proportional-integral

PWM	pulse-width modulation
PR	proportional-resonant
PSH	principal slot harmonic
PSHs	principal slot harmonics
rms	root mean square
SVR	spatial vector rotation
UTEM	universal theory of electric machines
VPI	vector proportional integral
VSD	vector space decomposition
VSI	voltage-source inverter
WFA	winding function analysis

Nomenclature

Variables

n	Number of phases.
η	Generic phase.
α_{c}	$= 2\pi/n$. Characteristic angle.
v	Voltage.
i	Current.
$[\psi]$	Linked flux vector.
ψ_η	Linked flux of phase η.
$[L]$	Impedance matrix.
$[R]$	Resistance matrix.
T_e	Electrical torque.
θ	Space angle in mechanical radians.
θ^{r}	Rotor position angle.
P	Pole pair number.
p	Index of the motor decomposed model subspace.
$[C]$	Clarke's transformation matrix.
$[T]$	Symmetrical components transformation matrix.
$\hat{\jmath}$	Imaginary unit.
α-β	Stator plane coupled with the rotor.
x-y	Stator low-impedance plane.
h	Homopolar axis.
ω_s	Fundamental frequency of the stator current.
f	Frequency.
t	Time.
ω_r	Rotational speed.
l_t	Order of the phase transposition in a series-connected multimotor drive.
δ	Spatial angle of the phase transposition in multimotor drives.

m	Angle delay step between consecutive phases.
k	generic constant.
F	Magnetomotive force (MMF).
H	Magnetic field intensity.
B	Flux density.
J	Current sheet.
N	Winding function.
g	Airgap.
μ_0	Magnetic permeability of free space.
r_s	Stator inner radius.
r_r	Rotor outer radius.
L	Rotor length.
Q_s	Number of stator slots.
Q_r	Number of rotor bars.
ν, ν'	Stator winding distribution harmonic order.
q	Converter time harmonic order.
h_s	Stator slots permeance harmonic order.
h_r	Rotor slots permeance harmonic order.
ρ	Iron saturation harmonic order.
h_{se}	Static eccentricity permeance harmonic order.
h_{de}	Dynamic eccentricity permeance harmonic order.
h_b	Rotor bar harmonic order.
ϕ	Delay angle.
e^s	Back electromotive force (EMF).
Λ	Magnetic permeance.
Z	Impedance.

Attributes

$\widehat{x}$	Amplitude or peak value of x.
x^s	x refers to the stator.
x^r	x refers to the rotor.
x^T	x refers to both stator and rotor.
$\mathbf{x}$	x is a complex variable.
$[x]$	Matrix.

$[x]^t$	Transposed matrix.
$[x]^{-1}$	Inverse matrix.
$[\mathbf{x}]^*$	Conjugate transposed matrix.
$x]_p$	p order row of the matrix $[x]$.
$x]_{i,j}$	i, j element of the matrix $[x]$.

Chapter 1

Introduction

1.1 Motivation and Objectives

The application of power electronics in electrical drive systems enables utilization of ac machines with a phase number higher than three. Some of the advantages of multiphase drives, when compared to the standard three-phase ones, are:

- The possibility to share the delivered power among more inverter legs, which reduces the current stress of each power device.
- Reduced current harmonic content in the direct current (DC) link in case of VSI fed drives.
- Higher reliability, since a multiphase machine can operate with an asymmetrical winding structure in case of loss of one or more inverter legs or machine phases.

Modeling the multiphase drives in the phase-variable reference frame leads to cross-coupled variables. To avoid the interdependence among variables some authors have proposed different methods that decompose the n-dimensional space model into decoupled orthogonal subspaces. These transformations simplify the multiphase drive model and the task of designing the control algorithm. One of these transformations is the VSD, in which each subspace current and voltage component is modeled as a complex number called spatial vector.

In a similar way as it happens in three-phase drives, in multiphase ones some non-linearities give rise to harmonics. Two main types of harmonics are going to be studied in this work, time and spatial harmonics [41–43]. Time harmonics are the harmonic components contained in the electrical signals (i.e., voltage and current waveforms). They can be produced by the converter deadtime, the PWM, fault states or imbalances of the converter feeding system. Spatial harmonics, on the other hand, are those in the magnetic field that are produced by flux saturation, the non-perfectly sinusoidal distribution of the windings or rotor eccentricity. These harmonics can generate undesirable effects such as torque ripple and electrical losses.

The study based on the VSD of the variables gives more information of each current and voltage component than the classical frequency analysis, i.e., the subspace where it maps and the SVR speed, that includes the frequency and the direction of rotation. This

analysis is useful for applications such as torque ripple prediction or cancellation, current harmonic compensation, sensorless speed measurement and machine current signature analysis. From the point of view of the drive performance the subspace where each component maps is important because, in motors with distributed windings, the harmonics that map into some specific subspaces generate electromechanical energy conversion, i.e., they can lead to torque ripple production; and in some subspaces the impedance is low, giving rise to high amplitude current harmonics even if voltage components are moderate. From the viewpoint of the current harmonics and torque ripple compensation, the subspace and SVR speed of each time harmonic is important for setting the controllers. In multiphase drives the common procedure to design the current controllers is to work with a decoupled model, such as the VSD model, where the signals that each controller governs are in one specific two-dimensional (2D) subspace. Therefore, for designing the current harmonic controllers it is necessary to know into which subspace each harmonic maps. Besides this, the current controllers to cancel each harmonic usually work in a rotating reference frame that must be set to the SVR speed of such current component.

Even in a healthy multiphase induction machine, stator current harmonics appear due to some non-ideal characteristics. The analysis of such harmonics, commonly called healthy machine current signature, by means of the VSD, helps in applications such as sensorless speed measurement and MCSA. For example, the identification of the subspace where the principal slot harmonics (PSHs) map and their SVR speeds, depending on the machine characteristics, helps in the designing process of sensorless speed measurement algorithms based on the principal slot harmonic (PSH) frequencies. From the standpoint of the MCSA methods, a good understanding of the healthy machine signature is necessary to make a correct interpretation of its changes under fault conditions; e.g., the static eccentricity detection systems by PSH monitoring used in three-phase motors need to know the healthy machine PSHs in order to compare them with the ones in fault condition.

The main objective of this dissertation is to develop a characterization of time and spatial harmonics in multiphase drives, conceived to be generic for any number of phases, that identifies the subspaces affected by each harmonic and predicts its SVR speed, which includes the frequency and the SVR direction. To accomplish this objective, the first step is to develop a simple method to predict the subspace where each time harmonic maps and its SVR speed in n-phase drives. The second step is to analyze the back EMF and stator induced current components produced by the spatial harmonics due to the stator and rotor current distributions, non-uniform airgap and magnetic saturation in n-phase motors. Then, the next step is to extend the harmonic mapping method to cover, besides the converter time harmonics, the induced stator currents due to the mentioned spatial harmonics in order to obtain the VSD of the healthy motor current signature. Finally, the last step is to develop a MCSA method for detecting pure static, dynamic and mixed eccentricities based on the VSD of the current signature.

1.2 Background and Review of Previous Research

1.2.1 The Symmetrical Multiphase Drive

Multiphase Drives

The terms multiphase motor drives and n-phase motor drives make reference to energy-conversion systems that use electric motors with a stator winding with more than three phases ($n > 3$) [4, 44–46]. The adoption of this technology in the industry has been increased, supported by the use of power converters in variable speed alternating current (AC) drives. The input stage of the drive has the same phase number of the main supply, but its output stage can have any number of phases. Therefore, the converter decouples the motor from the three-phase supply and allows to use machines with any number of phases in the stator windings [47, 48].

Multiphase Motor Model

In a symmetrical n-phase machine the angle between any consecutive two stator phases is $\alpha_c = 2\pi/n$ electrical degrees, called the Characteristic Angle, and each phase winding can be assumed to be equal to the others. The universal theory of electric machines (UTEM) is normally used to model this type of multiphase motors under the following assumptions [41, 49]:

- The stator windings are distributed in such a manner that the MMF it creates can be assumed to be sinusoidal. The rotor is also designed to produce a sinusoidal flux. Therefore, only the fundamental component of MMF is taken into account.

- The rotor MMF can be regarded as equivalent to the one produced by a winding with the same pole pairs and phases as the stator one. Thus, the effects of rotor bars in case of squirrel-cage rotor or the winding function harmonics in case of wounded rotor are neglected.

- The airgap is assumed to be uniform and its variations due to rotor eccentricities or rotor and stator slots are neglected.

- The magnetizing characteristic of the ferromagnetic material is assumed to be linear. Thus, the effects of magnetic saturation are not considered.

- The resistances and leakage inductances of the stator and rotor windings are regarded as constant. Their variations due to frequency or temperature changes are ignored.

- Hysteresis, eddy currents and parasitic capacitances are also neglected.

The equations that relate the stator voltage, currents and the flux linkage of a n-phase machine in the original phase variable domain provided by the UTEM are

$$\begin{aligned}[v^{\mathrm{s}}] &= [R^{\mathrm{s}}][i^{\mathrm{s}}] + \frac{d}{dt}[\psi^{\mathrm{s}}] \\ [v^{\mathrm{r}}] &= [R^{\mathrm{r}}][i^{\mathrm{r}}] + \frac{d}{dt}[\psi^{\mathrm{r}}]\end{aligned} \tag{1.1}$$

where

$$[v^{\mathrm{s}}] = [v_1^{\mathrm{s}}, v_2^{\mathrm{s}}, \ldots, v_n^{\mathrm{s}}]^t \qquad [v^{\mathrm{r}}] = [v_1^{\mathrm{r}}, v_2^{\mathrm{r}}, \ldots, v_n^{\mathrm{r}}]^t \tag{1.2}$$

are the stator and rotor voltage column vectors, respectively;

$$[i^{\mathrm{s}}] = [i_1^{\mathrm{s}}, i_2^{\mathrm{s}}, \ldots, i_n^{\mathrm{s}}]^t \qquad [i^{\mathrm{r}}] = [i_1^{\mathrm{r}}, i_2^{\mathrm{r}}, \ldots, i_n^{\mathrm{r}}]^t \tag{1.3}$$

are the stator and rotor current column vectors and

$$[\psi^{\mathrm{s}}] = [\psi_1^{\mathrm{s}}, \psi_2^{\mathrm{s}}, \ldots, \psi_n^{\mathrm{s}}]^t \qquad [\psi^{\mathrm{r}}] = [\psi_1^{\mathrm{r}}, \psi_2^{\mathrm{r}}, \ldots, \psi_n^{\mathrm{r}}]^t \tag{1.4}$$

are the stator and rotor flux linkage column vectors. The stator and rotor resistance matrices are diagonal $n \times n$ matrices, $[R^{\mathrm{s}}] = \mathrm{diag}(R^{\mathrm{s}})$ and $[R^{\mathrm{r}}] = \mathrm{diag}(R^{\mathrm{r}})$.

According to the multiple-coupled circuit theory, the flux linkage vectors can be rewritten as [50]

$$\begin{aligned}[\psi^{\mathrm{s}}] &= [L^{\mathrm{ss}}][i^{\mathrm{s}}] + [L^{\mathrm{sr}}][i^{\mathrm{r}}] \\ [\psi^{\mathrm{r}}] &= [L^{\mathrm{rr}}][i^{\mathrm{r}}] + [L^{\mathrm{rs}}][i^{\mathrm{s}}]\end{aligned} \tag{1.5}$$

where $[L^{\mathrm{ss}}]$ and $[L^{\mathrm{rr}}]$ are the stator and rotor inductance matrices, respectively, and $[L^{\mathrm{sr}}]$ and $[L^{\mathrm{rs}}]$ are the mutual stator-to-rotor and rotor-to-stator inductance matrices. Under the previously presented assumptions, the stator and rotor inductance matrices contain only constant coefficients and are $n \times n$ matrices:

$$[L^{\mathrm{ss}}] = \begin{bmatrix} L_{11}^{\mathrm{s}} & L_{12}^{\mathrm{s}} & L_{13}^{\mathrm{s}} & \ldots & L_{1n}^{\mathrm{s}} \\ L_{21}^{\mathrm{s}} & L_{22}^{\mathrm{s}} & L_{23}^{\mathrm{s}} & \ldots & L_{2n}^{\mathrm{s}} \\ \vdots & \vdots & \vdots & \ddots & \vdots \\ L_{n1}^{\mathrm{s}} & L_{n2}^{\mathrm{s}} & L_{n3}^{\mathrm{s}} & \ldots & L_{nn}^{\mathrm{s}} \end{bmatrix} \tag{1.6a}$$

$$[L^{\mathrm{rr}}] = \begin{bmatrix} L_{11}^{\mathrm{r}} & L_{12}^{\mathrm{r}} & L_{13}^{\mathrm{r}} & \ldots & L_{1n}^{\mathrm{r}} \\ L_{21}^{\mathrm{r}} & L_{22}^{\mathrm{r}} & L_{23}^{\mathrm{r}} & \ldots & L_{2n}^{\mathrm{r}} \\ \vdots & \vdots & \vdots & \ddots & \vdots \\ L_{n1}^{\mathrm{r}} & L_{n2}^{\mathrm{r}} & L_{n3}^{\mathrm{r}} & \ldots & L_{nn}^{\mathrm{r}} \end{bmatrix}. \tag{1.6b}$$

Based on the assumption that all individual phase windings in the stator are identical and the multiphase winding is symmetrical, phase self-inductances are equal, $L_{11}^{\mathrm{s}} = L_{22}^{\mathrm{s}} = \ldots = L_{nn}^{\mathrm{s}}$, and mutual inductances within the stator satisfy the condition $L_{ij}^{\mathrm{s}} = L_{ji}^{\mathrm{s}}$,

where $i \neq j$, $i, j = \{1, 2, \ldots, n\}$, [51]. Therefore, $[L^{\mathrm{ss}}]$ is at the same time symmetric and circulant matrix, i.e., its rows can be obtained by circular permutation. To obtain the $(j+1)$th row from the jth row, all elements of the hth row are shifted one step to the right and the last element of the kth row is copied in the first column of the (k + 1)th row [52]. $[L^{\mathrm{rr}}]$ is a symmetric and circulant matrix, according to the assumption that the rotor equivalent winding has all individual phases identical.

The stator-to-rotor $[L^{\mathrm{sr}}]$ and rotor-to-stator $[L^{\mathrm{rs}}]$ matrices have time-varying coefficients. This is caused by the fact that the relative position of the rotor windings regarding the stator windings and vice versa depend on the rotor angle θ_{r}, which changes due to the rotor rotation. Under the UTEM assumptions both flux densities, the one due to the stator and the one due to the rotor, are sinusoidal and the stator-to-rotor mutual inductance matrix is [53, 54]

$$[L^{\mathrm{sr}}] = M^{\mathrm{sr}} \begin{bmatrix} \cos(P\theta_{\mathrm{r}}) & \cos(P\theta_{\mathrm{r}}-\alpha_c) & \cos(P\theta_{\mathrm{r}}-2\alpha_c) & \ldots & \cos(P\theta_{\mathrm{r}}-(n-1)\alpha_c) \\ \cos(P\theta_{\mathrm{r}}+\alpha_c) & \cos(P\theta_{\mathrm{r}}) & \cos(P\theta_{\mathrm{r}}-\alpha_c) & \ldots & \cos(P\theta_{\mathrm{r}}-(n-2)\alpha_c) \\ \vdots & \vdots & \vdots & \ddots & \vdots \\ \cos(P\theta_{\mathrm{r}}+(n-1)\alpha_c) & \cos(P\theta_{\mathrm{r}}+(n-2)\alpha_c) & \cos(P\theta_{\mathrm{r}}+(n-3)\alpha_c) & \ldots & \cos(P\theta_{\mathrm{r}}) \end{bmatrix} \tag{1.7}$$

where, M is the mutual linkage between one stator and one rotor aligned phases, P are the pole pairs and θ_{r} is the rotor position angle. The rotor-to-stator is calculated as $[L^{\mathrm{rs}}] = [L^{\mathrm{sr}}]^t$. The stator-to-rotor $[L^{\mathrm{sr}}]$ and rotor-to-stator $[L^{\mathrm{rs}}]$ matrices are also symmetric and circulant.

The volt-ampere and torque equations of a n-phase machine can be written in matrix notation as [41, 42, 51, 55]

$$\begin{aligned} [v^{\mathrm{s}}] &= [R^{\mathrm{s}}][i^{\mathrm{s}}] + [L^{\mathrm{ss}}]\frac{d}{dt}[i^{\mathrm{s}}] + \frac{d}{dt}[L^{\mathrm{sr}}][i^{\mathrm{r}}] \\ [v^{\mathrm{r}}] &= [R^{\mathrm{r}}][i^{\mathrm{r}}] + [L^{\mathrm{rr}}]\frac{d}{dt}[i^{\mathrm{r}}] + \frac{d}{dt}[L^{\mathrm{rs}}][i^{\mathrm{s}}] \end{aligned} \tag{1.8}$$

and

$$T_{\mathrm{e}} = \begin{bmatrix} [i^{\mathrm{s}}]^t & [i^{\mathrm{r}}]^t \end{bmatrix} \frac{d}{d\theta_{\mathrm{r}}} \begin{bmatrix} [L^{\mathrm{ss}}] & [L^{\mathrm{sr}}] \\ [L^{\mathrm{sr}}] & [L^{\mathrm{rr}}] \end{bmatrix} \begin{bmatrix} [i^{\mathrm{s}}] \\ [i^{\mathrm{r}}] \end{bmatrix}. \tag{1.9}$$

Vector Space Decomposition

The variables in the machine model in the original phase-variable reference frame are cross-coupled. A variety of transformations has been proposed to avoid the coupling of variables [41, 56–58]. Such transformations decompose the n-dimensional space into orthogonal subspaces: several 2D subspaces (planes) and one or two one-dimensional (1D) subspaces (homopolar axes).

One of the methods to decompose the phase variables is the Clarke's decoupling transformation [47, 48, 59]. This transformation converts a vector of per-phase instantaneous real values (current or voltages) into n real values. The information of each plane is contained in sets of two consecutive rows of the matrix. The Clarke's transformation matrix

for a n-phase motor with n being an even number in its power invariant form is [48]

$$[\mathbf{C}] = \sqrt{\frac{2}{n}} \begin{bmatrix} 1 & \cos(\alpha_c) & \cos(2\alpha_c) & \cdots & \cos(2\alpha_c) & \cos(\alpha_c) \\ 0 & \sin(\alpha_c) & \sin(2\alpha_c) & \cdots & \sin(2\alpha_c) & \sin(\alpha_c) \\ 1 & \cos(2\alpha_c) & \cos(4\alpha_c) & \cdots & \cos(4\alpha_c) & \cos(2\alpha_c) \\ 0 & \sin(2\alpha_c) & \sin(4\alpha_c) & \cdots & \sin(4\alpha_c) & \sin(2\alpha_c) \\ \vdots & \vdots & \vdots & \ddots & \vdots & \vdots \\ 1 & \cos(\frac{n-2}{2}\alpha_c) & \cos(2\frac{n-2}{2}\alpha_c) & \cdots & \cos(2\frac{n-2}{2}\alpha_c) & \cos(\frac{n-2}{2}\alpha_c) \\ 0 & \sin(\frac{n-2}{2}\alpha_c) & \sin(2\frac{n-2}{2}\alpha_c) & \cdots & \sin(2\frac{n-2}{2}\alpha_c) & \sin(\frac{n-2}{2}\alpha_c) \\ \frac{1}{\sqrt{2}} & \frac{1}{\sqrt{2}} & \frac{1}{\sqrt{2}} & \cdots & \frac{1}{\sqrt{2}} & \frac{1}{\sqrt{2}} \\ \frac{1}{\sqrt{2}} & -\frac{1}{\sqrt{2}} & \frac{1}{\sqrt{2}} & \cdots & \frac{1}{\sqrt{2}} & -\frac{1}{\sqrt{2}} \end{bmatrix}. \quad (1.10)$$

The last two rows of the matrix $[\mathbf{C}]$ define the h^+ and h^- homopolar components, respectively. These two homopolar components appear in a motor with an even number of phases. In case the motor has an odd number of phases, there is not h^- component and the last row of the matrix $[\mathbf{C}]$ is omitted [48]. The equations that define the multiphase motor model decomposed into subspaces by applying the Clarke's decomposition (1.10) to the phase variable model (1.8) are

$$\begin{aligned}
\alpha_1\text{-}\beta_1 &\begin{cases} v^{\mathrm{s}}_{\alpha_1} = R^{\mathrm{s}}_{\alpha_1} i^{\mathrm{s}}_{\alpha_1} + L^{\mathrm{s}}_{\alpha_1} \frac{d}{dt} i^{\mathrm{s}}_{\alpha_1} + \frac{d}{dt} L^{\mathrm{sr}}_{\alpha_1} i^{\mathrm{r}}_{\alpha_1} \\ v^{\mathrm{s}}_{\beta_1} = R^{\mathrm{s}}_{\beta_1} i^{\mathrm{s}}_{\beta_1} + L^{\mathrm{s}}_{\beta_1} \frac{d}{dt} i^{\mathrm{s}}_{\beta_1} + \frac{d}{dt} L^{\mathrm{sr}}_{\beta_1} i^{\mathrm{r}}_{\beta_1} \end{cases} \\
\alpha_2\text{-}\beta_2 &\begin{cases} v^{\mathrm{s}}_{\alpha_2} = R^{\mathrm{s}}_{\alpha_2} i^{\mathrm{s}}_{\alpha_2} + L^{\mathrm{s}}_{\alpha_2} \frac{d}{dt} i^{\mathrm{s}}_{\alpha_2} + \frac{d}{dt} L^{\mathrm{sr}}_{\alpha_2} i^{\mathrm{r}}_{\alpha_2} \\ v^{\mathrm{s}}_{\beta_2} = R^{\mathrm{s}}_{\beta_2} i^{\mathrm{s}}_{\beta_2} + L^{\mathrm{s}}_{\beta_2} \frac{d}{dt} i^{\mathrm{s}}_{\beta_2} + \frac{d}{dt} L^{\mathrm{sr}}_{\beta_2} i^{\mathrm{r}}_{\beta_2} \end{cases} \\
&\vdots \\
\alpha_{p_m}\text{-}\beta_{p_m} &\begin{cases} v^{\mathrm{s}}_{\alpha_{pm}} = R^{\mathrm{s}}_{\alpha_{pm}} i^{\mathrm{s}}_{\alpha_{pm}} + L^{\mathrm{s}}_{\alpha_{pm}} \frac{d}{dt} i^{\mathrm{s}}_{\alpha_{pm}} + \frac{d}{dt} L^{\mathrm{sr}}_{\alpha_{pm}} i^{\mathrm{r}}_{\alpha_{pm}} \\ v^{\mathrm{s}}_{\beta_{pm}} = R^{\mathrm{s}}_{\beta_{pm}} i^{\mathrm{s}}_{\beta_{pm}} + L^{\mathrm{s}}_{\beta_{pm}} \frac{d}{dt} i^{\mathrm{s}}_{\beta_{pm}} + \frac{d}{dt} L^{\mathrm{sr}}_{\beta_{pm}} i^{\mathrm{r}}_{\beta_{pm}} \end{cases}
\end{aligned} \quad (1.11)$$

where $p_m = \lfloor \frac{n}{2} \rfloor$, for the stator volt-ampere equations; and

$$\begin{aligned}
\alpha_1\text{-}\beta_1 &\begin{cases} v^{\mathrm{r}}_{\alpha_1} = R^{\mathrm{r}}_{\alpha_1} i^{\mathrm{r}}_{\alpha_1} + L^{\mathrm{r}}_{\alpha_1} \frac{d}{dt} i^{\mathrm{r}}_{\alpha_1} + \frac{d}{dt} L^{\mathrm{rs}}_{\alpha_1} i^{\mathrm{s}}_{\alpha_1} \\ v^{\mathrm{r}}_{\beta_1} = R^{\mathrm{r}}_{\beta_1} i^{\mathrm{r}}_{\beta_1} + L^{\mathrm{r}}_{\beta_1} \frac{d}{dt} i^{\mathrm{r}}_{\beta_1} + \frac{d}{dt} L^{\mathrm{rs}}_{\beta_1} i^{\mathrm{s}}_{\beta_1} \end{cases} \\
\alpha_2\text{-}\beta_2 &\begin{cases} v^{\mathrm{r}}_{\alpha_2} = R^{\mathrm{r}}_{\alpha_2} i^{\mathrm{r}}_{\alpha_2} + L^{\mathrm{r}}_{\alpha_2} \frac{d}{dt} i^{\mathrm{r}}_{\alpha_2} + \frac{d}{dt} L^{\mathrm{rs}}_{\alpha_2} i^{\mathrm{s}}_{\alpha_2} \\ v^{\mathrm{r}}_{\beta_2} = R^{\mathrm{r}}_{\beta_2} i^{\mathrm{r}}_{\beta_2} + L^{\mathrm{r}}_{\beta_2} \frac{d}{dt} i^{\mathrm{r}}_{\beta_2} + \frac{d}{dt} L^{\mathrm{rs}}_{\beta_2} i^{\mathrm{s}}_{\beta_2} \end{cases} \\
&\vdots \\
\alpha_{p_m}\text{-}\beta_{p_m} &\begin{cases} v^{\mathrm{r}}_{\alpha_{pm}} = R^{\mathrm{r}}_{\alpha_{pm}} i^{\mathrm{r}}_{\alpha_{pm}} + L^{\mathrm{r}}_{\alpha_{pm}} \frac{d}{dt} i^{\mathrm{r}}_{\alpha_{pm}} + \frac{d}{dt} L^{\mathrm{rs}}_{\alpha_{pm}} i^{\mathrm{s}}_{\alpha_{pm}} \\ v^{\mathrm{r}}_{\beta_{pm}} = R^{\mathrm{r}}_{\beta_{pm}} i^{\mathrm{r}}_{\beta_{pm}} + L^{\mathrm{r}}_{\beta_{pm}} \frac{d}{dt} i^{\mathrm{r}}_{\beta_{pm}} + \frac{d}{dt} L^{\mathrm{rs}}_{\beta_{pm}} i^{\mathrm{s}}_{\beta_{pm}} \end{cases}
\end{aligned} \quad (1.12)$$

for the rotor volt-ampere equations.

Each subspace p in the decoupled model, shown in (1.11) and (1.12), contains two stator voltage components $v^{\mathrm{s}}_{\alpha_p}$ and $v^{\mathrm{s}}_{\beta_p}$, two rotor voltage components $v^{\mathrm{r}}_{\alpha_p}$ and $v^{\mathrm{r}}_{\beta_p}$, two stator current components $i^{\mathrm{s}}_{\alpha_p}$ and $i^{\mathrm{s}}_{\beta_p}$, and two rotor current components , $i^{\mathrm{r}}_{\alpha_p}$ and $i^{\mathrm{r}}_{\beta_p}$. Both variables in each of these pairs, e.g., $v^{\mathrm{s}}_{\alpha_p}$ and $v^{\mathrm{s}}_{\beta_p}$, are mutually perpendicular [49]. Therefore, by assuming one of the components as the real part and the other component as the imaginary part, each voltage or current variable in a plane can be defined as a complex number. Such complex variables are known as space vectors.

Another variable decoupling method, focused on obtaining the space vectors of the motor variables in each subspace, is the symmetrical components or Fortescue's transformation [41, 57, 60]. The symmetrical components VSD matrix is [41]

$$[\mathbf{T}] = \frac{1}{\sqrt{n}} \begin{bmatrix} \mathbf{a}^0 & \mathbf{a}^0 & \mathbf{a}^0 & \cdots & \mathbf{a}^0 \\ \mathbf{a}^0 & \mathbf{a}^1 & \mathbf{a}^2 & \cdots & \mathbf{a}^{1(n-1)} \\ \mathbf{a}^0 & \mathbf{a}^2 & \mathbf{a}^{2\cdot 2} & \cdots & \mathbf{a}^{2(n-1)} \\ \vdots & \vdots & \vdots & \ddots & \vdots \\ \mathbf{a}^0 & \mathbf{a}^p & \mathbf{a}^{p\cdot 2} & \cdots & \mathbf{a}^{p(n-1)} \\ \vdots & \vdots & \vdots & \ddots & \vdots \\ \mathbf{a}^0 & \mathbf{a}^{n-1} & \mathbf{a}^{(n-1)2} & \cdots & \mathbf{a}^{(n-1)(n-1)} \end{bmatrix} \tag{1.13}$$

where $\mathbf{a} = e^{\hat{\jmath}\cdot\alpha_c}$ and $p \in [0, n-1]$.

In the symmetrical components matrix each row vector corresponds to a complex subspace [41]. The first row of the matrix $[\mathbf{T}]$ gives the space vector of the components that map into the positive homopolar axis h^+. If the number of phases n is odd, rows from $p = 1$ to $p = (n-1)/2$ give the space vectors that map to planes α_p-β_p in complex form and rows from $p = (n+1)/2$ to $p = n-1$ are the conjugated form of the complex variables from $p = 1$ to $p = (n-1)/2$. If the number of phases n is even, rows from $p = 1$ to $p = n/2-1$ map to planes α_p-β_p in complex form and the $p = n/2$ row gives the components that map into the negative homopolar component axis h^-. The rows from $p = n/2+1$ to $p = n-1$ are the conjugated form of variables from $p = 1$ to $p = n/2-1$.

The original input variables can be real, imaginary or complex [41]. If this transformation receives per phase complex variables as input, it separates the space vectors rotating with positive and negative directions in different subspaces. The positive rotating space vectors are given by the first set of planes of the matrix and the negative rotating space vectors are given by their conjugated rows [41]. If, on the other hand, the symmetrical components matrix is used with a vector of real values as input, it combines the information of the positive and negative sequences in each plane [41, 61]. Therefore, the conjugated rows do not give any extra information about the subspaces and can be deprecated [41, 61].

The symmetrical components matrix is unitary, $[\mathbf{T}]^* = [\mathbf{T}]^{-1}$, and consequently, if $[A]$ is an $n \times n$ symmetrical and circulant matrix, it can be transformed into a diagonal matrix $[A]^t$ by using the transformation $[A]^t = [\mathbf{T}][A][\mathbf{T}]^{-1}$, [41, 52, 55]. The volt-ampere and torque equations transformed by using the symmetrical components method can be

written in matrix notation as [52, 55]

$$\begin{aligned}\underbrace{[\mathbf{T}][v^{\mathrm{s}}]}_{[\mathbf{v}^{\mathrm{s}}_{\alpha\beta}]} &= \underbrace{[\mathbf{T}]r_s[\mathbf{T}]^{-1}}_{[\mathbf{R}^{\mathrm{s}}_{\alpha\beta}]}\underbrace{[\mathbf{T}][i^{\mathrm{s}}]}_{[\mathbf{i}^{\mathrm{s}}_{\alpha\beta}]} + \underbrace{[\mathbf{T}][L^{\mathrm{ss}}][\mathbf{T}]^{-1}}_{[\mathbf{L}^{\mathrm{ss}}_{\alpha\beta}]}\frac{d}{dt}\underbrace{[\mathbf{T}][i^{\mathrm{s}}]}_{[\mathbf{i}^{\mathrm{s}}_{\alpha\beta}]} \\ &\quad + \frac{d}{dt}\underbrace{[\mathbf{T}][L^{\mathrm{sr}}][\mathbf{T}]^{-1}}_{[\mathbf{L}^{\mathrm{sr}}_{\alpha\beta}]}\underbrace{[\mathbf{T}][i^{\mathrm{r}}]}_{[\mathbf{i}^{\mathrm{r}}_{\alpha\beta}]} \\ \underbrace{[\mathbf{T}][v^{\mathrm{r}}]}_{[\mathbf{v}^{\mathrm{r}}_{\alpha\beta}]} &= \underbrace{[\mathbf{T}]r_r[\mathbf{T}]^{-1}}_{[\mathbf{R}^{\mathrm{r}}_{\alpha\beta}]}\underbrace{[\mathbf{T}][i^{\mathrm{r}}]}_{[\mathbf{i}^{\mathrm{r}}_{\alpha\beta}]} + \underbrace{[\mathbf{T}][L^{\mathrm{rr}}][\mathbf{T}]^{-1}}_{[\mathbf{L}^{\mathrm{rr}}_{\alpha\beta}]}\frac{d}{dt}\underbrace{[\mathbf{T}][i^{\mathrm{r}}]}_{[\mathbf{i}^{\mathrm{r}}_{\alpha\beta}]} \\ &\quad + \frac{d}{dt}\underbrace{[\mathbf{T}][L^{\mathrm{rs}}][\mathbf{T}]^{-1}}_{[\mathbf{L}^{\mathrm{rs}}_{\alpha\beta}]}\underbrace{[\mathbf{T}][i^{\mathrm{s}}]}_{[\mathbf{i}^{\mathrm{s}}_{\alpha\beta}]}\end{aligned} \tag{1.14}$$

and

$$T_{\mathrm{e}} = \begin{bmatrix}[\mathbf{i}^{\mathrm{s}}_{\alpha\beta}]^* & [\mathbf{i}^{\mathrm{r}}_{\alpha\beta}]^*\end{bmatrix}\frac{d}{d\theta_{\mathrm{r}}}\begin{bmatrix}[\mathbf{L}^{\mathrm{ss}}_{\alpha\beta}] & [\mathbf{L}^{\mathrm{sr}}_{\alpha\beta}] \\ [\mathbf{L}^{\mathrm{sr}}_{\alpha\beta}] & [\mathbf{L}^{\mathrm{rr}}_{\alpha\beta}]\end{bmatrix}\begin{bmatrix}[\mathbf{i}^{\mathrm{s}}_{\alpha\beta}] \\ [\mathbf{i}^{\mathrm{r}}_{\alpha\beta}]\end{bmatrix}. \tag{1.15}$$

As r_s, r_r, $[L^{\mathrm{ss}}]$, $[L^{\mathrm{rr}}]$, $[L^{\mathrm{sr}}]$ and $[L^{\mathrm{rs}}]$ are $n \times n$ symmetrical and circulant matrices, $[\mathbf{R}^{\mathrm{s}}_{\alpha\beta}]$, $[\mathbf{R}^{\mathrm{r}}_{\alpha\beta}]$, $[\mathbf{L}^{\mathrm{ss}}_{\alpha\beta}]$, $[\mathbf{L}^{\mathrm{rr}}_{\alpha\beta}]$, $[\mathbf{L}^{\mathrm{sr}}_{\alpha\beta}]$ and $[\mathbf{L}^{\mathrm{rs}}_{\alpha\beta}]$ are diagonal $n \times n$ matrices and the machine model equations in this reference frame are decoupled.

The stator voltage equations of multiphase motor model after the VSD are

$$\begin{aligned}\mathbf{v}^{\mathrm{s}}_{\alpha\beta}]_0 &= \mathbf{R}^{\mathrm{s}}_{\alpha\beta}]_0\mathbf{i}^{\mathrm{s}}_{\alpha\beta}]_0 + \mathbf{L}^{\mathrm{ss}}_{\alpha\beta}]_0\frac{d}{dt}\mathbf{i}^{\mathrm{s}}_{\alpha\beta}]_0 + \frac{d}{dt}\mathbf{L}^{\mathrm{sr}}_{\alpha\beta}]_0\mathbf{i}^{\mathrm{r}}_{\alpha\beta}]_0 \\ \mathbf{v}^{\mathrm{s}}_{\alpha\beta}]_1 &= \mathbf{R}^{\mathrm{s}}_{\alpha\beta}]_1\mathbf{i}^{\mathrm{s}}_{\alpha\beta}]_1 + \mathbf{L}^{\mathrm{ss}}_{\alpha\beta}]_1\frac{d}{dt}\mathbf{i}^{\mathrm{s}}_{\alpha\beta}]_1 + \frac{d}{dt}\mathbf{L}^{\mathrm{sr}}_{\alpha\beta}]_1\mathbf{i}^{\mathrm{r}}_{\alpha\beta}]_1 \\ &\dots \\ \mathbf{v}^{\mathrm{s}}_{\alpha\beta}]_p &= \mathbf{R}^{\mathrm{s}}_{\alpha\beta}]_p\mathbf{i}^{\mathrm{s}}_{\alpha\beta}]_p + \mathbf{L}^{\mathrm{ss}}_{\alpha\beta}]_p\frac{d}{dt}\mathbf{i}^{\mathrm{s}}_{\alpha\beta}]_p + \frac{d}{dt}\mathbf{L}^{\mathrm{sr}}_{\alpha\beta}]_p\mathbf{i}^{\mathrm{r}}_{\alpha\beta}]_p \\ &\dots \\ \mathbf{v}^{\mathrm{s}}_{\alpha\beta}]_n &= \mathbf{R}^{\mathrm{s}}_{\alpha\beta}]_n\mathbf{i}^{\mathrm{s}}_{\alpha\beta}]_n + \mathbf{L}^{\mathrm{ss}}_{\alpha\beta}]_n\frac{d}{dt}\mathbf{i}^{\mathrm{s}}_{\alpha\beta}]_n + \frac{d}{dt}\mathbf{L}^{\mathrm{sr}}_{\alpha\beta}]_n\mathbf{i}^{\mathrm{r}}_{\alpha\beta}]_n\end{aligned} \tag{1.16}$$

and the rotor voltage equations are

$$\begin{aligned}\mathbf{v}^{\mathrm{r}}_{\alpha\beta}]_0 &= \mathbf{R}^{\mathrm{r}}_{\alpha\beta}]_0\mathbf{i}^{\mathrm{r}}_{\alpha\beta}]_0 + \mathbf{L}^{\mathrm{rr}}_{\alpha\beta}]_0\frac{d}{dt}\mathbf{i}^{\mathrm{r}}_{\alpha\beta}]_0 + \frac{d}{dt}\mathbf{L}^{\mathrm{rs}}_{\alpha\beta}]_0\mathbf{i}^{\mathrm{s}}_{\alpha\beta}]_0 \\ \mathbf{v}^{\mathrm{r}}_{\alpha\beta}]_1 &= \mathbf{R}^{\mathrm{r}}_{\alpha\beta}]_1\mathbf{i}^{\mathrm{r}}_{\alpha\beta}]_1 + \mathbf{L}^{\mathrm{rr}}_{\alpha\beta}]_1\frac{d}{dt}\mathbf{i}^{\mathrm{r}}_{\alpha\beta}]_1 + \frac{d}{dt}\mathbf{L}^{\mathrm{rs}}_{\alpha\beta}]_1\mathbf{i}^{\mathrm{s}}_{\alpha\beta}]_1 \\ &\dots \\ \mathbf{v}^{\mathrm{r}}_{\alpha\beta}]_p &= \mathbf{R}^{\mathrm{r}}_{\alpha\beta}]_p\mathbf{i}^{\mathrm{r}}_{\alpha\beta}]_p + \mathbf{L}^{\mathrm{rr}}_{\alpha\beta}]_p\frac{d}{dt}\mathbf{i}^{\mathrm{r}}_{\alpha\beta}]_p + \frac{d}{dt}\mathbf{L}^{\mathrm{rs}}_{\alpha\beta}]_p\mathbf{i}^{\mathrm{s}}_{\alpha\beta}]_p \\ &\dots \\ \mathbf{v}^{\mathrm{r}}_{\alpha\beta}]_n &= \mathbf{R}^{\mathrm{r}}_{\alpha\beta}]_n\mathbf{i}^{\mathrm{r}}_{\alpha\beta}]_n + \mathbf{L}^{\mathrm{rr}}_{\alpha\beta}]_n\frac{d}{dt}\mathbf{i}^{\mathrm{r}}_{\alpha\beta}]_n + \frac{d}{dt}\mathbf{L}^{\mathrm{rs}}_{\alpha\beta}]_n\mathbf{i}^{\mathrm{s}}_{\alpha\beta}]_n\end{aligned} \tag{1.17}$$

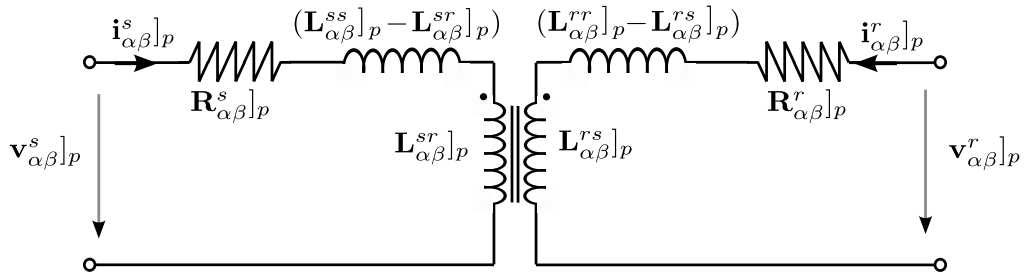

Figure 1.1: Equivalent circuit for the α_p-β_p subspace of the decoupled multiphase motor model.

where, for a vector $[X]$, the notation $X]_k$ makes reference to its kth element and, for a matrix $[Y]$, $Y]_k$ makes reference to the element in the kth column and kth row. Therefore, each subspace p can be modeled as an independent circuit with the scheme shown in Fig. 1.1 [41].

Sinusoidal Flux Density in Multiphase Induction Motors

The basic needed assumption for UTEM to be valid is that the magnetic flux in the airgap produced by each phase of the stator and rotor windings is sinusoidal, i.e., the flux is sinusoidally distributed in space [41, 52]. As a consequence of this hypothesis, the rotor-stator mutual inductances are sinusoidal functions of the machine angle and the transformed mutual inductance matrix becomes [41]

$$[\mathbf{L}^{\mathrm{sr}}_{\alpha\beta}] = [\mathbf{T}][L^{\mathrm{rs}}][\mathbf{T}]^{-1} = \begin{bmatrix} 0 & 0 & 0 & \dots & 0 \\ 0 & L^{sr}_{\alpha} + \hat{\jmath} L^{sr}_{\beta} & 0 & \dots & 0 \\ 0 & 0 & 0 & \dots & 0 \\ \vdots & \vdots & \vdots & \ddots & \vdots \\ 0 & 0 & 0 & \dots & L^{sr}_{\alpha} - \hat{\jmath} L^{sr}_{\beta} \end{bmatrix}. \tag{1.18}$$

Hence, under the flux sinusoidal condition, some of the transformed mutual inductances become 0, as it can be seen in (1.18), and the resulting mutual inductance matrix $[\mathbf{L}^{\mathrm{sr}}_{\alpha\beta}]$ is significantly simplified. Therefore, in the decoupled model shown in (1.14) the stator-to-rotor and rotor-to-stator coupling inductances of some subspaces are 0, so in such subspaces there is no coupling between the stator and the rotor. Hence, in this type of subspace, the equivalent circuit shown in Fig. 1.1 is simplified. To distinguish them from the subspaces where there is coupling between the stator and the rotor, the former are called x-y planes. Such subspaces do not contribute to the torque production and have a lower impedance than the α-β subspace [41, 48]. Thus, by using the UTEM simplification, the multiphase motor model is decomposed into three different types of subspaces: α-β, x-y and homopolar axes [48, 62].

Following this simplification, the volt-ampere equations particularized for a multiphase

induction motor with short-circuited rotor become

$$\begin{aligned}
\mathbf{v}^{\mathrm{s}}_{h+} &= \mathbf{R}^{\mathrm{s}}_{h+}\mathbf{i}^{\mathrm{s}}_{h+} + L^{\mathrm{ls}}\frac{d}{dt}\mathbf{i}^{\mathrm{s}}_{h+} \\
\mathbf{v}^{\mathrm{s}}_{\alpha\beta} &= \mathbf{R}^{\mathrm{s}}_{\alpha\beta}\mathbf{i}^{\mathrm{s}}_{\alpha\beta} + \mathbf{L}^{\mathrm{ss}}_{\alpha\beta}\frac{d}{dt}\mathbf{i}^{\mathrm{s}}_{\alpha\beta} + \frac{d}{dt}\mathbf{L}^{\mathrm{sr}}_{\alpha\beta}\mathbf{i}^{\mathrm{r}}_{\alpha\beta} \\
\mathbf{v}^{\mathrm{s}}_{xy1} &= \mathbf{R}^{\mathrm{s}}_{xy1}\mathbf{i}^{\mathrm{s}}_{xy1} + L^{\mathrm{ls}}\frac{d}{dt}\mathbf{i}^{\mathrm{s}}_{xy1} \\
&\cdots,
\end{aligned} \tag{1.19}$$

where L^{ls} is the stator leakage inductance, for the stator, and

$$0 = \mathbf{R}^{\mathrm{r}}_{\alpha\beta}\mathbf{i}^{\mathrm{r}}_{\alpha\beta} + \mathbf{L}^{\mathrm{rr}}_{\alpha\beta}\frac{d}{dt}\mathbf{i}^{\mathrm{r}}_{\alpha\beta} + \frac{d}{dt}\mathbf{L}^{\mathrm{rs}}_{\alpha\beta}\mathbf{i}^{\mathrm{s}}_{\alpha\beta} \tag{1.20}$$

for the rotor. The equivalent circuit of each type of subspace for steady-state operation is shown in Fig. 1.2 [62, 63]. If the motor model is decoupled by using the [**T**] matrix VSD, the row $p = 0$ belongs to the h^+ homopolar axis. If there is neutral connection between the motor and the converter, the equivalent circuit of this subspace is the one shown in Fig. 1.2.c. The row $p = 1$ corresponds to the α-β plane of the motor. This subspace is the one where the electromechanical energy conversion takes place and its equivalent circuit in steady state is shown in Fig. 1.2.a. If the motor has an odd number of phases, the rows from $p = 2$ to $p = (n-1)/2$ and from $p = (n+1)/2$ to $p = n-1$ correspond to x-y planes; the equivalent circuit is shown in Fig. 1.2.b. If the number of phases of the motor n is even, the rows from $p = 2$ to $p = n/2 - 1$ and from $p = n/2 + 1$ to $p = n - 1$ correspond to x-y planes, and the $p = n/2$ row is associated to the h^- axis and its equivalent circuit is shown in Fig. 1.2.c.

Multiphase Induction Motor Control

The model of the multiphase induction motor with short-circuited rotor, which is shown in Fig. 1.2 and described by (1.19) and (1.20), only produces torque with the current components in the α-β plane. The equivalent circuit of such plane in the multiphase induction motor, when analyzed by means of the VSD, is analogous to the one in its three-phase counterpart [48, 64]. Therefore, under the assumption of sinusoidal flux density in the airgap, the control of the torque, speed and position of a multiphase induction motor can be derived from the ones known for three-phase induction motors [48]. Control algorithms for n-phase induction motors obtained from the three-phase field oriented control (FOC) and direct torque control systems are described in [48].

The block diagram of an indirect FOC for a n-phase induction motor is shown in Fig. 1.3, where ϕ_r represents the rotor flux angle [65]. The control scheme is practically equal to the three-phase one. The main difference is the transformation matrix used to obtain the decoupled 2D subspaces at which each current controller is implemented.

In the multiphase motors, the current control can be also done in a non-rotational frame (i.e., in the α-β or x-y instead of the $d-q$ frame) by using any of the already known AC current regulators, such as proportional-integral (PI) controllers in a rotating reference frame [48], proportional-resonant (PR) controllers [4] or vector PI controllers [23].

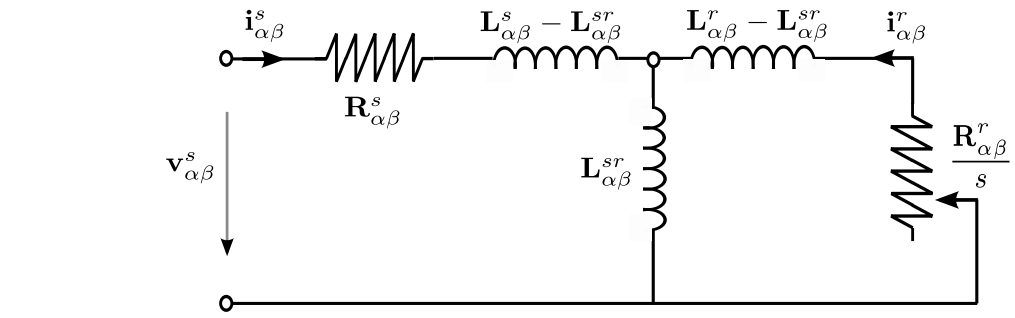

(a) α-β subspace.

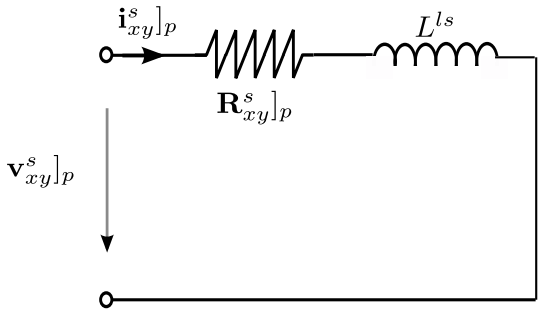

(b) x_p-y_p subspaces.

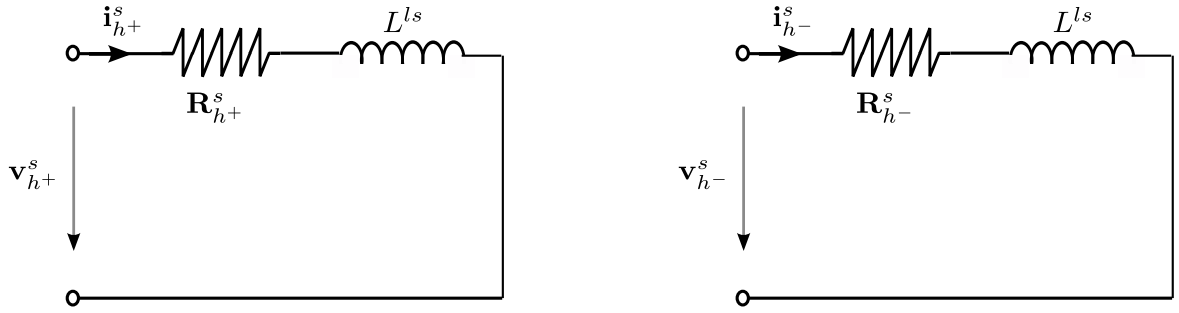

(c) Homopolar axes (if there is neutral connection).

Figure 1.2: Subspace equivalent circuit of a multiphase induction motor.

The x-y planes in multiphase induction motors with sinusoidal flux density have a lower impedance than the α-β plane, as it can be seen in the model described by (1.19) and (1.20) [48, 65]. The fundamental component of the current maps into the α-β subspace, but due to some converter nonlinearities such as the deadtime, voltage harmonics that map into some of the x-y planes of the induction motor arise [65]. These voltage harmonics, even with low amplitudes, can produce current harmonics with a considerable amplitude due to the low impedance of such subspace [53, 65]. This fact can lead to additional losses in the motor. Owing to this problem, some authors have proposed control algorithms for multiphase motors that cancel those harmonics that map into the x-y subspaces [4, 65, 66].

In the last few years, new controls have been proposed for multiphase motors, such as the direct torque control and predictive controls [67–71]. Another field of research in multiphase motors that has increased its importance in the last few years is the fault tolerant motor control [68, 71–74].

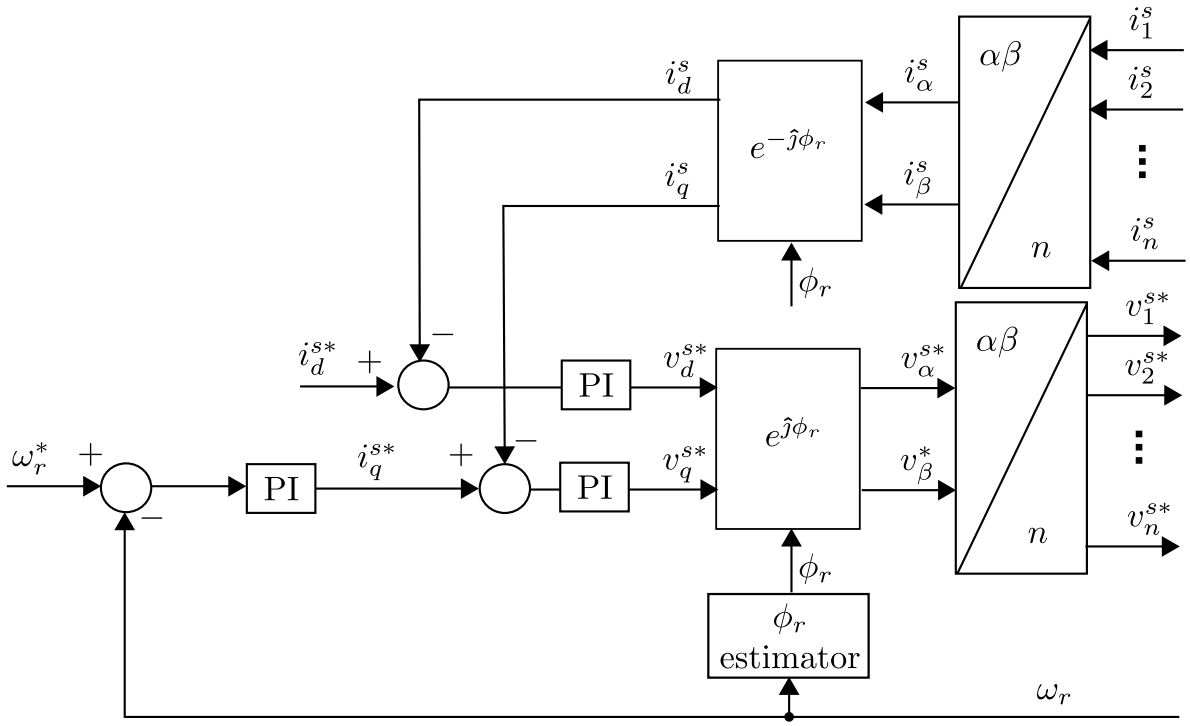

Figure 1.3: Indirect FOC control of a n-phase induction motor.

Series-Connected Multimotor Drives

As the previous section explains, the torque and flux of sinusoidally distributed multiphase machines can be controlled by using only two stator components. This means that, in machines with a phase number greater than three there exist additional degrees of freedom. Instead of using them to enhance the torque production [75] or for fault tolerance [76], in a multimotor drive system they may be also employed to independently control a group of series-connected machines fed from a single current controlled VSI [54, 77–82].

In order to achieve such an independent control it is necessary to connect the stator windings of the machines in series with an appropriate phase transposition, as it is shown in Fig. 1.4 [54, 77–79, 81–83]. In this figure, l_t represents the order of the phase transposition and $\delta = l_t 2\pi/n$ is the spatial angle in electrical degrees between two consecutive phases. In the multiphase motor model proposed by the UTEM, the electromechanical energy conversion occurs only in the α-β plane. With the phase transposition in the series connection between motors, the current components that go to the electromechanical conversion related plane in one machine go to other than the electromechanical conversion plane in the other machines [54, 77–79, 81–83]. Examples of the phase transposition in the series connection, in the specific cases of a 5-5 and 6-6 multimotor drive, are shown in Fig. 1.5 [5, 80] and Fig. 1.6 [21, 78, 79], respectively.

To control the series-connected multimotor system, the reference for the converter current control is the summation of the multiphase current set to control each machine

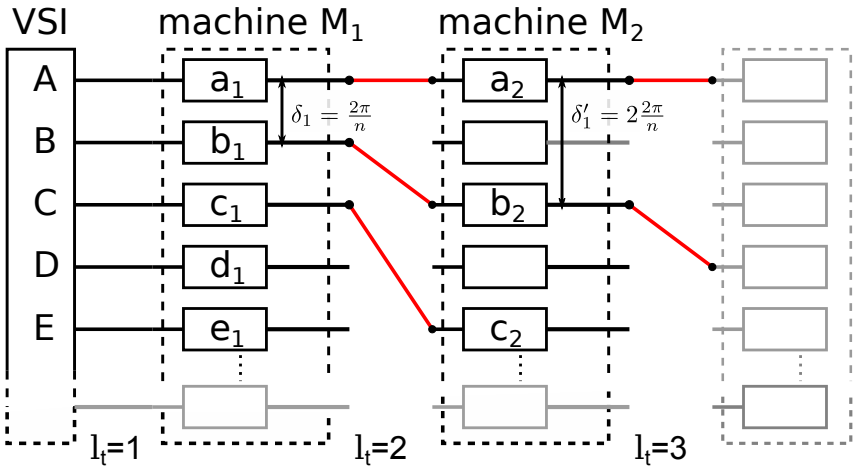

Figure 1.4: Physical phase transposition in the series connection in a multimotor drive.

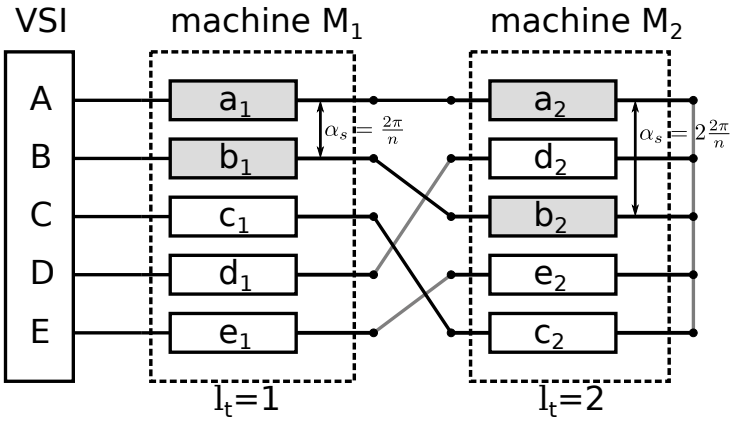

Figure 1.5: Example of series connection of a 5-5 multimotor drive.

[78, 79, 82]:

$$[i^s]^* = [i^s_{M_1}]^* + [i^s_{M_2}]^* + ... = \widehat{i}_1 \begin{bmatrix} \sin(\omega_{s,1}t) \\ \sin(\omega_{s,1}t + \frac{2\pi}{n}) \\ \sin(\omega_{s,1}t + \frac{4\pi}{n}) \\ \vdots \\ \sin(\omega_{s,1}t + \eta\frac{2\pi}{n}) \\ \vdots \end{bmatrix} + \widehat{i}_2 \begin{bmatrix} \sin(\omega_{s,2}t) \\ \sin(\omega_{s,2}t + \frac{4\pi}{n}) \\ \sin(\omega_{s,2}t + \frac{8\pi}{n}) \\ \vdots \\ \sin(\omega_{s,2}t + \eta\frac{4\pi}{n}) \\ \vdots \end{bmatrix} + \dots \quad (1.21)$$

where the subindex 1 represents the control variables of M_1, $\widehat{i}_1$ and $\widehat{i}_2$ are the current amplitudes, $\omega_{s,1}$ and $\omega_{s,2}$ are the angular frequency and $\eta = 0, ..., (n-1)$ represents the phase index.

The multi-motor topologies more commonly studied for industrial applications are the two-motor five-phase and six-phase drives [82]. It has been suggested that the two-motor five-phase drive can be a good option in winder applications, when compared to the standard solution with two three-phase motors supplied by two three-phase VSIs. Its three

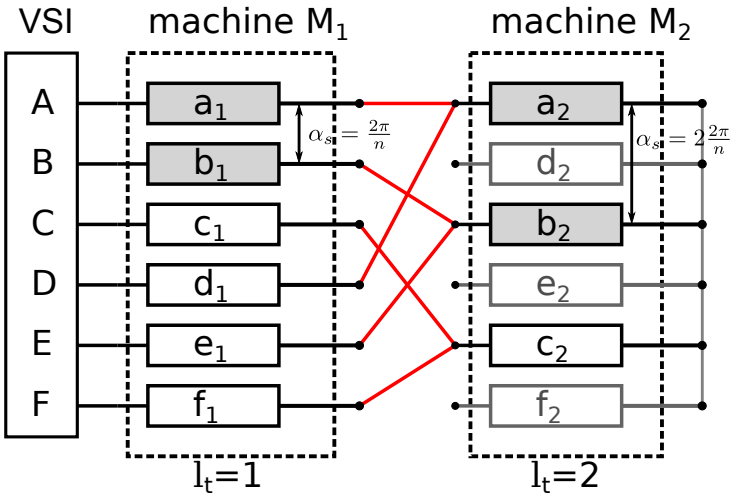

Figure 1.6: Example of series connection of a 6-6 multimotor drive.

main advantages over the three-phase counterpart are: a saving in the number of inverter legs, easiness in implementing the vector control algorithm in a single microcontroller and direct transmission of the braking energy between motors. Its main disadvantage is an increase in the stator winding losses in each of the two machines, since flux/torque producing currents of both machines pass through the stator windings of each one. The specific case of the series-connected six-phase two-motor drive has been developed and studied in [78–80], where the equivalence between a system of two series-connected six-phase motors and a system with series-connected six- and three-phase motors is presented. Because of the phase transposition in the series connection, only three phases in the second six-phase machine are used, so it can be physically substituted in the system by a three-phase machine. The main advantage of this multimotor topology, compared with other series-connected two-motor drive configurations, is that the series-connection does not produce any losses because of the circulation of the flux- and torque-producing currents of the six-phase machine through the three-phase windings [78, 79]. In addition, if the six-phase power rating is large compared to the three-phase one, the extra losses produced by the circulation of the three-phase motor flux- and torque-producing currents through the six-phase machine can be neglected [78]. The main disadvantage of the six-phase two-motor drive configuration is that there is no reduction in the total number of inverter legs compared to the system formed from two independent three-phase drives.

To achieve the independent control of the machines in a multi-motor drive, a sinusoidal spatial flux distribution in all the machine stators is needed and only sinusoidal MMF distribution ensures that there is no coupling between the machines [80, 84]. Due to nonlinearities, low order harmonics appear in the system. These harmonics produce additional losses and parasitic torques in the series-connected system. Two main types of harmonics are present in multiphase machines: time and spatial harmonics [41–43].

The effects of the spatial harmonics in a five- and a six-phase two-motor drive are taken into account in [84]. Such paper studies the influence on the M_I torque due to the interactions between the winding function harmonics of M_I and the fundamental current of M_{II}. The resulting rotating fields in M_I due to $[i^s_{M_2}]$ in a five-phase two-motor drive are shown in Table 1.1, where MMF+ and MMF- indicate that the interaction between the

TABLE 1.1
i_{II} INTERACTIONS WITH THE SPATIAL $\mathrm{M_I}$ MOTOR HARMONICS IN A FIVE-PHASE TWO-MOTOR DRIVE

$\mathrm{M_I}$ spatial harmonic set	$[i^s_{M_2}]$ effects in $\mathrm{M_I}$ field
$5k-3$	MMF+
$5k-2$	MMF-
$5k-1$	-
$5k$	-
$5k+1$	-
$5k+2$	MMF+
$5k+3$	MMF-

spatial harmonic set and the fundamental current of the second motor generates a positive and negative rotating field in the airgap, respectively. In the second row, − indicates that the interaction between the spatial harmonic set and the second motor current does not produce a rotating field in the airgap. The direction in which a certain field component rotates is considered as positive or negative depending on whether it coincides with that of the fundamental or not. The conclusions of [84] have shown that the spatial harmonics of $\mathrm{M_{II}}$ produce crossed interactions in $\mathrm{M_I}$ torque. However, the effects on the $\mathrm{M_{II}}$ torque due to the current of $\mathrm{M_I}$ are not studied. In addition to this fact, a more general study that covers the mapping of time harmonics in each motor in a series-connected multimotor drive and that can be applied to all the known valid combinations of phase numbers and series-connected motors (i.e., 5-5, 6-6, 7-7-7, 9-9-9-3, ...) is still to be done.

Time Harmonic Mapping

Time harmonics are the harmonic components contained in the electrical signals (i.e., voltage and current waveforms). They can be produced by deadtime [65, 85], the PWM [63, 86, 87] or imbalances of the feeding system [88].

In the multiphase motor model decoupled by using the sinusoidal flux density assumption, shown in Fig. 1.2, the time harmonics that are involved in the electromechanical energy conversion are mapped in the first plane, commonly called α-β plane, while the harmonics that are not can be found in the remaining planes, commonly called x-y planes, or in the homopolar axes, commonly called h^+ and h^- axis [41, 48, 62, 89]. Therefore, only the current harmonic components in the α-β can contribute to the torque production or generate torque ripple. The equations that describe this model, (1.19) and (1.20), show that the x-y plane impedance only includes the stator resistance and leakage inductance. Hence, low voltage harmonics may lead to high current harmonics [47, 48, 56, 62]. The impedance of the homopolar axes is usually very high or very low depending on whether the neutrals are connected or not [48]. Consequently, the non-mechanical energy conversion related harmonics should be controlled to reduce the extra losses in the machine [65]. In this manner, mapping each input voltage harmonic into the corresponding subspace helps to identify which voltage harmonics will contribute to the air-gap flux (and, thus,

to electromechanical conversion) and which ones will not.

Knowing the speed and direction of rotation of the vector space of each harmonic is important for the current harmonic compensation, where the controller should be set to the same frequency and sequence as the harmonic to be canceled. The SVR speed identification of the current harmonics in all the planes is important as in the case of concentrated winding machines, because in them, all the subspaces contribute to flux and torque production [75, 90–92]. Depending on the speed and direction of rotation of the vector space of each current harmonic, the torque produced by such harmonic can contribute or drain the overall torque or produce torque ripple.

Most of the previous work about time harmonic mapping deals with machines with a specific number of phases and with specific stator winding distributions. Multiphase machines can be classified into two groups attending to their stator winding distribution, symmetrical and asymmetrical machines. In symmetrical multiphase machines, the spatial displacement between any two consecutive stator phases is always the same and equals $\alpha = 2\pi/n$. In asymmetrical multiphase machines, the stator phases are not placed equidistantly along the circumference of the machine [47, 48]. The asymmetrical six-phase machine was studied in [62] by considering a two independent plane model: one that involves electromechanical energy conversion and another one that does not. The study in [62] was extended in [53, 56, 93], which carried out the full harmonic plane mapping for an asymmetrical six-phase machine including both homopolar axes as a third plane that is orthogonal to the other two. A general equation to map the time harmonics for asymmetrical machines is provided by [94].

In multiphase symmetrical machines, a remarkable contribution to the study of harmonic mapping has been done in [43]. This paper provides a harmonic mapping equation of the α-β plane for a generic n-phase symmetrical machine and for odd order harmonics. Nevertheless, the planes not related to electromechanical conversion were not considered, and equations for harmonic identification in the x-y planes and homopolar axes were not provided. The harmonic plane mapping of five-phase induction machines was carried out in [95, 96], obtaining the same results as in [43] for the α-β plane. For the x-y subspace harmonic identification, each proposal has introduced a new equation for odd harmonics. However, none of these two studies takes into account the homopolar axis harmonics. The work in [95] has been extended in [47, 63, 87] with the full subspace mapping of odd harmonics for five- and seven-phase machines. The full subspace mapping of a symmetrically distributed six-phase machine is presented in [88], where both odd and even low-order harmonics are taken into account. Most of the harmonic studies are focused just on odd harmonics, which are the typical ones produced by nonlinearities such as PWM and dead-time [65, 84, 97]. The presence of even harmonics is smaller, given that they usually have lower amplitudes and are hence less important. The contribution of previous works to the field of current harmonic mapping in multiphase induction motors is summarized in Table 1.2.

As far as the author know, time harmonic mapping in the multimotor drives is an under-researched topic and a study that identifies the mapping of the current harmonics in each of the series-connected motors, despite its interest, is still to be done.

TABLE 1.2
PREVIOUS WORKS ABOUT HARMONIC MAPPING IN MULTIPHASE MACHINES

Ref.	Machine type	α-β harm.	x-y harm.	h^+ harm.	h^- harm.	Even harm.
[62]	dual 3-phase asym.	yes	yes	no	no	no
[53, 56, 93]	6-phase asym.	yes	yes	yes	yes	no
[94]	n-phase asym.	yes	yes	yes	yes	no
[43]	n-phase symm.	yes	no	no	-	no
[95, 96]	5-phase	yes	yes	no	-	no
[47, 63, 87]	5-phase and 7-phase	yes	yes	yes	-	no

1.2.2 Non-Sinusoidal Flux Density in Multiphase Induction Motors

In the real multiphase machines two main types of harmonics are present: the time harmonics, already introduced, and the spatial harmonics. The spatial harmonics are those that cause the flux density to be non-sinusoidal, even if the motor is fed with a sinusoidal current. They are produced by flux saturation, non-perfectly sinusoidal distribution of the windings and non-uniform airgap [41–43, 52].

To define the $[L^{ss}]$, $[L^{sr}]$ and $[L^{rr}]$ matrices, the UTEM makes the assumption that the flux is a sinusoidal function of space and does not take into account its spatial harmonics. This model is capable of predicting the fundamental component of the current and the average torque production around the rated operating conditions. However, a model based on the winding distribution, on the machine geometry and on the magnetic permeance is needed if the focus of study is condition monitoring, fault tolerance, rotor eccentricities and performance analysis or an enhanced current control [61, 65, 98].

Winding Distribution Harmonics

The first required assumption in the model proposed in section §1.2.1 is that the stator windings and the rotor conductors are distributed in the space in such a way that the produced MMFs can be considered to be sinusoidal. However, in real motors, the winding allocation in a finite number of slots produces MMF harmonics, as it can be seen in the Fig. 1.7 example [99–101].

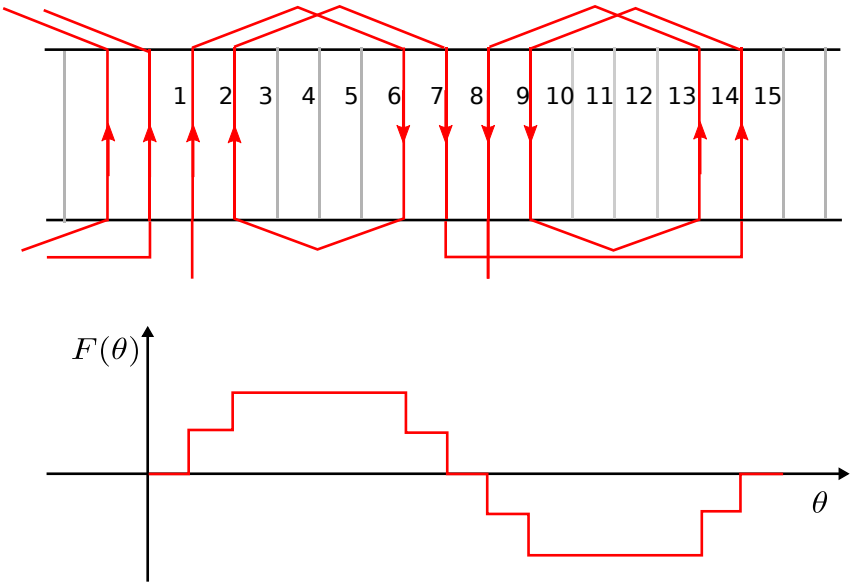

Figure 1.7: Example of an stator winding distribution and the MMF, $F(\theta)$, produced.

To study the winding distribution harmonics and calculate the produced MMF in the airgap, two procedures are followed in the literature: one models the current allocation in the space by using current sheets [41, 43, 102] and the other models the winding disposal through the winding function [103–105]. Both methods are closely related.

The current sheet analysis (CSA) is explained in [41, 102]. It is characterized by modeling the windings as a set of infinite thin blocks with the same current distribution in the space. This current distribution is modeled through a function $J(\theta)$ that represents the current density as a function of the spatial angle θ. Giving a function $K_\eta(\theta)$ which describes the winding distribution of the phase η in the space, the current density of such phase can be calculated as $K_\eta(\theta)i_\eta(t)$. The total current density function is obtained as the summation of all the phases.

The winding function analysis (WFA) is explained in [103]. In this method, the distribution of each phase winding is modeled by a function $n(\theta)$ that describes de number of turns at any specific angle θ. The winding function of the phase η is its turns function without its average value (to eliminate the DC component) [103]: $N_\eta(\theta) = n_\eta(\theta) - \overline{n_\eta(\theta)}$. The MMF produced by the η phase is calculated as the product of its winding function and the current per phase [103].

Both the WFA and the CSA are based on the Ampere's law, [41, 103]. This law, assuming the permeability of iron to be infinite, can be expressed as [106, 107]

$$\oint_c \vec{H}_\eta(\theta,t)d\vec{l} = \int_s \vec{J}_\eta(\theta,t)d\vec{s} \tag{1.22}$$

where c is a closed path, $H_\eta(\vec{\theta},t)$ is the field intensity produced by the phase η, s is the surface enclosed by c and J_η is the current density produced by phase η that crosses such surface. The field intensity $H_\eta(\vec{\theta},t)$ and the MMF $F_\eta(\vec{\theta},t)$ are related by the equation $H_\eta(\vec{\theta},t) = F_\eta(\vec{\theta},t)/g$, where g is the airgap. The MMF produced by the phase η, $F_\eta(\theta,t)$, is calculated by choosing the c path to pass through two consecutive poles of the winding

distribution [103, 107]:

$$F_\eta(\theta,t)=\frac{1}{2}\int_\theta^{\theta+2\pi/P}\underbrace{J_\eta(\theta,t)}_{\textbf{CSA}}d\theta=i_\eta(t)\frac{1}{2}\int_\theta^{\theta+2\pi/P}K_\eta(\theta)d\theta=\underbrace{N_\eta(\theta)}_{\textbf{WFA}}i_\eta(t) \tag{1.23}$$

This equation shows the relationship between the CSA and WFA. It can be seen that both approaches are equivalent and lead to the same results.

By using the current sheet procedure and under the assumption of uniform airgap and negligible magnetic saturation, [41] extends the motor model provided by the UTEM to include the stator and rotor distribution harmonics. Based on the rotational symmetry that a healthy motor presents, [41] proposes a $[L^{sr}(\nu)]$ matrix that includes the effects of the stator and rotor distribution harmonics in multiphase induction motors, its i-jth element is

$$\begin{aligned}&L^{sr}(\nu)]_{i,j}=\widehat{L}_\nu\left[\cos\nu(P\theta_{\mathrm{r}}-(i-j)\alpha_{\mathrm{c}})\right]\\&i=\{0,1,2,\ldots,(n-1)\}\text{ and }j=\{0,1,2,\ldots,(n-1)\}\end{aligned} \tag{1.24}$$

where ν is the winding distribution harmonic order, $\widehat{L}_\nu$ represents the average inductance and is constant for each harmonic and θ_{r} is the rotor angle. The stator-to-rotor mutual inductance matrix defined in (1.24) is symmetrical and circulant. Therefore, it can also be decoupled by using the transformation process described in (1.19) and (1.20).

Squirrel Cage Rotor Bar Harmonics

The second assumption in the model proposed in section §1.2.1 is that the rotor MMF can be approximated by the one produced by a wound rotor with the same pole pairs and phases as the stator. To overcome this limitation and to model induction motors with a different phase number in the stator and the rotor, [42, 52, 55, 58] have proposed models for a n_s-n_r multiphase induction motors where n_s is the stator phase number and n_r is the rotor phase number. Such models maintain the assumptions of negligible saturation and uniform airgap and are also based on (1.8), but the stator voltage and current vectors have n_s elements and the length of rotor voltage and current vectors is n_r. The $[L^{sr}(\nu)]$ proposed by [41] is extended by [55] to model the mutual inductance matrix in motors where the stator n_s and the rotor n_r phase numbers are different, its i-jth element is

$$\begin{aligned}&L^{sr}(\nu)]_{i,j}=\widehat{L}_\nu\left[\cos\nu(P\theta_{\mathrm{r}}-i\alpha_s+j\alpha_r)\right]\\&i=\{0,1,2,\ldots,(n_s-1)\}\text{ and }j=\{0,1,2,\ldots,(n_r-1)\}\end{aligned} \tag{1.25}$$

where α_s is the characteristic angle of the stator ($\alpha_s=2\pi/n_s$) and α_r is the angle between two consecutive phases of the rotor ($\alpha_r=2\pi/n_r$).

The n_s-n_r model presented by [52] uses the mutual inductance matrix described in (1.25) to study the effects of the stator and rotor winding harmonics in a n_s-n_r induction motor. It also proposes a transformation equivalent to the one shown in (1.19) and (1.20), i.e., for decoupling the n_s-n_r induction motor taking into account spatial harmonics:

$$[T]=\begin{bmatrix}[T_\nu(\nu=1)]\\[T_\nu(\nu=3)]\\\vdots\end{bmatrix} \tag{1.26}$$

where

$$[T_\nu(\nu)] = \sqrt{\frac{n_h}{2}} \begin{bmatrix} \sin\nu(\omega_r t) & \sin\nu(\omega_r t - \frac{2\pi}{n_h}) & \dots & \sin\nu(\omega_r t - (n_h-1)\frac{2\pi}{n_h}) \\ \cos(\nu\omega_r t) & \cos\nu(\omega_r t - \frac{2\pi}{n_h}) & \dots & \cos\nu(\omega_r t - (n_h-1)\frac{2\pi}{n_h}) \end{bmatrix}, \quad (1.27)$$

$n_h = \max\{n_S, n_r\}$ and ν represents the distribution harmonic order. By applying such transformation, the n_s-n_r motor model is decomposed in $(n_s-1)/2$, if n_s is odd, or $n_s/2-1$, if n is even, equivalent circuits in the stator side and $(n_r-1)/2$ or $n_r/2-1$ ones in the rotor side.

This decomposed model is also used in [42]. Hence, such proposal is also based on the uniform airgap and negligible saturation assumptions. In this paper the distribution harmonics are grouped in sets. Each set includes the distribution harmonics that produce flux linkage in the same equivalent circuit of the decoupled model. The stator distribution harmonics that can affect, if present, each stator equivalent circuit are [42]

$$\nu_i = K_1 n_s + i \qquad K_1 = 0, \pm1, \pm2, ... \quad (1.28)$$

where $i = 1, ..., (n_s-1)/2$ is the decomposed stator equivalent circuit index. The rotor distribution harmonics that affect each rotor equivalent circuit are [42]

$$\nu_j = K_2 \frac{n_r}{P} + j \qquad K_2 = 0, \pm1, \pm2, ... \quad (1.29)$$

where $j = 1, ..., (n_r-1)/2$ is the decomposed rotor equivalent circuit index. Only the spatial harmonics common to the stator and the rotor, i.e., $\nu_i = \nu_j$, produce flux linkage [42].

In the motor decomposed model proposed in [42], only specific combinations of stator and rotor distribution harmonic sets produce flux linkage between the rotor and the stator. Therefore, only such distribution harmonic combinations produce back EMF in the particular stator subspace equivalent circuit. This property of the decomposed model of a multiphase motor can be useful to identify the distribution harmonic that produces a specific back EMF and induced current harmonic by studying the subspace where the current harmonic maps. Hence, it is interesting to extend this motor model to cover other spatial harmonics that are important for monitoring induction motors, such as the ones produced by a non-uniform airgap or magnetic saturation.

MMF Harmonics Produced by Stator Current and Winding Distribution Harmonics

The MMF in the airgap produced by the windings can be obtained by using the current sheet approximation or the winding function method. The resulting MMF in the airgap is a function of the current spatial distribution in the stator inner and rotor outer surfaces. These current distributions depend on the winding allocation and the instantaneous current that flows through each winding conductor. Therefore, the MMF harmonic components in the airgap are not only produced by a non-sinusoidal winding distribution; the stator current harmonics also affect them. The motor models proposed by [41, 42, 52, 55, 108] include the effects of the stator and rotor distribution harmonics, but they do not study the effects of the stator current harmonics over the motor MMF.

Therefore, how the time harmonics in combination with the distribution harmonics affect the motor flux is not analyzed in these works.

A study about the airgap MMF harmonics produced by a multiphase stator taking into account time and distribution harmonics is carried out in [109] by using the winding function procedure. In this paper, the effects of the interactions between time harmonics and distribution harmonics is studied for three-, five-, six-, seven- and nine-phase induction motors. Tables that relate the low order time and distribution harmonics ($q = 1, ..., 15$ and $\nu = 1, ..., 15$) and give the resulting MMF in the airgap are provided under the assumptions of negligible saturation, uniform airgap, symmetrical winding and integral slots.

Furthermore, [43] presents a study of the MMF harmonics produced by the interaction of time and stator distribution harmonics for induction motors with a general number of phases n. In this paper, the field harmonics produced by a multiphase dual layer and integral slot winding are analyzed and a function that relates the harmonic order combinations that produce MMF in the airgap is provided. For any phase number of the induction motor n, the νth distribution and qth time harmonic combinations that satisfied

$$\nu = P(q - 2Kn) \qquad K = 0, \pm 1, \pm 2, ... \tag{1.30}$$

produce MMF [43]. The sign of K denotes the rotating direction of the resulting field. If $K > 0$ the produced MMF rotates in the same direction as the main flux, and vice versa.

Such equation is obtained by the CSA under the assumptions of negligible saturation, uniform airgap and integral slot winding. The harmonic study in [43] is also focused in the low order distribution harmonics. Under these simplifications, the even order distribution harmonics can be omitted and this is reflected in (1.30), which only studies odd order harmonics.

A time and spatial harmonic analysis of the n-phase induction motors that combines the non-ideal characteristics analyzed by [41], [55] [42] and [43], but which also covers different types of stator winding distributions such as fractional-slot windings and other nonlinearities such as saturation and non-uniform airgap in multiphase motors, despite its interest, has still not been developed.

Non-Uniform Airgap Modeling

All the previously presented works, [41–43, 52, 55, 103, 108, 109], analyze the flux harmonics under the assumptions of negligible saturation and uniform airgap. Therefore, these studies cover the stator and rotor winding distribution harmonics, but do not take into account the non-uniform airgap harmonics, nor the magnetic saturation ones [110].

Under some conditions the uniform airgap assumption is not valid and the motor model needs to be extended. Non uniform airgap can be produced by rotor eccentricities [111–114], stator and rotor slots [115, 116] and other causes, such as salient poles [112, 117] and rotor or stator mechanical deformations [118, 119]. Furthermore, in order to effectively use the magnetic material, the majority of the motors are designed to work under moderate saturation in normal operation [120, 121]. Hence, it would be also interesting to extend the multiphase motor model that includes the effects of time and winding distribution harmonics presented by [43] to cover the non-uniform airgap and magnetic saturation.

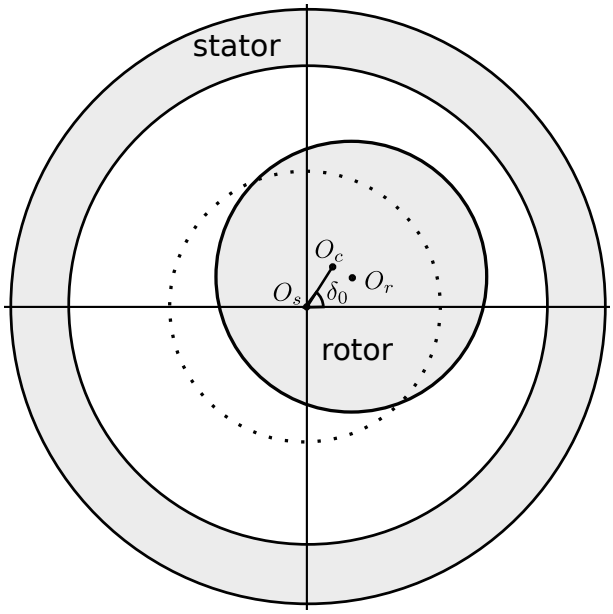

Figure 1.8: Geometric displacements associated with the eccentricity.

Under the uniform airgap and infinite magnetic permeability assumptions, the flux density in the airgap is calculated as [41, 43, 109]

$$B(\theta,t) = \frac{\mu_0}{g} F(\theta,t) \tag{1.31}$$

where $B(\theta,t)$ is the flux density in the airgap and μ_0 is the permeability of free space.

But, due to any of the mentioned mechanical conditions, the airgap can vary with the spatial angle and time $g(\theta,t)$. Therefore, to include the non-uniform airgap in the flux density calculation, (1.31) is rewritten as [113, 119]

$$B(\theta,t) = \frac{\mu_0}{g(\theta,t)} F(\theta,t) = \Lambda(\theta,t) F(\theta,t) \tag{1.32}$$

where $\Lambda(\theta,t) = \mu_0/g(\theta,t)$ is the magnetic permeance function.

One of the possible causes of a non-uniform airgap is the rotor eccentricity [111, 113]. As it is represented in Fig. 1.8, it is produced by a displacement of the axis of rotation of the rotor. Rotor eccentricities can be classified in three types: static, dynamic and mixed eccentricity. In the static eccentricity, the rotor spinning axis O_c and its symmetry axis O_r are the same but they do not coincide with the stator symmetry axis O_s. Thus, the position of the minimum and maximum airgap in the space is constant. This type of eccentricity can be produced by bearings misalignment, machine misaligned frame or stator ovality [111, 112]. In the dynamic eccentricity, the rotor spinning axis O_c coincides with the stator symmetry axis O_s but it is different form the rotor symmetry axis O_r. Hence the position of the minimum and maximum airgap in the space rotates with the rotor. This type of eccentricity can be produced by shaft deflection, shaft bent or a misaligned load. The mixed eccentricity is a combination of the static and dynamic types and so the rotation axis is different from both the stator and rotor symmetry axes. The

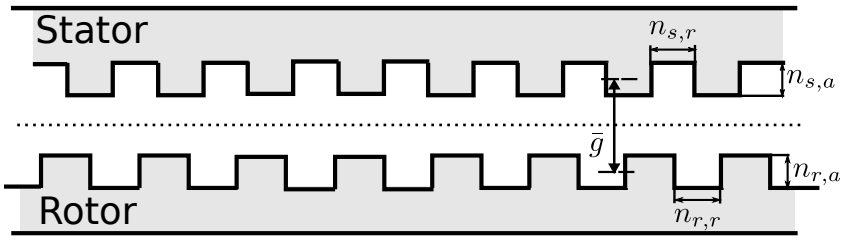

Figure 1.9: Effects of the rotor and stator slots over the motor airgap.

airgap function that models the eccentricity is [111, 122]

$$g(\theta, \theta_r) = \bar{g}(1 - \underbrace{a_1 \cos(\theta)}_{static} - \underbrace{a_2 \cos(\theta - \theta_r)}_{dynamic}) \tag{1.33}$$

where $a_1 = \overline{O_c O_s}/\bar{g}$ is the static eccentricity severity, $a_2 = \overline{O_c O_r}/\bar{g}$ is the dynamic eccentricity severity and θ_r is the angular position of the rotor with respect to the stator reference.

In case of three-phase [110, 116] and dual three-phase motors [122], the rotor eccentricity is modeled by using the magnetic permeance function $\Lambda(\theta, t)$ presented in (1.32). In case of static eccentricity, this permeance function, expressed using harmonic decomposition, is [116]

$$\Lambda_{se} = \sum_{h_{se}=1}^{\infty} \widehat{\Lambda}_{h_{se}} \cos(h_{se}\theta) \tag{1.34}$$

where h_{se} is the static eccentricity harmonic order and

$$\widehat{\Lambda}_{h_{se}} = \frac{\mu_0}{\bar{g}} \frac{2(1 - \sqrt{1 - a_1^2})^{h_{se}}}{a_1^{h_{se}} \sqrt{1 - a_1^2}}. \tag{1.35}$$

The permeance function for a dynamic eccentricity of the rotor can be represented as [116]

$$\Lambda_{de} = \sum_{h_{de}=1}^{\infty} \widehat{\Lambda}_{h_{de}} \cos(h_{de}(\theta - \omega_r t)) \tag{1.36}$$

where h_{de} is the dynamic eccentricity harmonic order, ω_r is the rotor angular speed and [111, 116]

$$\widehat{\Lambda}_{h_{de}} = \frac{\mu_0}{\bar{g}} \frac{2(1 - \sqrt{1 - a_2^2})^{h_{de}}}{a_2^{h_{de}} \sqrt{1 - a_2^2}}. \tag{1.37}$$

Another condition of the machine to include in the non-uniform airgap model is the effect of the stator and rotor slotting. The produced variation over the motor airgap is represented in Fig. 1.9.

The variation of the airgap due to the stator and rotor slots has been calculated in the case of three-phase [110, 116] and dual three-phase motors [122]. In such cases, the permeance function corresponding to the stator and rotor slotting, decomposed by using

the Fourier series, is

$$\begin{aligned}\Lambda_{slt} &= \Lambda_s + \Lambda_r + \Lambda_{rs} \\ &= \sum_{h_s=1}^{\infty} \widehat{\Lambda}_s \cos\left(h_s Q_s \theta\right) + \sum_{h_r=1}^{\infty} \widehat{\Lambda}_r \cos\left(h_r Q_r(\theta - \theta_{\mathrm{r}})\right) \\ &+ \sum_{h_s=1}^{\infty}\sum_{h_r=1}^{\infty} \widehat{\Lambda}_{rs}[\cos\left(h_s Q_s \theta + h_r Q_r(\theta - \theta_{\mathrm{r}})\right) \\ &+ \cos\left(h_s Q_s \theta - h_r Q_r(\theta - \theta_{\mathrm{r}})\right] \end{aligned} \tag{1.38}$$

where Λ_s is the permeance variation due to the stator slots, Λ_r is the variation due to the rotor slots and Λ_{rs} is due to the interaction between rotor and stator slots; $h_s = 1, 2, ...$ is the order of the stator slot harmonics, $h_r = 1, 2, ...$ is the order of the rotor slot harmonics, Q_r is the rotor slots number, Q_s is the stator slots number,

$$\begin{aligned}\widehat{\Lambda}_s &= \frac{2n_{s,r}}{\pi h_s} \sin\left(h_s \pi n_{s,\Theta}/n_{s,a}\right) \\ \widehat{\Lambda}_r &= \frac{2n_{r,r}}{\pi h_s} \sin\left(h_s \pi n_{r,\Theta}/n_{r,a}\right)\end{aligned} \tag{1.39}$$

$\widehat{\Lambda}_{rs} = \widehat{\Lambda}_s \widehat{\Lambda}_r$ and $n_{s,r}$, $n_{r,r}$, $n_{s,a}$ and $n_{r,a}$ are the radial and angular dimensions of the stator or rotor slots and $n_{s,\Theta}$ and $n_{r,\Theta}$ are the angles between two consecutive slots [119].

The summations in (1.38) can be simplified as [116]

$$\begin{aligned}\Lambda_{slt} = \sum_{h_s=0}^{\infty}\sum_{h_r=0}^{\infty} \frac{1}{2}\widehat{\Lambda}_{rs}\Big(&\cos\left(h_s Q_s \theta + h_r Q_r(\theta - \theta_{\mathrm{r}})\right) \\ &+ \cos\left(h_s Q_s \theta - h_r Q_r(\theta - \theta_{\mathrm{r}})\right)\Big).\end{aligned} \tag{1.40}$$

In the field of the multiphase motors the study of non-uniform airgaps is not as extensive as in three-phase machines. The analysis of non-uniform airgap in [113] is not phase specific and some of its findings can be extended for the multiphase machine case. In case of slots and static and dynamic eccentricity modelling, [122] presents such study for a specific dual three-phase induction motor. Therefore, developing a model for a generic number of stator and rotor phases that includes the effects of the non-uniform airgap due to slots and eccentricities is of interest. Furthermore, the already published three-phase studies analyze the frequencies of the resulting back EMF or the induced stator current harmonics due to the non-uniform airgaps. However, in n-phase motors an analysis of the subspace where each of these harmonics maps can be helpful for designing the current controllers if the objective is to cancel them. It also can be used, in case the objective is to monitor those harmonics, to predict if the back EMF harmonics map into a low impedance plane, producing high amplitude current harmonics, or into a homopolar axis, where, in absence of neutral connection induced current harmonics do not circulate.

Modeling Saturation Harmonics

The multiphase motor model and permeance calculation expressions shown are based on the assumption of infinite magnetic permeability. However, the normal magnetization

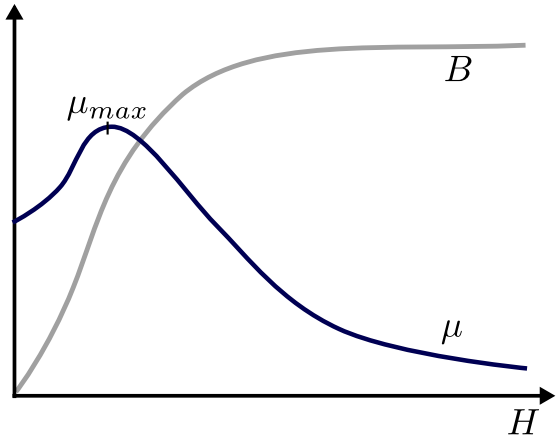

Figure 1.10: Flux density B and magnetic permeability μ as a function of the field intensity H in a ferromagnetic material.

curve or B-H curve of any ferromagnetic material, i.e., Fig. 1.10 , shows that the relation between the flux density B and the field intensity H is not linear and the magnetic permeability $\mu = B/H$ varies with the field intensity [123, 124]. It increases with the value of H until its maximum is reached; then, saturation occurs, the correlation is inverted and its value decreases toward one.

In order to get an optimum utilization of the magnetic materials, induction machines usually incorporate a certain degree of magnetic saturation at rated operating conditions. As a consequence of this saturation, the magnetic field waveform changes and hence flux harmonics are produced. There are two types of saturation effects depending the place where saturation occurs: saturation of the teeth and saturation of the core. In case of teeth saturation harmonics, their phases are such that tend to flatten the waveform of the flux that caused the saturation, and in the case of core saturation, their phases tend to produce a peaked waveform in the corresponding flux [97, 110, 120]. These harmonic flux components travel in the airgap with the same angular speed as the corresponding airgap flux component, always keeping the phase synchronism with it. In most machines the teeth are more saturated than the core [120].

There are several different procedures to model the saturation harmonics in induction machines. Most of the works are centered into modeling only the dominant third harmonic component of the saturation flux, such as [110, 120, 125] that study the flux saturation in a three-phase squirrel cage motor by modifying the airgap as a function of the flux position and amplitude. Or, for example, the method proposed by [120], which is based on directly modeling the flux density harmonic components and is focused only on modeling the dominant third harmonic component. In [120], the flux density, including the effect of the magnetic saturation of the teeth, is

$$B^t(\theta,t) = B_1^t(\theta,t) + B_3^t(\theta,t) = \widehat{B}_1 \cos\left[\theta - \sigma(t)\right] + \widehat{B}_3 \cos 3[\theta - \sigma(t)]. \tag{1.41}$$

where $\widehat{B}_1$ is the fundamental flux density amplitude, $\sigma(t)$ is the angular position of the magnetic axis of the fundamental field.

However, the magnetic saturation of the teeth produces flux density harmonics of the orders $\rho = 1, 3, 5, 7, 9, ...$ [116]. The total flux density modeled taking into account the

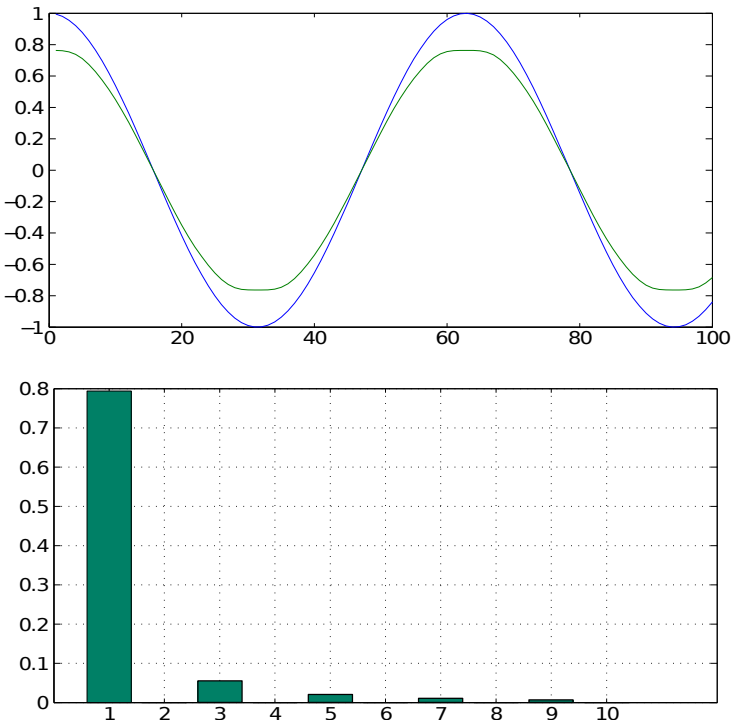

Figure 1.11: Effects of the 1st, 3rd, 5th, 7th and 9th saturation harmonics on the total flux density B^t and resulting flux spectrum.

1st, 3rd, 5th, 7th and 9th saturation harmonics is depicted in Fig. 1.11. The methods of modeling the flux saturation that cover more than the dominant third harmonic are more complex, such as [116], which models the saturation by using the magnetic permeance function, or [118], where the saturation is modeled as an increase in the slot opening. The permeance function to model flux saturation in three-phase motors, if only the fundamental component of the field is saturated, is [116]

$$\Lambda_\rho = \sum_{\rho=1}^{\infty} \frac{1}{2} \widehat{\Lambda}_\rho \cos\left[2\rho(P\theta - \omega_s t)\right]. \tag{1.42}$$

In the field of the multiphase motors there are some works that study saturation in motors with a specific number of phases, such as [97, 124] that analyze the flux saturation in a five-phase squirrel cage motor by applying a correction factor to the mutual inductances. The former, [97], is focused on the study of the effect of the saturation over the fundamental component of the flux and does not analyzes the other flux harmonics that the saturation produces. The latter, [124], studies the fundamental and the third harmonic of the flux.

Motor Current Signature Analysis

All the previously mentioned nonlinearities, the distribution and time harmonics, nonuniform airgap and magnetic saturation produce flux density harmonics in the machine airgap. These flux harmonics produce back EMF harmonics [126, 127] that can affect the machine behavior in two ways: producing torque harmonics [118, 128] or induced currents that lead to additional losses [65, 88].

The motor model in (1.1) shows that the stator voltage, stator current and flux linkage are directly related. If the stator winding links flux due to the spatial harmonics, then back EMF harmonics appear. If the motor is fed from a VSI, the stator voltage is fixed by the converter. Therefore, the back EMF harmonics produce current components in the stator that can be measured in order to make an indirect analysis of the flux harmonics and the non-ideal motor characteristics that produce them.

MCSA is a diagnostic technique based on the stator current spectrum monitoring. Machine problems can be detected by knowing the induced stator current harmonics related to the healthy motor operation and the ones produced by motor defects [115, 116]. The main advantage of the MCSA is that it is an online non-invasive technique [114, 129–131]. Another important advantage of the MCSA resides in the fact that it only needs to sense the stator current. This makes the latter technique cost effective because, normally, drives already include current sensors for the machine control [132]. This avoids the necessity to introduce vibration, temperature or electromagnetic field sensors that other monitoring techniques require [130]. Having a good knowledge and understanding of the current signature of the machine under monitoring is an essential requisite to obtain a good performance [115].

The main faults that can affect an induction motor can be classified as stator faults, broken rotor bars or cracked rotor end-rings, static and dynamic eccentricities, rotor short field windings and bearings and gearbox failures [130]. In three-phase motors the percentage of failure gathered in industrial surveys are 40% bearing and eccentricity related failures, 38% stator related ones, 10% rotor related and 12% others [129, 130]. The early detection of motor failures is important, because it will prevent the motor failure from getting worse. For example, in the case of a motor eccentricity the early detection can prevent vibration related problems, bearing damage due to the asymmetric forces and even a rotor-to-stator rub that can produce a damage to the stator core and winding [130, 133, 134]. In industrial applications, the fault detection methods are important, because an unscheduled machine failure can cause production downtimes and economic losses.

In the field of three-phase induction motors, the study of the motor currents to detect faults is a broadly researched field. There exist works about broken bar detection since the early 1980s. For example, in 1982, Williamson and Smith presented the model of a three-phase squirrel cage motor under broken rotor bar faults [135] and, in 1988, Kliman *et al.* [136] developed a method to detect broken rotor bars by monitoring the stator current. There are also stator winding fault studies such as [137], published in 1985, and eccentricity detection through the stator currents such as [116] in 1989. The effects of the bearing damages into the stator current signatures were studied in the early 1990s [138]. Nowadays MCSA in three-phase induction motors is still a prolific field of research. A number of papers have been published recently on the topic. In 2013, MCSA papers such as [115], which studies the healthy three-phase squirrel cage current signature; [139], which identifies the backslash problem in the gearbox through MCSA; [140], which studies open switch faults detection by MCSA and [141, 142], which propose different algorithms for broken bar detection using MCSA, were published. From 2014, there are MCSA published papers such as, [143], which uses a notch finite impulse response filter to detect eccentricities in the current signature; [144], which recognizes outer cage defects in double squirrel cage motors; [145, 146], which detect broken rotor bars and [147], which identi-

fies stator winding faults. From 2015, there are papers such as [148], which proposes a method to detect mechanical imbalances; [149], which presents gear tooth surface damage detection using MCSA and [150–152], that propose advanced fault diagnosis techniques for MCSA.

Most of the MCSA methods to detect the fault symptoms are based on the monitoring of specific frequencies of the current spectrum [130]. The symptom frequencies for the most common induction motor faults are [130]

- For bearing faults:
$$f_h = |f_s \pm k_{br} f_v| \tag{1.43}$$
where f_s is the synchronous frequency, $k_{br} = 1, 2, 3, ...$ and f_v is one of the characteristic vibration frequencies.

- For broken rotor bar faults: detection can be done by monitoring the current harmonics at
$$f_h = (1 \pm 2sk_{bk}) f_s \tag{1.44}$$
where $k_{bk} = 1, 2, 3, ...$, or the current harmonics at
$$f_h = [k(1 - s) \pm s] f_s \tag{1.45}$$
where $k = 1, 3, 5, ...$

- For static or dynamic eccentricities:
$$f_h = \left[(k_r Q_r \pm h_{de}) \frac{1 - s}{P} \pm 1 \right] f_s \tag{1.46}$$
where $k_r = 1, 2, 3...$, $h_{de} = 0$ in the case of static eccentricities and $h_{de} = 1, 2, 3...$ in the case of dynamic eccentricities.

- For mixed eccentricities (both static and dynamic):
$$f_h = |h_{me} \frac{1 - s}{P} \pm 1| f_s \tag{1.47}$$
where $h_{me} = 1, 2, 3....$

Detecting the machine faults by monitoring the current harmonics produced at specific frequencies has the disadvantage of symptom overlapping. It appears when some symptoms of different nonlinearities emerge at the same frequency [153]. Besides, in the last case, which defines the motor mixed eccentricity symptoms, it has been proved that, in three phase motors, (1.47) is valid only when both static and dynamic eccentricities exist together (mixed eccentricity) [130]. It also has been proved that (1.46) is valid to detect pure-static and pure-dynamic eccentricities only if the machine has a specific combination of pole pairs and rotor slot numbers [126, 130, 154], i.e., in three-phase motors this technique is valid only if the P and Q_r values are related by
$$Q_r = P[3k \pm r] \tag{1.48}$$

where $k \in \mathbb{N}$ and $r = 0$ or 1. Therefore, some complementary methods were proposed for the cases the standalone frequency analysis is not valid to detect only-static or only-dynamic eccentricities in three-phase machines, such as zero sequence current analysis [154] flux harmonics measurement [155], power signature analysis [153] or a method that uses the amplitude of the negative sequence of the fundamental current and voltage as static eccentricity fault symptom [156]. The last method, the one based on the measurement of the negative sequence of the fundamental, can separate the effects of the static eccentricity from the ones produced by an unbalanced load and it is independent from the motor parameters [157].

In the multiphase motor field, to the author's knowledge, the fault detection and MCSA are not broadly studied. In [122], the eccentricity symptoms described by (1.46) and (1.47) are used to detect static, dynamic and mixed eccentricity in the specific case of a dual three-phase induction motor with isolated neutrals and $Q_r = 28$ and $P = 1$. A method to detect mixed eccentricity that uses the symptom depicted in (1.47) and that involves the Park transformation of the current signal is presented in [158]. In such paper, this method is claimed to be valid for multiphase motors, although it is only tested for the three-phase case. A method to detect the symptoms of broken rotor bars in multiphase motors with a general number of phases n is proposed in [60]. In the field of stator winding fault detection in multiphase motors there are several works, such as [159–162], since one of the common uses of multiphase machines is in applications where stator winding fault tolerance is required. As far as the author knows, an analysis of the motor current signature and an eccentricity detection method for motors with a n number of phases is still to be done and is an interesting contribution to the MCSA field.

1.3 Major results

The work in this dissertation is divided into the following major parts:

1.3.1 Chapter 2: "Stator Voltage and Current Mapping in a Sinusoidally Distributed Multiphase Motor "

This chapter presents a simple graphical method for time harmonic mapping in symmetrical multiphase machines derived from the Symmetrical Components Theory [41]. This method provides a general (for any number of phases) solution for subspace and sequence identification and extends the n-phase equation for the α-β time harmonics identification given in [43] with full subspace and sequence detection and both odd and even harmonic consideration. One of the contributions of the proposed method is that it is valid to identify into which subspace and with which SVR direction is mapped each harmonic in each machine in a series-connected multimotor drive. A set of experiments is carried out to validate the proposed method using a five- and a six-phase single motor drive and a series-connected six-phase two-motor drive.

1.3.2 Chapter 3: "Stator Voltage and Current Mapping in a Non-Sinusoidally Distributed Multiphase Motor "

This chapter presents an analysis of the back EMF and stator currents in n-phase squirrel cage motors due to the non-ideal characteristics of the drive, such as the converter time harmonics, stator and rotor windings distribution harmonics, non-uniform airgap and magnetic saturation. This study is used to extend the analysis of the stator currents of a n-phase motor presented in chapter §2 to cover the effects caused by these harmonics and to obtain the VSD of the current signature of the healthy motor. The effects of the static and dynamic rotor eccentricities over the motor current signature are assessed and the detection of these faults in n-phase motors by means of MCSA is evaluated. Then a MCSA method to detect static, dynamic and mixed eccentricities in n-phase squirrel cage motors, based on the VSD of the motor current signature is proposed. Finally, experimental results with two different five-phase squirrel cage motors are provided to evaluate the predicted healthy motor current signature, analyzed by means of the VSD, and the proposed eccentricity detection method.

1.3.3 Chapter 4: "Conclusions and Future Research"

The main conclusions of this dissertation are summarized in this chapter and some recommendations for future research topics are provided.

Chapter 2

Time Harmonic Mapping in Multiphase Induction Motors without Spatial Harmonics

The method presented in this chapter has been published in the journal *IEEE Transactions on Industrial Electronics* [5]. Its particularization for a series-connected six-phase two-motor drive has been presented at the *IEEE Industrial Electronics Society Conference 2012 (IECON'12)* [21]. Its analysis of the effects of the non-sinusoidal flux on a multimotor drive has been presented at the *IEEE Industrial Electronics Society Conference 2013 (IECON'13)* [10].

Abstract

The multiphase machines are usually modeled by a reference frame transformation to avoid the cross-coupling of variables. This transformation decomposes the original n-dimensional vector space into orthogonal subspaces. Mapping the voltage and current harmonics into the subspaces in distributed machines is important because it allows to identify which components are related to the torque and which ones just increase the machine losses. The space vector identification and mapping of each harmonic is also important in closed-loop current harmonic compensation to set the controllers. In addition, the harmonic mapping is interesting in multimotor systems to know how harmonics from one machine can affect the other machines in the system. In this chapter a simple graphical method for time harmonic subspace and SVR direction identification is proposed. This method is valid for symmetrical machines of any phase number n, and it can be used in multimotor systems. Experimental results using a five- and a six-phase motor in single drive configuration and a series-connected two-motor six-phase drive validate the proposed method. Finally, an experimental evaluation of the disturbances produced by the spatial harmonics in a series-connected two-motor five-phase drive and their effects in the developed method is performed.

2.1 Introduction

Modeling the multiphase machine in the non-transformed phase-variable reference frame leads to an n-dimensional vector space model. The control of this kind of machine in such phase-variable reference frame is difficult because phase-variables are cross coupled [53]. A variety of transformations has been proposed to avoid the coupling of variables [41, 56, 59, 163]. Such transformations decompose the n-dimensional space into orthogonal subspaces: several 2D subspaces (planes) and one or two 1D subspaces (homopolar axes). Since there is no coupling among them, they lead to a significant simplification of the machine model and control.

Two main types of harmonics are present in multiphase machines [41–43, 52]. Spatial harmonics are those in the magnetic field due to flux saturation, the non-perfectly sinusoidal distribution of the windings and non-uniform airgap. Time harmonics, on the other hand, are the harmonic components contained in the electrical signals (i.e., voltage and current waveforms).

Under the assumption of sinusoidally distributed stator and rotor windings, and neglecting the effects of the magnetic saturation, the healthy motor does not have spatial harmonics in the magnetic field. The time harmonics that are involved in the electromechanical energy conversion are mapped in the first plane, commonly called α-β plane, while the harmonics that are not can be found in the remaining planes, commonly called x-y planes, or in the homopolar axes, commonly called h^+ and h^- axis [41, 48, 62, 89]. Only the current harmonic components in the α-β plane are coupled to the rotor and hence only these components can produce torque ripple. In the decoupled equivalent circuit model of the sinusoidally distributed multiphase machine [41], the x-y planes impedance only includes the stator resistance and leakage inductance, so low voltage harmonics may lead to high current harmonics [47, 48, 56, 62]. The impedance of the homopolar axes is usually very high or very low depending on whether the neutrals are connected or not [48]. Consequently the non-mechanical energy conversion related harmonics should be controlled to reduce the extra losses in the machine [65]. In this manner, mapping each input voltage harmonic into the corresponding subspace helps to identify which voltage harmonics will contribute to the air-gap flux (and, thus, to electromechanical conversion) and which ones will not. The SVR speed identification of each harmonic is important for the compensation of the current harmonics, where each controller should be set to the same frequency and SVR direction as the harmonic to be compensated [4].

As only one pair of current components is required for the flux and torque control in one multiphase machine with sinusoidally distributed stator windings, additional degrees of freedom can be utilized to independently control other machines within a multimotor drive [77–79, 81–83]. In order to achieve such an independent control it is necessary to connect the stator windings of the machines in series with an appropriate phase transposition. With such phase transposition, the α-β plane of every machine becomes an x-y plane in the remaining series-connected machines [77–79, 81–83]. Therefore, the mapping of the time harmonics, e.g., the ones introduced by the converter deadtime, in series-connected multimotor systems is useful to predict which harmonics affect each machine.

Most of the previous work about time harmonic mapping deals with machines with a specific number of phases and with specific stator winding distributions.

In multiphase symmetrical machines, [43] provides an α-β plane current harmonic

mapping equation for a generic n-phase symmetrical machine and for odd order harmonics. Nevertheless, it does not study the harmonic mapping in the x-y planes and homopolar axes. The harmonic plane mapping of five-phase induction machines was carried out in [95, 96], obtaining the same results as in [43] for the α-β plane. For the x-y subspace harmonic identification, each paper has introduced a new equation which maps odd harmonics. However, none of these two papers takes into account the homopolar axis harmonics. The work in [95] has been extended for five- and seven-phase machines in [47, 63, 87]. These works include the mapping of the homopolar components. The subspace mapping of a symmetrically distributed six-phase machine is done in [88]. Most of the harmonic studies are focused just on odd harmonics, given that they are the typical ones produced by nonlinearities such as PWM and dead times [65, 84, 97] and the even harmonic amplitudes are smaller.

This chapter presents an analysis of time harmonic mapping in symmetrical multiphase machines derived from the Symmetrical Components Theory [41]. As a result of this analysis, equations and a graphical method to determine to which subspace and with which SVR direction maps each time harmonic is provided. The proposed mapping diagram can be also used in multimotor drives to identify which is the plane and SVR direction into which each harmonic is mapped in each machine of the system. A set of experiments is carried out to validate the proposed method using a five- and a six-phase single motor drives and a series-connected six-phase two-motor drive. Finally, an additional experiment with a series-connected five-phase two-motor drive is carried out to assess how the spatial harmonics produce crossed interactions between the motors and how they affect the proposed method.

The chapter is divided into six sections. The second one presents the graphical method for time harmonic mapping in symmetrical multiphase machines derived from the Symmetrical Components Theory. The third section highlights the differences between the proposed method and the previous works. The fourth section extends the proposed mapping diagram to cover series-connected multimotor drives. The fifth section provides the experimental evaluation of the identification method and, finally, the chapter ends with the conclusions of the work.

2.2 Harmonic Mapping Diagram

2.2.1 Vector Space Decomposition and Mapping Diagram

In a symmetrical n-phase machine, the electrical displacement between any consecutive stator phases is called the characteristic angle $\alpha_c = 2\pi/n$ [48]. The symmetrical components transformation uses the matrix shown in (1.13) to decompose the original n-dimensional vector space into several subspaces.,

Given that the input vector is considered to be real-valued, the conjugated rows do not give any extra information about the subspaces [41], from here on these rows of matrix [**T**] are not going to be taken into account. Therefore, the rows that are going to be studied are $p \in [0, n/2]$ for even phase machines and $p \in [0, (n-1)/2]$ for odd phase machines:

$$p = \{\underbrace{0}_{h^+}, \underbrace{1, \ldots, n/2-1}_{\alpha_p\text{-}\beta_p}, \underbrace{n/2}_{h^-}\} \qquad \text{if } p \text{ is even} \tag{2.1a}$$

$$p = \{\underbrace{0}_{h^+}, \underbrace{1, \ldots, (n-1)/2}_{\alpha_p\text{-}\beta_p}\} \qquad \text{if } p \text{ is odd.} \tag{2.1b}$$

If only the fundamental voltage component is considered, then the n-phase voltage input vector in the phase-variable reference frame, which excites the machine stator, is

$$[V] = [V_0, V_1, V_2, \ldots, V_\eta, \ldots, V_{n-1}]^t \tag{2.2}$$

where V_η is the instantaneous voltage of phase η. Assuming that the amplitude is the same in all phases, it can be written as

$$V_\eta = \widehat{v}_\eta \cos(\omega_s\, t - \phi_\eta) \tag{2.3}$$

where $\widehat{v}_\eta$ is the voltage amplitude, ω_s is the angular frequency, t is the time variable and ϕ_η is the delay angle of phase η with respect to phase 0. In the case of symmetrical machines, a common assumption is that the delay angle between two consecutive phases is equal to α_c [41, 47, 48, 53, 56, 59]. In order to make the problem more general, in this study the voltage delay angle between phases is assumed to be any multiple of α_c:

$$\phi_\eta = m\, \eta\, \alpha_c \tag{2.4}$$

where m is an integer number that defines the temporal delay angle step between electrical consecutive phases. This parameter is used to represent changes in the phase order of the fundamental voltage that feeds the motor. In n-phase single motor drives, the delay angle between consecutive phases usually equals the characteristic angle, i.e., $m = 1$, but it can be different ($m \neq 1$) in standstill equivalent circuit parameter identification of multiphase machines [163]. In series-connected multimotor drives the parameter m is used to control individual motors of the system [77–79, 81–83].

If the input voltage of phase η is not sinusoidal, it can be decomposed by using Fourier series as

$$V_\eta = \sum_q \widehat{v}_{\eta,q} \cos(q(\omega_s\, t - m\, \eta\, \alpha_c) + \phi_q) \tag{2.5}$$

where q is the harmonic order, $\widehat{v}_{\eta,q}$ is the voltage amplitude and ϕ_q is the delay angle between the qth order harmonic and the fundamental component. In this expression, each qth order harmonic is supposed to accomplish the same restrictions as in (2.3) and (2.4): equal voltage amplitude for all the phases and angle delay between two consecutive phases equal to a multiple of α_c. These assumptions are common in harmonic mapping studies [41, 43, 48, 53, 56, 88] and quite approximately cover the most common cases in multiphase motor drives. It is also assumed that sub-harmonics are absent.

If the cosine function is written in complex form as $\cos\alpha = (e^{\hat{\jmath}\,\alpha} + e^{-\hat{\jmath}\,\alpha})/2$ then the decomposition in (2.5) can be rewritten as

$$\mathbf{V}_\eta = \sum_q \mathbf{V}_{\eta,q} = \sum_q \widehat{v}_{\eta,q} \frac{e^{\hat{\jmath}(q(\omega_s\, t - m\,\eta\,\alpha_c)+\phi_q)} + e^{-\hat{\jmath}(q(\omega_s\, t - m\,\eta\,\alpha_c)+\phi_q)}}{2}. \tag{2.6}$$

If the qth-harmonic of the input voltage vector $\mathbf{V}_{\eta,q}$ is transformed to the symmetrical component reference frame, through matrix $[\mathbf{T}]$, then the qth harmonic component mapped into each α_p-β_p subspace is obtained as

$$\mathbf{V}_{p,q} = \frac{\widehat{v}_{\eta,q}}{\sqrt{n}} \cdot \sum_{\eta=0}^{n-1} \left[\frac{e^{\hat{\jmath}(q(\omega_s\, t - m\,\eta\,\alpha_c)+\phi_q)} + e^{-\hat{\jmath}(q(\omega_s\, t - m\,\eta\,\alpha_c)+\phi_q)}}{2} e^{\hat{\jmath}\,p\eta\alpha_c} \right]. \tag{2.7}$$

The above equation can be rewritten as

$$\mathbf{V}_{p,q} = \mathbf{A}^+_{p,q} \cdot e^{\hat{\jmath}(q\omega_s t+\phi_q)} + \mathbf{A}^-_{p,q} \cdot e^{\hat{\jmath}(-q\omega_s t-\phi_q)} \tag{2.8}$$

where

$$\mathbf{A}^+_{p,q} = \frac{\widehat{v}_{\eta,q}}{2\sqrt{n}} \underbrace{\sum_{\eta=0}^{n-1} e^{\hat{\jmath}(p-q\,m)\eta\,\alpha_c}}_{\mathbf{a}^+_{p,q}} \tag{2.9}$$

$$\mathbf{A}^-_{p,q} = \frac{\widehat{v}_{\eta,q}}{2\sqrt{n}} \underbrace{\sum_{\eta=0}^{n-1} e^{\hat{\jmath}(p+q\,m)\eta\,\alpha_c}}_{\mathbf{a}^-_{p,q}} \tag{2.10}$$

are the amplitude of the positive and the negative SVR directions, respectively, of harmonic q in the α_p-β_p subspace. The coefficients $\mathbf{a}^+_{p,q}$ and $\mathbf{a}^-_{p,q}$ take the value 0 or n depending on p, q, m and α_c. It is because, taking into account the Roots of Unity theory, due to rotational symmetry, the summation

$$\sum_{\eta=0}^{n-1} e^{\hat{\jmath}\eta \overbrace{k(2\pi/n)}^{\phi_k}} \qquad \text{with } k \in \mathbb{Z} \tag{2.11}$$

is equal to n if the factor ϕ_k is an integer multiple of 2π and otherwise the summation equals zero [164]. Fig. 2.1 shows examples of rotational symmetry representation of elements $e^{\hat{\jmath}\phi_k}$ for $n = \{1, 2, ..., 8\}$. In other words, the summation in (2.11) is equal to n for values of k such that $e^{\hat{\jmath}\phi_k}$ becomes a real positive number, and it is otherwise equal to

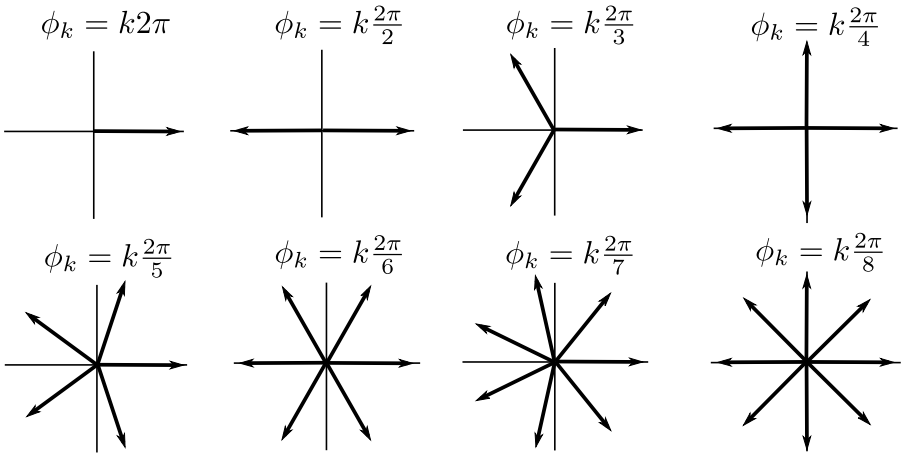

Figure 2.1: Examples of rotational symmetry representation of elements $e^{\hat{\jmath}\phi_k}$ of the summation in (2.11) for $n = \{1, 2, ..., 8\}$.

zero. Consequently, $\mathbf{a}^{+}_{p,q} \neq 0$, and the α_p-β_p subspace has non-zero positive rotating space vector for q and m combinations such that

$$e^{\hat{\jmath}(p-q\,m)\alpha_c} \tag{2.12}$$

becomes a real positive number. Then, $\mathbf{a}^{-}_{p,q} \neq 0$, and hence the α_p-β_p subspace has non zero negative rotating space vector for q and m combinations such that

$$e^{\hat{\jmath}(p+q\,m)\alpha_c} \tag{2.13}$$

becomes a real positive number. If the combination of q and m implies that both $\mathbf{a}^{+}_{p,q}$ and $\mathbf{a}^{-}_{p,q}$ are non-zero simultaneously in the same subspace, then the combination of both negative and positive rotating space vectors creates a pulsating voltage along the real axis and such subspace can be represented as 1D one (homopolar axis).

The expressions in (2.12) and (2.13), which determine the value of $\mathbf{a}^{+}_{p,q}$ and $\mathbf{a}^{-}_{p,q}$, can be split as a product of two complex numbers, one that depends on the spatial factor p and another one that depends on the temporal factors q and m:

$$e^{\hat{\jmath}(p-q\,m)\alpha_c} = e^{\hat{\jmath}\,p\,\alpha_c} \cdot e^{\hat{\jmath}(-q\,m)\alpha_c} \tag{2.14a}$$

$$e^{\hat{\jmath}(p+q\,m)\alpha_c} = e^{\hat{\jmath}\,p\,\alpha_c} \cdot e^{\hat{\jmath}\,q\,m\,\alpha_c}. \tag{2.14b}$$

The product of two complex numbers is a real positive number if each factor is the conjugated form of the other one. Therefore, the α_p-β_p subspace has non-zero positive rotating space vector ($\mathbf{a}^{+}_{p,q} \neq 0$) for q and m combinations such that

$$e^{\hat{\jmath}\,p\,\alpha_c} = e^{\hat{\jmath}\,q\,m\,\alpha_c} \tag{2.15}$$

and α_p-β_p subspace has non-zero negative rotating space vector ($\mathbf{a}^{-}_{p,q} \neq 0$) for q and m combinations such that

$$e^{\hat{\jmath}(-p)\alpha_c} = e^{\hat{\jmath}\,q\,m\,\alpha_c}. \tag{2.16}$$

Fig. 2.2 represents the left side of (2.15) and (2.16), in the complex plane, for even and odd phase machines. The values of p are limited to the range in (2.1). All the values

of $e^{\hat{\jmath}\, p\, \alpha_c}$ corresponding to positive SVR directions lie on the positive imaginary zone of the complex plane and all $e^{\hat{\jmath}(-p)\alpha_c}$ values corresponding to negative SVR directions lie on the negative imaginary zone. That is represented in Fig. 2.2 by two areas shaded in different tones, one for the positive SVR directions and another one for the negative SVR directions. Additionally, the conjugated values $e^{\hat{\jmath}\, p\, \alpha_c}$ and $e^{\hat{\jmath}(-p)\alpha_c}$ that correspond to the two possible SVR directions on α_p-β_p subspace lie over the same vertical line.

Fig. 2.3 shows the proposed graphical diagram, which is based on Fig. 2.2, for subspace and SVR direction identification of the harmonic distribution considered in (2.5). This diagram can be easily represented by an n-sided regular polygon, which is circumscribed inside the unit circle, with one of its vertices on the real positive axis (reference vertex). Each subspace is represented by a vertical line that passes through polygon vertices. The lines that link two vertices (symmetrical with respect to the real axis) correspond to 2D subspaces, i.e., planes. On the other hand, lines that pass through a single vertex correspond to 1D subspaces, i.e., homopolar axes. All vertices placed above the real axis correspond to positive rotating space vectors, all vertices placed below the real axis correspond to negative rotating space vectors and the one or two vertices placed on the real axis correspond to the zero sequence harmonics.

The right side of (2.15) and (2.16) is used to identify which subspace and SVR direction gets a specific harmonic q, which are graphically obtained by the position of the tip of the $e^{\hat{\jmath}\, q\, m\, \alpha_c}$ vector in the diagram. The tip positions of vector $e^{\hat{\jmath}\, q\, m\, \alpha_c}$ are allocated on the unit circle by an angle multiple of α_c. Since vertices of the n-sided regular polygon are distributed at consecutive multiples of α_c, along the unit circle, the harmonic plane mapping and their SVR direction can be obtained by numbering the vertices of the polygon counterclockwise, starting from zero at the reference vertex and jumping in steps of m vertices. Consequently, the steps to map the voltage harmonic distribution among planes and SVR directions for an n-phase symmetrical motor in a simple graphical way are the following:

1. Draw a horizontal line that represents the real axis. The area over this line represents positive SVR direction area and the area under it represents negative SVR direction area.

2. Draw an n-sided regular polygon with the center and one vertex on the real axis. This vertex is the reference vertex.

3. Draw vertical lines crossing the vertices of the regular polygon that are symmetrical with respect to the real axis and number them from the closest to the reference vertex to the farthest. These lines represent the subspaces α_p-β_p.

4. The subspace and SVR direction of a specific voltage harmonic q is obtained by numbering the vertices of the regular polygon counterclockwise from zero to q starting at the reference vertex and jumping in steps of m vertices.

2.2.2 Examples and Comparison with Previous Works

Fig. 2.4 shows the diagrams for five-, six- and seven-phase symmetrical machines considering two delay angle steps: $m = 1$ and $m = 2$. These diagrams show the plane and

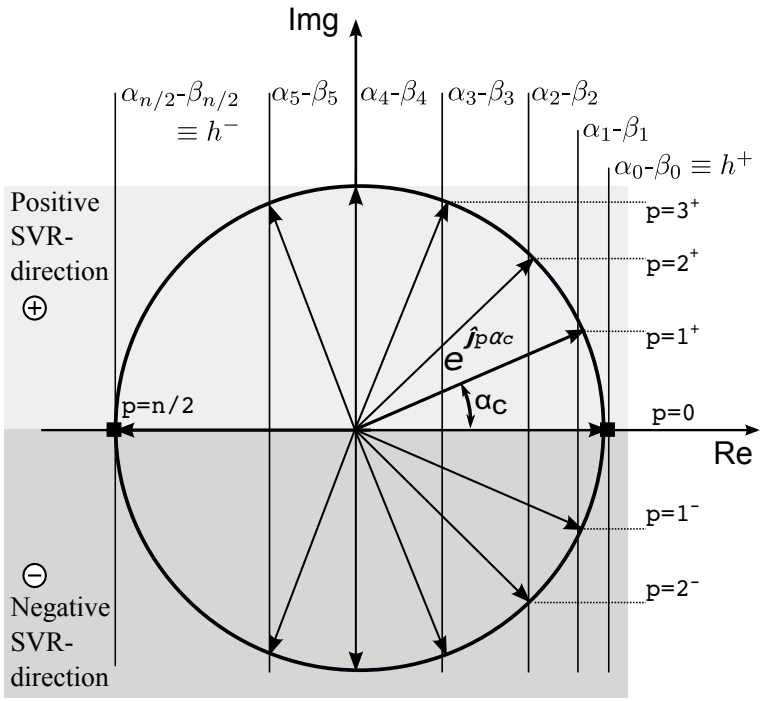

(a) Even number of phases.

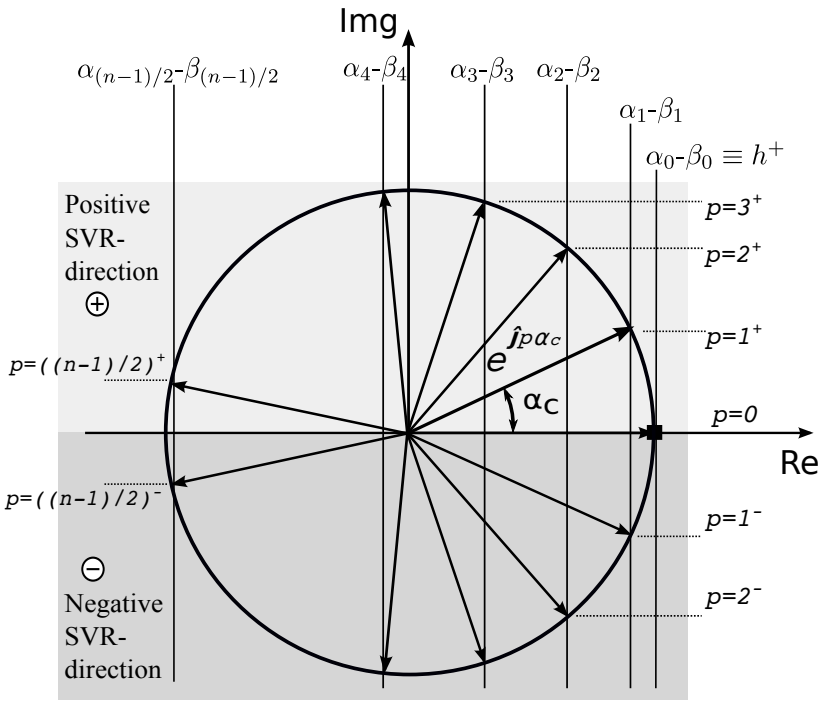

(b) Odd number of phases.

Figure 2.2: Representation of $e^{\hat{j}\,p\,\alpha_c}$ in the complex plane.

SVR direction mapping for harmonics from $q = 0$ to $q = 14$ in the five-phase case, from $q = 0$ to $q = 17$ in the six-phase case and from $q = 0$ to $q = 20$ in the seven-phase case. For example, Fig. 2.4a shows that in the five-phase machine and with $m = 1$, the 5th and 10th harmonics map into the positive homopolar axis α_0-$\beta_0 \equiv h^+$ as zero sequence,

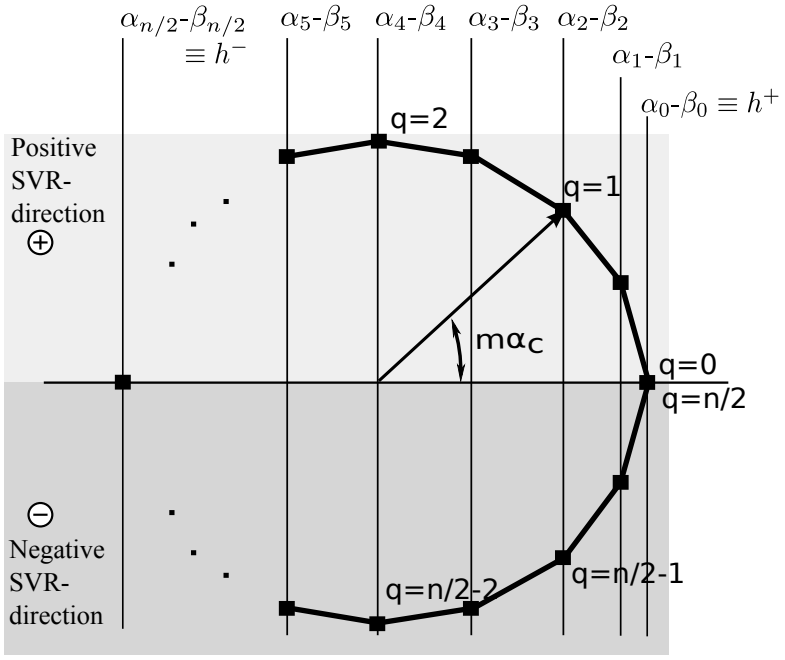

(a) Even number of phases.

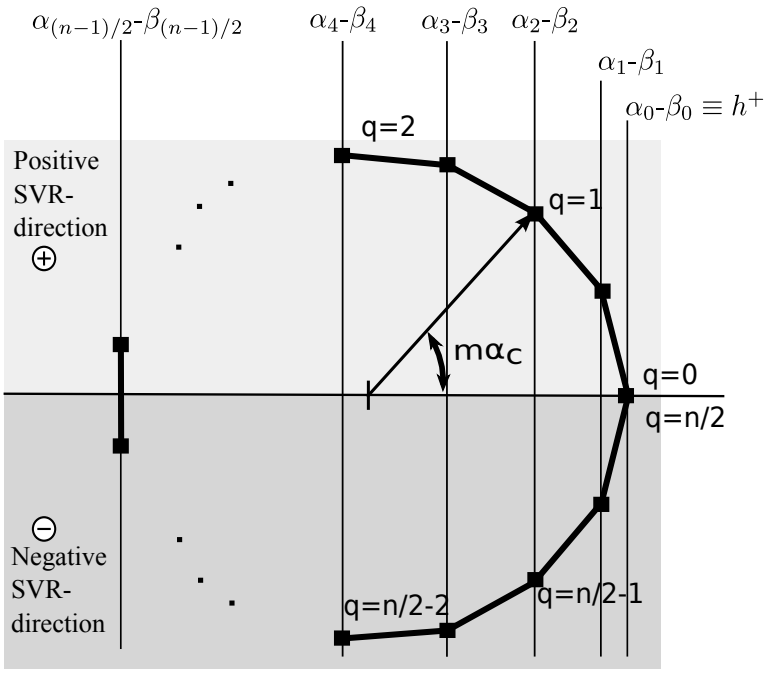

(b) Odd number of phases.

Figure 2.3: Subspace and SVR direction determination of the harmonic of order q (example with $m = 2$).

the 1st, 6th and 11th harmonics map into the α_1-β_1 plane and they have positive SVR direction, the 2nd, 7th and 12th harmonics map into the α_2-β_2 plane with positive SVR direction, the 3rd, 8th and 13th harmonics map into the α_2-β_2 plane with negative SVR direction and the 4th, 9th and 14th harmonics map into the α_1-β_1 plane with negative SVR direction. In the case of $m = 2$ (see Fig. 2.4a), the diagram is similar, but numbering

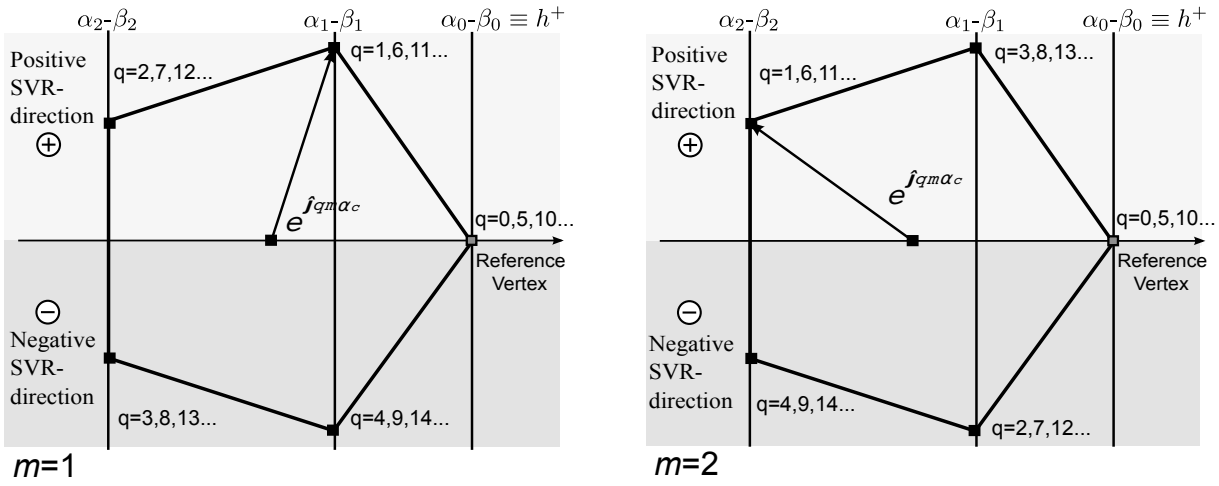

(a) Five-phase machine.

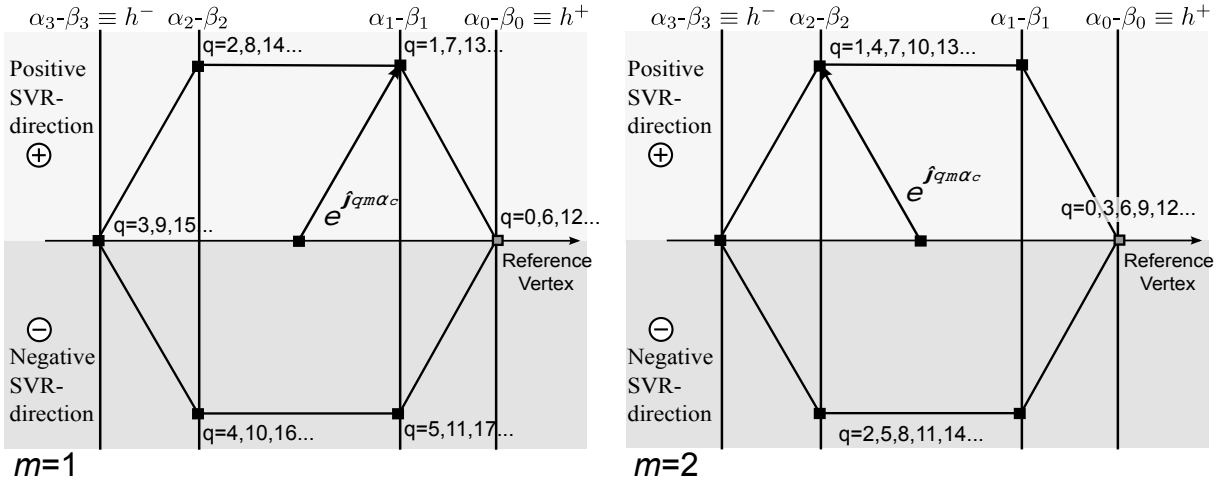

(b) Six-phase machine.

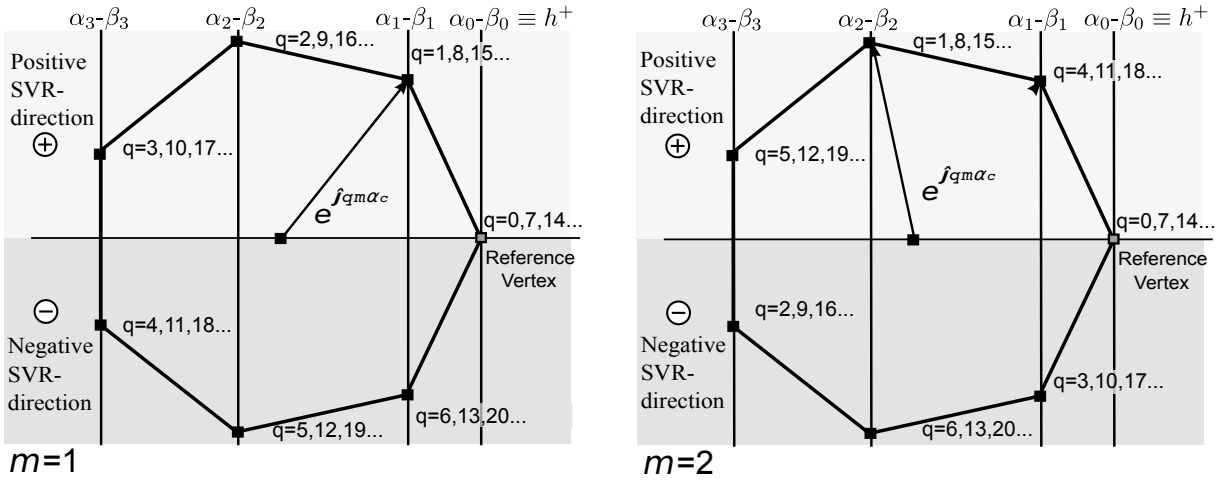

(c) Seven-phase machine.

Figure 2.4: Plane and SVR direction determination of the q order harmonic in the $m = 1$ and $m = 2$ cases.

the vertices by jumping in steps of two. Therefore, the 5th and 10th harmonics, as in the previous case, map onto h^+ axis, the 3rd, 8th and 13th harmonics map into the α_1-β_1 plane with positive SVR direction, the 1st, 6th and 11th harmonics map into the α_2-β_2 plane with positive SVR direction, the 4th, 9th and 14th harmonics map into the α_2-β_2 plane with negative SVR direction and the 2nd, 7th and 12th harmonics map into the α_1-β_1 plane with negative SVR direction.

The results of the harmonic studies made in [47, 63, 89, 95, 96], for a five-phase machine and odd harmonics, match with the results obtained in the specific five-phase diagram in Fig. 2.4a, and the harmonic mapping in a symmetrical six-phase motor shown in [88] matches with the six-phase diagram in Fig. 2.4b. In the seven-phase machine case, the expressions in [47, 87] (for odd harmonics) also match with the results of the seven-phase diagram, with $m = 1$, in Fig. 2.4c. Concerning the equation in [43] for mapping of the α_1-β_1 odd harmonics in symmetrical n-phase machines, it coincides with the diagram presented here; it can be observed in the diagrams that for an n-phase machine with $m = 1$ the harmonics $q = nj + 1$ are allocated on the α_1-β_1 plane with positive SVR direction and the harmonics $q = nj - 1$, with negative SVR direction.

Hence, the proposed graphical diagram extends the results obtained in previous works about harmonic identification in symmetrical machines, by mapping odd and even harmonics in an n-phase machine and providing extra information about their SVR direction in a simple graphical way. Furthermore, (2.15) and (2.15) show that the plane and SVR direction where one harmonic maps into is determined by the delay angle between two consecutive phases. This delay angle depends on the time harmonic order q, the angle delay step m in the converter reference and the order followed to connect the phases of the converter to the motor. Most of the previous works about time harmonic mapping in multiphase motors study only the influence of the time harmonic order variable q. This could lead to the misconception that the harmonic frequency and the plane and SVR direction into where it maps are directly related. This is only valid in the case $m = 1$ and the phases of the converter and of the motor are connected in the same order, i.e., the electrical angle between two consecutive phases is $\alpha_c = 2\pi/n$.

2.3 Application of the Mapping Diagram to Multimotor Drives

For each voltage and current component, the variable that determines to which plane and with which SVR direction it is mapped into is the delay angle between two consecutive phases. A good case to study this is the series-connected multimotor drives, because in these systems the independent control of the motors is achieved by applying a physical phase transposition in the series connection and injecting voltages with different angle delay step m between phases.

The proposed mapping diagram can be used in these multimotor drives for plane and SVR direction mapping of each harmonic for every machine of the drive. The rules and the required connection transposition between consecutive machines to achieve independent motor control are described in [54, 77–79, 81–83]. The connection transposition effect on each machine within the multimotor drive is characterized by the electrical angle α_s between two machine phases that are connected to two consecutive converter phases. This angle can be expressed as $\alpha_s = l_t\,\alpha_c$ where the factor l_t represents the phase transposition in the machine connection. As an example, Fig. 1.5 and Fig. 1.6 show the connection diagrams for a multimotor drive with two five-phase machines and two six-phase machines, respectively. Equations from (2.5) to (2.10), regarding the single machine drive, are still valid for all the machines within the multimotor system if the characteristic angle α_c is replaced with the shifted characteristic angle α_s. Therefore, (2.15) and (2.16) turn into

$$e^{\hat{\jmath}\,p\,l_t\alpha_c} = e^{\hat{\jmath}\,q\,m\,\alpha_c} \tag{2.17}$$

and

$$e^{\hat{\jmath}(-p)\,l_t\alpha_c} = e^{\hat{\jmath}\,q\,m\,\alpha_c}. \tag{2.18}$$

Consequently, the complex vector that places the subspaces on the diagram becomes

$$e^{\hat{\jmath}\,p\,l_t\,\alpha_c} \tag{2.19}$$

and

$$e^{\hat{\jmath}(-p)\,l_t\,\alpha_c} \tag{2.20}$$

for positive and negative sequence, respectively. The phase transposition factor l_t represents a physical change in the phase order and modifies the left side of (2.17) and (2.18). Therefore, l_t changes the position of the subspace in the diagram. The angle delay step m represents a change in the phase sequence of the voltage reference and modifies the right side of (2.17) and (2.18). Therefore, m varies the harmonic distribution in the diagram. For $l_t > 1$ the position of the α_p-β_p subspace in the diagram changes and the conclusions drawn from (2.15) and (2.16) are no longer valid, because not all vectors rotating in the positive direction ($e^{\hat{\jmath}\,p\,l_t\,\alpha_c}$) lie on the positive imaginary area of the complex plane and not all the vectors rotating in the negative direction ($e^{\hat{\jmath}\,(-p)\,l_t\,\alpha_c}$) lie on the negative imaginary zone of the complex plane. Consequently, for $l_t > 1$ the sign of the imaginary zone where the vector lies can be different from the sign of the SVR direction, which makes necessary to indicate in the diagram the sign of the SVR direction in each particular case.

The harmonic mapping in the series-connected multimotor system is obtained in a simple graphical way by representing the mapping diagram of every machine within the

system, taking into account the l_t value of each machine. The steps to draw the diagram of every series-connected machine within the multimotor system are the same as in the single machine case, but using (2.19) and (2.20) rather than (2.15) and (2.16) to place the vertical lines that represent the subspaces. Consequently, the steps to map the voltage harmonic distribution among planes and SVR directions for an n-phase symmetrical motor should be adapted as follows by taking into account the value of l_t:

1. Draw a horizontal line that represents the real axis. The imaginary areas over and below this line represent the two possible SVR directions for each plane.

2. Draw an n-sided regular polygon with the center and the reference vertex over the real axis.

3. For each value of p draw a vertical line, which represents the α_p-β_p subspace, through the vertex corresponding to the tip of the vector $e^{jl_tp\alpha_c}$. Add the sign of the imaginary zone where such vertex lies to the name of the plane, in order to indicate the sign of the SVR direction.

4. The subspace and SVR direction of a specific harmonic q is obtained by numbering the vertices of the regular polygon counterclockwise from zero to q starting at the reference vertex and jumping in steps of m vertices, which represents the positions of the tip of the vector $e^{\hat{\jmath}\,q\,m\,\alpha_c}$. If the vertex corresponding to q lies in the positive imaginary zone then the sign of the SVR direction of harmonic q is equal to the sign indicated in the plane name, and if it lies on the negative imaginary zone then the sign of such SVR direction is the opposite.

The most useful application of the delay angle step m is in series-connected multimotor drives. It follows from (2.17) that, for a specific l_t, the fundamental voltage and current ($q = 1$) map into the α_1-β_1 plane when the delay angle step of the reference is $m = l_t$. This fact points out that the machine that has a certain l_t value can be controlled by selecting $m = s_t$ in the source reference. Consequently, the mapping diagram obtained with certain values of m and l_t shows how the harmonics of the voltage that controls the machine with a phase transposition equal to m affect the machine with a phase transposition equal to l_t in the multimotor system.

As an example, the mapping diagrams for the two-motor drives in Fig. 1.5 and Fig. 1.6 are depicted in Fig. 2.5 and Fig. 2.6, respectively. Fig. 2.6, which corresponds to the six-phase two-motor drive, shows the diagrams corresponding to the four combinations of the phase transposition factors of both machines $l_t = 1$ and $l_t = 2$ with the two fundamental angle delay steps $m = 1$ and $m = 2$ that allow to control each motor. The diagrams corresponding to cases with $l_t = 2$ show a smaller number of planes, because the tip of the vector in (2.19) just points to three of the six vertices. Consequently, just a single α_1-β_1 plane and a single homopolar h^+ axis are obtained, which is the case of a three-phase machine. This is in agreement with the connection diagram in Fig. 1.6, which shows that in a six-phase two-motor drive just three phases of $\mathrm{M_{II}}$ machine are used, so it can be substituted by a three-phase one [54, 77]. The reference voltage to control the $\mathrm{M_I}$ machine requires a fundamental component with $m = 1$, which maps into the α_1-β_1 plane of $\mathrm{M_I}$ with positive SVR direction. Such fundamental component maps to a vertex without any related plane in the $\mathrm{M_{II}}$ machine and it does not affect $\mathrm{M_{II}}$. The same applies to the sets

of harmonics $q = \{7, 13\}$ and $q = \{5, 11, 17\}$ that produce torque ripple in M_I machine but they do not in M_{II}. The harmonic sets $q = \{2, 8, 14\}$ and $q = \{4, 10, 16\}$, which produce losses in M_I machine because they map into its α_2-β_2 plane, map into the α_1-β_1 plane of M_{II} with positive and negative SVR direction, respectively, producing torque disturbances in M_{II}. The harmonics $q = \{3, 9, 15\}$ which map onto the h^- axis of M_I do not affect M_{II} machine. The harmonics $q = \{0, 6, 12\}$ map onto the h^+ axis of both machines. It is important to remark that the usual odd harmonics of the voltage that controls M_I do not have any influence on M_{II} and the unusual even harmonics are the ones that influence the M_{II} machine. The reference voltage to control the M_{II} machine requires a fundamental component with $m = 2$. Such fundamental component and harmonics $q = \{4, 7, 10, 13\}$ map into the α_1-β_1 plane of the M_{II} machine and into the α_2-β_2 plane of M_I with positive SVR direction in both cases. The harmonics $q = \{2, 5, 8, 11, 14\}$ map into the α_1-β_1 plane of M_{II} machine and into the α_2-β_2 plane of M_I with negative SVR direction in both cases. The harmonics $q = \{0, 3, 6, 9, 12\}$ map onto the h^+ axis of both machines. In all cases, the harmonics of the voltage to control the M_{II} machine do not produce torque ripple in M_I machine and they can only produce extra losses in some cases.

Fig. 2.5, which corresponds to the five-phase two-motor drive, shows the diagrams corresponding to the four combinations of the phase transposition factors of both machines $l_t = 1$ and $l_t = 2$ with the two angle delay steps $m = 1$ and $m = 2$, which allow to control each one of them. The mapping diagram obtained with $l_t = 1$ and $m = 1$ shows how the harmonics of the voltage that controls the M_I machine torque affect itself. As expected, the obtained results are the same as those obtained in the case $m = 1$ of Fig. 2.4a. The mapping diagram obtained with $l_t = 1$ and $m = 2$, which shows how the harmonics of the voltage that controls the M_{II} machine torque affect the M_I machine, is identical to the diagram obtained in the case $m = 2$ of Fig. 2.4a, and consequently the same conclusions are derived. That is, the fundamental voltage that controls M_{II} and the harmonic sets $q = \{6, 11\}$ and $q = \{4, 9, 14\}$ map into the α_2-β_2 plane of M_I and thus they produce extra losses in M_I machine. The harmonic sets $q = \{3, 8, 13\}$ and $q = \{2, 7, 12\}$ map into the α_1-β_1 plane of M_I with positive and negative SVR direction, respectively, so they produce torque ripple in M_I machine. Harmonics $q = \{0, 5, 10\}$ map onto the homopolar h^+ axis and therefore, they do not affect to M_I machine. The mapping diagram obtained with $l_t = 2$ and $m = 1$ shows the effect of the harmonics of the voltage that controls the M_I machine in the M_{II} machine. In this case, the fundamental voltage that controls the M_I and the harmonics $q = \{6, 11\}$ maps into the α_2-β_2 plane of M_I with negative SVR direction, so they produces extra losses in M_{II} machine. Harmonics $q = \{4, 9, 14\}$ map into the same plane but with positive SVR direction and thus they produce extra losses in M_{II} as well. The harmonics sets $q = \{2, 7, 12\}$ and $q = \{3, 8, 13\}$ map into the α_1-β_1 plane with positive and negative SVR direction, respectively, and consequently they produce torque disturbances in M_{II}. The mapping diagram obtained with $l_t = 2$ and $m = 2$, which shows how the harmonics of the voltage that controls M_{II} machine affect this machine, provides the same harmonic mapping as in the case of $l_t = m = 1$ regarding the effects in the M_I machine of harmonics of the voltage that controls this machine.

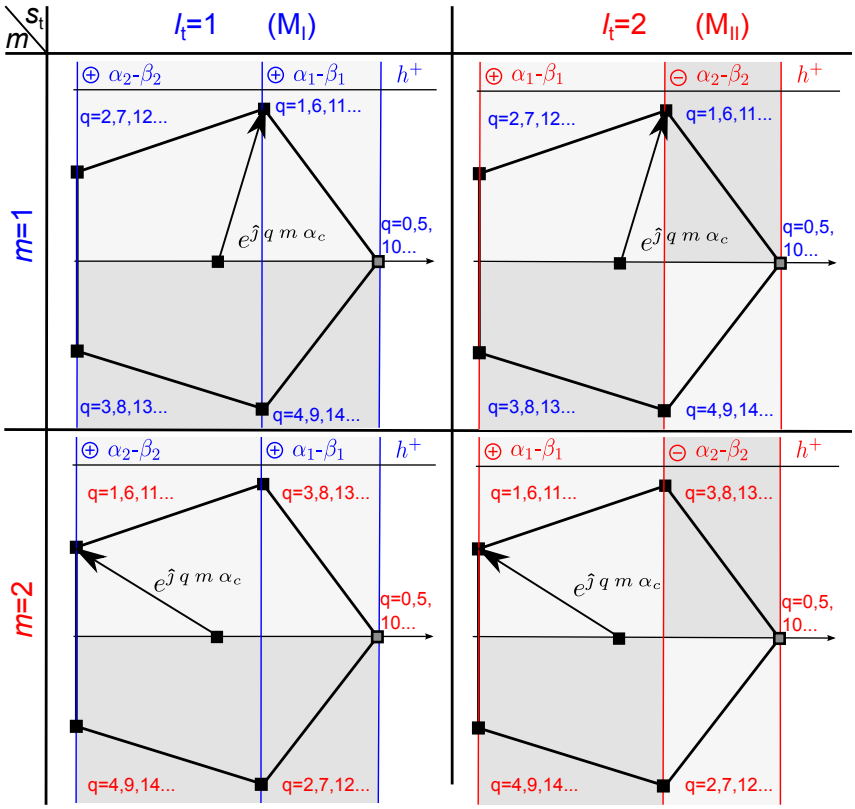

Figure 2.5: Mapping diagram in a series-connected five-phase two-motor drive.

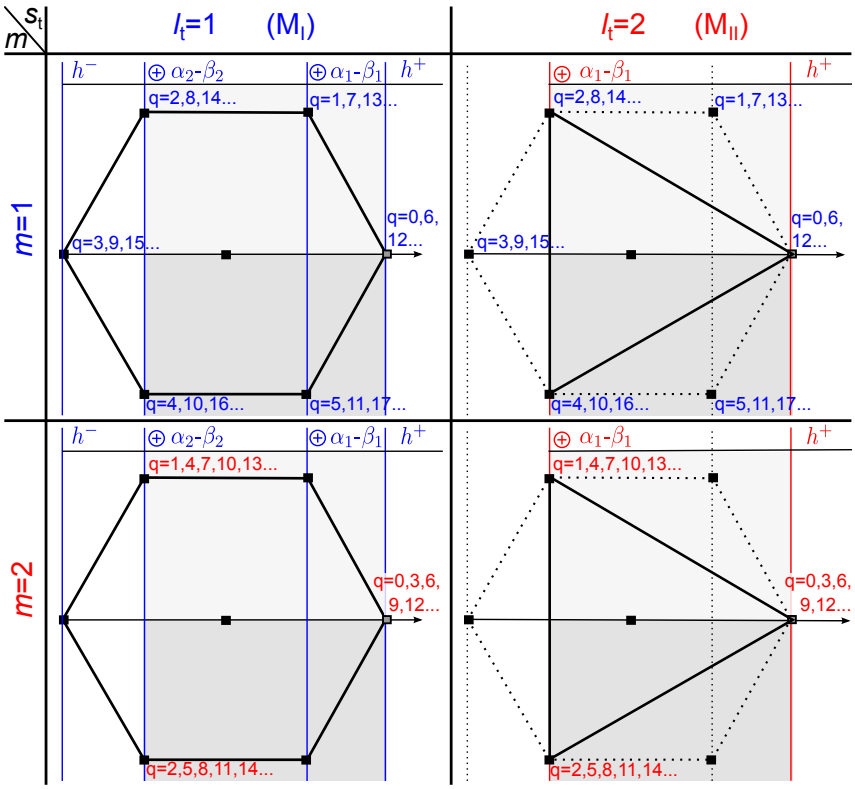

Figure 2.6: Mapping diagram in a series-connected six-phase two-motor drive.

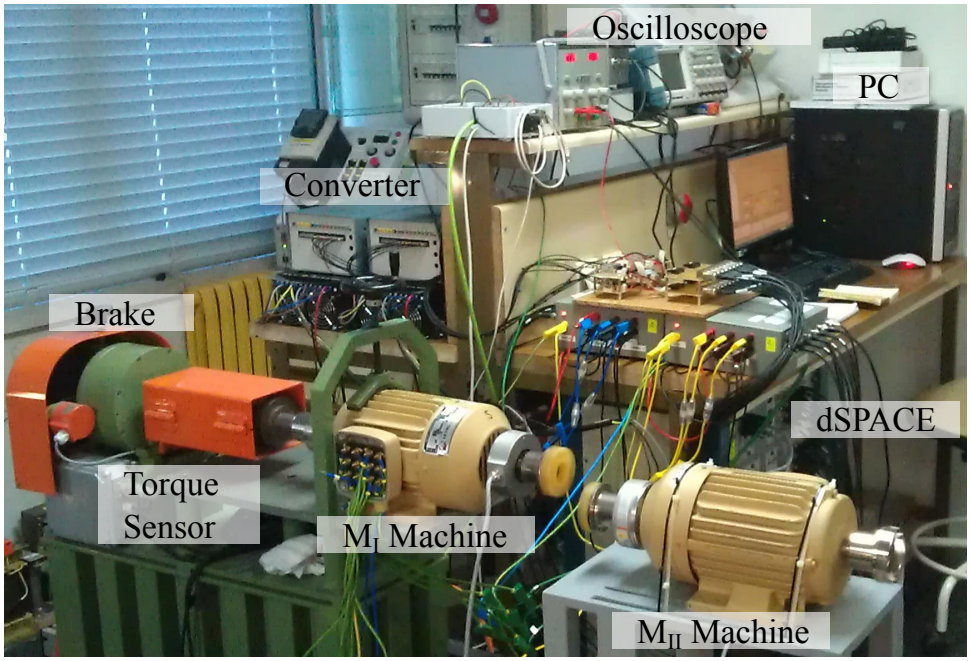

Figure 2.7: Experimental setup.

2.4 Experimental Evaluation of the Harmonic Mapping Diagram

The proposed diagram is validated by using a five- and a six-phase motor drives. The experimental setup is shown in Fig. 2.7. Two three-phase VSI Semikron Semistack SKS 35F B6U+E1CIF+B6CI21V modules are used to build a six-phase VSI. The dc bus voltage is $V_{dc} = 300$ V. In the five-phase experiments just five of the six legs of the VSI are used. The converter control is implemented in a dSPACE DS1006 real-time rapid prototyping platform based on an Advanced Micro Devices (AMD) Operton processor with the DS5001 PWM board. The PWM is configured with a switching frequency equal to 10 kHz. The voltages are measured between each phase of the machine and the medium point of the dc bus, using LEM LV 25-P sensors through a low-pass filter with a cut-off frequency of 3.0 kHz. The phase currents are measured by means of LEM LA 55-P sensors. The analog-to-digital converter DS2004 board with 16 parallel channels is used to capture all the measured signals. The fast Fourier transformation (FFT)s shown in this chapter are obtained offline by using the Matlab 'fft' function in the complex mode with measures of 5120 samples and, thus, a resolution of 1.953 Hz.

Two different experiments have been done with single motor drive configuration. The first one is to verify the subspace and SVR direction mapping of stator voltage and current harmonics, and the second one is to verify the influence of m on the plane and SVR direction harmonic mapping. A five- and a six-phase motors are tested in each experiment, respectively. An additional experiment with a six-phase two-motor drive has been carried out to demonstrate that the presented graphical method can be used in multimotor systems to determine the plane and the SVR direction mapping of every harmonic in each machine. Finally, the effects of the spatial harmonic distortion in a series-

connected five-phase two-motor drive and the voltage and current harmonic mapping in such system are experimentally evaluated.

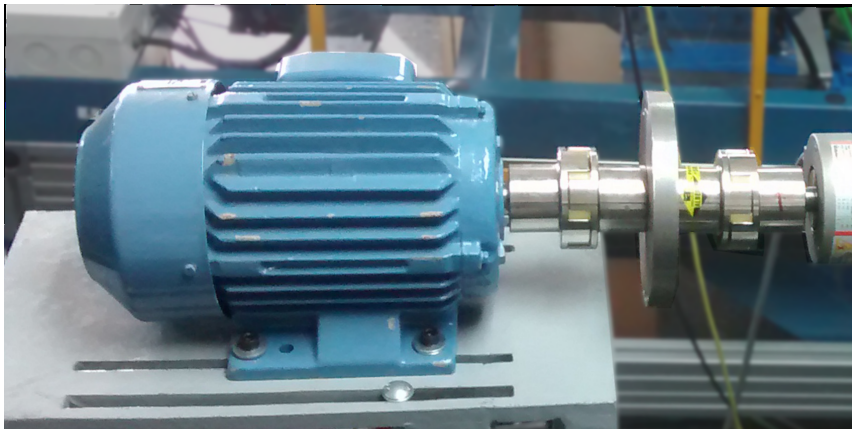

Figure 2.8: Five-phase induction motor.

2.4.1 Five-Phase Single Motor Drive

In this experiment, the drive includes a symmetrical four-pole five-phase induction machine, shown in Fig. 2.8. It was made by rewinding a 0.75 kW three-phase induction motor with 30 stator slots, and it has five non-perfectly distributed star-connected windings. In the first experiment the motor is operated in open-loop mode without mechanical load. The reference voltage to feed the machine has a 100 V root mean square (rms) fundamental component at 50 Hz and a fundamental step delay between phases $m = 1$. Harmonics up to $q = 12$ are injected with an amplitude of 20% the fundamental voltage amplitude. The voltage and current measurements are transformed through matrix $[\mathbf{T}]$ into symmetrical components. The spectrum of each symmetrical component, obtained by the complex fast Fourier transformation (CFFT), is depicted in Fig. 2.9. The CFFTs show that the fundamental component and the 6th and 11th harmonics map into α_1-β_1 plane with positive SVR direction, the 4th and 9th harmonics map into α_1-β_1 plane with negative SVR direction, the 2nd, 7th and 12th harmonics map into α_2-β_2 plane with positive SVR direction, the 3rd and 8th harmonics map into α_2-β_2 plane with negative SVR direction and the 5th and 10th harmonics of the machine voltage map onto the h^+ axis. There is no current harmonic component on the h^+ axis, because the neutral of the motor is isolated. The harmonic subspace and SVR direction mapping obtained through the experiments matches with the mapping predicted by the diagram in Fig. 2.4a for the harmonics of a voltage with an angle delay step $m = 1$ feeding a five-phase machine.

The objective of the second experiment is to check how a sinusoidal voltage component of 50 Hz maps into different subspaces by only modifying its angle delay step m. In this experiment the rotor is blocked and the torque is measured using the test bench. The VSI is operated in open-loop mode and the voltage reference is set in order to obtain the same per phase current in all the tests. Five tests are done by injecting only a sinusoidal voltage component of 50 Hz with m from one to five, to test the influence of m on the mapping.

Fig. 2.10 merges measurements obtained in the five experiments. Fig. 2.10a shows the voltage references of phase A in each test to obtain phase current values around 1.5 A, Fig. 2.10b shows the phase A current waveform and Fig. 2.10c shows the torque measurements. In the cases $m = 1$ and $m = 4$ a high amplitude voltage reference is

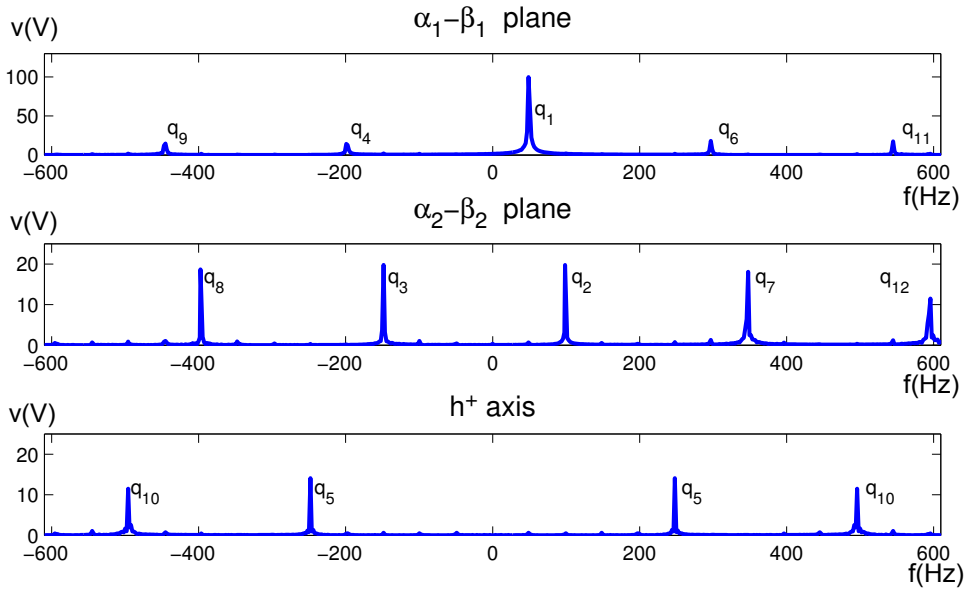

(a) Voltage spectrum.

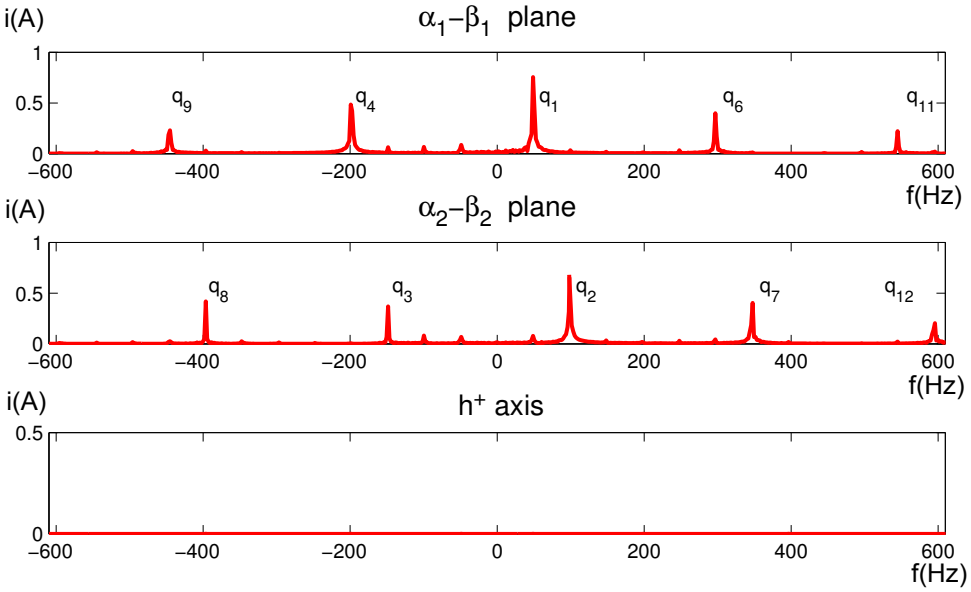

(b) Current spectrum.

Figure 2.9: Five-phase machine symmetrical components spectrum analysis.

required to obtain the current set point and the torque produced is also high, which shows that with $m = 1$ and $m = 4$ the voltage and current 50 Hz component map into the α_1-β_1 plane, which is responsible for the electromechanical energy conversion. With $m = 1$ the torque is positive and with $m = 4$ it is negative; consequently, for $m = 1$ and $m = 4$, the SVR directions are positive and negative, respectively. In the cases $m = 2$ and $m = 3$ a lower amplitude voltage reference is required to obtain the current set point. In both cases the torque produced is low, which shows that the voltage and current 50 Hz component map into the α_2-β_2 plane, which does not allow electromechanical energy conversion. The torque in a perfect sinusoidally distributed machine should be zero in the α_2-β_2 plane;

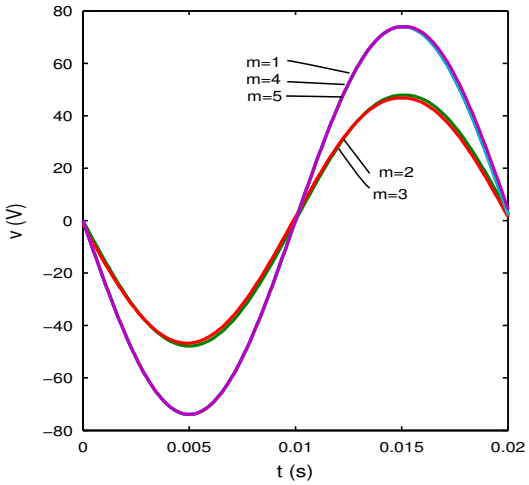

(a) Phase A voltage reference.

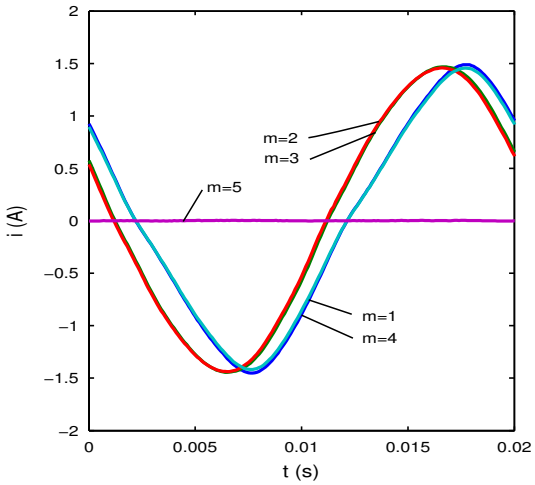

(b) Phase A current.

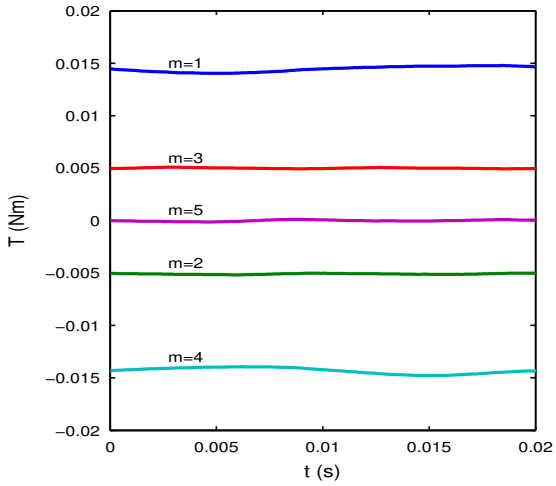

(c) Torque.

Figure 2.10: Angle delay step m influence in torque in five-phase machine.

nevertheless, the machine used in the tests has a non-perfectly sinusoidally-distributed stator winding, which explains the fact that the torque is not zero. In the $m = 5$ case, even with a high voltage amplitude the phase current does not flow. That is because of the absence of neutral connection; therefore, with $m = 5$ the voltage 50 Hz component maps onto the h^+ homopolar axis. All these experimental results validate the mapping diagram for the five-phase machine case shown in Fig. 2.4a.

2.4.2 Six-Phase Single Motor Drive

The six-phase motor drive includes a three-phase 1.5 kW induction motor with 24 stator slots that was rewound to form a symmetrical two-pole six-phase star-connected machine. It is shown in Fig. 2.11. As in the first five-phase experiment the motor is operated in open-loop mode without mechanical load. The reference voltage to feed the machine has a 100 V rms fundamental component at 50 Hz and $m = 1$. Harmonics up

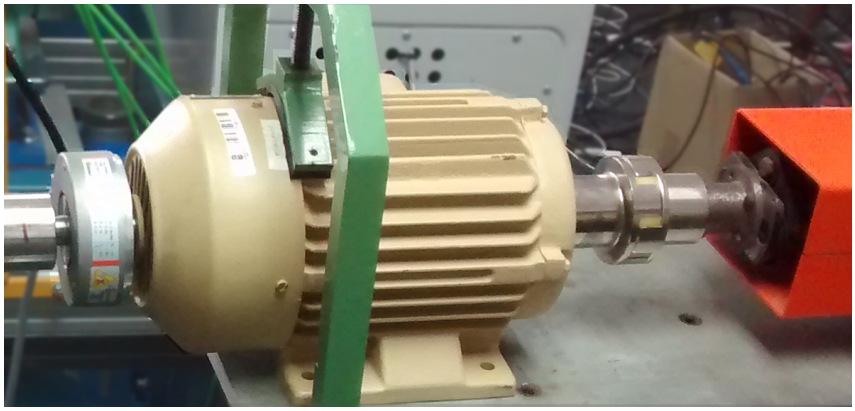

Figure 2.11: Six-phase induction motor.

to $q = 12$ are injected with an amplitude of 20% the fundamental voltage amplitude. The neutral points of both three-phase subsets of the six-phase machine are connected, which allows zero negative sequence current circulation. The CFFT of each symmetrical component of the motor voltages and currents, which is depicted in Fig. 2.12, shows that the fundamental component and the 7th harmonic of the machine voltage map into the α_1-β_1 plane with positive SVR direction, the 5th and 11th harmonics map into the α_1-β_1 plane with negative SVR direction, the 2nd and 8th harmonics map into the α_2-β_2 plane with positive SVR direction, the 4th and 10th harmonics map into the α_2-β_2 plane with negative SVR direction, the 3rd and 9th harmonics map onto the h^- axis and the 6th and 12th harmonics of the machine voltage map onto the h^+ axis. As happened in the five-phase experiment, there is no current harmonic component on the h^+ axis because there is no neutral connection between the VSI and the motor. The harmonic plane and SVR direction mapping obtained in this experiment matches with the results predicted by the diagram in Fig. 2.4b for $m = 1$.

In the second experiment, as in the five-phase case, the VSI is operated in open-loop mode and the voltage amplitude is set in order to obtain per phase currents of 1.5 A. In each test, the rotor is locked and the per phase current, produced torque and current between neutral points are measured. In this case six tests are carried out by feeding the machine with just sinusoidal voltage at 50 Hz and six different values of the angle delay step $m = 1, 2, 3, ..., 6$ in each one. With $m = 1$ the machine produces a positive torque, so in this case the voltage and current 50 Hz component maps into the α_1-β_1 plane with positive SVR direction. In the $m = 5$ case the torque is negative; therefore, in this case the 50 Hz component of voltage and current maps into the α_1-β_1 plane, but with negative SVR direction. With $m = 3$ the measurements show no torque and a high current between the winding neutrals, so, in this case the 50 Hz component of voltage and current maps into h^- axis. With $m = 2$ and $m = 4$ there is no torque and a high phase current for a low voltage amplitude, so, in both cases the 50 Hz component of voltage and current maps into α_2-β_2 plane. In the $m = 6$ case, even with a high voltage amplitude, the phase current does not flow. That is because of the absence of neutral connection; therefore, with $m = 6$ the 50 Hz component of the voltage maps onto the h^+ axis. All these experimental results validate the six-phase mapping diagram.

In the above six experiments with different values of m the voltage of the dc link was

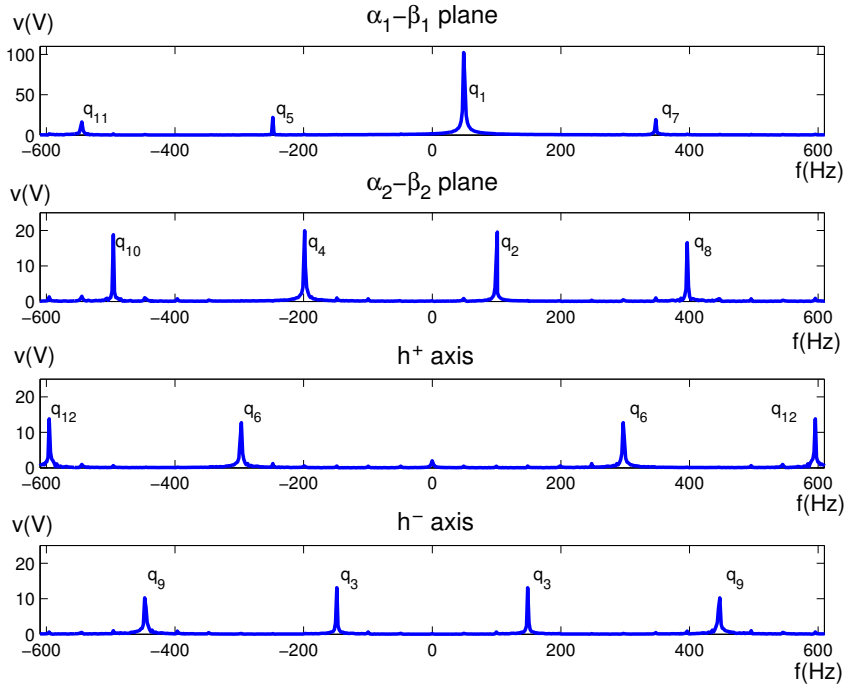

(a) Voltage spectrum.

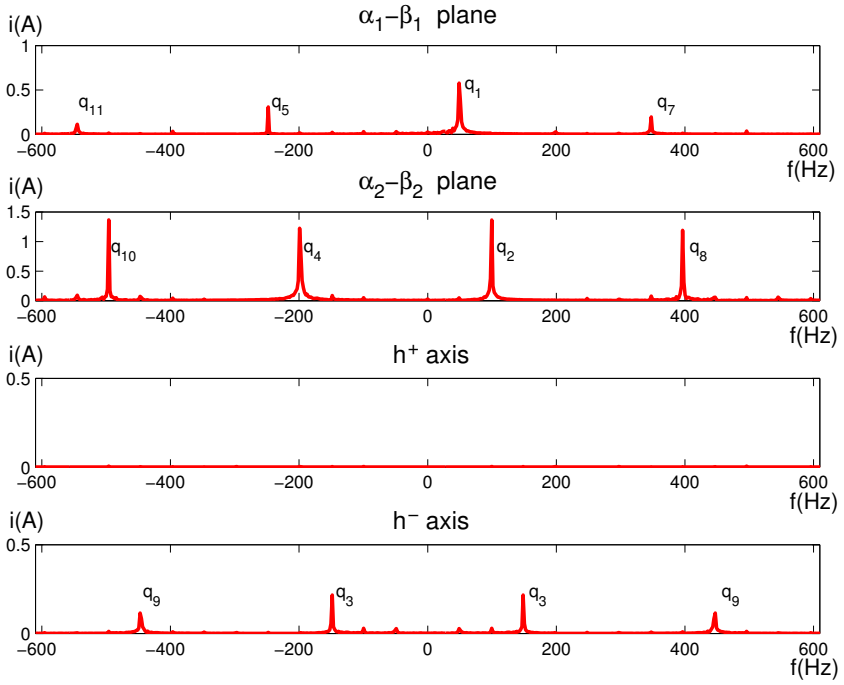

(b) Current spectrum.

Figure 2.12: Six-phase machine symmetrical components spectrum analysis.

increased up to 500 V so that the system nonlinearities cause large harmonic amplitudes [65, 85]. The plane mapping and the SVR direction of all those harmonics can be also predicted with the proposed six-phase diagram in Fig. 2.4b. The traces corresponding to $m = 1$ and $m = 5$ in Fig. 2.13b have a low 3rd harmonic ($q = 3$). The subspace mapping

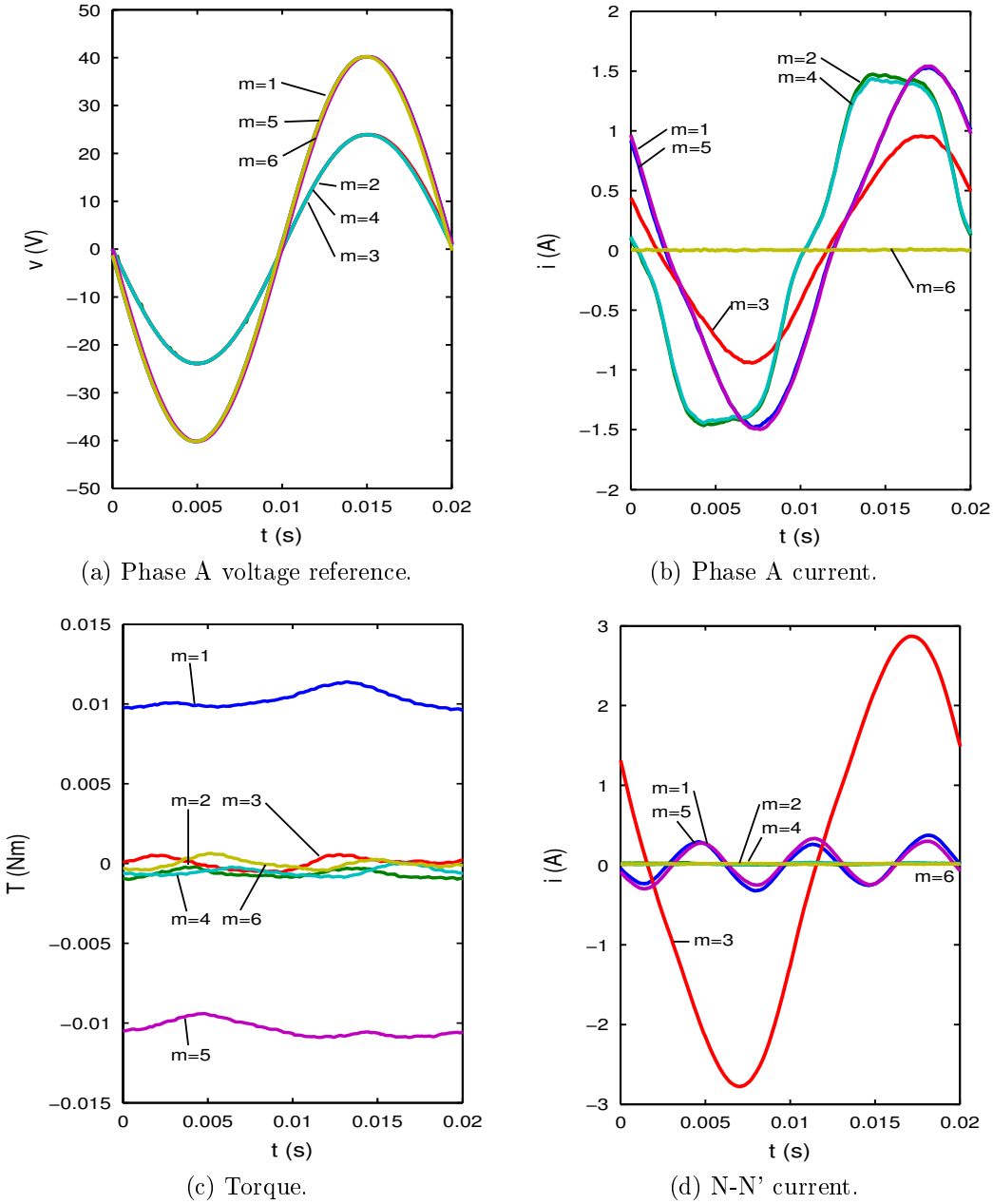

(a) Phase A voltage reference.

(b) Phase A current.

(c) Torque.

(d) N-N' current.

Figure 2.13: Angle delay step m influence in six-phase machine.

of the 3rd harmonic is obtained by counting the vertices of the hexagon counterclockwise by jumping in steps of m from zero to $q = 3$. In both cases, $m = 1$ and $m = 5$, the obtained vertex is the same, which corresponds to the homoplar h^- axis. Consequently, the 3rd harmonic current flows between the winding neutrals, as it is shown in Fig. 2.13d. The traces corresponding to $m = 2$ and $m = 4$ in Fig. 2.13b do not have a 3rd current harmonic and they show significant 5th and 7th harmonics. By means of the six-phase diagram with $m = 2$ in Fig. 2.4b, the vertices corresponding to $q = 3$, $q = 5$ and $q = 7$ lie on the h^+ axis, the α_2-β_2 plane with negative SVR direction and the α_2-β_2 plane with positive SVR direction, respectively. With $m = 4$ the vertices corresponding to $q = 3$,

$q = 5$ and $q = 7$ lie on the h^+ axis, the α_2-β_2 plane with positive SVR direction and the α_2-β_2 plane with negative SVR direction, respectively. In both cases, $m = 2$ and $m = 4$, the 3rd harmonic maps onto the h^+ axis, which explains the absence of the 3rd harmonic current in the measurements. The 5th and the 7th current harmonics map into the low impedance α_2-β_2 plane, which explains the high amplitude of such harmonics in the measurements.

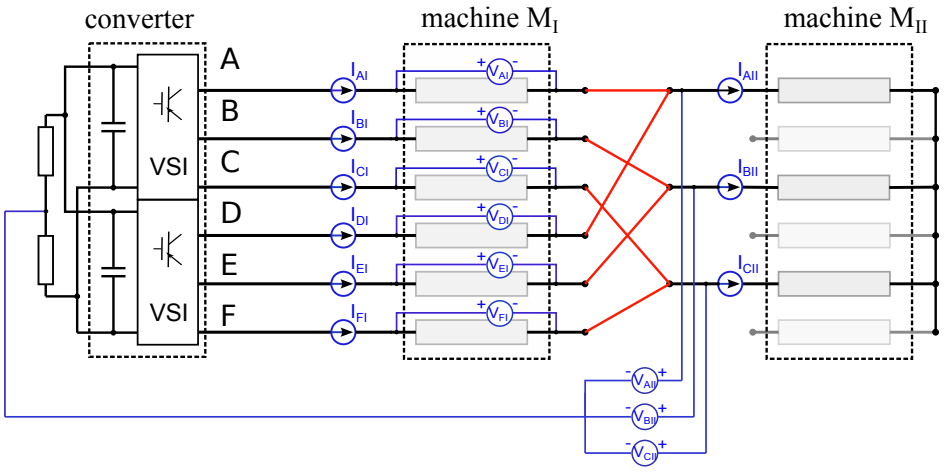

Figure 2.14: Connection diagram of the six-phase two-motor drive experiment

2.4.3 Experimental Evaluation of the Series-Connected Six-Phase Two-Motor Drive

The laboratory setup shown in Fig. 2.7, with a series-connected six-phase two-motor drive, is used to validate the mapping diagram in a multimotor system. Fig. 2.14 and Fig. 2.6 represent the connection and the mapping diagrams of the six-phase two-motor system, respectively. In this experiment two similar 1.5 kW two-pole six-phase machines, with 24 stator slots each one, are series connected. One of them is the motor previously used in the single machine experiment.

Both motors are operated in open-loop mode and controlled independently by adding two different voltage references, one reference $[\mathrm{V}]^*_{\mathrm{I}}$ with a delay angle step $m_{\mathrm{I}} = 1$ and $[\mathrm{V}]^*_{\mathrm{II}}$ with a delay angle step $m_{\mathrm{II}} = 2$:

$$[\mathrm{V}]^* = [\mathrm{V}]^*_{\mathrm{I}} + [\mathrm{V}]^*_{\mathrm{II}} = [\mathrm{V}^*_0, \mathrm{V}^*_1, \ldots, \mathrm{V}^*_\eta, \ldots, \mathrm{V}^*_{n-1}]' \tag{2.21}$$

with

$$\mathrm{V}^*_\eta = \mathrm{A}^*_{\mathrm{I}} \cos\left(\omega^*_{\mathrm{I}} t - \eta\alpha_c\right) + \mathrm{A}^*_{\mathrm{II}} \cos\left(\omega^*_{\mathrm{II}} t - 2\eta\alpha_c\right) \tag{2.22}$$

where V^*_η is the inverter voltage reference of phase η, $\mathrm{A}^*_{\mathrm{I}}$ and ω^*_{I} are the amplitude and the frequency references of $\mathrm{M_I}$, respectively, and $\mathrm{A}^*_{\mathrm{II}}$ and ω^*_{II} are the amplitude and the frequency references of $\mathrm{M_{II}}$. The mapping diagram for a six-phase two-motor drive in Fig. 2.6 shows that the first reference, with $m_{\mathrm{I}} = 1$, maps into the α_1-β_1 plane of $\mathrm{M_I}$ machine with positive SVR direction, and does not affect the second machine and the second reference, with $m_{\mathrm{II}} = 2$, maps into the α_2-β_2 plane in $\mathrm{M_I}$ machine and in the α_1-β_1 plane in $\mathrm{M_{II}}$ machine with positive SVR direction. Therefore, $[\mathrm{V}]^*_{\mathrm{I}}$ controls the $\mathrm{M_I}$ flux and torque and $[\mathrm{V}]^*_{\mathrm{II}}$ controls the $\mathrm{M_{II}}$ flux and torque.

Two experiments are done to map low-order voltage harmonics of $[\mathrm{V}]^*_{\mathrm{I}}$ and $[\mathrm{V}]^*_{\mathrm{II}}$ in both motors:

- In the first experiment, the VSI voltage reference is the sum of $[\mathrm{V}]^*_{\mathrm{I}}$, $[\mathrm{V}]^*_{\mathrm{II}}$ and the

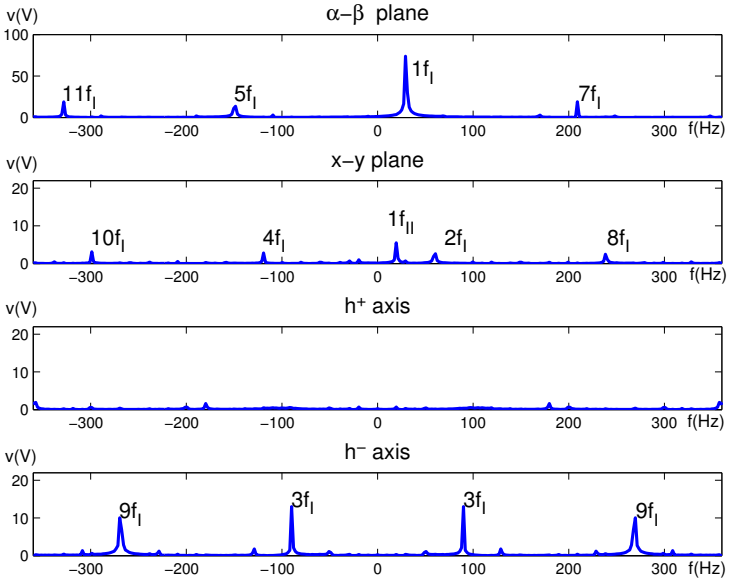

(a) M_I (six-phase) voltage spectrum.

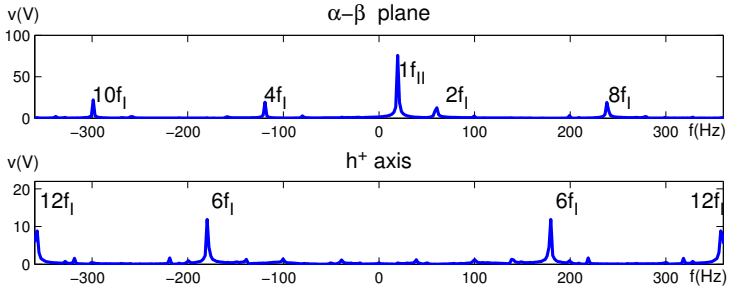

(b) M_{II} (three-phase) voltage spectrum.

Figure 2.15: Distribution of $[v]_I$ harmonics in both motors.

harmonics of $[V]^*_I$ from the 2nd to the 12th:

$$V^*_\eta = A^*_I \cos(\omega^*_I t - \eta\alpha_c) + A^*_{II} \cos(\omega^*_{II} t - 2\eta\alpha_c) + \sum_{q=2}^{12} A^*_I \cos q(\omega^*_I t - \eta\alpha_c). \quad (2.23)$$

- In the second experiment, the VSI reference is the sum of $[V]^*_I$, $[V]^*_{II}$ and the harmonics of $[V]^*_{II}$ from the 2nd to the 12th:

$$V^*_\eta = A^*_I \cos(\omega^*_I t - \eta\alpha_c) + A^*_{II} \cos(\omega^*_{II} t - 2\eta\alpha_c) + \sum_{q=2}^{12} A^*_{II} \cos q(\omega^*_{II} t - \eta\alpha_c). \quad (2.24)$$

In both experiments the amplitude and the frequency of $[V]^*_I$ are set to 120 V and 30 Hz, respectively. The amplitude and frequency of $[V]^*_{II}$ are set to 80 V and 20 Hz, respectively, and the amplitude of the injected harmonics is 20% of the fundamental.

Fig. 2.15 and Fig. 2.16 show the resulting complex spectrum of M_I and M_{II} with $[V]^*_I$ harmonic injection. In this experiment it is also proved that the harmonic voltages and currents that map into a vertex without any related plane in the M_{II} machine diagram

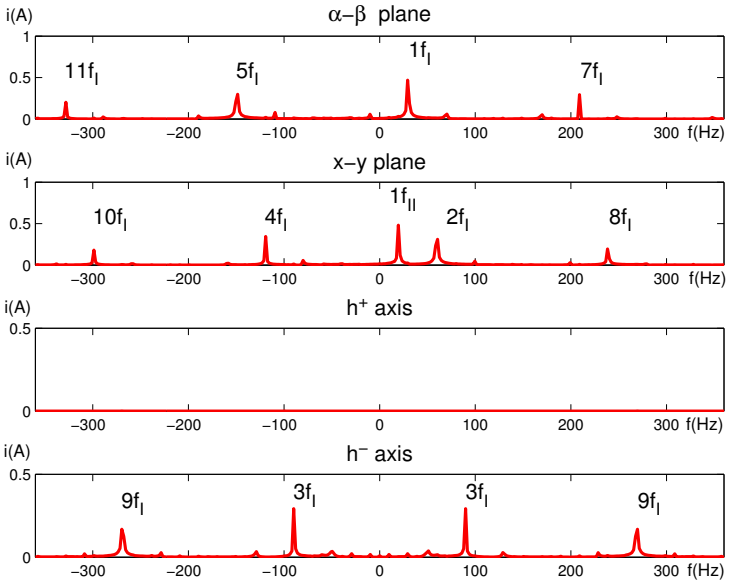

(a) M_I (six-phase) current spectrum.

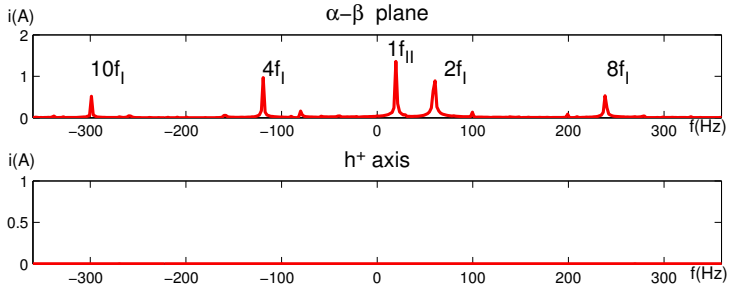

(b) M_{II} (three-phase) current spectrum.

Figure 2.16: Distribution of the current harmonics due to $[v]_I$.

(see Fig. 2.6) do not affect M_{II}. These harmonics are canceled at the connection points between M_I and M_{II} and do not have any influence on the M_{II} machine. Therefore, in the M_{II} machine only the α_1-β_1 plane and h^+ axis are available, so the other planes are not represented in the CFFT figures of M_{II}. This can be also determined by the equivalence of the second six-phase machine to a three-phase machine. As in the single machine experiment, the fundamental, 5th, 7th and 11th harmonics of $[V]_I^*$ map into the α_1-β_1 plane of M_I and the 2nd, 4th, 8th and 10th harmonics of $[V]_I^*$ map into the α_2-β_2 plane of M_I. The voltage harmonics that map into the α_2-β_2 plane of M_I map into the α_1-β_1 plane of M_{II}. Therefore, the 2nd, 4th, 8th and 10th harmonics of $[V]_I^*$ produce distortion in the M_{II} machine torque. Odd order harmonics of $[V]_I^*$ do not have influence on M_{II}. The 6th and 12th harmonics of $[V]_I^*$ maps onto the h^+ axis of M_{II}. The amplitude of the voltage harmonics in the α_2-β_2 plane of M_I is much lower than in the α_1-β_1 plane of M_{II}. It is because both planes share the same current and the α_2-β_2 plane of M_I has lower impedance. Table 2.1 summarizes the experimental $[V]_I^*$ harmonic distribution in the multimotor system. These results validate the proposed diagram for a series-connected six-phase two-motor drive in the $m = 1$ case represented in Fig. 2.6.

Fig. 2.17 and Fig. 2.18 show the resulting voltage and current complex spectra of M_I

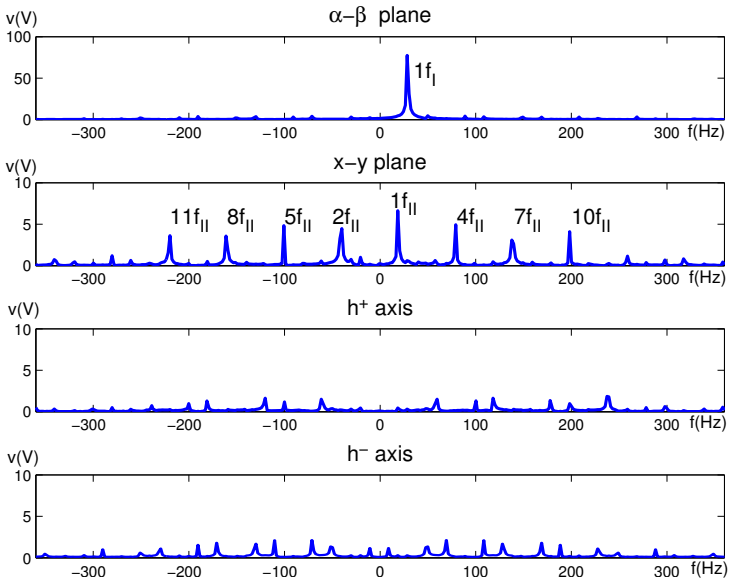

(a) M_I (six-phase) voltage spectrum.

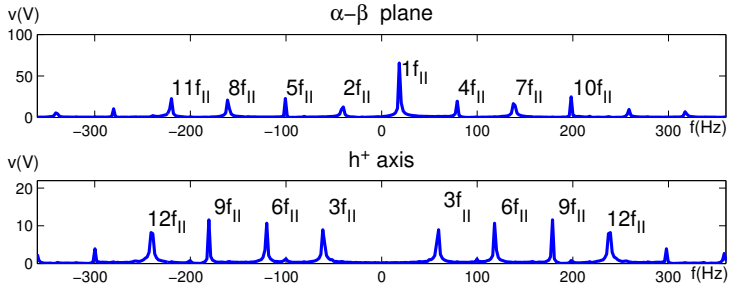

(b) M_{II} (three-phase) voltage spectrum.

Figure 2.17: Distribution of $[v]_{II}$ harmonics.

TABLE 2.1
$[V]^*_I$ HARMONIC DISTRIBUTION IN THE MULTIMOTOR SYSTEM

Harmonic order	1	2	3	4	5	6
M_I machine	α_1-β_1^+	α_2-β_2^+	h^-	α_2-β_2^-	α_1-β_1^-	—
M_{II} machine	—	α_1-β_1^+	—	α_1-β_1^-	—	h^+
Harmonic order	7	8	9	10	11	12
M_I machine	α_1-β_1^+	α_2-β_2^+	h^-	α_2-β_2^-	α_1-β_1^-	—
M_{II} machine	—	α_1-β_1^+	—	α_1-β_1^-	—	h^+

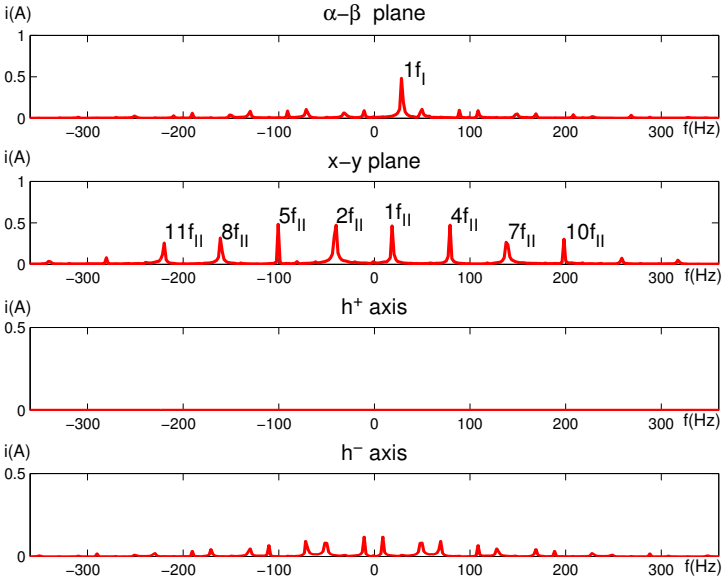

(a) M_I (six-phase) current spectrum.

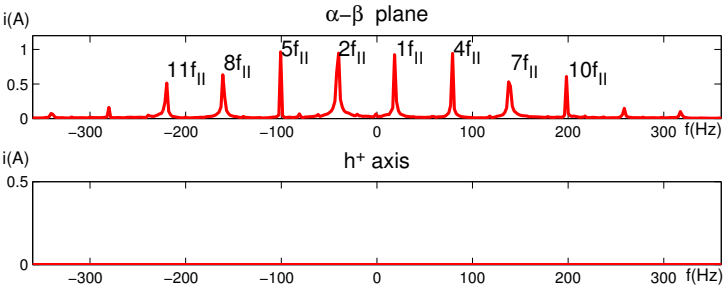

(b) M_{II} (three-phase) current spectrum.

Figure 2.18: Distribution of $[v]_{II}$ harmonics.

and M_{II} with $[V]^*_{II}$ harmonic injection, which are summarized in Table 2.2. It shows that the 2nd, 4th, 5th, 7th, 8th, 10th and 11th harmonics of $[V]^*_{II}$ map into the α_1-β_1 plane of M_{II} and into the α_2-β_2 plane of M_I. Therefore, any of them has influence on the M_I machine torque. The 3rd, 6th, 9th and 12th harmonics of $[V]^*_{II}$ map onto the h^+ axis of M_{II}. These results match with the diagram for series-connected six-phase two-motor

TABLE 2.2
$[V]^*_{II}$ HARMONIC DISTRIBUTION IN THE MULTIMOTOR SYSTEM

Harmonic order	1	2	3	4	5	6
M_{II} machine	α_1-β_1^+	α_1-β_1^-	h^+	α_1-β_1^+	α_1-β_1^-	h^+
M_I machine	α_2-β_2^+	α_2-β_2^-	—	α_2-β_2^+	α_2-β_2^-	—
Harmonic order	7	8	9	10	11	12
M_{II} machine	α_1-β_1^+	α_1-β_1^-	h^+	α_1-β_1^+	α_1-β_1^-	h^+
M_I machine	α_2-β_2^+	α_2-β_2^-	—	α_2-β_2^+	α_2-β_2^-	—

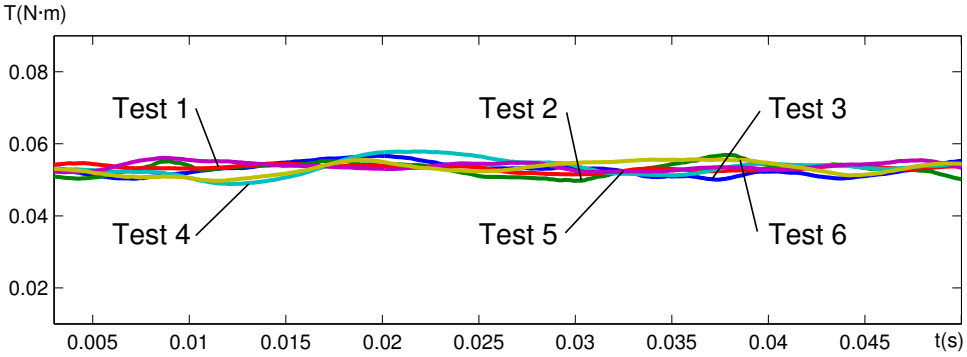

(a) M_I (six-phase machine) torque.

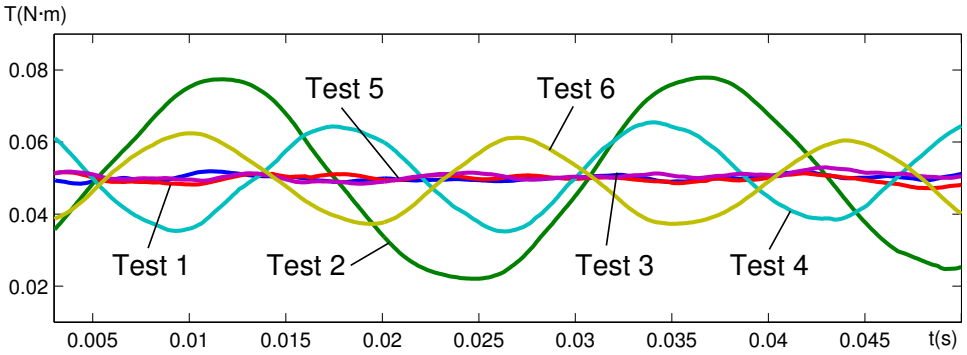

(b) M_{II} (three-phase machine) torque.

Figure 2.19: Torque ripple due to harmonic interaction.

drive in the $m = 2$ case represented in Fig. 2.6.

Torque Ripple Tests

The results shown in Table 2.1 and Table 2.2 are validated through the measurement of the torque ripple produced by each harmonic in M_I and M_{II}. As in the previous experiments, the six-phase machine is driven with a voltage reference $[v]_I$ with $A_I^* = 100\,V$, $f_I = 30\,Hz$ and the three-phase machine with a voltage reference $[v]_{II}$ with $A_{II}^* = 100\,V$ and $f_{II} = 20\,Hz$. The torque in each machine is meassured by using a Apicom FR5ME motor test bench equipped with a CCT Transducers TR-100 torque sensor. The torque sensor bandwidth is low, so torque harmonics higher than 100 Hz cannot be measured. The electrical brake of the test bench is used to set the machine torque production around 0.05 N m in all experiments. A set of six experiments are done.

- In the first experiment, Test 1 in Table 2.3, the torque in each machine is measured when the system is fed with only the three- and six-phase machines fundamental voltages in order to compare their torque and speed curves with the ones obtained with harmonic disturbances.

- The next two experiments, Test 2 and Test 3, assess the $[v]_I$ harmonics interaction with the torque in M_I and M_{II} when the driver is fed with both fundamental voltages ($[v]_I$ and $[v]_{II}$) and 2nd harmonic of $[v]_I$ in one experiment and the 3rd harmonic in the other one.

TABLE 2.3
TORQUE RIPPLE TEST SET

Harmonic order	Voltage reference to converter
Test 1	$[v]_{\mathrm{I}} + [v]_{\mathrm{II}}$
Test 2	$[v]_{\mathrm{I}} + [v]_{\mathrm{II}}$ + 2nd harmonic of $[v]_{\mathrm{I}}$
Test 3	$[v]_{\mathrm{I}} + [v]_{\mathrm{II}}$ + 3rd harmonic of $[v]_{\mathrm{I}}$
Test 4	$[v]_{\mathrm{I}} + [v]_{\mathrm{II}}$ + 2nd harmonic of $[v]_{\mathrm{II}}$
Test 5	$[v]_{\mathrm{I}} + [v]_{\mathrm{II}}$ + 3rd harmonic of $[v]_{\mathrm{II}}$
Test 6	$[v]_{\mathrm{I}} + [v]_{\mathrm{II}}$ + 4th harmonic of $[v]_{\mathrm{II}}$

- The last three experiments, Test 4, Test 5 and Test 6 in Table 2.3, test the $[v]_{\mathrm{II}}$ harmonics interaction with torque in $\mathrm{M_I}$ and $\mathrm{M_{II}}$ when the driver is fed with both fundamental voltages ($[v]_{\mathrm{I}}$ and $[v]_{\mathrm{II}}$) and with the 2nd, 3rd and 4th harmonics of $[v]_{\mathrm{II}}$ in each experiment.

Fig. 2.19 shows the torque measurement of the $\mathrm{M_I}$ and $\mathrm{M_{II}}$ machines in the six experiments merged into two plots, one for the torque of machine $\mathrm{M_I}$ and the other one for the torque of machine $\mathrm{M_{II}}$. Measurements in Test 2 show that the 2nd order harmonic of $[v]_{\mathrm{I}}$ does not affect $\mathrm{M_I}$ torque but produces torque ripple in $\mathrm{M_{II}}$. In Test 3 and Test 5 the measurements show no torque ripple in any of the two machines; so, the 3rd harmonics of $[v]_{\mathrm{I}}$ and $[v]_{\mathrm{II}}$ do not produce torque ripple in the dual six-phase motor drive. In both Test 4 and Test 6, Fig. 2.19 shows that there is torque ripple in the machine $\mathrm{M_{II}}$. Therefore, the 2nd and 4th harmonics of $[v]_{\mathrm{II}}$ produce torque disturbances in the three-phase machine but do not affect the six-phase machine. These results corroborate the harmonic distribution reflected in Tables 2.1 and 2.2.

The harmonics of the three-phase source do not affect the six-phase machine torque and only even harmonics of the six-phase source affect the three-phase machine, harmonics with the order multiple of six, which map onto the positive homopolar axis, and the others, 2nd, 4th, 8th, 10th,..., $k = 6j \pm 2$ ($j = 0, 1, 2, 3...$), which map into the α-β plane. Non-linearities, such as deadtime produce symmetrical distortion of the currents, so they only cause odd order harmonics [65]. Faults and imbalance of the feeding system can produce non-symmetrical distortion and, as a result, odd and even harmonics [84, 88]. Therefore, in normal operation with a balanced feeding system and if both machines have sinusoidal stator winding distribution, even current harmonics, and hence, the effect of torque interactions between both machines can be neglected.

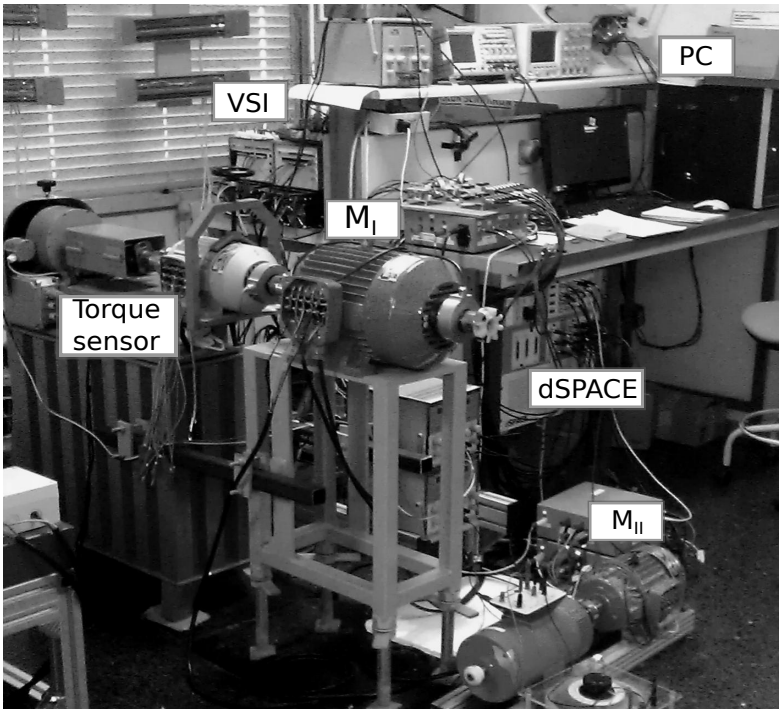

Figure 2.20: Experimental setup.

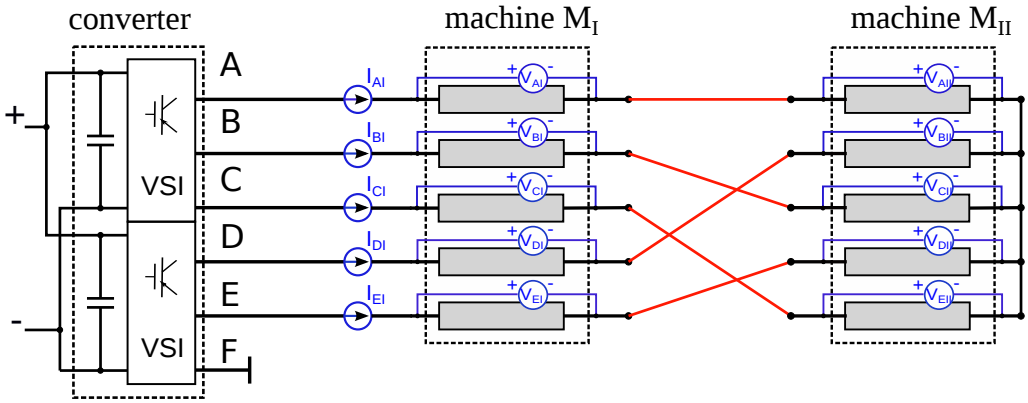

Figure 2.21: Connection diagram of the five-phase two-motor drive experiment.

2.4.4 Experimental Evaluation of the Series-Connected Five-Phase Two-Motor Drive with Spatial Harmonics

The laboratory setup shown in Fig. 2.20 is used to study the harmonic distribution in the series-connected five-phase two-motor drive and the cross harmonic interactions in the torque production between the machines. Fig. 2.21 represents the connection diagram of the system. The first series-connected motor M_I is a 1.5 kW fractional-slot four-pole five-phase motor with 50 slots. The second motor M_{II} is a 0.75 kW fractional-slot four-pole five-phase motor with 30 slots. The converters, the hardware platform for the control and the sensors are the same used in the previous six-phase two-motor drive experiment.

The spatial harmonic content of both motors, due to the winding distribution, is

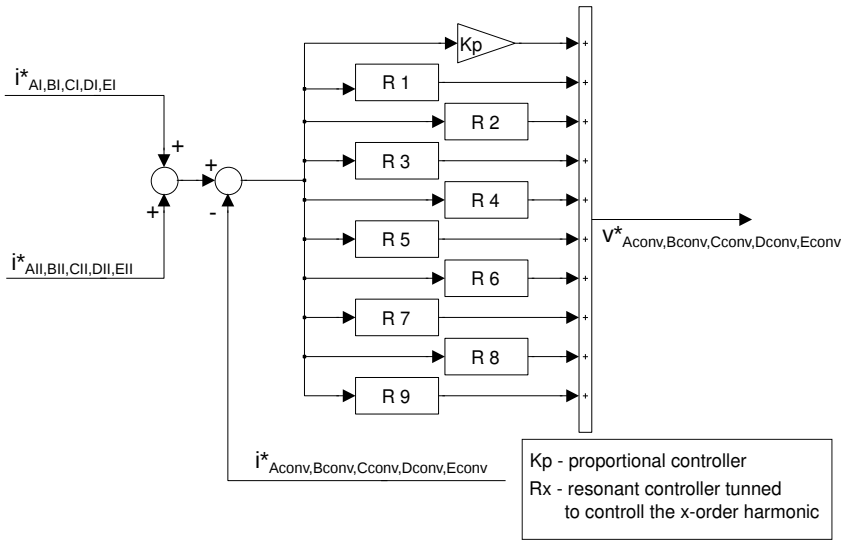

Figure 2.22: Block diagram of the current control of the VSI.

significant and cannot be neglected[1]. These winding function harmonics, in combination with the flux saturation and other nonlinearities of each motor will produce back EMF harmonics in the stator of both motors. If this experiment is carried out operating the multimotor drive in open-loop mode as the in the previous ones, the voltage components due to the spatial harmonics and the converter time harmonics coexist and it is difficult to differentiate them. In addition, this multimotor drive presents higher crossed interactions and more harmonic distortion than the previous one. This fact suggests that the back EMF harmonics due to the spatial harmonics also produce crossed interactions between the two motors. The mapping of these back EMF harmonics in the multimotor drive and an analysis of the crossed harmonics between motors helps in the modeling and control of this system.

The study of the effects of the back EMF harmonics due to the spatial harmonics in the five-phase two-motor drive is done by feeding the motors with a current with fundamental component and without low order harmonics, to avoid the effects of the time harmonics. To achieve this current without low order harmonics, the VSI current is controlled by a set of resonant controllers in parallel [11]. The block diagram of the current control is shown in Fig. 2.22. If the current that feeds the system is sinusoidal, Fig. 2.23, the voltage harmonics that appear in each motor are due to the back EMFs produced by each motor spatial harmonics:

$$[v^s] = \underbrace{[R^s][i^s] + [L^{ss}]\frac{d}{dt}[i^s]}_{\text{controlled}} + \underbrace{\frac{d}{dt}[L^{sr}][i^r]}_{\nu \text{ related}}. \tag{2.25}$$

With this experimental setup, two different experiments are carried out. In the first experiment the system is fed with a sinusoidal current i_{I} whose sequence is set to map into the α_1-β_1 plane of the $\mathrm{M_I}$ motor and into the α_2-β_2 of the $\mathrm{M_{II}}$ motor. In the second experiment, the system is fed with a sinusoidal current i_{II} whose sequence is set to map

[1] An exhaustive analysis of the stator winding function harmonics of each of these five-phase motors is carried out in chapter §3.

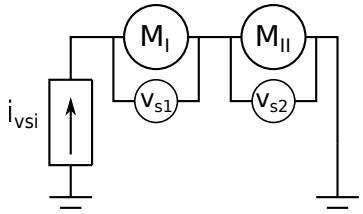

Figure 2.23: Simplified block diagram of the five-phase series-connected drive.

TABLE 2.4
BACK EMF HARMONIC DISTRIBUTION IN THE MULTIMOTOR SYSTEM WHEN $i_{\mathrm{VSI}} = i_{\mathrm{I}}$.

Harmonic order	1	2	3	5	7	9	11
$\mathrm{M_I}$ machine	α_1-β_1^+	α_2-β_2^+	α_2-β_2^-	h^+	α_2-β_2^+	α_1-β_1^-	α_1-β_1^+
$\mathrm{M_{II}}$ machine	α_2-β_2^-	α_1-β_1^+	α_1-β_1^-	h^+	α_1-β_1^+	α_2-β_2^+	α_2-β_2^-

into the α_1-β_1 plane of the $\mathrm{M_{II}}$ motor and into the α_2-β_2 of the $\mathrm{M_I}$ motor. In each experiment the voltages of both motors and the converter output current per phase are measured. The complex spectra of these measured signals are shown in Fig. 2.24 and Fig. 2.25. The back EMF harmonics mapping of the first and second experiment are summarized in Table 2.4 and Table 2.5, respectively.

The back EMF harmonics produced by the stator winding function and saturation harmonics when the system is fed with i_1 map in the same subspaces in each motor as the series-connected five-phase mapping diagram, shown in Fig. 2.5, predicts. The back EMF harmonics produced by the spatial harmonics when the system is fed with i_2 also map in the same subspaces in each motor as the series-connected five-phase mapping diagram predicts.

In the first experiment, the current spectrum in Fig. 2.24a shows only the spectrum of the current with just a fundamental component at 30 Hz in the α_1-β_1 plane with positive SVR direction. In such test, the voltage spectrum of M_{II} in Fig. 2.24c shows that, although the system is fed only with i_1, back EMF harmonics rise up in M_{II}. Thus, contrary to what happens in sinusoidally distributed motors, in this machine the time harmonics that map into the α_2-β_2 plane (in this case, i_1) produce flux in the airgap. This is also corroborated with the torque measure in this motor.

In the second experiment, the current spectrum in Fig. 2.25a shows only the spectrum of the current with just a fundamental component at 30 Hz in the α_2-β_2 plane with positive SVR direction. In such test, the voltage spectrum of M_I in Fig. 2.25b shows back EMF harmonics. Hence, in M_I the time harmonics that map into the α_2-β_2 plane (in this case, i_2) also produce flux in the airgap, as its torque measure corroborates.

2.4.5 Spatial Harmonic Distortion in Multiphase Motors

In the five-phase (at section §2.4.1) and six-phase (at section §2.4.2) second experiments, the ones where the motors are fed with sinusoidal voltage and the angle delay step is changed, the harmonic distortion that can be appreciated is not only due to the converter deadtime; spatial harmonics also contribute to it. These spatial harmonics are

TABLE 2.5
BACK EMF HARMONIC DISTRIBUTION IN THE MULTIMOTOR SYSTEM WHEN $i_{\mathrm{VSI}} = i_{\mathrm{II}}$.

Harmonic order	1	2	3	5	7	9	11
$\mathrm{M_I}$ machine	α_2-β_2^+	α_1-β_1^-	α_1-β_1^+	h^+	α_1-β_1^-	α_2-β_2^-	α_2-β_2^+
$\mathrm{M_{II}}$ machine	α_1-β_1^+	α_2-β_2^+	α_2-β_2^-	h^+	α_2-β_2^+	α_1-β_1^-	α_1-β_1^+

due to the motor nonlinearities such as the magnetic saturation, non-uniform airgap and winding distribution.

The effects of these harmonics are more remarkable in the five-phase case shown in section §2.4.1, where the spatial harmonics due the stator winding distribution and magnetic saturation are high enough in this motor to give rise to torque production in the α_2-β_2. In a perfectly distributed motor and in absence of other spatial harmonics the α_2-β_2 is not related to the electromechanical energy conversion and does not produce torque, as it is explained in section §1.2.1.

The effects of the spatial harmonics in the multiphase motor voltage and current mapping in single motor drives is studied in section §3.

In series-connected multimotor drives, the absence of torque production in planes different from the α_1-β_1 plane is a required condition for independent motor speed and position control. Given that the series-connected motors share stator currents, the multimotor drive uses the phase transposition in the series connection to make sure that the torque producing currents in one motor map into a non-electromechanical conversion plane in the other motors. Therefore, motors with high level of spatial harmonics are not suitable for series-connected multimotor drives.

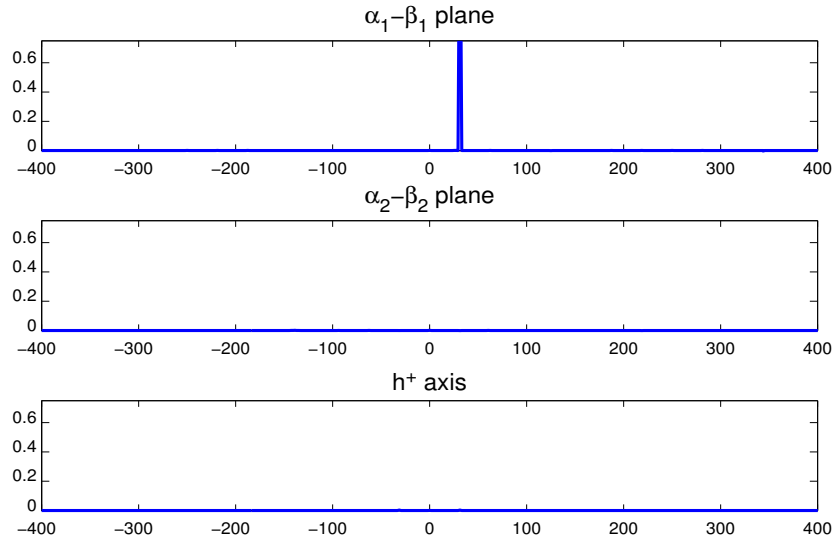

(a) VSI current spectrum.

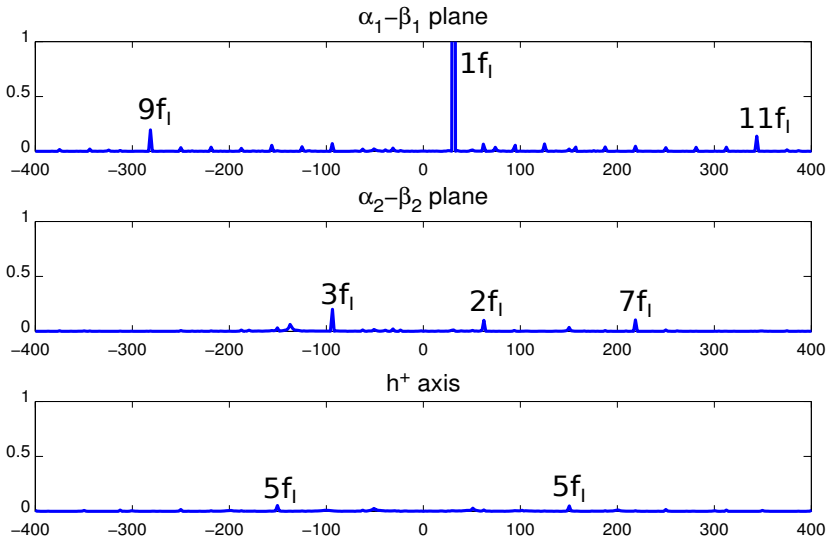

(b) M_I voltage spectrum.

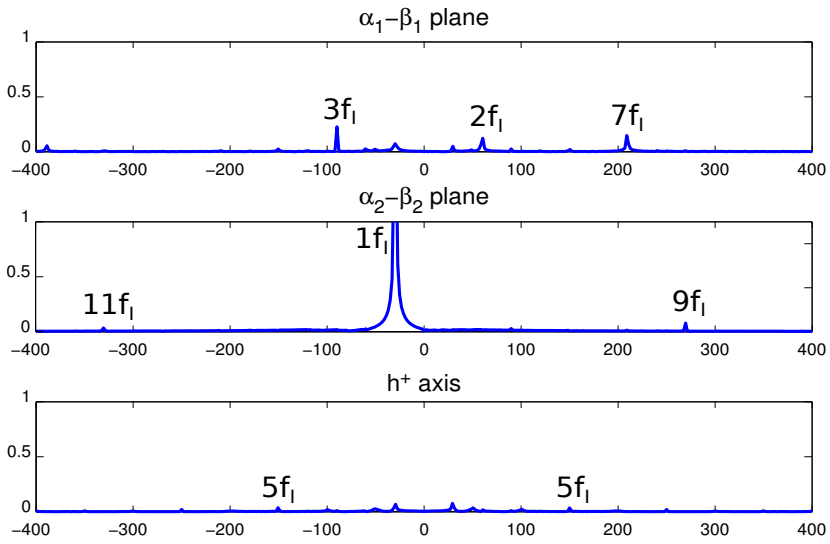

(c) M_{II} voltage spectrum.

Figure 2.24: Harmonic Distribution with $i_{VSI} = i_I$.

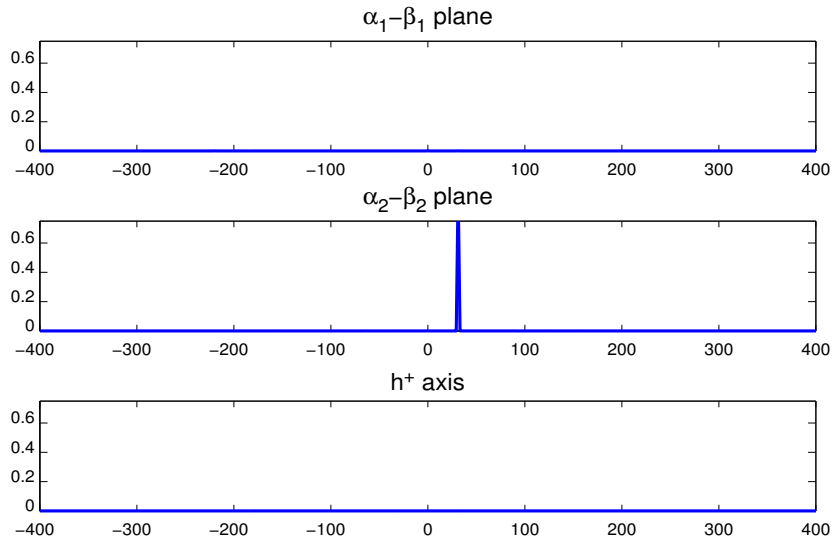

(a) VSI current spectrum.

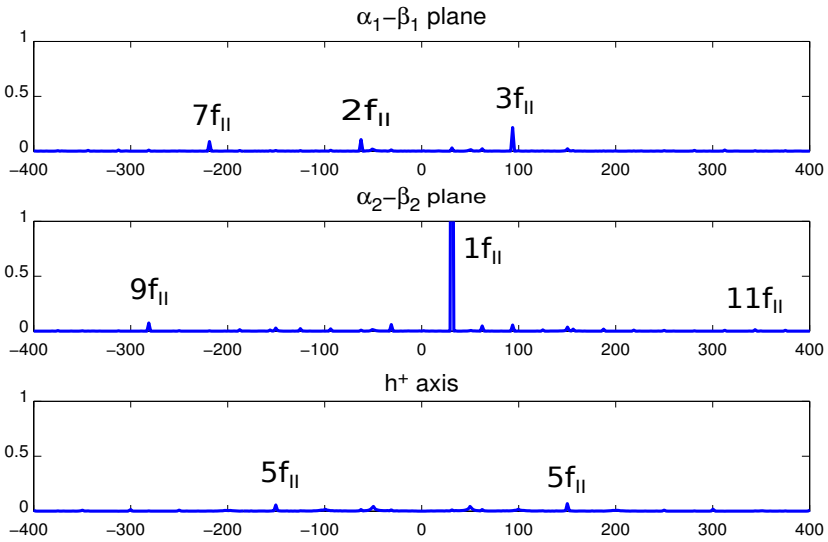

(b) M_I voltage spectrum.

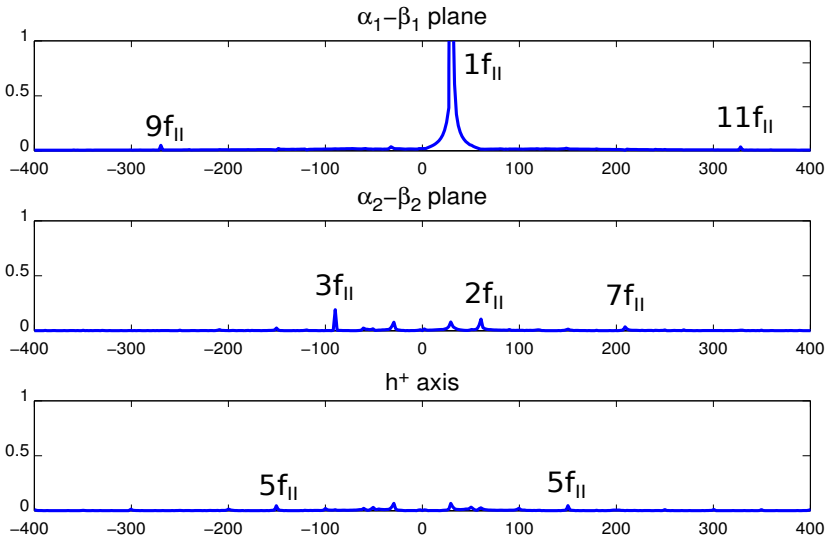

(c) M_{II} voltage spectrum.

Figure 2.25: Harmonic Distribution with $i_{VSI} = i_{II}$.

2.5 Conclusion

In this chapter, a general (for any number of phases) graphical method for subspace and SVR direction identification of time harmonics in symmetrical multiphase machines has been proposed. This graphical method is a simple and fast analytical tool for harmonic mapping. Through the diagram, subspace and SVR direction identification for even and odd harmonics can be done. This technique is based in the Unified Electrical Machine Theory and is valid for synchronous and asynchronous machines. The proposed mapping diagram can be used in multimotor drives for plane and SVR direction mapping of each harmonic for every machine of the drive, and it predicts the crossed harmonics between the series-connected machines. The developed method has been proved for the single motor drive case through a set of experiments using a five- and a six-phase symmetrical induction machine and for the multimotor case using a six-phase series-connected two-motor drive.

The last section of the chapter studies the effects of the low-order spatial harmonics in a series-connected five-phase two-motor drive through experimental results collected from a laboratory setup.

Chapter 3

Effects of the Non-Linearities and Flux Distortion in a Multiphase Motor

Abstract

Squirrel cage motors contain significant stator current distortion. These current harmonics are produced by nonlinearities such as the stator winding distribution, stator and rotor slots, rotor eccentricities, magnetic saturation, rotor current distribution and converter nonlinear behavior (e.g., deadtime). The study of the current signature and the causes behind each harmonic is useful for applications such as machine condition monitoring, stator current harmonic compensation, sensorless speed estimation and torque ripple analysis. Numerous publications have addressed the stator current harmonics topic in the context of three-phase induction motors, from detailed analysis of specific harmonic origins to more general works, such as the healthy motor current signature studies that include the most common harmonics causes in a healthy motor. In the multiphase motor field, the studies about the spatial harmonics are not so common and the majority of them are focused on particular spatial harmonics origins, such as specific faults. In addition, most of the studies applied to multiphase cases are directly adapted from three-phase cases and, thus, do not take into account some specific characteristics of the multiphase motors, such as the different types of subspaces. A general study of the healthy motor signature of n-phase induction motors that studies together the effects of the most common spatial harmonics is still to be done. This chapter presents an analysis of the VSD of the stator currents in n-phase induction motors that extends the one shown in §2. In addition to the time harmonics due to the converter, this study also covers the harmonics due to the stator and the rotor winding distributions, non-uniform airgap and magnetic saturation. This model is used to analyze the healthy n-phase motor current spectrum by means of the VSD. Then, as an example of application, a static, dynamic and mixed eccentricity detection method, based on the VSD of the motor current signature, is presented. Finally, the proposed healthy motor current signature and the eccentricity detection method are experimentally evaluated with two different five-phase squirrel cage motors.

3.1 Introduction

The use of multiphase motor drives is an increasingly important trend nowadays due to some advantages such as fault tolerance and the reduction of current stress in power devices [45, 47, 48, 165, 166]. The stator current of induction motors, both in three-phase and multiphase ones, usually contains a substantial harmonic distortion. Such harmonics can be divided into spatial MMF harmonics, caused by the distribution of the conductors in the stator and the rotor [43]; magnetic permeance harmonics, which are due to the stator and rotor slots, magnetic saturation and rotor eccentricities [116]; and those produced by the converter nonlinear behavior, mainly due to deadtime [65, 167].

A detailed knowledge of the stator current harmonics, which define the motor current signature, and of the causes behind each of them, is useful for applications such as condition monitoring [115], current harmonic compensation [4], sensorless rotor speed estimation based on the rotor slot harmonics [127] or on high frequency signals injection [123], rotor bar fault detection [168], torque ripple analysis [118] and torque density enhancement based on harmonic current injection [46].

The effects of spatial harmonics in three-phase induction motors is a broadly researched topic. The works in the literature go from the most detailed studies focused on the analysis of motor harmonics due to specific causes, such as magnetic saturation [120], stator and rotor slots [119] or specific motor faults like rotor eccentricity [111, 153] broken bars [135, 136] or bearing problems [138]; to more general studies that comprise groups of harmonics in the healthy motor current spectrum [115, 116, 169] or harmonics produced by the most common faults [129–131].

In the multiphase induction motor field, to the author's knowledge, the effects of the motor nonlinearities on the stator currents are not as broadly analyzed. There are publications that study motors with a definite phase number, such as [97, 170], which assess the effects of the magnetic saturation in five-phase induction motors or [122], which studies the healthy current signature and the eccentricity harmonics in a dual three-phase induction motor. With a more general point of view, there are studies about the effects of nonlinearities for any number of phases, but focused on the torque ripple and the mechanical vibration and noise, not on the current signature [43, 118]. The multiphase motor model presented by [42] is valid for analyzing the stator current symmetrical components and includes the effects of the stator winding distribution and rotor bar harmonics, but it is obtained under the assumptions of uniform airgap and negligible saturation. Hence, it is not valid to study the induced currents due the stator and rotor slots, saturation harmonics and eccentricities. In the field of the MCSA, Bruzzese [60] addresses rotor bar breakage detection in n-phase motors by using transformations based on symmetrical components to detect the particular current signature symptoms of broken rotor bars in the stator current. Furthermore, from the previously mentioned multiphase works, only [97, 170] take into account specific characteristics of multiphase motors, such as the low impedance planes, where back EMFs with a modest amplitude can produce important current harmonics, but, as has been mentioned previously, they are focused only on saturation harmonics in five-phase motors. Therefore, an analysis of the current signature for any number of phases and including the harmonics due to a wide variety of types of non-ideal motor characteristics, despite its practical interest, is still to be performed.

It is a common practice in works that propose the use of MCSA to detect static

eccentricity, for three-phase [116] or dual three-phase [122] drives, to study first the healthy motor current signature. The reason is that static eccentricity does not produce any new harmonic in the current spectrum of the motor, although it can modify the amplitude of the ones the healthy motor already has [133]. The most extended static eccentricity MCSA method in three-phase motors is the one based on the monitoring of the rotor slot and bar harmonics [114, 116, 171]. However, in three-phase drives, this method is proved to be valid only for specific neutral connection configurations and specific values of Q_s, Q_r and P [126, 130], and, in the multiphase motors field it was only tested for a specific dual three-phase motor [122].

This chapter analyzes the stator currents VSD in a n-phase squirrel cage motor. The proposed equations to model the stator current harmonics extend the ones shown in chapter §2 and include the effects of the stator winding distribution harmonics, non constant airgap, rotor bar harmonics and magnetic flux saturation on the stator current spectrum. By using this model, the healthy n-phase motor current signature is studied by means of the VSD and the subspace and the SVR speed of each current component is obtained. Mapping of the stator current by means of VSD reduces the harmonic overlapping, in comparison to three-phase studies or to methods based only on frequency, and provides more information about the harmonic origin. Then, a MCSA method to detect pure static, pure dynamic and mixed eccentricity, based on the VSD of the healthy motor current spectrum is proposed. Finally, experimental results with two different five-phase squirrel cage motors validate the predicted healthy motor current signature and the proposed MCSA method.

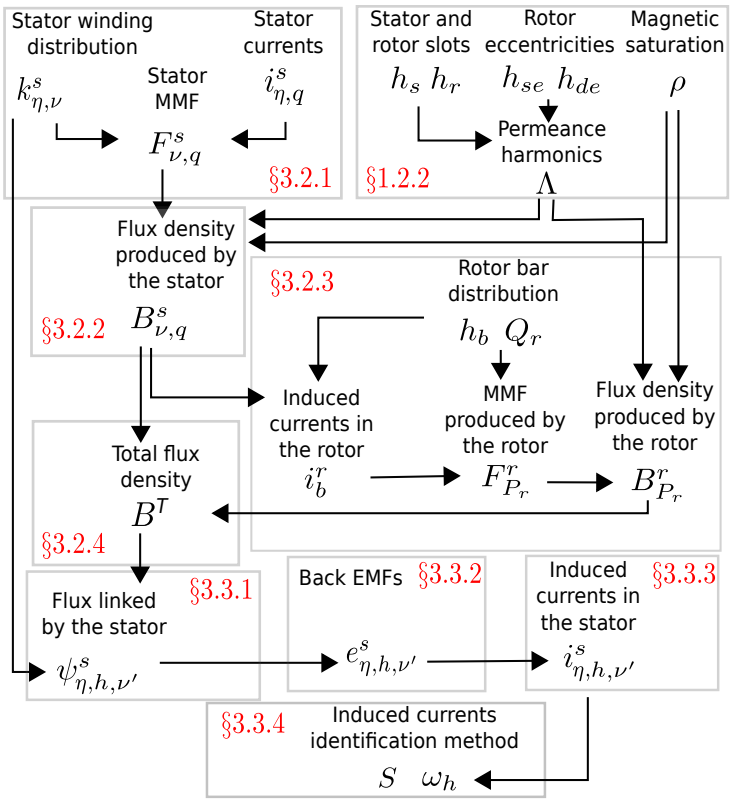

Figure 3.1: Harmonic analysis workflow graph and correspondence with section numbers (in red).

3.2 n-Phase Healthy Motor Drive Flux Harmonics

The workflow diagram of the current signature study in symmetrical multiphase squirrel cage motors is depicted in Fig. 3.1. In section §3.2.2, the airgap flux density due to the stator is obtained from the MMF harmonics of the multiphase winding calculated in section §3.2.1 in combination with the permeance harmonics and the magnetic saturation. The total flux density in the airgap is calculated in section §3.2.4 by adding the rotor flux studied in section §3.2.3 to the stator flux. The stator currents induced by the flux harmonics are assessed in section §3.3.2, after the identification of the flux harmonics linked by the multiphase stator winding in section §3.3.1. Finally, in section §3.3.4 the multiphase mapping of all these induced stator currents is determined.

3.2.1 Stator MMF Harmonics

To obtain the MMF in the airgap produced by the multiphase stator, one option is to use the current sheets [41, 43].

Multiphase motor fed from a VSI

To obtain the stator MMF, it is necessary to know the stator current distribution in the space. If the motor is fed from a current source, the input current is known. However,

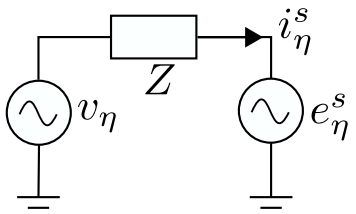

Figure 3.2: Equivalent circuit of the stator phase η.

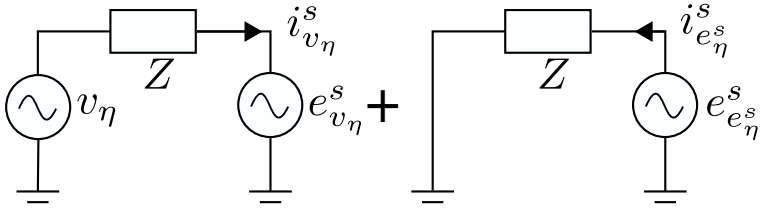

Figure 3.3: Equivalent circuit of the η phase decomposed into source synchronous harmonics and non-synchronous harmonics.

in most cases multiphase motors are fed from a voltage source, such as a VSI. In these cases, the input voltage is known and can be represented in a generic form as in (2.5).

The equivalent circuit of a η phase of the stator is depicted in Fig. 3.2, in which Z is the phase impedance and e^{s}_η is the back EMF. The back EMF can contain voltage harmonics synchronous with the voltage source and harmonics with a frequency which varies with the rotational speed of the motor [169]. The back EMF harmonics can be represented in a general form as

$$e^{\mathrm{s}}_\eta = \sum_{q=1}^{\infty}\sum_{q'=1}^{\infty}\sum_{\substack{m=-\infty \\ m\neq 0}}^{\infty} \widehat{e}_{q,q',m} \sin\left(q\omega_s t + q'\omega_r t - m\eta\alpha_{\mathrm{c}} + \phi_{q,q',m}\right) \tag{3.1}$$

where q' is the order of the time harmonics related to the rotor speed, ω_r is the rotational speed and $\phi_{q,q',m}$ is the back EMF delay angle.

The back EMF described in (3.1) can be decomposed into two components as

$$\begin{aligned} e^{\mathrm{s}}_\eta =& \underbrace{\sum_{q=1}^{\infty} \widehat{e}_q \,|_{\substack{q'=0 \\ m=q}} \sin\left(q\omega_s t - q\eta\alpha_{\mathrm{c}} + \phi_q \,|_{\substack{q'=0 \\ m=q}}\right)}_{e^s_{v_\eta}} \\ &+ \underbrace{\sum_{q=1}^{\infty}\sum_{q'=1}^{\infty}\sum_{\substack{m=-\infty \\ m\neq q}}^{\infty} \widehat{e}_{q,q',m} \sin\left(q\omega_s t + q'\omega_r t - m\eta\alpha_{\mathrm{c}} + \phi_{q,q',\nu}\right)}_{e_{e_\eta}} \\ =& e^s_{v_\eta} + e^s_{e^s_\eta} \end{aligned} \tag{3.2}$$

where $e^s_{v_\eta}$ is the component of the back EMF synchronous with the voltage source and $e^s_{e^s_\eta}$ is the non-synchronous component.

The equivalent phase circuit for each of these components are depicted in Fig. 3.3. The current in the stator phase η can be calculated as the summation of the two components shown in this figure, $i^s_{v_\eta}$ and $i^s_{e^s_\eta}$:

$$i^s_\eta = i^s_{v_\eta} - i^s_{e^s_\eta} \tag{3.3}$$

where $i^s_{v_\eta} >> i^s_{e^s_\eta}$.

It is assume that the contribution of $i^s_{e^s_\eta}$ to the stator current sheets is lower than the contribution of $i^s_{v_\eta}$. Hence, in this work the stator MMF is calculated by taking into account only the latter. Therefore, in order to calculate the stator MMF, the current through each phase η of the windings is represented in a general form as

$$i^{\mathrm{s}}_\eta = \sum_{q=1}^{\infty} i^{\mathrm{s}}_{\eta,q} = \sum_{q=1}^{\infty} \widehat{i}_{\eta,q} \sin\left(q(\omega_s t - \eta\alpha_{\mathrm{c}}) + \phi_q\right) \tag{3.4}$$

where $\widehat{i}_{\eta,q}$ is the current harmonic amplitude.

Current Sheets in a Multiphase Stator

According to [41, 43] the current sheets are obtained from the winding distribution and the phase currents of the stator. The spatial winding distribution of a phase η can be expressed by using the Fourier series decomposition [107, 170] as

$$K^{\mathrm{s}}_\eta = \sum_{\nu=1}^{\infty} K^{\mathrm{s}}_{\eta,\nu} = \sum_{\nu=1}^{\infty} \widehat{K}^s_{\eta,\nu} \cos\left(\nu(P\theta - \eta\alpha_{\mathrm{c}}) + \phi_\nu\right). \tag{3.5}$$

The next step is to study how these harmonics interact with the phase currents to produce the MMF in the airgap.

The current sheet in the airgap produced by the current i^{s}_η flowing through one phase with the winding distribution function K^{s}_η is [41, 43]

$$J^{\mathrm{s}}_\eta = \sum_{q=1}^{\infty}\sum_{\nu=1}^{\infty} J^{\mathrm{s}}_{\eta,\nu,q} = \sum_{q=1}^{\infty}\sum_{\nu=1}^{\infty} K^{\mathrm{s}}_{\eta,\nu} i^{\mathrm{s}}_{\eta,q} \tag{3.6}$$

and, by applying (3.5) and (3.4), it becomes

$$J^{\mathrm{s}}_\eta = \sum_{q=1}^{\infty}\sum_{\nu=1}^{\infty} \widehat{J}^{\mathrm{s}}_{\eta,\nu,q} \sin\left(q\omega_s t - \eta q\alpha_{\mathrm{c}} + \phi_q\right) \cos(\nu P\theta - \eta\nu\alpha_{\mathrm{c}} + \phi_\nu) \tag{3.7}$$

where $\widehat{J}^{\mathrm{s}}_{\eta,\nu,q} = \widehat{i}_{\eta,q}\widehat{K}^s_{\eta,\nu}$, is the current sheet amplitude per phase.

MMF Produced by the Current Sheets

The MMF in the airgap due to the stator current sheets generated by phase η is calculated by Ampere's Law [107]:

$$F^{\mathrm{s}}_\eta = \sum_{q=1}^{\infty}\sum_{\nu=1}^{\infty} \Big(\frac{r_s}{2} \int_{\theta}^{\theta+\pi/(\nu P)} J^{\mathrm{s}}_{\eta,\nu,q} d\theta\Big) \tag{3.8}$$

where r_s is the stator inner radius. Therefore, from (3.7) and (3.8),

$$F_{\eta}^{\mathrm{s}} = \sum_{q=1}^{\infty}\sum_{\nu=1}^{\infty} \widehat{F}_{\eta,\nu,q}^{\mathrm{s}}[\cos(\nu P\theta - q\omega_s t - (\nu-q)\eta\alpha_{\mathrm{c}} + \phi_\nu - \phi_q) - \cos(\nu P\theta + q\omega_s t - (\nu+q)\eta\alpha_{\mathrm{c}} + \phi_\nu + \phi_q)] \tag{3.9}$$

where $\widehat{F}_{\eta,\nu,q}^{\mathrm{s}} = r_s \widehat{J}_{\eta,\nu,q}^{\mathrm{s}}/(2\nu P)$. By allowing ν to take positive and negative values, (3.9) can be rewritten as

$$F_{\eta}^{\mathrm{s}} = \sum_{q=1}^{\infty}\sum_{\substack{\nu=-\infty \\ \nu\neq 0}}^{\infty} \widehat{F}_{\eta,\nu,q}^{\mathrm{s}} \cos(\nu P\theta - q\omega_s t - (\nu-q)\eta\alpha_{\mathrm{c}} + \underbrace{\phi_\nu - \phi_q}_{\phi_{q,\nu}}) \tag{3.10}$$

where $\phi_\nu = -\phi_{-\nu}$ and $\widehat{F}_{\eta,\nu,q}^{s} = -\widehat{F}_{\eta,-\nu,q}^{s}$, and consequently, for every stator distribution harmonic, both the positive ν and negative $-\nu$ values should be evaluated.

A balanced system, in which the current sheets have the same amplitude for all the phases, is considered. The stator MMF calculated as the summation of all the phases in (3.10) becomes

$$F_{\nu,q}^{\mathrm{s}} = \sum_{\eta=0}^{n-1} F_{\eta,\nu,q}^{\mathrm{s}} = \widehat{F}_{\nu,q}^{\mathrm{s}} \sum_{\eta=0}^{n-1} \cos(\nu P\theta - q\omega_s t - (\nu-q)\eta\alpha_{\mathrm{c}} + \phi_{q,\nu}) \tag{3.11}$$

where $\widehat{F}_{\nu,q}^{\mathrm{s}} = \widehat{F}_{\eta,\nu,q}^{\mathrm{s}} \quad \forall\eta = \{0,1,...,n-1\}$. This summation can be simplified by using the roots of unity theory [5] as

$$F_{\nu,q}^{\mathrm{s}} = \widehat{F}_{\nu,q}^{\mathrm{s}} a_{\nu,q} \cos(\nu P\theta - q\omega_s t + \phi_{q,\nu}) \tag{3.12}$$

where

$$a_{\nu,q} = \begin{cases} n \text{ if } \nu = q+kn \\ 0 \text{ if } \nu \neq q+kn \end{cases} \tag{3.13}$$

with k being an integer number. Hence, the stator winding distribution harmonics ν that produce MMF in the airgap for a given stator current harmonic q can be calculated by

$$\nu = q + kn. \tag{3.14}$$

Concerning (3.14), for a given time harmonic q, the following aspects can be remarked.

- The combinations $\{\nu, q\}$ that satisfy (3.14) produce a MMF in the airgap with pole pairs νP and rotational speed $q\omega_s/(\nu P)$.
- If none of the stator distribution harmonics makes (3.14) true for a given time harmonic q, this current harmonic does not produce MMF in the airgap.

For positive values of $q\omega_s/(\nu P)$ the resulting MMF rotates in the same direction as the fundamental one; this direction is considered as positive. The opposite direction is considered as negative. There are combinations $\{\nu, q\}$ that satisfy (3.14) for the positive and

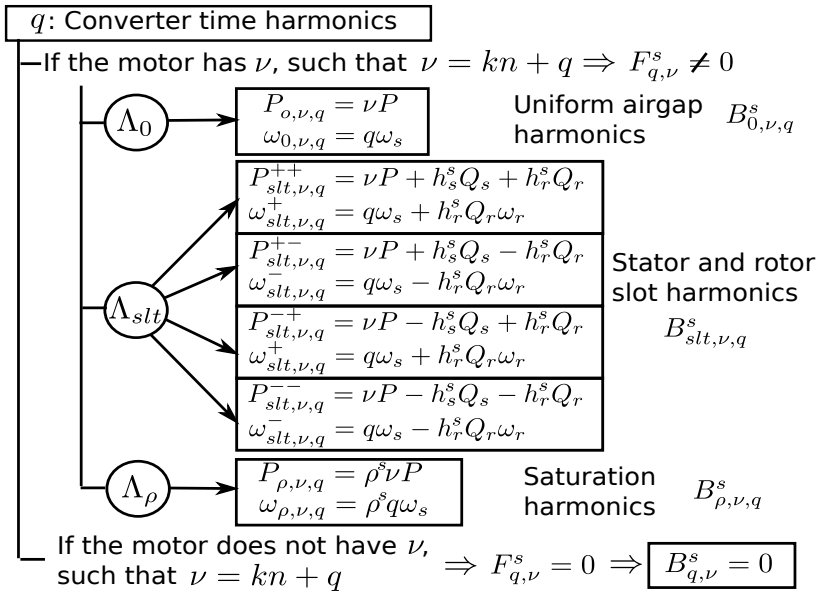

Figure 3.4: Stator field B^s harmonics classification in a healthy motor.

negative values of ν at the same time. These $\{\nu, q\}$ combinations produce MMF components rotating in the positive and negative rotation directions, which, when combined, result in a pulsating MMF in the airgap, which does not rotate.

For example, in a five-phase ($n = 5$) four pole ($P = 2$) motor fed only with a sinusoidal current ($q = 1$), according to (3.14) the distribution harmonics that produce MMF in the airgap are $\nu = \{..., -14, -9, -4, 1, 6, 11, ...\}$. If the stator winding distribution harmonics are $\nu = \{\pm 1, \pm 3, \pm 5, \pm 7, \pm 9\}$, only the combination of time and distribution harmonics $\{\nu, q\} = \{1, 1\}$ causes a MMF with positive rotation direction in the airgap with 2 pole pairs and a rotational speed $\omega_s/2$. Additionally, the combination $\{\nu, q\} = \{-9, 1\}$ produces a MMF with negative rotation direction with -18 pole pairs and a rotational speed $-\omega_s/18$. In case the current feeding this motor contains a fifth harmonic $q = 5$, the combination $\{\nu, q\} = \{5, 5\}$ causes a MMF with positive rotation direction and $\{\nu, q\} = \{-5, 5\}$ produces a MMF with negative one, both with equal amplitude. The union of the two waves results in a pulsating MMF in the airgap.

Equation (3.14) extends the one presented in [43] with the consideration of even stator winding distribution harmonics. The study of such harmonics is needed in the case of fractional slot motors [100, 172] or in case the even ν harmonics arise due to the number of stator slots [99, 172].

3.2.2 Flux Density Harmonics Produced by the Stator

The MMF in the airgap in combination with each of the permeances considered in section §3.2.1 produces additional flux density components in the airgap.

In case of a uniform airgap, the flux density component produced by the stator MMF shown in (3.12) and the uniform airgap permeance Λ_0 is

$$B^s_{0,\nu,q} = F^s_{\nu,q}\Lambda_0 = \widehat{B}^s_{0,\nu,q}\cos\left(\nu P\theta - q\omega_s t + \phi_{q,\nu}\right) \tag{3.15}$$

where $\widehat{B}^{\mathrm{s}}_{0,\nu,q} = \Lambda_0 a_{\nu,q} \widehat{F}^{\mathrm{s}}_{\nu,q}$. The $B^{\mathrm{s}}_{0,\nu,q}$ flux density has $P_{o,\nu,q} = \nu P$ pole pairs and its frequency is $\omega_{o,\nu,q} = q\omega_s$ and its delay angle is $\phi_{q,\nu}$. The rotation speed and direction in the airgap of each $B^{\mathrm{s}}_{0,\nu,q}$ component is given by the relation $\omega_{0,\nu,q}/P^{s}_{0,\nu,q}$, and the values of ν and q must accomplish (3.14).

The amplitude, the pole pairs, the frequency and the delay angle, characterize any flux density component in the airgap, but in this work only the frequency and the pole pair number are studied, because they are the parameters that are used to identify the origin of the harmonics in the current signature. Fig. 3.4 summarizes the pole pairs and frequency of the stator flux density harmonics due to different causes. Each branch of the diagram covers the harmonics produced by one type of the considered permeances. As a case in point, the Λ_0 branch shows the pole pairs and angular frequencies of the flux density due to the uniform airgap permeance, $B^{\mathrm{s}}_{0,\nu,q}$.

In the previous five-phase motor example, the pole pairs and angular frequency of the flux density components produced by the MMF with positive rotation direction, $\{\nu, q\} = \{1, 1\}$, and the uniform airgap permeance Λ_0 are $P_{0,1,1} = P = 2$ and $\omega_{0,1,1} = \omega_s$, while the flux produced by the MMF with negative rotation direction, $\{\nu, q\} = \{-9, 1\}$, has $P_{0,-9,1} = -18$ and $\omega_{0,-9,1} = \omega_s$.

Flux Density Harmonics Due to the Stator and Rotor Slots

In addition to the flux density considering uniform airgap, the flux has extra components because of the variation of the airgap due to the stator and the rotor slots. Such extra components are calculated from the permeance shown in (1.40) and the stator MMF shown in (3.12) as

$$\begin{aligned} B^{\mathrm{s}}_{slt,\nu,q} = F^{\mathrm{s}}_{\nu,q}\Lambda_{slt} = \widehat{B}^{\mathrm{s}}_{slt,\nu,q}[&\cos\left(P^{++}_{slt}\theta - \omega^{+}_{slt}t + \phi^{+}_{q,\nu}\right) + \cos\left(P^{--}_{slt}\theta - \omega^{-}_{slt}t + \phi^{+}_{q,\nu}\right) \\ &\cos\left(P^{+-}_{slt}\theta - \omega^{-}_{slt}t + \phi^{+}_{q,\nu}\right) + \cos\left(P^{-+}_{slt}\theta - \omega^{+}_{slt}t + \phi^{+}_{q,\nu}\right)] \end{aligned} \quad (3.16)$$

where $\widehat{B}^{\mathrm{s}}_{slt,\nu,q} = \widehat{B}^{\mathrm{s}}_{0,\nu,q}\widehat{\Lambda}_{slt}$ and

$$\begin{aligned} P^{++}_{slt} &= \nu P + h^s_s Q_s + h^s_r Q_r & P^{+-}_{slt} &= \nu P + h^s_s Q_s - h^s_r Q_r \\ P^{-+}_{slt} &= \nu P - h^s_s Q_s + h^s_r Q_r & P^{--}_{slt} &= \nu P - h^s_s Q_s - h^s_r Q_r \\ \omega^{+}_{slt} &= q\omega_s + h^s_r Q_r \omega_r & \omega^{-}_{slt} &= q\omega_s - h^s_r Q_r \omega_r \end{aligned} \quad (3.17)$$

where h^s_s represents the stator slot harmonic order that affects the stator produced flux and h^s_r represents the rotor slot harmonic order that affects the stator flux. Equations (3.16) and (3.17) show that, for each combination of h^s_s and h^s_r, the $F^{\mathrm{s}}_{\nu,q}$ component of the stator MMF produces several flux density waveforms in the airgap with P^{++}_{slt}, P^{+-}_{slt}, P^{-+}_{slt} and P^{--}_{slt} pole pairs and ω^{+}_{slt} and ω^{-}_{slt} angular frequencies.

For example, considering just the fundamental component of the MMF $F^{\mathrm{s}}_{1,1}$ produced by $\{\nu, q\} = \{1, 1\}$ in the five-phase squirrel cage motor represented by $M^{n,P}_{Q_s,Q_r} = M^{5,2}_{30,22}$, with two pole pairs, $Q_s = 30$ stator slots and $Q_r = 22$ rotor slots. From Fig. 3.4, the slots permeance Λ_{slt} produces four flux components in the airgap; their pole pairs and frequencies are $P^{++}_{slt} = 2 + 30h^s_s + 22h^s_r$, $P^{-+}_{slt} = 2 - 30h^s_s + 22h^s_r$ with a frequency $\omega^{+}_{slt} = \omega_s + 22\omega_r h^s_r$, and $P^{+-}_{slt} = 2 + 30h^s_s - 22h^s_r$ $P^{--}_{slt} = 2 - 30h^s_s - 22h^s_r$ with a frequency $\omega^{-}_{slt} = \omega_s - 22\omega_r h^s_r$.

Saturation Harmonics

As a consequence of iron saturation, the magnetic field waveform changes and hence, new harmonics are produced. Saturation harmonics can be modeled as a series of odd harmonics in the airgap flux distribution. These harmonic flux components travel in the airgap with the same angular speed as the corresponding airgap flux component, always keeping the phase synchronism with it. In the case of teeth saturation harmonics, their phases are such that tend to flatten the waveform of the flux that caused the saturation, and in the case of core saturation, their phases tend to produce a peaked waveform in the corresponding flux [97, 110, 120]. Therefore, in the case where the airgap flux density component that causes the iron saturation harmonics is $B^{\mathrm{s}}_{0,\nu,q}$, the produced harmonics are

$$B^{\mathrm{s}}_{\rho,q,\nu} = K_{\rho^s}\widehat{B}^{\mathrm{s}}_{0,\nu,q}\cos\left(\rho^s\nu P\theta - \rho^s q\omega_s t + \rho^s\phi^{+}_{q,\nu} + \phi_{\rho^s}\right) \tag{3.18}$$

where ρ^s represents the saturation harmonic order that affects the stator flux and K_{ρ^s} is the amplitude factor corresponding to each ρ^s.

For example, in $M^{n,P}_{Q_s,Q_r} = M^{5,2}_{30,22}$, the interaction between the fundamental component of the flux $B^{\mathrm{s}}_{0,1,1}$ and the third order saturation harmonic $\rho^s = 3$ produces a flux component with $P_{\rho^s,\nu,q} = P_{3,1,1} = 3P = 6$ and $\omega_{\rho^s,\nu,q} = \omega_{3,1,1} = 3\omega_s$.

Total Flux Density Produced by the Stator

The total flux density produced by the stator can be calculated as

$$\begin{aligned} B^s_{\nu,q} &= F^{\mathrm{s}}_{\nu,q}(\Lambda_0 + \Lambda_{slt}) + B^s_{\rho,\nu q} \\ &= B^{\mathrm{s}}_{0,\nu,q} + B^{\mathrm{s}}_{slt,\nu,q} + B^{\mathrm{s}}_{\rho,q,\nu}. \end{aligned} \tag{3.19}$$

Fig. 3.4 gathers the pole pair number and frequencies of the different harmonics of the stator flux calculated in (3.15), (3.17) and (3.18). The first step to use the figure is to choose the q and ν values to study, whose combination produces the MMF in the airgap. The next step is to locate the branch of the harmonic permeance to analyze. Each permeance branch in Fig. 3.4 indicates if it produces one, two or four simultaneous flux density components in the airgap, as well as their pole pair number and frequency equations. For example, the interaction of the fundamental component of the motor current $q = 1$ with the fundamental component of the stator winding distribution $\nu = 1$ satisfies the equation $\nu - q = kn$ of Fig. 3.4. Therefore, the set of harmonics it produces belongs to the first group in the figure, the harmonics generated by the MMF with positive rotation direction. The first branch of this harmonic group in Fig. 3.4 gives the frequency $\omega_{0,1,1} = \omega_s$ and pole pairs $P_{0,1,1} = P$ of the flux density produced by this MMF and the ideal permeance Λ_0. The second branch of this harmonic set in Fig. 3.4 covers the slot harmonics. Without taking into account the stator slot harmonics $h_s = 0$, the first order rotor slot harmonic $h_r = 1$ produces two flux density components. One of them has a frequency and a pole pair number of $\omega_{h_r=1} = \omega_s + Q_r\omega_r$ and $P_{h_r=1} = P + Q_r$ and the other one has a frequency $\omega_{h_r=1} = \omega_s - Q_r\omega_r$ and pole pair number of $P_{h_r=1} = P - Q_r$. On the contrary, if only the first order stator slot harmonics $h_s = 1$ are evaluated, two flux density components of the same frequency $\omega_{h_s=1} = \omega_s$ and pole pair numbers of $P_{h_s=1} = P + Q_s$ and $P_{h_s=1} = P + Q_s$ arise. The frequency and pole pairs of the flux density due to the

$\rho = 3$ saturation harmonic, in the Λ_ρ branch of Fig. 3.4, are $\omega_{\rho=3} = 3\omega_s$ and $P_{\rho=3} = 3P$, respectively, whereas, for the $\rho = 7$ harmonic, $\omega_{\rho=7} = 7\omega_s$ and $P_{\rho=7} = 7P$.

3.2.3 Flux Density Harmonics Produced by the Rotor

In the following, the distribution of the induced rotor current is calculated first. Then, it is employed to obtain the rotor current sheets and, by applying Ampere's Law, the rotor MMF and the flux density.

Rotor Flux Linkage

All the flux density harmonics obtained in section §3.2.2: (3.15), (3.16), (3.48), (3.49) and (3.18) can be written in a general form as

$$B_x^{\mathrm{s}}(\theta, t) = A_x \cos\left(P_x\theta - \omega_x t + \phi_x\right) \tag{3.20}$$

where $x = \{0, slt, h_{se}, h_{de}, \rho\}$ denotes the harmonic type and A_x, P_x, ω_x and ϕ_x are the amplitude, pole pair number, angular frequency and delay angle of the harmonic, respectively.

General expressions to calculate the pole pairs and frequency of each flux harmonic produced by the stator can be obtained by combining (3.19) with (3.15), (3.16), (3.17), (3.48), (3.49) and (3.18), or from Fig. 3.4:

$$P_x = \rho^s \nu P \pm h_s^s Q_s \pm h_r^s Q_r \tag{3.21}$$

$$\omega_x = \pm h_r^s Q_r \omega_r \pm \rho^s q \omega_s. \tag{3.22}$$

By applying the Faraday's Law, the voltage induced in one rotor bar for each B_x^{s} is $e_b^{\mathrm{r}}(t) = B_x^{\mathrm{s}}(\theta_b, t) L v_b$, while v_b denotes the linear speed between the bar and the field [107]. By combining this expression with (3.20), the induced voltage in one rotor bar is

$$e_b^{\mathrm{r}}(t) = \widehat{e}_b^{\mathrm{r}}(\omega_x - P_x\omega_r)\cos\left((P_x\omega_r - \omega_x)t + P_x\frac{2\pi}{Q_r}b + \phi_x\right) \tag{3.23}$$

where $b = \{0, 1..., Q_r - 1\}$ is the bar index and $\widehat{e}_b^{\mathrm{r}} = A_x L r_r$.

Rotor Current Distribution

If the equivalent rotor bar impedance is $Z_b\angle\phi_b$ [107, 173], then, from (3.23), the current induced in each bar is

$$i_b^{\mathrm{r}}(t) = \widehat{i}_b^{\mathrm{r}}(\omega_x - P_x\omega_r)\cos\left((P_x\omega_r - \omega_x)t + P_x\frac{2\pi}{Q_r}b + \phi_x - \phi_b\right) \tag{3.24}$$

where $\widehat{i}_b^{\mathrm{r}} = \widehat{e}_b^{\mathrm{r}}/Z_b$. This spatial distribution can be represented as current sheets by using the Fourier series decomposition [107]:

$$J_b^{\mathrm{r}}(t) = \sum_{P_r=1}^{\infty} i_b^{\mathrm{r}}(t)\frac{1}{\pi P_r}\sin\left(P_r(\theta - \omega_r t - \frac{2\pi}{Q_r}b)\right) \tag{3.25}$$

where P_r is the pole pair number for each harmonic.

The total rotor current sheet is calculated as the sum of each bar spatial current distribution

$$J^{\mathrm{r}}(t) = \sum_{b=0}^{Q_r-1} J_b^{\mathrm{r}} \tag{3.26}$$

and, by using the roots of unity simplification [5] in this summation, it yields

$$J_{P_r}^{\mathrm{r}} = \widehat{J}_{P_r}^{\mathrm{r}}(\omega_x - P_x\omega_r)[b_{P_r}^{+}\sin(P_r\theta - \omega_{P_r}^{+}t + \phi_{P_r}) - b_{P_r}^{-}\sin(P_r\theta - \omega_{P_r}^{-}t + \phi_{P_r})] \tag{3.27}$$

where $\widehat{J}_{P_r}^{\mathrm{r}} = \widehat{i}_b^{\mathrm{r}}/(2\pi P_r)$, $\omega_{P_r}^{+} = \omega_x + (P_x - P_r)\omega_r$, $\omega_{P_r}^{-} = \omega_x - (P_r + P_x)\omega_r$, $\phi_{P_r} = \phi_x - \phi_b$ and

$$b_{P_r}^{+} = \begin{cases} Q_r & \text{if } P_r = P_x + h_b Q_r \\ 0 & \text{if } P_r \neq P_x + h_b Q_r \end{cases} \qquad b_{P_r}^{-} = \begin{cases} Q_r & \text{if } P_x = P_r - h_b Q_r \\ 0 & \text{if } P_x \neq P_r - h_b Q_r \end{cases} \tag{3.28}$$

where $h_b = 0, 1, 2, 3, ...$

By simplifying and rewriting (3.27) and (3.28), the rotor current sheets are assessed as

$$J_{P_r}^{\mathrm{r}} = \widehat{J}_{P_r}^{\mathrm{r}} Q_r(\omega_x - P_x\omega_r)[\sin(P_r^{+}\theta - \omega_{P_r}^{+}t + \phi_{P_r}) - \sin(P_r^{-}\theta + \omega_{P_r}^{-}t - \phi_{P_r})] \tag{3.29}$$

where

$$P_r^{+} = P_x + h_b Q_r \qquad \omega_{P_r}^{+} = \omega_x + h_b Q_r \omega_r$$
$$P_r^{-} = P_x - h_b Q_r \qquad \omega_{P_r}^{-} = \omega_x - h_b Q_r \omega_r.$$

Flux Density Produced by the Rotor

By applying the Ampere's Law to (3.29), the MMF generated by the rotor is

$$F_{P_r}^{r} = \widehat{F}_{P_r}^{\mathrm{r}}(\omega_x - P_x\omega_r)[b_{P_r}^{+}\cos(P_r\theta - \omega_{P_r}^{+}t + \phi_{P_r}^{+}) - b_{P_r}^{-}\cos(P_r\theta - \omega_{P_r}^{-}t + \phi_{P_r}^{-})] \tag{3.30}$$

where $\widehat{F}_{P_r}^{\mathrm{r}} = \widehat{J}_{P_r}^{\mathrm{r}} r_r/(2P_r)$. Equation (3.30) shows that, apart from the fundamental component of the rotor MMF with the same frequency ω_x and pole pairs P_x of the airgap flux that produces it, some sideband harmonics arise: ones with $P_r = P_x + h_b Q_r$ and $\omega_{P_r} = \omega_x + h_b Q_r \omega_r$ and others with $P_r = P_x - h_b Q_r$ and $\omega_{P_r} = \omega_x - h_b Q_r \omega_r$. This fact is due to the discrete distribution of the current in the rotor bars. For example, if the rotor MMF of $M_{Q_s,Q_r}^{n,P} = M_{30,22}^{5,2}$ is induced only by the fundamental component of the flux density produced by the stator $B_{0,1,1}^{\mathrm{s}}$, the first component of the rotor MMF, $h_b = 0$, has the same pole pairs and frequency as $B_{0,1,1}^{\mathrm{s}}$. On the other hand, the first order rotor bar harmonic, $h_b = 1$, produces two MMF components, one with $P_r^{+} = 24$ and $\omega_{P_r}^{+} = \omega_s + 22\omega_r$ and another one with $P_r^{-} = 20$ and $\omega_{P_r}^{-} = \omega_s - 22\omega_r$.

The flux density in the airgap produced by the rotor is obtained in a similar way as in the stator case by applying the different permeance functions in (1.40), (1.34) and (1.36) to

$$B_{P_r}^{r} = F_{P_r}^{r}(\Lambda_0 + \Lambda_{slt}) + B_{\rho,P_r}^{r} \tag{3.31}$$

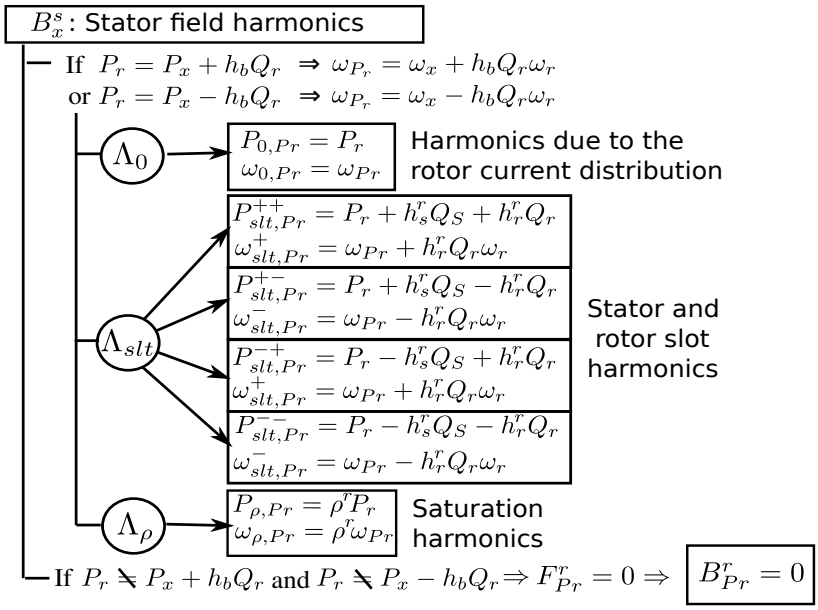

Figure 3.5: Rotor field B^r harmonics classification in a healthy motor.

where $B^r_{\rho,Pr}$ is calculated following the same process described in section §3.2.2 for $B^s_{\rho,q,\nu}$.

The summary of pole pairs and frequencies of the rotor flux density harmonics due to the different nonlinearities is shown in Fig. 3.5. The flux density harmonics due to the rotor MMF are calculated by replacing the P_r and ω_{P_r} values in each branch of the diagram. For example, the pole pairs and frequencies of flux density harmonics due to the interaction between Λ_0 and the first order rotor bar harmonics of $M^{n,P}_{Q_s,Q_r} = M^{5,2}_{30,22}$ are obtained by replacing the corresponding values of the pole pairs and frequencies for the specific rotor MMF in the Λ_0 branch of Fig. 3.5. Two flux harmonics arise, one with $P_{0,P_r} = P_r = 2 + 22$ and $\omega_{0,\mathrm{Pr}} = \omega_{P_r} = \omega_s + 22\omega_r$ and another one with $P_{0,P_r} = 2 - 22$ and $\omega_{0,P_r} = \omega_s - 22\omega_r$.

3.2.4 Total Flux Density Harmonics in the Airgap

Finally, the total airgap flux density is calculated as the addition of the stator (3.19) and the rotor flux (3.31):

$$B^T = \sum_{q,\nu} B^{\mathrm{s}}_{\nu,q} + \sum_{P_r} B^r_{P_r}. \tag{3.32}$$

3.3 Healthy Motor Current Signature

3.3.1 Airgap Flux Linked by the Stator

All the harmonic components of the addends in (3.32) are sinusoidal waveforms; consequently, each component can be expressed in a general form as

$$B^T_h(\theta, t) = \widehat{B}^T_h \cos\left(P_h \theta - \omega_h t + \phi_h\right) \tag{3.33}$$

where $\widehat{B}_h^T$, P_h, ω_h and ϕ_h are the amplitude, pole pair number, angular frequency and delay angle of the specific harmonic, respectively.

From Figs. 3.4 and 3.5, a general equation to calculate the resulting frequency of any flux density component caused by any combination of the studied harmonics can be obtained:

$$\omega_h = k_r Q_r \omega_r + k_\rho q \omega_s \tag{3.34}$$

where $k_r = \pm\rho^r(h_r^s \pm h_b) \pm h_r^r$ and $k_\rho = \rho^s\rho^r$. The variable k_r combines the effects of the rotor slots, rotor bars and saturation on the stator and rotor field. For all harmonic orders and their combinations, the values of k_r and k_ρ are integer numbers.

It is important to remark that according to the frequencies calculated through (3.34), harmonics of the flux density can be divided into two groups: rotor-synchronized harmonics and stator-synchronized harmonics. Harmonics whose frequency is related to the rotor speed, and thus, which are subject to the slip, go in the first group. The second group contains the harmonics whose frequency does not depend on the slip.

In the same manner as in (3.34), a general equation to calculate the pole pairs of each flux density component is also obtained from the expressions in Figs. 3.4 and 3.5:

$$P_h = k_\rho \nu P + k_s Q_s + k_r Q_r \tag{3.35}$$

where $k_s = \pm\rho^r h_s^s \pm h_s^r$, and thus, $k_s \in \mathbb{Z}$.

Despite the fact that each B_h^T field component is produced by a specific stator distribution harmonic ν, each component is likely to interact with all the stator distribution harmonics. Therefore, the flux due to B_h^T linked by phase η of the stator winding is

$$\psi_{\eta,h}^{\mathrm{s}} = \sum_{\nu'=1}^{\infty} \psi_{\eta,h,\nu'}^{\mathrm{s}} \tag{3.36}$$

where $\psi_{\eta,h,\nu'}^{\mathrm{s}}$ is the flux linked by phase η that is due to each of its winding distribution harmonic ν', which does not need to be equal to the one that produces the flux, i.e., ν. It can be obtained as

$$\psi_{\eta,h,\nu'}^{\mathrm{s}} = \int_{\theta}^{\theta+2\pi} K_{\eta,\nu'}^{\mathrm{s}} \int_{\theta}^{\theta+\pi/P_h} B_h^T(\theta', t) d\theta' d\theta. \tag{3.37}$$

From (3.5), (3.33) and (3.37), the flux linked by phase η of the stator winding is

$$\psi_{\eta,h,\nu'}^{\mathrm{s}} = \begin{cases} 0 & \text{if } \nu' P \neq P_h \\ -\widehat{\psi}_{\eta,h,\nu'}^{\mathrm{s}} \sin(\omega_h t + \nu'\eta\alpha_{\mathrm{c}} + \phi_\psi) & \text{if } \nu' P = P_h \end{cases} \tag{3.38}$$

where $\widehat{\psi}_{\eta,h,\nu'}^{\mathrm{s}} = 2\pi A_y \widehat{N}_{\eta,\nu}^s / P_h$ and $\phi_\psi = \phi_{\nu'} - \phi_h$. Thus, one specific airgap field component B_h^T only interacts with the spatial harmonic of the stator windings ν' if their pole pair numbers are equal.

For example, if the pole pairs of the first order rotor bar harmonics of the $M_{30,22}^{5,2}$ motor are $P_{0,P_r}^{+} = 24$ and $P_{0,P_r}^{-} = -20$, these rotor slot harmonics will be linked by the stator windings if its winding function has the distribution harmonic $\nu' = 12$ and $\nu' = 10$, respectively. Furthermore, the first order rotor bar harmonics of another induction motor

$M^{5,2}_{50,44}$, $P_{0,P_r} = 46$ and $P_{0,P_r} = -42$, are linked if the stator winding function has a distribution harmonic of order $\nu' = 23$ or $\nu' = 21$, respectively.

From (3.35) and (3.38), the equation that gives the distribution harmonic ν' that links one specific flux density harmonic is

$$\nu' P = P_h = k_\rho \nu P + k_s Q_s + k_r Q_r. \tag{3.39}$$

Hence, the flux harmonics produced in the air gap by ν, k_ρ, k_s and k_r are linked by the stator only if there is a ν' that satisfies (3.39). This equation can be merged with (3.14) to express the linking condition in (3.39) as a function of q:

$$\nu' = \frac{P_h}{P} = kn + k_\rho q + \frac{k_s}{P} Q_s + \frac{k_r}{P} Q_r. \tag{3.40}$$

For example, the pole pairs and frequencies of flux density harmonics due to the interaction between Λ_0 and the first order rotor bar harmonics of $M^{n,P}_{Q_s,Q_r} = M^{5,2}_{30,22}$ are obtained by replacing the corresponding values of the pole pairs and frequencies for the specific rotor MMF in the Λ_0 branch of Fig. 3.5: $P_{0,\mathrm{Pr}} = P_r = P \pm 22$ and $\omega_{0,\mathrm{Pr}} = \omega_{P_r} = \omega_s \pm 22\omega_r$. The flux harmonics due to Λ_0 and the first order rotor bar harmonics of $M^{n,P}_{Q_s,Q_r} = M^{5,2}_{50,44}$ pole pairs and frequencies are $P_{0,\mathrm{Pr}} = P_r = P \pm 44$ and $\omega_{0,\mathrm{Pr}} = \omega_{P_r} = \omega_s \pm 44\omega_r$.

As an example of application, this analysis can be used to evaluate if one squirrel cage motor with $Q_r = 22$ and $P = 2$ is suitable for sensorless applications. To measure the motor speed through the PSH frequencies, it has to be studied if the harmonics produced by the rotor bars and slots are linked by the stator windings and, thus, they produce stator current harmonics.

3.3.2 Back-EMF Harmonics

The back EMF corresponding to the linked flux $\psi^{\mathrm{s}}_{\eta,h,\nu'}$ is calculated using the Faraday-Lenz equation and (3.38).

$$e^{\mathrm{s}}_{\eta,h,\nu'} = -\frac{d}{dt}\psi^{\mathrm{s}}_{\eta,h,\nu'} = \widehat{e}^{\mathrm{s}}_{\eta,h,\nu'} \cos\left(\omega_h t + \nu' \eta \alpha_{\mathrm{c}} + \phi_\psi\right) \tag{3.41}$$

where $\widehat{e}^{\mathrm{s}}_{\eta,h,\nu'} = \widehat{\psi}^{\mathrm{s}}_{\eta,h,\nu'}/\omega_h$.

3.3.3 Stator Induced Current Harmonics

It is shown in (3.2) that the back EMF can been decomposed into the voltage harmonics $e^s_{v_\eta}$, which are synchronous with the voltage source that feeds the motor, and the non-synchronous $e^s_{e^s_\eta}$ ones. Both components of the back EMF generate induced currents in the stator. Given the equivalent circuits shown in Fig. 3.3 and (3.3), the induced current is calculated as

$$i^s_\eta = i^s_{v_\eta} - i^s_{e^s_\eta} = \frac{v_\eta - e^s_{v_\eta}}{\mathbf{Z}} - \frac{e^s_{e^s_\eta}}{\mathbf{Z}}. \tag{3.42}$$

The first current components depicted in (3.42), denoted as $i^s_{v_\eta}$, are current harmonics synchronous with the voltage source. The second ones, $i^s_{e^s_\eta}$, are non-synchronous current

harmonics produced by the spatial harmonics of the motor, i.e., stator and rotor slots, magnetic saturation, rotor bars or stator winding distribution. Therefore, the induced current in the stator, which includes both current harmonic sets, can be characterized as

$$i^{\mathrm{s}}_{\eta,h,\nu'} = i^{s}_{v_\eta} - i^{s}_{e^{s}_{\eta}} = \widehat{i}^{\mathrm{s}}_{\eta,h,\nu'} \cos\left(\omega_h t - \frac{P_h}{P}\eta\alpha_{\mathrm{c}} + \phi_\psi - \phi_{\eta,\nu'}\right) \tag{3.43}$$

where $\widehat{i}^{\mathrm{s}}_{\eta,h,\nu'}$ is the current component amplitude.

3.3.4 Stator Current Harmonics Mapping

A parallelism between the induced current harmonics equation (3.43) produced by the drive non-ideal conditions and the converter voltage harmonics equation (2.5), mapped into spatial vectors in section §2.2.1, is identified. By applying the same procedure followed in such section from (2.5) to (2.8), the spatial vector corresponding to each component $i^{\mathrm{s}}_{\eta,h,\nu'}$ is

$$\mathbf{i}^{s}_{p,h,\nu'} = \frac{1}{\sqrt{n}} \sum_{\eta=0}^{n-1} \mathbf{a}^{\eta p} i^{s}_{\eta,h,\nu'} = \widehat{i}^{s+}_{p,h,\nu'} e^{\hat{\jmath}(\omega_h + \phi^{+}_{p,h})} - \widehat{i}^{s-}_{p,h,\nu'} e^{\hat{\jmath}(-\omega_h + \phi^{-}_{p,h})} \tag{3.44}$$

where

$$\begin{aligned} \widehat{i}^{s+}_{p,h,\nu'} &= \frac{\widehat{i}^{s}_{p,h,\nu'}}{2\sqrt{n}} \sum_{\eta=0}^{n-1} e^{\hat{\jmath}(p - \frac{P_h}{P})\eta\,\alpha_c} \\ \widehat{i}^{s-}_{p,h,\nu'} &= \frac{\widehat{i}^{s}_{p,h,\nu'}}{2\sqrt{n}} \sum_{\eta=0}^{n-1} e^{\hat{\jmath}(p + \frac{P_h}{P})\eta\,\alpha_c}. \end{aligned} \tag{3.45}$$

By applying the property of the Roots of Unity theory shown in (2.11), the expression in (3.45) can be simplified as

$$\widehat{i}^{s+}_{p,h,\nu'} = \begin{cases} \widehat{i}^{\mathrm{s}}_{\eta,h,\nu'}\sqrt{n} & \text{if } 0{\le}\sigma{\le}\frac{n}{2} \text{ or } -n{<}\sigma{\le}-\frac{n}{2} \\ 0 & \text{otherwise} \end{cases}$$

$$\widehat{i}^{s-}_{p,h,\nu'} = \begin{cases} \widehat{i}^{\mathrm{s}}_{\eta,h,\nu'}\sqrt{n} & \text{if } \frac{n}{2}{\le}\sigma{<}n \text{ or } -\frac{n}{2}{\le}\sigma{\le}0 \\ 0 & \text{otherwise} \end{cases}$$

where $\sigma = \mathrm{mod}(P_h/P, n)$. Hence, the space vector $\mathbf{i}^{s}_{p,h,\nu'}$ is different from zero, i.e., it maps in the subspace p only if

$$p = \min\{\sigma, n - \sigma\}. \tag{3.46}$$

If $\sigma = 0$ or $\sigma = n/2$, the space vector $\mathbf{i}^{s}_{p,h,\nu'}$ maps into a homopolar axis, producing a pulsating vector that does not rotate. If $\sigma \neq 0$ and $\sigma \neq n/2$, the spatial vector of the current component rotates with a speed

$$\omega_{p,h} = \begin{cases} \omega_h & \text{if } 0{<}\sigma{<}n/2 \text{ or } -n{<}\sigma{\le}-\frac{n}{2} \\ -\omega_h & \text{if } n/2{<}\sigma{<}n \text{ or } -\frac{n}{2}{\le}\sigma{\le}0. \end{cases} \tag{3.47}$$

TABLE 3.1
EXAMPLE OF HEALTHY MOTOR CURRENT HARMONIC VSD CHARACTERIZATION

Motor characteristics: n=5, P=2, Qr=22 and Qs=30							
qk_ρ	k_s/P	k_r/P	ω_h	P_h/P	$\omega_{p,h}$	p	Subspace
1	0	0	ω_s	1	ω_s	1	α – β
		1	$22\omega_r+\omega_s$	12	$22\omega_r+\omega_s$	2	$x-y$
		-1	$-22\omega_r+\omega_s$	-10		0	h_+
		2	$44\omega_r+\omega_s$	23	$-44\omega_r-\omega_s$	2	$x-y$
		-2	$-44\omega_r+\omega_s$	-21	$44\omega_r-\omega_s$	1	α – β
	⋮						
	1	0	ω_s	16	ω_s	1	α – β
		1	$22\omega_r+\omega_s$	27	$22\omega_r+\omega_s$	2	$x-y$
		-1	$-22\omega_r+\omega_s$	5		0	h_+
	⋮						
	2	0	ω_s	31	ω_s	1	α – β
	⋮						
3	0	0	$3\omega_s$	3	$-3\omega_s$	2	$x-y$
		1	$22\omega_r+3\omega_s$	14	$-22\omega_r-3\omega_s$	1	α – β
		-1	$-22\omega_r+3\omega_s$	-8	$-22\omega_r+3\omega_s$	2	$x-y$
	⋮						
5	0	0	$5\omega_s$	5		0	h_+
	⋮						
7	0	0	$7\omega_s$	7	$7\omega_s$	2	$x-y$
	⋮						
⋮							

In the case the saturation and slot harmonics are neglected, equation (3.46) is equivalent to the one proposed in [42] that associates sets of stator and rotor distribution harmonics with the multiphase motor subspaces. This fact, proves that the winding distribution harmonic mapping proposed in [42] can be extended to cover non-uniform airgap and saturation harmonics by applying (3.40).

Table 3.1, elaborated with (3.34), (3.46) and (3.47), shows some examples of the frequency, the mapping subspace and the SVR speed of the current harmonics induced by the studied non-ideal characteristics of a five-phase squirrel cage motor with $P = 2$, $Q_r = 22$ and $Q_s = 30$. For example, in the first row, Table 3.1 represents the current component characterized by $qk_\rho = 1$, $k_s/P = 0$ and $k_r/P = 0$, i.e., the fundamental component of the current. The table shows that this current component maps into the α-β plane with a frequency ω_s as it is already known. The second and third rows of Table 3.1 address the PSH of this motor ($qk_\rho = 1$, $k_s/P = 0$ and $k_r/P = \pm 1$). That is, those rows show the frequency and the subspace where they map, calculated by using (3.34), (3.46) and (3.47).

Comparing the spatial vector equations (2.8), (2.9) and (2.10) of the voltage time harmonics mapped in section §2.2.1 with the spatial vector equations of the induced

currents (3.44) and (3.45), a parallelism can be established that permits to conclude that the time harmonic mapping diagram presented in section §2.2.1 can be adapted for mapping the induced stator current harmonics caused by the spatial harmonics. The steps to draw the mapping diagram for the induced currents due to the spatial harmonics are:

1. Draw a horizontal line that represents the real axis, as in the mapping diagram of section §2.2.1. The surface over this line represents the $\omega_{p,h} = \omega_h$ area and that under it represents the $\omega_{p,h} = -\omega_h$ area.

2. Draw an n-sided regular polygon with the center and one vertex on the real axis. This vertex is the reference vertex.

3. Draw vertical lines crossing the vertices of the regular polygon that are symmetrical with respect to the real axis and number them from the closest to the reference vertex to the farthest one. These lines represent the subspaces α_p-β_p.

4. The subspace and SVR direction of a specific induced current harmonic is obtained by numbering the vertices of the regular polygon counterclockwise from zero to $\nu' = P_h/P$ starting at the reference vertex.

5. Remove the P_h/P values of the equivalent pole pairs of the flux density for which the motor does not have its associated stator distribution harmonic $\nu' = P_h/P$, i.e., they are not going to be linked by the stator.

Examples of the mapping diagram for the induced currents in a $n = 5$ and a $n = 6$ healthy induction motor are shown in Fig. 3.6 and Fig. 3.7, respectively. It is interesting to remark that in the healthy integral slot 6-phase machine the induced current harmonics due to the non-ideal conditions do not map into the x-y plane. This fact is important because, as it has been mentioned, this plane is a low impedance one and low order back-EMF harmonics can give rise to high current harmonics and produce losses.

3.4 Induced Current Harmonics due to the Rotor Eccentricity

The spatial vector equation (3.44) shows also that the origin of the stator current harmonic h can be identified through the subspace p where the spatial vector of such harmonic maps and its rotating speed $\omega_{p,h}$. The use of these two parameters to identify the origin of each stator current harmonic helps in case that different nonlinearities induce current harmonics that coincide in one of the identification parameters (e.g., two different origins that produce harmonics with the same frequency ω_h [126]).

3.4.1 Harmonics Produced by Rotor Static, Dynamic and Mixed Eccentricities

In case the motor has rotor eccentricities, additional sets of field harmonics arise. From (1.34) and (3.12), the flux density harmonics due to the static eccentricity are obtained

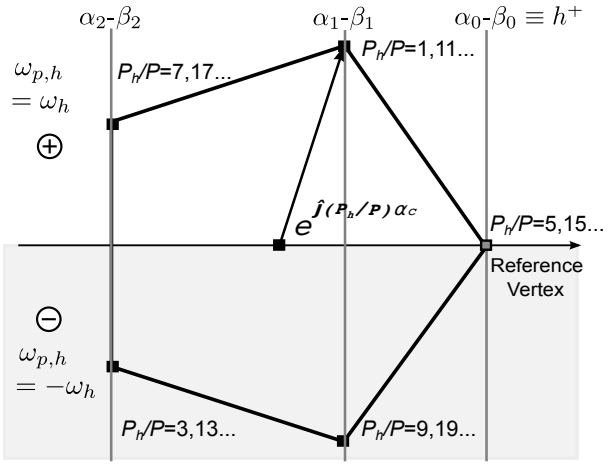

(a) Five-phase integral slot induction motor ($\nu' = 1, 3, 5, 7, ...$)

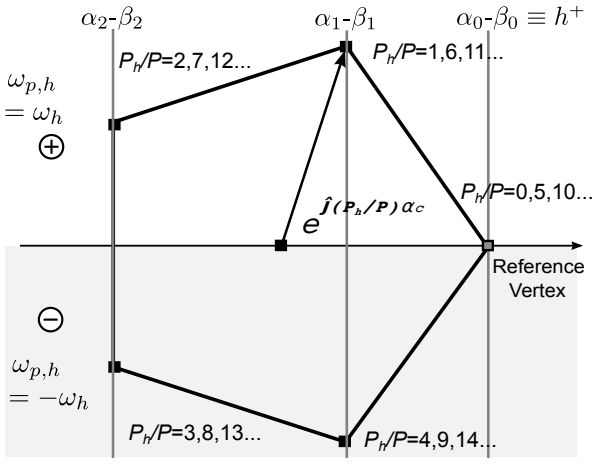

(b) Five-phase fractional slot induction motor ($\nu' = 1, 2, 3, 4, 5, ...$)

Figure 3.6: Example of the induced current mapping diagram for a five-phase healthy induction motor.

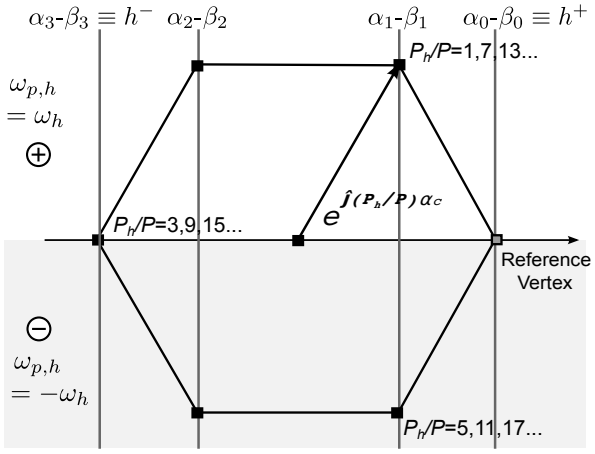

(a) Six-phase integral slot induction motor ($\nu' = 1, 3, 5, 7, ...$)

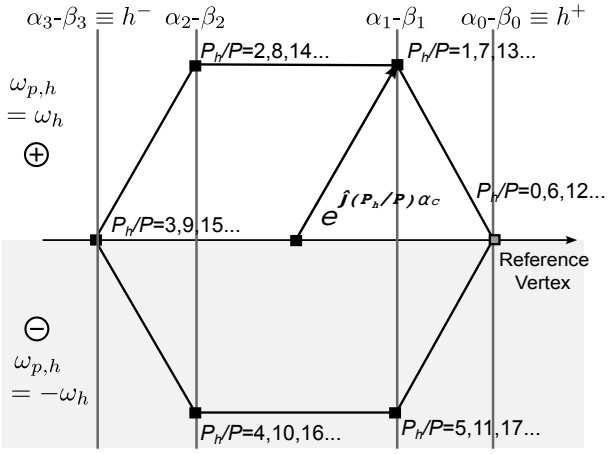

(b) Six-phase fractional slot induction motor ($\nu' = 1, 2, 3, 4, 5, ...$)

Figure 3.7: Example of the induced current mapping diagram for a six-phase healthy induction motor.

as

$$B^{\mathrm{s}}_{se,\nu,q} = F^{\mathrm{s}}_{\nu,q}\Lambda_{se} = \widehat{B}^{\mathrm{s}}_{se,\nu,q}[\cos(P^+_{se}\theta - \omega_{se}t + \phi^+_{q,\nu}) + \cos(P^-_{se}\theta - \omega_{se}t + \phi^+_{q,\nu})] \tag{3.48}$$

where $\widehat{B}^{\mathrm{s}}_{se,\nu,q} = \widehat{B}^{\mathrm{s}}_{0,\nu,q}\widehat{\Lambda}_{h_{se}}$ and

$$P^+_{se} = \nu P + h^s_{se} \qquad \omega_{se} = q\omega_s$$
$$P^-_{se} = \nu P - h^s_{se}$$

This equation shows that, for each harmonic of the static eccentricity h_{se}, each component of the stator MMF produces two flux density waveforms in the airgap, one with P^+_{se}

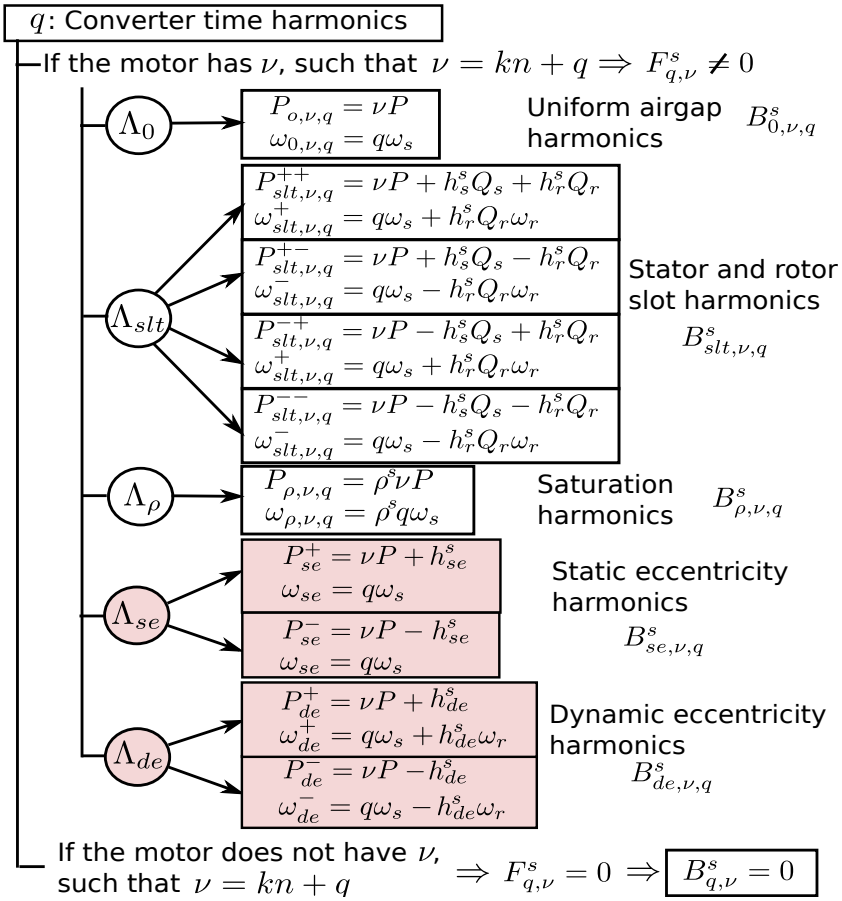

Figure 3.8: Stator field B^{s} harmonics classification taking into account static and dynamic eccentricities.

and the other with P_{se}^{-} equivalent pole pairs. For example, if the static eccentricity harmonic $h_{se}^{s}=4$ arises in $M_{Q_s,Q_r}^{n,P}=M_{30,22}^{5,2}$, the flux produced by the interaction between the fundamental component of the MMF, $\{\nu,q\}=\{1,1\}$, and the static eccentricity permeance Λ_{se} has two components, one with $P_{se}^{+}=6$ and another one with $P_{se}^{-}=-2$, both with a frequency $\omega_{se}=\omega_s$.

Analogously, from (1.36) and (3.12), the flux density harmonics due to the dynamic eccentricity are

$$B_{de,\nu,q}^{\mathrm{s}}=F_{\nu,q}^{\mathrm{s}}\Lambda_{de}=\widehat{B}_{de,\nu,q}^{\mathrm{s}}[\cos\left(P_{de}^{+}\theta-\omega_{de}^{+}t+\phi_{de}^{+}\right)+\cos\left(P_{de}^{-}\theta-\omega_{de}^{-}t+\phi_{de}^{+}\right)] \tag{3.49}$$

where $\widehat{B}_{de,\nu,q}^{\mathrm{s}}=\widehat{B}_{0,\nu,q}^{\mathrm{s}}\widehat{\Lambda}_{h_{de}}$ and

$$\begin{aligned} P_{de}^{+}&=\nu P+h_{de}^{s} & \omega_{de}^{+}&=q\omega_s+h_{de}^{s}\omega_r\\ P_{de}^{-}&=\nu P-h_{de}^{s} & \omega_{de}^{-}&=q\omega_s-h_{de}^{s}\omega_r. \end{aligned}$$

The diagrams that summarize the pole pairs and frequencies of the stator (i.e., Fig. 3.4) and rotor (i.e., Fig. 3.5) flux harmonics are extended to include the static and dynamic eccentricities in Fig. 3.8 and Fig. 3.9.

Taking into consideration the flux density components produced by the static (3.48) and dynamic (3.49) eccentricities, the equation (3.34) that defines the rotation speed of

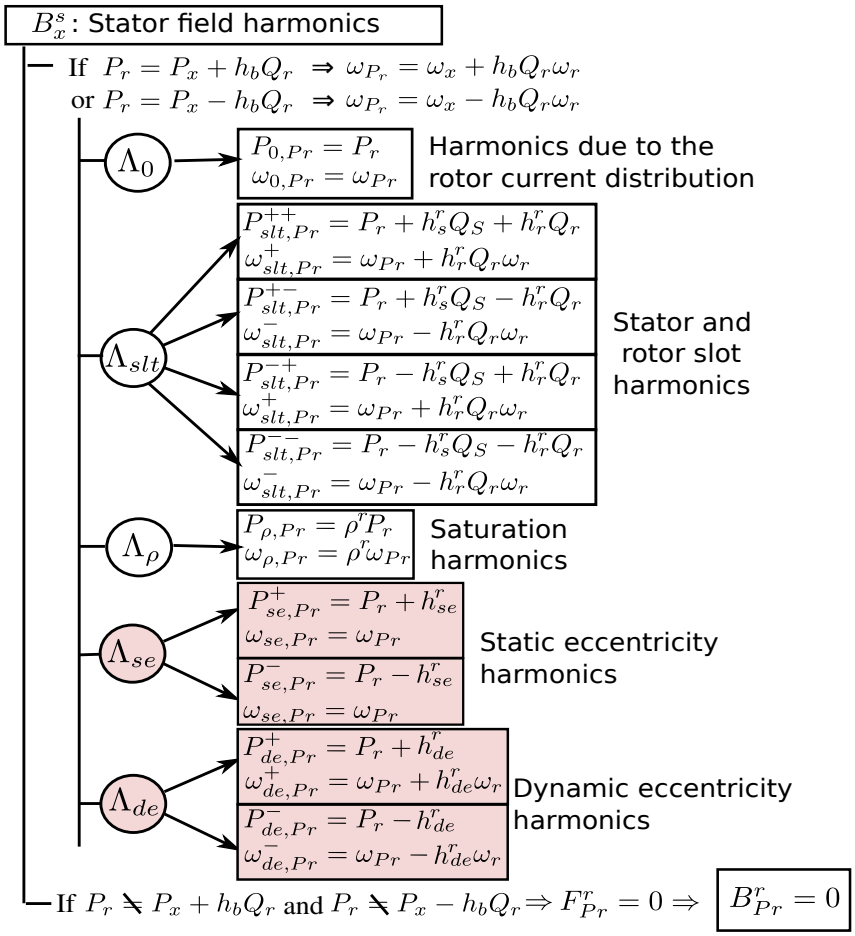

Figure 3.9: Rotor field B^r harmonics classification taking into account static and dynamic eccentricities.

the flux density harmonics in the airap becomes

$$\omega_h = (k_r Q_r + k_{de})\omega_r + k_\rho q \omega_s, \tag{3.50}$$

where $k_{de} = \pm\rho^r h^s_{de} \pm h^r_{de}$ is an integer number, and the equation (3.35) that defines the equivalent pole pairs of each flux density component becomes

$$P_h = k_\rho \nu P + k_s Q_s + k_r Q_r + k_{de} + k_{se} \tag{3.51}$$

where $k_{se} = \pm\rho^r h^s_{se} \pm h^r_{se}$ is an integer number.

Equations (3.50) and (3.51) do not depend on the number of phases of the motor and agree with the one proposed in [116] for three-phase motors. The difference between the n-phase and the three-phase equations is the relation between the orders of the time harmonics q and the stator distribution harmonic ν that produces MMF in the airgap, which is defined by (3.14). Hence, from (3.14), (3.38) and (3.51), the flux harmonics produced in the air gap by q, k_ρ, k_s, k_r, k_{se} and k_{de} in the general n-phase case are linked by the stator ν' winding distribution harmonic

$$\nu' = \frac{P_h}{P} = kn + k_\rho q + \frac{k_s}{P} Q_s + \frac{k_r}{P} Q_r + \frac{k_{de}}{P} + \frac{k_{se}}{P}. \tag{3.52}$$

The equations (3.50) and (3.52) show that the static eccentricity does not cause flux components with a different rotating speed of the flux density and, thus, the stator induced current harmonic that the static eccentricity produces have the same frequencies as the ones already present in the motor; however, the flux density harmonics the static eccentricity produces have different pole pairs than the current harmonics that the healthy motor has. Therefore, the induced stator current harmonics produced by the static eccentricity map into different planes and have different SVR directions than the harmonics caused by other non-ideal characteristics of the motor, but their frequencies are equal to the ones of other current harmonics present in the healthy motor model. The static eccentricities do not produce harmonics with a specific frequency that can be used as the fault detection symptom. Thus, MCSA methods based on monitoring harmonics at specific frequencies of the stator current need to use an indirect method to detect static eccentricities. On the other hand, the flux density harmonics produced by dynamic eccentricity have particular rotation speeds and pole pairs.

3.4.2 Three-Phase Classical Eccentricity Detection Methods

In section §1.2.2 the classical symptoms used to detect rotor eccentricity by means of MCSA are introduced. Those symptoms, shown in (1.46) and (1.47), were initially defined for eccentricity detection in three-phase integral slot motors [116, 134]. The eccentricity symptoms of a three-phase motor with integral slot, analyzed by using the VSD are shown in Table 3.2.

The frequencies of the sideband eccentricity symptoms described by (1.47) are the ones of the current harmonics produced by the dynamic eccentricity. Therefore, the MCSA method to detect eccentricities based on these sideband symptoms cannot identify standalone static eccentricity. In the case of only dynamic eccentricity appear in the motor, Table 3.2 shows that, for $k_{se} = 0$, only some sidebands among the ones described by (1.47) appear in the stator current. Those are the reasons why the symptoms at the frequencies shown in (1.47) are commonly used to detect only mixed eccentricities in three-phase integral slot motors.

On the other hand, the frequencies of the eccentricity symptoms described by (1.46) are a combination of the ones of the rotor bar and rotor slots and the ones due to dynamic eccentricity harmonics. These symptoms can be used to detect pure-static eccentricities by using an indirect method based on the monitoring of the current harmonics due to the rotor bars and slots [116, 126, 129, 174]. However, as it is mentioned in section §1.2.2, this MCSA technique is proved to detect pure-static eccentricities in three-phase motors only if the P and Q_r values satisfy (1.48). This is due to the fact that, in a three-phase machine with any of these values of Q_r, the rotor bar and slot harmonics produce flux components with $k_P P$ pole pairs, where k_P can be a multiple of 3 or an even number [126]. In a three-phase motor, the induced stator currents produced by flux components with $3kP$ pole pairs, if present, map onto the homopolar axis. Hence, if the machine does not have even ν' order distribution harmonics and there is not neutral connection between the motor and the converter, they do not produce induced current harmonics in the stator. When the machine is affected by a static eccentricity, the combination of the rotor bar, rotor slots and the eccentricity produces flux components with $(k_P \pm k_{se})P$ pole pairs, which map into a subspace different from the homopolar component and they can

TABLE 3.2
STATIC AND DYNAMIC SYMPTOMS IN A THREE-PHASE INTEGRAL SLOT MOTOR

$\frac{k_{se}}{P}$	$\frac{k_{de}}{P}$	$\nu' = 1 + \frac{k_{de}}{P} + \frac{k_{se}}{P}$	Linked by the stator	Subspace	$\omega_h = \omega_s(1 + k_{de}\frac{1-s}{P})$
	-4	-4	no	-	
	-3	-3	yes	h	
	-2	-2	no	-	
	-1	-1	yes	$\alpha - \beta$	$\omega_s(s)$
	0	0	no	-	
-1	1	1	yes	$\alpha - \beta$	$\omega_s(2 - s)$
	2	2	no	-	
	3	3	yes	h	
	4	4	no	-	
	-4	-3	yes	h	
	-3	-2	no	-	
	-2	-1	yes	$\alpha - \beta$	$\omega_s(2s - 1)$
	-1	0	no	-	
	0	1	yes	$\alpha - \beta$	ω_s
0	1	2	no	-	
	2	3	yes	h	
	3	4	no	-	
	4	5	yes	$\alpha - \beta$	$\omega_s(5 - 4s)$
	-4	-2	no	-	
	-3	-1	yes	$\alpha - \beta$	$\omega_s(3s - 2)$
	-2	0	no	-	
	-1	1	yes	$\alpha - \beta$	$\omega_s(s)$
	0	2	no	-	
1	1	3	yes	h	
	2	4	no	-	
	3	5	yes	$\alpha - \beta$	$\omega_s(4 - 3s)$
	4	6	yes	h	

be detected in the current signature.

In the case of multiphase motors, these techniques have been tested in a dual three-phase induction motor with isolated neutral points, integral slots and specific values of Q_s and Q_r, [122]. In this type of motor, the induced stator currents produced by flux components with $3kP$ pole pairs map into the positive or negative homopolar axis, and, in absence of neutral connections, these currents do not flow. Thus, in this case, (1.46) can be used to detect pure static rotor eccentricity. In [158] a reference frame transformation is proposed for detecting mixed eccentricity in multiphase motors by using the sideband frequencies defined by (1.47), but this method cannot be used to detect pure-static eccentricity.

3.4.3 Extension of the Classical Static Eccentricity Detection Method for n-Phase Drives

Equation (1.48) can be extended to the general n-phase case by calculating the relation between the P and Q_r values that makes the rotor bar and slot harmonics map onto the homopolar component, or in case of an integral slot motor, that produces even order pole pairs. The extension of the equation that describes the P and Q_r combinations that allow to apply the static eccentricity Rotor bar and slot harmonics MCSA method to a n-phase motor is

$$Q_r = P(nk \pm 1) \tag{3.53}$$

where $k = 0, 1, 2, 3, ...$

For n values that are not a prime number (e.g., $n = 6, 8, 9, ...$), there are more than one homopolar component. In such cases, these homopolar components do not allow current flow in absence of neutral connection. Then, (3.53) becomes

$$Q_r = P(n'k \pm 1) \tag{3.54}$$

where n' is the phase number of the smallest winding subset that composes the stator winding. For example, in a six-phase motor with isolated neutral points $n' = 3$, as it has been seen in the dual three-phase induction motor case at the end of section §3.4.2, and in a nine-phase motor with isolated neutral points $n' = 3$.

3.4.4 VSD MCSA Eccentricity Detection Method

VSD MCSA Static Eccentricity Symptoms

For the cases the classical static eccentricity detection MCSA system based on the rotor slot and bar harmonics cannot be applied, another fault detection method should be used. To detect static eccentricity in the three-phase motors where the classical method is not valid, a method based on the analysis of the current spectrum of the zero sequence component is proposed in [154]. In a similar way, a method to detect pure static eccentricity in three-phase motors based on the analysis of the negative sequence of the fundamental current is proposed in [156]. Both methods are based on the fact that the analysis of the stator current harmonics of a three-phase motor by means of sequence decomposition provides more information than the current harmonic analysis in one phase.

In multiphase motors, the VSD of the stator current provides the information of the sequences in each subspace of the motor. Therefore, by studying how the static eccentricity affects the VSD of the current signature of healthy multiphase motors, a MCSA method to detect static eccentricities in multiphase motors similar to the ones shown in [154] and [156] for three-phase motors can be proposed.

Equations (3.50) and (3.52) show that the flux components that the static eccentricity produces have the same frequencies and different pole pairs as the ones already present in the motor, such as the ones produced by the slots, the current sheets or the magnetic saturation. Hence, the induced current harmonics due to the static eccentricity, despite having the same frequencies as the current harmonics already present in the healthy motor, map into different subspaces.

From all the induced current harmonics that can be produced by the combination of the motor flux density components and the static eccentricity harmonics, the best option to use as the fault symptom is the current harmonic produced by the combination of the fundamental component of the flux and the airgap eccentricity. The main reason is because in normal operation of the motor, the fundamental component of the flux is the one with the highest amplitude. Thus, the amplitude of the induced current harmonic produced by the combination of this flux component and the static eccentricity should be bigger than the ones produced by the other flux components.

From (3.51), the equivalent pole pairs of the flux harmonic produced by the combination of the fundamental flux and the static eccentricity are

$$P_{se} = P + k_{se}. \tag{3.55}$$

The stator winding distribution harmonics that links them are

$$\nu'_{se} = \frac{P_h}{P} = 1 + \frac{k_{se}}{P} \tag{3.56}$$

and their rotation speed, calculated by using (3.50), is ω_s. The key symptom of the static eccentricity is the induced current components produced by the stator winding distribution harmonics ν'_{se}. Among all the possible options, the value of ν'_{se} is chosen to be the stator distribution harmonic with the highest amplitude, which produces an induced current that maps into a different subspace (or at least with a different SVR direction) than the fundamental current. If the induced current produced by ν'_{se} maps into a low impedance plane (i.e., a x-y plane), the amplitude of such static eccentricity symptom become larger than if the same harmonic maps into a high impedance (α-β) plane.

The subspace where the static eccentricity symptom maps can be calculated by replacing $\sigma = \text{mod}(\nu'_{se}, n)$ into (3.46) or searching ν'_{se} in the motor mapping diagram extended to spatial harmonics. The SVR speed of the static eccentricity symptom is calculated by replacing $\sigma = \text{mod}(\nu'_{se}, n)$ and $\omega_h = \omega_s$ into (3.47). For example, if the chosen stator distribution harmonic to monitor the static eccentricity symptom is $\nu'_{se} = 1 + \frac{k_{se}}{P} = 3$ (which is going to be the most common case), the induced current maps into the x-y plane, and its SVR speed is $-\omega_s$.

The proposed method, based on the analysis of the VSD of the stator currents, can be used to detect static eccentricities in multiphase induction motors. Its advantage over the classical static eccentricity MCSA method, based on the rotor bar and slot harmonics, is

that the VSD MCSA method does not depend on the Q_r motor parameter. Compared with the three-phase method shown in [154], the VSD MCSA method does not require a neutral connection between the motor and the converter. Multiphase motors, in comparison with three-phase ones, also present advantages due to the higher number of degrees of freedom and the low impedance subspaces. The number of subspaces into which a multiphase motor model can be decomposed depends on the number of phases n, the higher the value of n, the larger the number of subspaces, and hence, the possibility of harmonic overlapping is reduced and the detection of the eccentricity symptoms is easier. One of the advantages of the proposed VSD MCSA method when compared with the one shown in [156] arises when the static eccentricity symptoms map into a different subspace than the fundamental current. In this case, due to the fact that the current control in multiphase drives are normally designed to be independent in each subspace, the fundamental current control loop does not affect the symptom amplitude. In addition, if the static eccentricity symptom maps into a low impedance plane, its amplitude is higher and low eccentricity amplitudes can be detected.

VSD MCSA Dynamic Eccentricity Symptoms

The stator winding distribution harmonics that links the induced current harmonics produced by the combination of the fundamental flux and the dynamic eccentricity is

$$\nu'_{de} = \frac{P_h}{P} = 1 + \frac{k_{de}}{P}. \tag{3.57}$$

and its frequency is

$$\omega_{de} = k_{de}\omega_r + \omega_s = [k_{de}\frac{1-s}{P} + 1]\omega_s. \tag{3.58}$$

The subspace where the static eccentricity symptom maps can be calculated by replacing $\sigma = \text{mod}(\nu'_{de}, n)$ into (3.46). The SVR speed of the dynamic eccentricity symptom is calculated by replacing $\sigma = \text{mod}(\nu'_{de}, n)$ and $\omega_h = \omega_{de}$ into (3.47).

The SVR speed of the induced current due to the dynamic and static frequencies are different. Hence, the same stator winding distribution harmonic for detecting the static eccentricity is used to detect the dynamic one. For example, in the previous case, where $\nu'_{se} = 3$, the dynamic eccentricity symptom maps into the x-y plane ($\nu'_{de} = 3$), and its SVR speed is $-[2(1-s)+1]\omega_s$ ($k_{de} = 4$) or $[-4(1-s)+1]\omega_s$ ($k_{de} = -8$).

The advantages of this method, when compared with the classical ones based on (1.47) and (1.46), are the ones related to the multiphase nature of the motor already mentioned in the static eccentricity case, the higher number of degrees of freedom, which reduces harmonic overlapping, and the low impedance subspaces.

Proposed VSD MCSA Eccentricity Detection Method

The Proposed VSD MCSA Eccentricity Detection Method requires the following steps.

First Step: Apply the discrete Fourier transformation (DFT) to the stator winding function to obtain the order and amplitude of its harmonics ν [10, 100], and assess into which subspace and with which SVR direction map the induced currents linked to each of them by using (3.46). Then, choose the stator winding distribution harmonic ν with the

highest amplitude that maps into a different subspace than the fundamental current (or at least with a different SVR direction). This stator distribution harmonic is the one used to sense the static and dynamic eccentricities ν'_{se} and ν'_{de}. Then, calculate the subspace and the VSD speed of the static and dynamic eccentricity symptoms by following sections §3.4.4 and §3.4.4, respectively.

Second Step: Measure the healthy motor stator currents with the motor spinning at steady state with different values of the mechanical load, i.e., at different slip values. Apply the VSD to the measured stator currents and then, the DFT, to obtain the complex spectrum of each subspace. This procedure gives the subspace and the SVR speed of every current harmonic at various slips in the healthy motor. Then, measure in the healthy motor the amplitude of the current harmonics that map into the same subspace and with the same VSD speed of the static and dynamic eccentricity symptoms. This is needed because, even in healthy motors, non-zero values of static and dynamic eccentricity can be found. There are also other system non-ideal characteristics that can lead to current harmonics similar to the static eccentricity symptoms, like non-balanced stator phase impedances.

Third Step: The static and dynamic eccentricities are detected by measuring the amplitude of the current harmonics that map into the subspace and with the VSD speed predicted for their symptoms and comparing them to the ones measured in the healthy motor case.

By testing the evolution of each symptom amplitude with the increase of its corresponding eccentricity, a threshold value for each symptom amplitude can be set. When one of the symptoms amplitude surpass its chosen threshold value, it indicates that the motor needs maintenance.

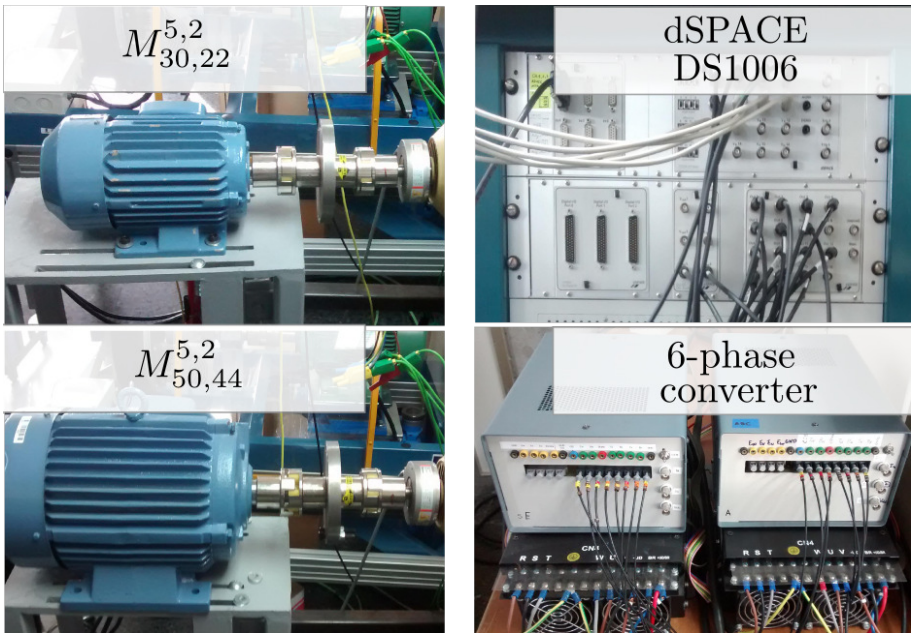

Figure 3.10: Experimental setup.

3.5 Experimental Evaluation

3.5.1 Experimental Setup

The proposed method is validated by using two different five-phase motors. The elements of the experimental setup are shown in Fig. 3.10. Two three-phase voltage source inverter (VSI) Semikron Semistack SKS 35F B6U+E1CIF+B6CI21V modules are used to build a six-phase VSI, but just five of the six legs are employed. The dc-link voltage is 300 V. The converter control is implemented in a dSPACE DS1006 platform, based on an AMD Operton processor with the DS5001 pulse width modulation (PWM) board. The switching frequency is set to 5 kHz; this frequency is high enough not to affect the studied current components. The voltages are measured using LEM LV 25-P sensors with a bandwidth of 25 kHz and the currents are measured using LEM LA 55-P sensors with a bandwidth of 200 kHz. The analog-to-digital converter DS2004 board with 16 parallel channels is employed to capture all the measured signals at a sample rate of 100 kHz. The FFTs shown in this chapter are obtained offline by using the Matlab 'fft' function in the complex mode with measures of 10240 samples and, thus, a resolution of 0.98 Hz.

The first motor to be tested is $M^{5,2}_{30,22}$. It is a 0.75-kW fractional-slot five-phase squirrel cage motor and it has $P = 2$, $Q_s = 30$ and $Q_r = 22$. The stator distribution harmonic spectrum is obtained by applying the DFT to the corresponding winding function of all the phases and it is shown in Fig. 3.11b. The classification of the possible values of P_h/P and their induced stator currents mapping are shown in Table 3.3. The second motor, $M^{5,2}_{50,44}$, is also a fractional-slot four-pole five-phase induction machine, but it has $Q_s = 50$ and $Q_r = 44$. Its nominal power is 1.5 kW and its stator winding distribution harmonic content is depicted in Fig. 3.12b. The classification of the possible values of P_h/P and their induced stator currents mapping is shown in Table 3.4.

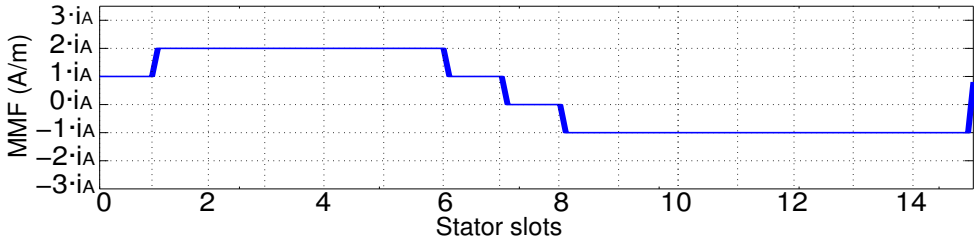

(a) Phase A stator winding function.

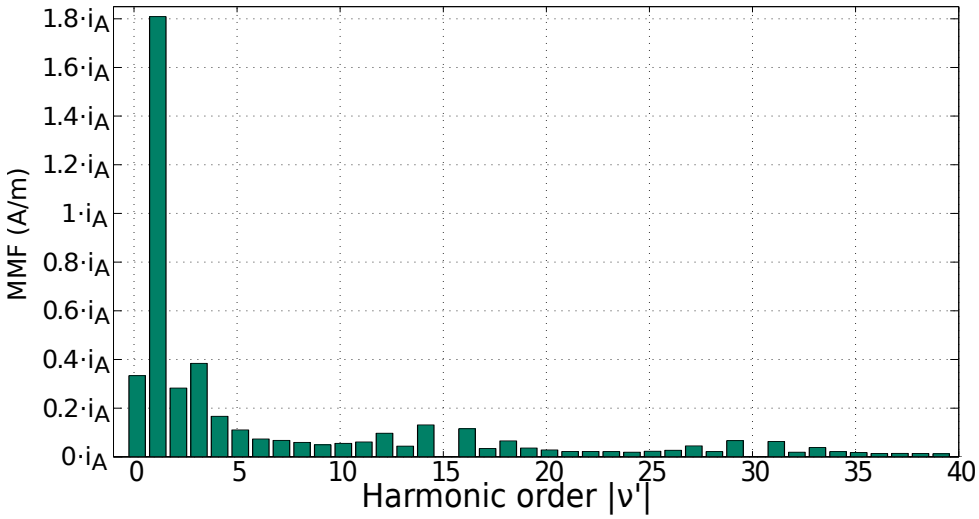

(b) Harmonic content of the stator winding function.

Figure 3.11: Stator winding distribution analysis of $M_{30,22}^{5,2}$.

TABLE 3.3
CLASSIFICATION OF THE POSSIBLE VALUES OF P_h/P AND THEIR INDUCED STATOR CURRENTS MAPPING IN $M_{30,22}^{5,2}$

	$\omega_{S,h} = \omega_h$	$\omega_{S,h} = -\omega_h$
α-β	...,-14, -4, -9, 1, 6, 11, 16, ...	...,-11, -6, -1, 4, 9, 14, 19,...
x-y	...,-13, -8, -3, 2, 7, 12, 17, ...	...,-12, -7, -2, 3, 8, 13, 18,...
h^+	..., -10, -5, 5, 10, ...	

TABLE 3.4
CLASSIFICATION OF THE POSSIBLE VALUES OF P_h/P AND THEIR INDUCED STATOR CURRENTS MAPPING IN $M_{50,44}^{5,2}$

	$\omega_{S,h} = \omega_h$	$\omega_{S,h} = -\omega_h$
α-β	...,-24, -9, 1, 26,...	..., -26, -1, 9, 24,...
x-y	..., -18, -3, 7, 22,...	..., -22, -7, 3, 18, 28,...
h^+	..., -20, -5, 5, 20, 30, ...	

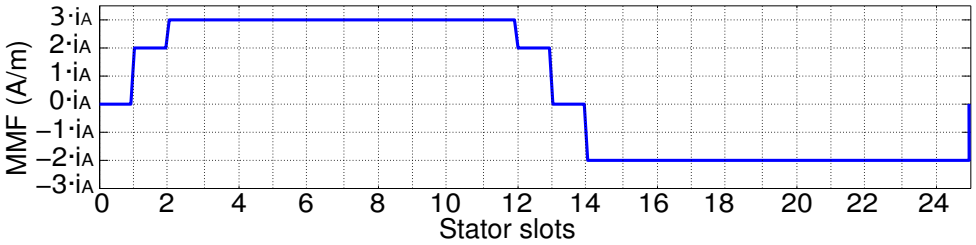

(a) Phase A stator winding function.

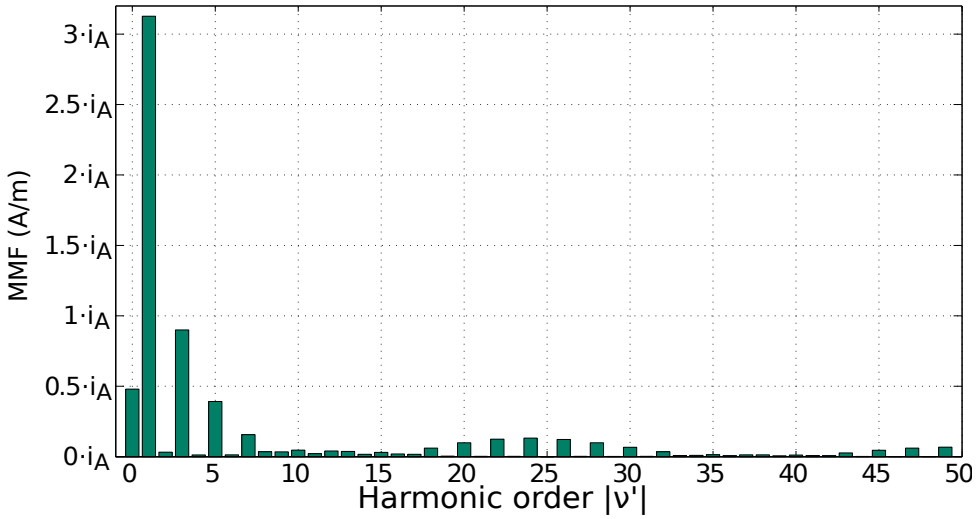

(b) Harmonic content of the stator winding function.

Figure 3.12: Stator winding distribution analysis of $M^{5,2}_{50,44}$.

3.5.2 VSD of the Healthy Motor Current Spectrum

Both motors are controlled in open loop with a fundamental frequency $f_s = 50\,\text{Hz}$ and are tested with three different mechanical loads. The complex spectrum of the stator current of $M^{5,2}_{30,22}$, decomposed into the two motor planes, is shown in Fig. 3.13, and the spectrum of the $M^{5,2}_{50,44}$ stator current is shown in Fig. 3.14. The frequencies and planes of the harmonics identified in Figs. 3.13 and 3.14 are reflected in their respective columns in Tables 3.5 and 3.6.

The first harmonic to be identified in the VSD of stator current spectrum is the fundamental component of the current, i.e., $k_\rho q = 1$ and $k_s = k_r = k_{se} = k_{de} = 0$ in (3.50) and (3.52). The rotation speed of the flux density component that it produces is $\omega_s = 50\,\text{Hz}$ and its pole pairs are $P = 2$. By applying the mapping equation (3.46), or by using the mapping diagram shown in Fig. 3.6b, the induced current component maps into the α-β plane. Equation (3.47) shows that its SVR speed is 50 Hz in both motors. This current component is labeled as #1 in Figs. 3.13 and 3.14 and in Tables 3.5 and 3.6.

The second harmonic to be identified in Figs. 3.13 and 3.14 is the 3rd order time ($q = 3$, $k_\rho = 1$) or saturation harmonic ($q = 1$, $k_\rho = 3$), i.e., $k_\rho q = 3$ and $k_s = k_r = k_{se} = k_{de} = 0$. The mapping diagram Fig. 3.6b shows that it maps into the x-y plane and its SVR speed is $-150\,\text{Hz}$ in both motors. This current harmonic is labeled as #3 in Figs. 3.13 and 3.14 and in Tables 3.5 and 3.6.

Following the same procedure, the plane and SVR speed of the 7th order time or

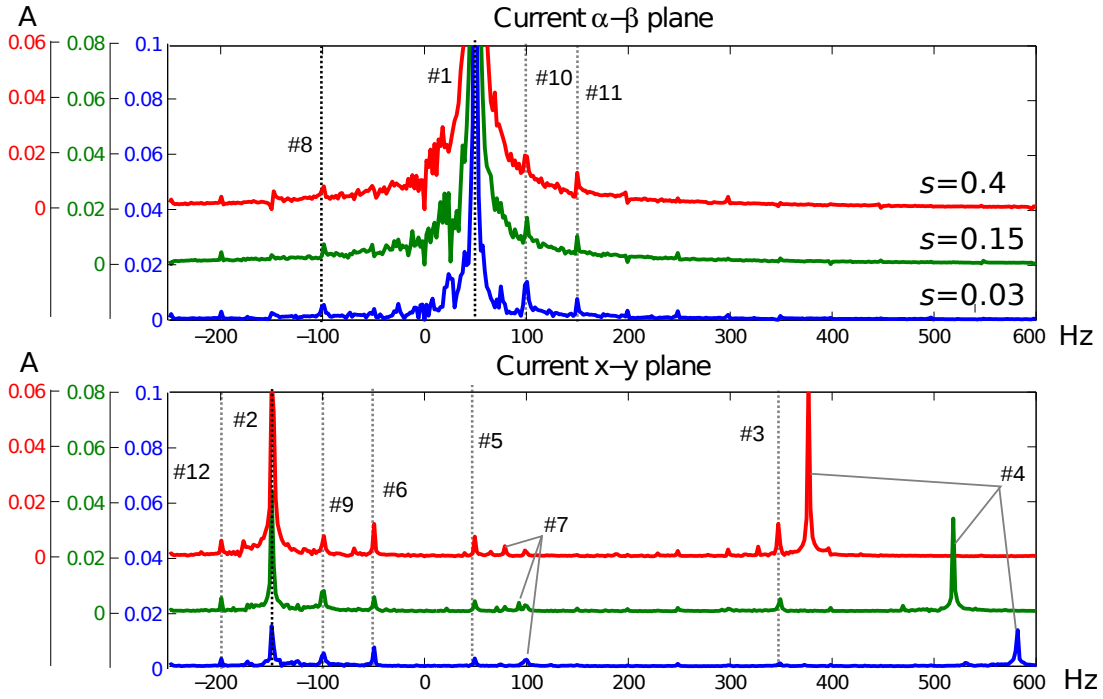

Figure 3.13: $M^{5,2}_{30,22}$ stator current complex spectrum, in the two motor planes.

TABLE 3.5
$M^{5,2}_{30,22}$ STATOR CURRENT HARMONICS IDENTIFICATION

	qk_ρ	k_s	k_r	k_{se}	k_{de}	Sync.	SVR speed (Hz)			Subspace	
							s=0.4	s=0.15	s=0.03		
#1	1	0	0	0	0	Stator	50	50	50	$\alpha-\beta$	Healthy
#2	3	0	0	0	0	Stator	-150	-150	-150	$x-y$	
#3	7	0	0	0	0	Stator	350	350	350	$x-y$	
#4	1	0	1	0	0	Rotor	380	517.5	583.5	$x-y$	
#5	1	0	0	2	0	Stator	50	50	50	$x-y$	Static Ecce.
#6	1	0	0	4	0	Stator	-50	-50	-50	$x-y$	
#7	1	0	0	0	2	Rotor	80	92.5	99	$x-y$	Dynamic
#8	2	0	0	-6	0	Stator	-100	-100	-100	$\alpha-\beta$	Mixed Origins
#9	2	0	0	2	0	Stator	-100	-100	-100	$x-y$	
#10	2	0	0	-2	0	Stator	100	100	100	$\alpha-\beta$	
#11	3	0	0	-4	0	Stator	150	150	150	$\alpha-\beta$	
#12	4	0	0	-2	0	Stator	-200	-200	-200	$x-y$	

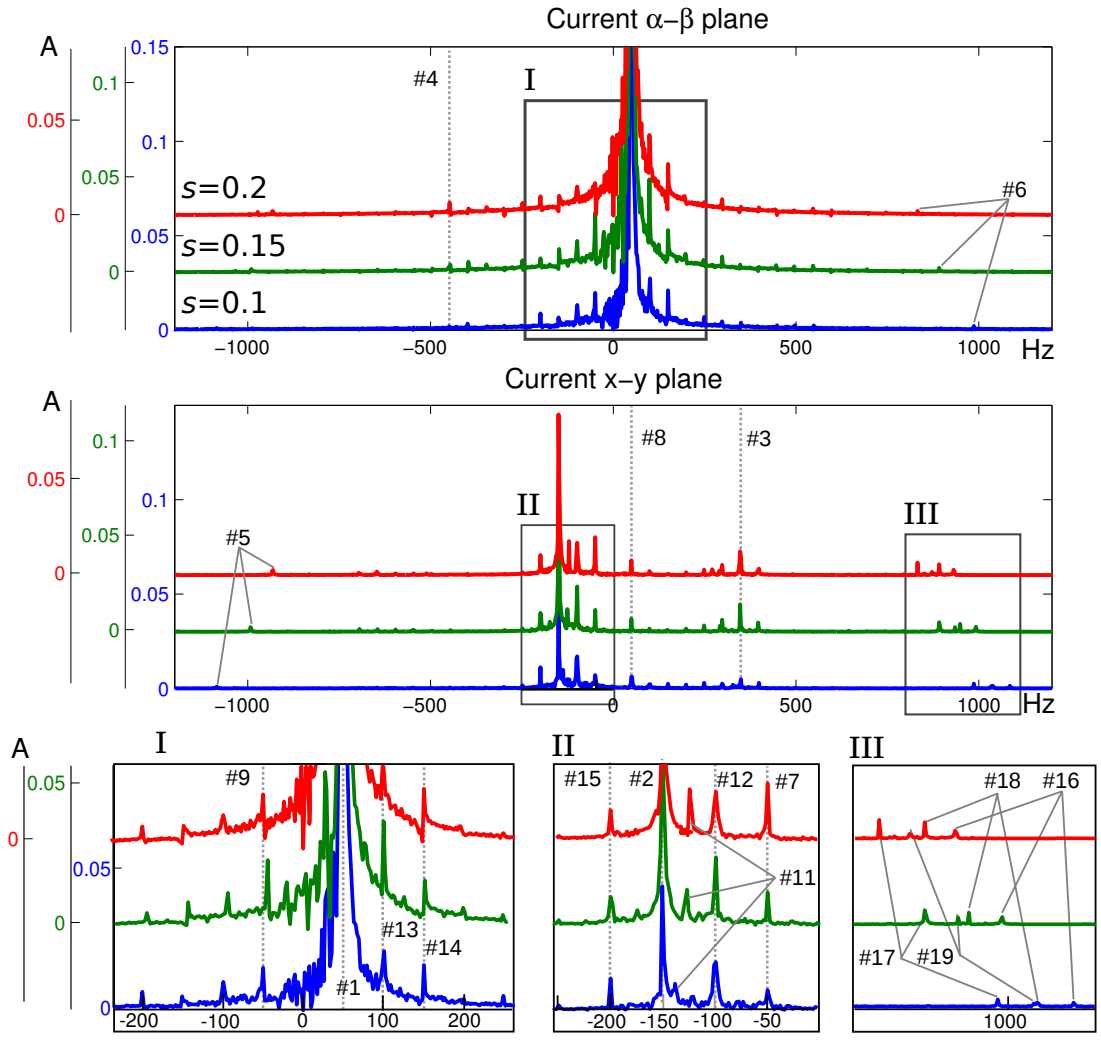

Figure 3.14: $M^{5,2}_{50,44}$ stator current complex spectrum, in the two motor planes.

saturation harmonic (i.e., $k_\rho q = 7$ and $k_s = k_r = k_{se} = k_{de} = 0$) is assessed to be x-y and 350 Hz, respectively, in both motors. This current harmonic is labeled as #3.

The next induced harmonic to identify is the one produced by the 9th order time or saturation harmonic, $k_\rho q = 9$ and $k_s = k_r = k_{se} = k_{de} = 0$. This harmonic maps into the α-β plane and has a SVR speed of -450 Hz. The amplitude of this induced current harmonic makes difficult its identification in the $M^{5,2}_{30,22}$ current spectrum. In Fig. 3.14 and Table 3.6, this harmonic is labeled as #4.

Both motors have a number of phases such that Q_s/P is a multiple of the phase number, i.e., $Q_s/P = 30/2 = 15$ in $M^{5,2}_{30,22}$ and $Q_s/P = 50/2 = 25$ in $M^{5,2}_{50,44}$. As a consequence, for the different values of k_s, the values of ν' and P_h/P in (3.52) evolve in steps multiples of the phase number, which neither changes the subspace where the induced current map nor its SVR speed. Therefore, the effects of the stator slots in the VSD current spectrum cannot be observed. This finding can be extended to multiphase motors with $Q_s/P = kn$, where $k = 1, 2, ...$

The rotation speed of the flux harmonics produced by the rotor bar harmonics depends on the number of rotor bars Q_r, as it can be seen in (3.50). This equation shows that

TABLE 3.6
$M^{5,2}_{50,44}$ STATOR CURRENT HARMONICS IDENTIFICATION

	qk_ρ	k_s	k_r	k_{se}	k_{de}	Sync.	SVR speed (Hz)			Subspace	
							s=0.2	s=0.15	s=0.1		
#1	1	0	0	0	0	Stator	50	50	50	$\alpha-\beta$	Healthy
#2	3	0	0	0	0	Stator	-150	-150	-150	$x-y$	
#3	7	0	0	0	0	Stator	350	350	350	$x-y$	
#4	9	0	0	0	0	Stator	-450	-450	-450	$\alpha-\beta$	
#5	1	0	1	0	0	Rotor	-932	-991	-1085	$x-y$	
#6	1	0	-1	0	0	Rotor	832	891	985	$\alpha-\beta$	
#7	1	0	0	4	0	Stator	-50	-50	-50	$x-y$	Static Ecce.
#8	1	0	0	-8	0	Stator	50	50	50	$x-y$	
#9	1	0	0	-4	0	Stator	-50	-50	-50	$\alpha-\beta$	
#10	1	0	0	0	4	Rotor	-110	-120	-130	$x-y$	Dynamic Ecce.
#11	1	0	0	0	-8	Rotor	-130	-135	-140	$x-y$	
#12	2	0	0	2	0	Stator	-100	-100	-100	$x-y$	Mixed Origins
#13	2	0	0	-2	0	Stator	100	100	100	$\alpha-\beta$	
#14	3	0	0	-4	0	Stator	150	150	150	$\alpha-\beta$	
#15	4	0	0	-2	0	Stator	-200	-200	-200	$x-y$	
#16	1	0	1	-2	0	Rotor	932	991	1035	$x-y$	
#17	1	0	-1	2	0	Rotor	832	891	985	$x-y$	
#18	1	0	1	0	-2	Rotor	891	949	1037	$x-y$	
#19	1	0	-1	0	2	Rotor	872	935	1033	$x-y$	

the rotation speed of the flux due to the fundamental MMF and the rotor bar harmonics is $\omega_{k_r} = \omega_s + k_r Q_r \omega_r = \omega_s[1 + (1-s)k_r Q_r/P]$. To limit the current components to be analyzed and represented in the stator current spectrum, only the first order rotor bar harmonics, i.e., $k_r = \pm 1$, are studied in this work. The value of P_h/P of the produced flux density is assessed by using (3.52) as $P_h/P = 1 \pm Q_r/P$.

In the $M^{5,2}_{30,22}$ motor, the induced current produced by the fundamental component of the MMF ($k_\rho q = 1$) and $k_r = 1$ maps into the x-y plane and has a SVR speed of $50(12 - 11s)$ Hz. This harmonic is labeled as #4 in Fig. 3.13 and in Table 3.5. In this motor, the back EMF produced by $k_\rho q = 1$ and $k_r = -1$ maps into the h^+ axis. The neutral point of the motor and the converter are not connected, and hence, the corresponding induced current harmonic cannot circulate.

In the $M_{50,44}^{5,2}$ motor, the induced current produced by $k_\rho q = 1$ and $k_r = 1$ maps into the x-y plane and has a SVR speed of $-50(23 - 22s)$ Hz. The one produced by $k_\rho q = 1$ and $k_r = -1$ maps into the α-β plane and has a SVR speed of $50(21 - 22s)$ Hz. These harmonics are labeled in Fig. 3.14 and Table 3.6 #5 and #6, respectively.

The stator current spectra of $M_{30,22}^{5,2}$ and $M_{50,44}^{5,2}$ shown in Figs. 3.13 and 3.14 are evaluated on the healthy motors. However, healthy motors also present a small degree of static and dynamic eccentricity due some mechanical non-ideal conditions such as fabrication tolerances, couplings or due to a non-perfect alignment of the motor test bench.

The rotation speed of the flux harmonics produced by the fundamental MMF and the static eccentricity, assessed by using (3.50), is ω_s. The value of P_h/P of the produced flux density is assessed by using (3.56). This equation shows that these flux components are linked by the stator if there is one distribution harmonic that accomplishes $\nu' = P_h/P$. Therefore, the values of k_{se} that do not have an associated ν' to satisfy (3.56) are not evaluated.

In the $M_{30,22}^{5,2}$ motor, the values $k_{se} = 2$ ($\nu' = P_h/P = 2$) and $k_{se} = 4$ ($\nu' = P_h/P = 3$) are evaluated. The former maps into the x-y plane and has a SVR speed of 50 Hz; it is labeled as #5 in Fig. 3.13 and Table 3.5. The latter maps into the x-y plane and has a SVR speed of -50 Hz; it is labeled as #6 in Fig. 3.13 and Table 3.5.

In the $M_{50,44}^{5,2}$ motor, the values $k_{se} = 4$ ($\nu' = P_h/P = 3$) and $k_{se} = -8$ ($\nu' = P_h/P = -3$) are assessed. The former maps into the x-y plane and has a SVR speed of -50 Hz; it is labeled as #7 in Fig. 3.14 and Table 3.6. The latter maps into the x-y plane and has a SVR speed of 50 Hz; it is labeled as #8 in Fig. 3.14 and Table 3.6.

Equation (3.58) is used to calculate the speed of the flux harmonics produced by the dynamic eccentricity and the fundamental MMF. The value of P_h/P of the produced flux density is given by (3.57).

The dynamic eccentricities in the $M_{30,22}^{5,2}$ motor are low and only $k_{de} = 2$ ($P_h/P = 2$) are noticeable in Fig. 3.13. The produced current harmonic maps into the x-y plane and has a SVR speed $50(2 - s)$ Hz. It is labeled as #7 in Fig. 3.13 and Table 3.5.

In the $M_{50,44}^{5,2}$ motor, the current harmonics due to the fundamental MMF and the dynamic $k_{de} = 4$ ($P_h/P = 3$) and $k_{de} = -8$ ($P_h/P = -3$) are identified. Both harmonics map into the x-y plane. The first one has a SVR speed of $50(3 - 2s)$ Hz and the second one, of $-50(1 - 2s)$ Hz. They are labeled as #10 and #11 ,respectively, in Fig. 3.14 and Table 3.6.

Figs. 3.13 and 3.14 and Tables 3.5 and 3.6 also show induced current harmonics produced by combinations of the previously studied origins. The current harmonics in $M_{30,22}^{5,2}$ labeled as #9 and #10 in Fig. 3.13 and Table 3.5 and the ones in $M_{50,44}^{5,2}$, labeled as #12 and #13 in Fig. 3.14 and Table 3.6, are due to the combination of time or saturation harmonics $qk_\rho = 2$ and the static eccentricity $k_{se} = \pm 2$. The current harmonic labeled as #11 in $M_{30,22}^{5,2}$ and #14 in $M_{50,44}^{5,2}$ is also produced by the combination of time or saturation harmonics $qk_\rho = 3$ and the static eccentricity $k_{se} = -4$. The same happens with the current harmonic labeled as #12 in $M_{30,22}^{5,2}$ and #15 in $M_{50,44}^{5,2}$. In the $M_{50,44}^{5,2}$ motor, the harmonics due to the combined effects of the rotor bar and slots and the static eccentricity, #16 and #17, and the ones due to the combined effects of the rotor bar and slots and the dynamic eccentricity, #18 and #19 are also identified.

3.5.3 MCSA Eccentricity Detection in n-Phase Induction Motors

To test the proposed VSD MCSA eccentricity detection method, both motors are analyzed with an imposed increment in the eccentricity. The $M_{30,22}^{5,2}$ motor is tested only with variations in the static eccentricity. The static eccentricity is increased by introducing a misalignment between the motor shaft and the motor test bench, as in [133, 175]. The $M_{50,44}^{5,2}$ motor is tested under the effects of mixed eccentricity with variations in the static an dynamic eccentricities. To produce the dynamic eccentricity, a load with different degrees of misaligned weight is introduced between the motor and the mechanical load. The radial forces produced by the unbalanced load produce the rotor misalignment.

Three MCSA methods are going to be evaluated: the classical static eccentricity detection method, based on the rotor bar and slot harmonics, extended to n-phase motors; the classical mixed eccentricity detection method based on the fundamental current sidebands and the proposed VSD MCSA method.

MCSA Static Eccentricity Detection Method Based on the Rotor Bar and Slot Harmonics

The motor $M_{30,22}^{5,2}$ is tested only for the case of static eccentricity. This motor is suitable for the MCSA eccentricity detection method based on the monitoring of the rotor bar and slot harmonics because the motor parameters satisfy (3.53). It has been seen in section §3.5.2 that, in a healthy $M_{30,22}^{5,2}$ motor, the back EMF harmonic due to the PSH with $k_r = -1$ maps into the h^+ axis. Since the neutrals of the motor and the inverter are isolated, the induced current harmonics due to this back EMF cannot circulate. When the static eccentricity affects this motor, for the fundamental MMF, $k_r = -1$ and $k_{se} \neq 0$, the expression (3.52) becomes $P_h/P = -10 + k_{se}/P$. For $k_{se} = \pm 2$, the back EMFs map into the α-β plane and, for $k_{se} = \pm 4$, the back EMFs map into the x-y plane; and hence, the induced current harmonics appear in the stator current spectrum with an absolute value of the SVR speed equal to $50(10 - 11s)$ Hz.

The evolution of the amplitude of the induced current harmonics due the PSH ($k_r = -1$) of $M_{30,22}^{5,2}$ when the static eccentricity is increased is shown in Fig. 3.15. The variable α_u indicates the misalignment angle between the motor shaft and the motor test bench. In this experiment, four degrees of misalignment are tested: motor aligned (black line), $\alpha_u = 0.02$ rad (green line), $\alpha_u = 0.04$ rad (blue line) and $\alpha_u = 0.06$ rad (red line). The imposed static eccentricity in this experiment is low in comparison with a real fault state. Hence, the amplitude of the symptom (PSH with $k_r = -1$) is low. However, an increase in the amplitude of the symptom with the increment of the static eccentricity can be observed in Fig. 3.15.

MCSA Static Eccentricity Detection Method Based on VSD

The eccentricity detection method, proposed in section §3.4.4, based on the analysis of the stator current spectrum by means of the VSD is divided in three steps.

In the first step, the order and amplitudes of the stator winding harmonics are obtained by applying the DFT to the stator winding function. The harmonic content of the $M_{30,22}^{5,2}$ can be seen in Fig. 3.11b. Then, the subspaces and SVR speeds of their linked induced currents are obtained by using (3.46). This classification is shown in Table 3.3. Finally,

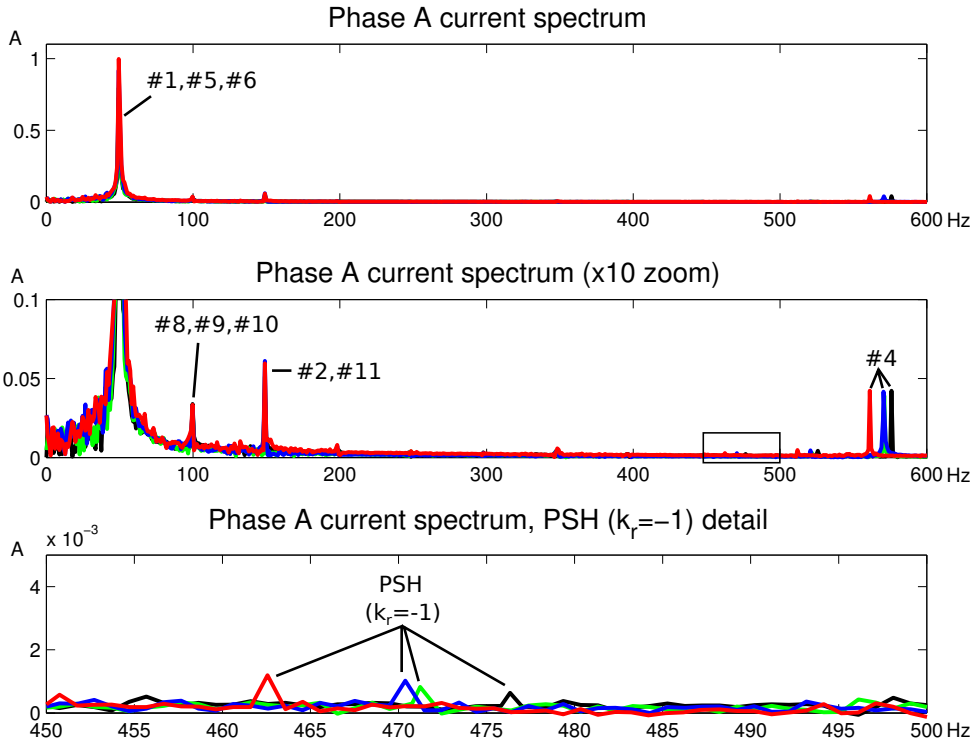

Figure 3.15: Variation of the phase A current spectrum of the $M^{5,2}_{30,22}$ motor when the static rotor eccentricity is increased: black line, $\alpha_u = 0$ rad and $s = 0.044$; green line, $\alpha_u = 0.02$ rad and $s = 0.053$; blue line, $\alpha_u = 0.04$ rad and $s = 0.052$ and red line, $\alpha_u = 0.06$ rad and $s = 0.071$.

the stator distribution harmonic chosen for the static eccentricity monitoring is $\nu' = 3$. This stator winding distribution harmonic is chosen because it is the one with the highest amplitude that maps into a different subspace than the fundamental current. Thus, the static eccentricity symptom maps into the x-y plane and its SVR speed is -50 Hz. This static eccentricity symptom is labeled as #6 and is highlighted in Table 3.5.

In the second step, the VSD spectrum of the healthy motor is obtained by using the CFFT with a resolution of 1 Hz. It is exposed in Fig. 3.13. This figure shows that the proposed static eccentricity symptom already has a non-depreciable amplitude in the healthy motor. This is due to the fact that even healthy motors present some degree of eccentricity and because of some other non-ideal characteristics of the system. Furthermore, the x-y plane is a low impedance plane, and thus, low amplitude back EMFs can produce high current harmonics.

In the third step, the amplitude of the chosen symptom is monitored to detect when the static eccentricity increases. The evolution of the chosen symptom amplitude when the static eccentricity is increased is shown in Fig. 3.16. In this experiment, the same four degrees of static misalignment than in the previous one are tested: motor aligned (black line), $\alpha_u = 0.02$ rad (green line), $\alpha_u = 0.04$ rad (blue line) and $\alpha_u = 0.06$ rad (red line). The results of the experiment shown in Fig. 3.16 corroborate the amplitude of the symptom (#6) rises when the static eccentricity increases. Additionally, this figure shows that the amplitudes of the harmonics #5, #8, #9 and #10, which are related with the static eccentricity too, are also increased.

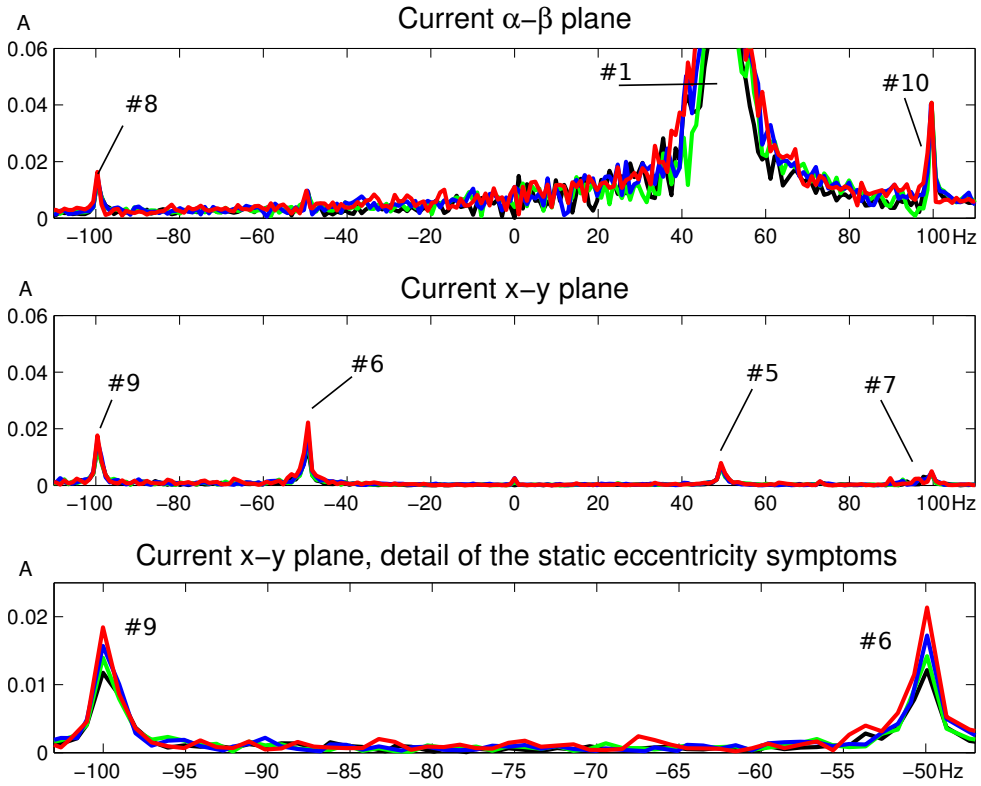

Figure 3.16: VSD analysis of the current spectrum of $M_{30,22}^{5,2}$ when the static rotor eccentricity is increased: $\alpha_u = 0$ rad and $s = 0.044$ (black), $\alpha_u = 0.02$ rad and $s = 0.053$ (green), $\alpha_u = 0.04$ rad and $s = 0.052$ (blue) and $\alpha_u = 0.06$ rad and $s = 0.071$ (red).

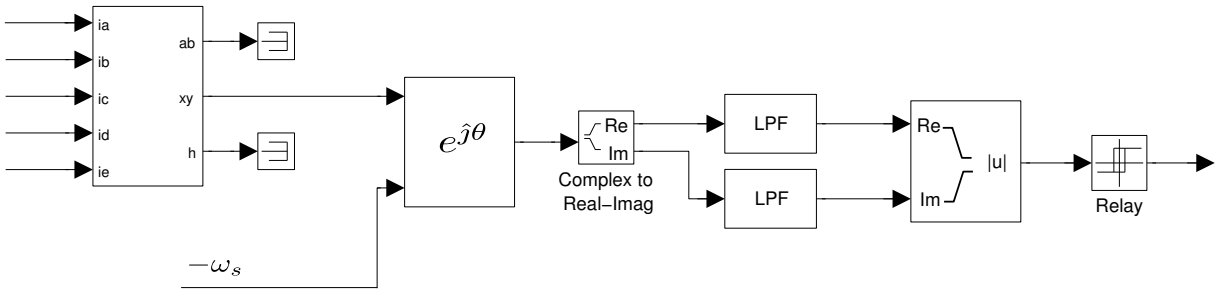

Figure 3.17: Static eccentricity detection algorithm based on the VSD MCSA.

The change in the amplitude of the symptom due to the static eccentricity is higher in the MCSA method based on the VSD than in the one based on the PSH. In addition, the frequency of the current harmonics to monitor is lower, thus, the required bandwidth of the current sensors in this method is smaller. A simple algorithm for monitoring the amplitude of the proposed static eccentricity symptom (#6) is shown in Fig. 3.17. In the first block, the current per phase is decomposed into subspaces. Then, the current component at $-\omega_s$ in the x-y plane is obtained by using a rotating reference frame and a low pass filter (with a cut frequency of 0.1 Hz).

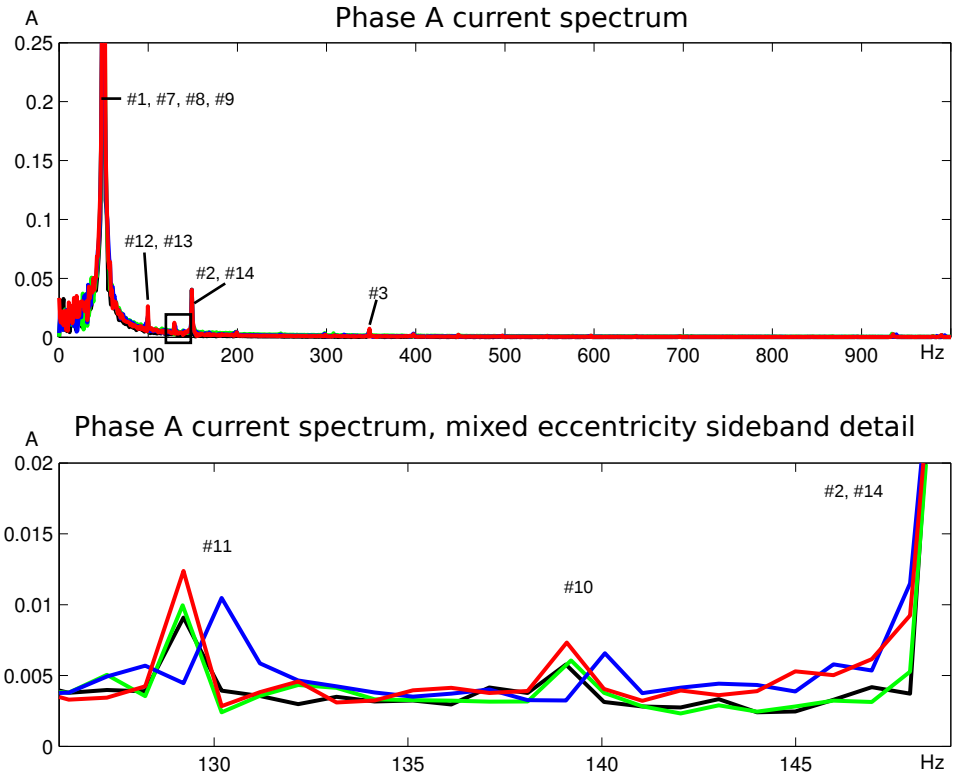

Figure 3.18: Fundamental current sideband variation with an increase in the dynamic eccentricity: $F_u = 0\,\mathrm{g}$ and $s = 0.11$ (black), $F_u = 23\,\mathrm{g}$ and $s = 0.11$ (green), $F_u = 43\,\mathrm{g}$ and $s = 0.095$ (blue) and $F_u = 63\,\mathrm{g}$ and $s = 0.11$ (red).

Mixed Eccentricity Detection Method Based on the fundamental current sidebands

The eccentricity detection method based on the fundamental current sidebands at the frequencies show in (1.47) is tested with mixed eccentricity in the $M^{5,2}_{50,44}$ motor. Two experiments are carried out. In the first one, the evolution of the sidebands amplitude is tested when the dynamic eccentricity varies, and in the second one, it is tested with variations in the static eccentricity.

In the first experiment, the $M^{5,2}_{50,44}$ motor is tested with a fixed level of static eccentricity (the healthy motor static eccentricity level) and four different levels of dynamic eccentricity. These four levels are created by using a load with a variable misaligned weight. The obtained phase A current spectrum is shown in Fig. 3.18. The first test (black line) is done without any misaligned weight (the healthy $M^{5,2}_{50,44}$ motor dynamic eccentricity level), in the second test (green line) a misaligned weight of $F_u = 23\,\mathrm{g}$ is added to the load, in the third test (blue line) $F_u = 43\,\mathrm{g}$ and in the fourth test $F_u = 63\,\mathrm{g}$ (red line). Fig. 3.18 shows that the monitored sidebands amplitude rises when dynamic eccentricity is increased.

In the second experiment, the $M^{5,2}_{50,44}$ motor is tested with a fixed level of dynamic eccentricity (the healthy motor dynamic eccentricity level) and four different levels of static eccentricity: the first test is done with $\alpha_u = 0\,\mathrm{rad}$ (black line); the second one, with $\alpha_u = 0.01\,\mathrm{rad}$ (green line); the third one, with $\alpha_u = 0.02\,\mathrm{rad}$ (blue) and in the last one,

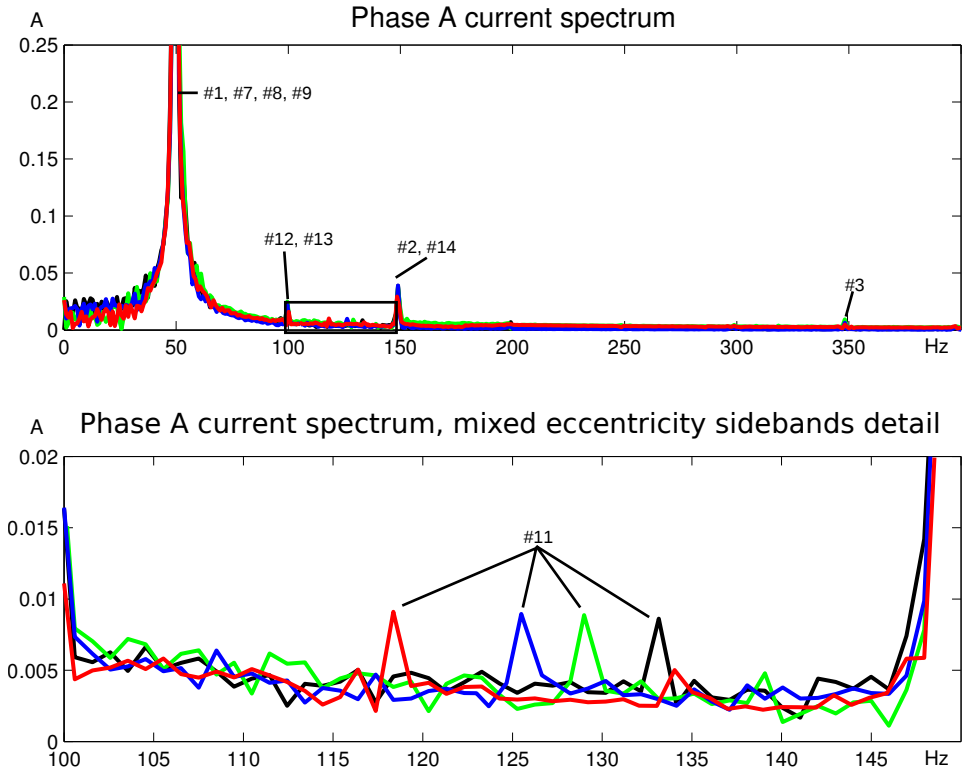

Figure 3.19: Fundamental current sideband variation with an increase in the static eccentricity: $\alpha_u = 0\,\text{rad}$ and $s = 0.075$ (black), $\alpha_u = 0.01\,\text{rad}$ and $s = 0.105$ (green), $\alpha_u = 0.02\,\text{rad}$ and $s = 0.125$ (blue) and $\alpha_u = 0.03\,\text{rad}$ and $s = 0.160$ (red).

$\alpha_u = 0.03\,\text{rad}$ (red). The obtained phase A current spectra are shown in Fig. 3.19.

Fig. 3.19 shows that the monitored fundamental current sidebands do not change their amplitude due to the increase in the static eccentricity level. This effect is due to the fact that, in the five-phase motor, these current sidebands are produced by dynamic eccentricity and not by static eccentricity. This result differs from the three-phase case, in which some of the fundamental current sidebands are due to the combination of the static and dynamic eccentricity (as it is shown in Table 3.2) and, thus their amplitude depends on the two rotor misalignments.

MCSA Mixed Eccentricity Detection Method Based on VSD

The motor $M^{5,2}_{50,44}$ is tested with a combination of static and dynamic eccentricities.

In the first step, the stator distribution harmonics are shown in Fig. 3.12b and the subspaces and SVR speeds of their linked induced currents are shown in Table 3.4. The stator distribution harmonic chosen for the static eccentricity monitoring is also $\nu' = 3$, as with the previous motor. Thus, the static eccentricity symptom is an increased amplitude of the space vector that maps into the x-y plane and has a SVR speed of $-50\,\text{Hz}$. This static eccentricity symptom is labeled as #7 and it is highlighted in Table 3.6. The dynamic eccentricity symptoms also map into the x-y plane and their SVR speeds are $-50(3-2s)\,\text{Hz}$ (#11) and $-50(1-2s)\,\text{Hz}$ (#10). These symptoms are highlighted in Table 3.6.

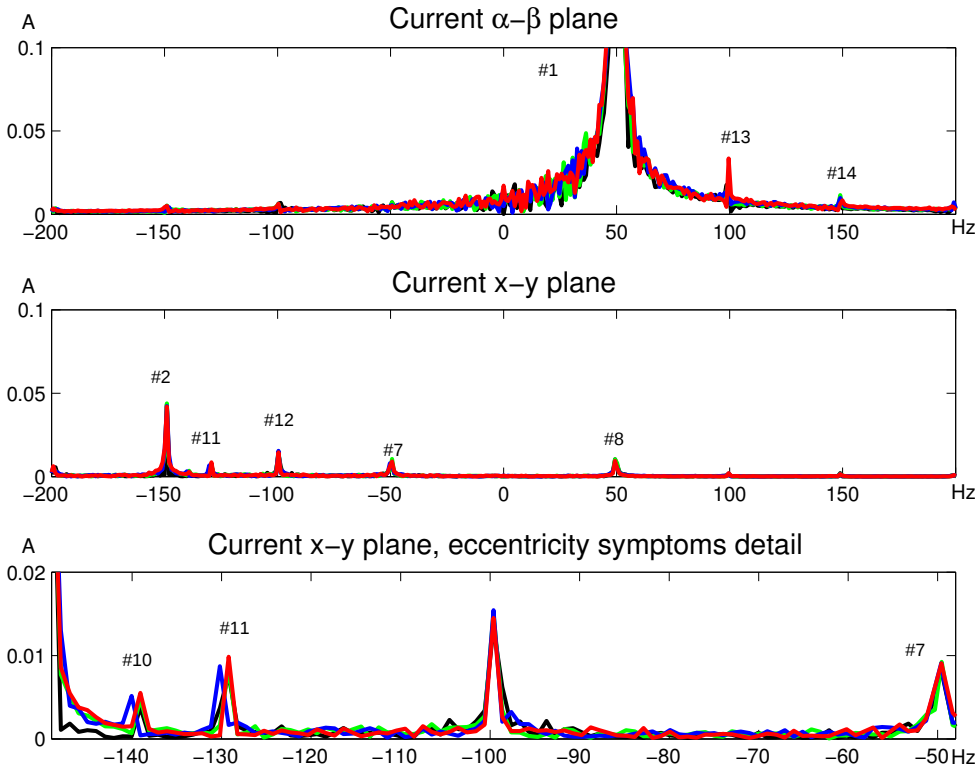

Figure 3.20: Analysis by means of the VSD of the $M^{5,2}_{50,44}$ stator current spectrum with an increase in the dynamic rotor eccentricity: $F_u = 0\,\mathrm{g}$ and $s = 0.11$ (black), $F_u = 23\,\mathrm{g}$ and $s = 0.11$ (green), $F_u = 43\,\mathrm{g}$ and $s = 0.095$ (blue) and $F_u = 63\,\mathrm{g}$ and $s = 0.11$ (red).

In the second step, the VSD spectrum of the healthy motor is shown in Fig. 3.14. It can be seen in the figure that the amplitudes of #7 and #11 are different from zero even in the healthy motor.

In the third step of the method, the amplitudes of the selected eccentricity symptoms are monitored. As in the previous section, where the eccentricity detection method based on the current sidebands is tested, two experiments are going to be done, in the first one the $M^{5,2}_{50,44}$ motor is going to be tested with four degrees of dynamic eccentricity and in the second one, with four degrees of static eccentricity.

Fig. 3.20 shows the evolution of the chosen dynamic (#10 and #11) and static (#7) eccentricity symptoms with an increase in the dynamic eccentricity. The dynamic eccentricity levels are the same as the ones used to test the current sideband method: $F_u = 43\,\mathrm{g}$ (black line), $F_u = 23\,\mathrm{g}$ (green line), $F_u = 43\,\mathrm{g}$ (blue line) and $F_u = 63\,\mathrm{g}$ (red line). This picture shows that, when the dynamic eccentricity is increased while keeping the other motor parameters constant, the amplitudes of the #10 and #11 current harmonics become larger and the amplitude of #7 does not vary.

Fig. 3.21 shows the evolution of the chosen dynamic and static eccentricity symptoms with an increase in the static eccentricity. The dynamic eccentricity levels are also the same ones as in the current sideband experiment: $\alpha_u = 0\,\mathrm{rad}$ (black), $\alpha_u = 0.01\,\mathrm{rad}$ (green), $\alpha_u = 0.02\,\mathrm{rad}$ (blue) and $\alpha_u = 0.03\,\mathrm{rad}$ (red). This experiment reflects that the increase in the static eccentricity rises the amplitude of #7, while the amplitudes of #10 and #11 remain unchanged. Therefore, the proposed VSD MCSA method allows to

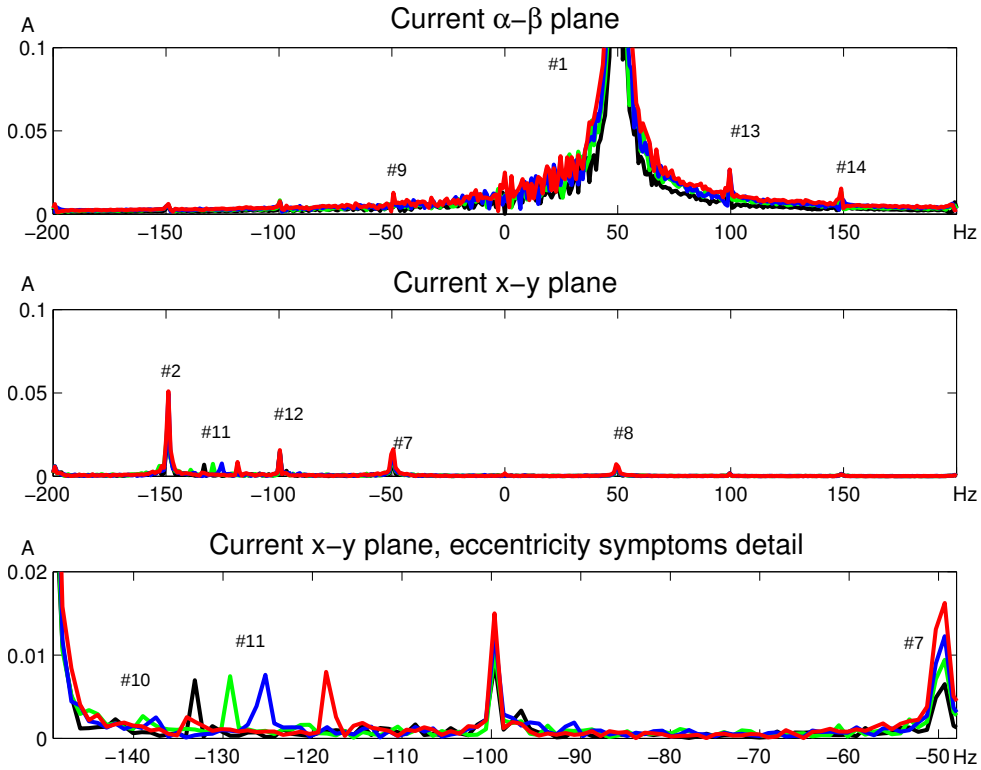

Figure 3.21: Analysis by means of the VSD of the $M^{5,2}_{50,44}$ stator current spectrum with an increase in the static eccentricity: $\alpha_u = 0$ rad and $s = 0.075$ (black), $\alpha_u = 0.01$ rad and $s = 0.105$ (green), $\alpha_u = 0.02$ rad and $s = 0.125$ (blue) and $\alpha_u = 0.03$ rad and $s = 0.160$ (red).

distinguish between a static or a dynamic eccentricity increment.

The algorithm shown in Fig. 3.17 can be used to monitor the amplitude of the static eccentricity symptom #7. A similar algorithm for monitoring the amplitude of the dynamic eccentricity symptoms #10 and #10 is shown in Fig. 3.22.

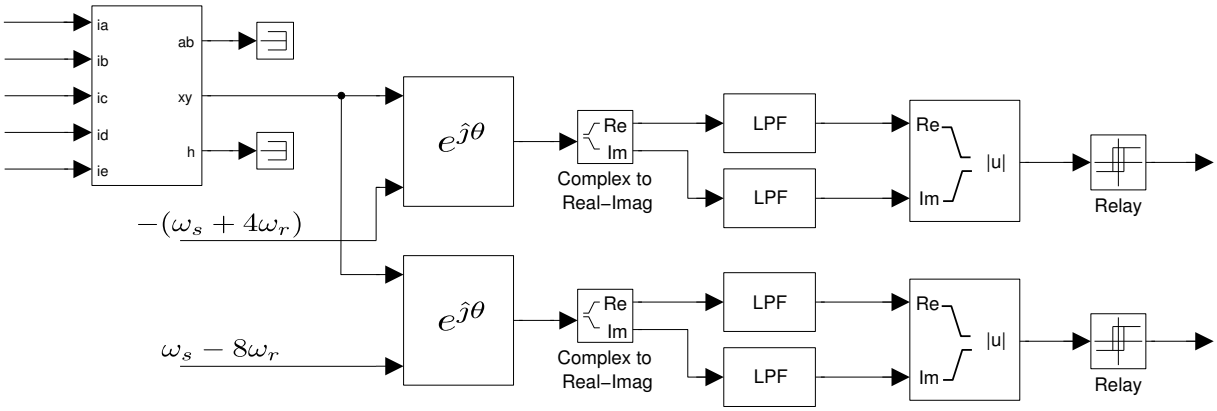

Figure 3.22: Dynamic eccentricity detection algorithm based on the VSD MCSA.

3.6 Conclusion

In this chapter, the model used to study the time harmonic mapping by means of the VSD is extended to cover the current harmonics produced by non-ideal characteristics of real squirrel cage motors, such as the ones due to the winding distribution, rotor bars, stator and rotors slots, rotor eccentricities and magnetic saturation.

This model is used to analyze the VSD of the current signature of healthy multiphase squirrel cage motors. This analysis provides more information of each current harmonic (i.e., the subspace where it maps and the SVR speed) than the classic approach, based only on the amplitudes and frequencies in the stator current spectrum.

The most common method to detect static eccentricity is the classic approach based on monitoring the amplitudes of the rotor slot and bar harmonics. The information obtained from the VSD analysis of the stator current spectrum of multiphase motors is used to assess the motor characteristics to determine when the classic static eccentricity method based on the monitoring of the rotor slot and bar harmonics is valid for a specific n-phase motor.

A MCSA method to detect pure-static, pure-dynamic and mixed eccentricities in multiphase induction motors is proposed as an example of application of the VSD stator current analysis. The symptoms that the proposed method uses to detect the static eccentricity have higher amplitudes and lower frequencies than the ones used by the classic MCSA method, the rotor bar and slot harmonics,. The developed method can be used in the cases the classic method is not valid to detect pure-static eccentricity due to the n-phase motor characteristics. In addition, in cases of mixed eccentricity, by using the proposed VSD MCSA method it is possible to distinguish between increases in the static or in the dynamic eccentricity.

Finally, experimental results were obtained with two five-phase motors with different stator and rotor slot numbers and winding distributions to evaluate the VSD healthy motor current signature and the proposed VSD MCSA eccentricity detection method.

Chapter 4

Conclusion and Future Research

4.1 Conclusion

This thesis presents the study and characterization of the stator current and voltage components produced by time and spatial harmonics in a n-phase induction motor with a symmetrical arrangement of phases by means of the VSD. Its main contributions and conclusions are summarized below.

- First, an analysis by means of the VSD of the stator voltage and current harmonics in multiphase induction motors is developed. This study takes into account the effects of the time harmonic order and the phase sequence on the harmonic mapping.
- From this analysis, a simple time harmonic mapping method is obtained. The proposed method is valid to predict the subspace where each time harmonic maps and its SVR speed (frequency and direction) in symmetrical multiphase induction motors of any phase number. It can be applied to single motor and series-connected multimotor drives.
- This method can be used to predict in single and multimotor drives whether the time harmonic maps into a low impedance plane, producing extra losses, or into a rotor coupled plane, producing torque ripple. In series-connected systems, the crossed interactions between motors are also identified.
- Then, the model used to analyze the time harmonic VSD is extended to cover the current harmonics produced for some non-ideal characteristics of a squirrel cage motor, such as non-perfect sinusoidal winding distributions, rotor bars, non-uniform airgap and magnetic saturation.
- Due to the fact that the study of the harmonics by means of the VSD provides more information, i.e., the subspace where each harmonic maps and its SVR speed, than the classic current per phase spectrum, it is applied to analyze the n-phase healthy motor current signature.
- With the proposed analysis of the current spectrum by means of VSD it can be predicted the subspace where the current component due to one specific cause, among the studied ones, maps. By knowing the subspace where it maps, it can also

be predicted if the current is going to have high amplitude, if it is a low impedance plane, or if it is not going to circulate, in case it maps into a homopolar component and there is no neutral connection. This information is used to extend the classic MCSA static eccentricity detection method based on the rotor slot and bar current harmonics to the case of n-phase motors.

- The analysis of the MCSA by means of the VSD also helps to distinguish between harmonics with the same frequency in the stator current spectrum. This fact is used to propose a new MCSA method to detect pure-static, pure-dynamic and mixed eccentricities based on the VSD of the current signature of the motor.

- The static eccentricity symptoms monitored in this method have higher amplitudes and lower frequencies than the ones in the classic MCSA method based on the rotor bar and slot harmonics. Furthermore, the proposed VSD MCSA method can be used in the cases the classic method is not valid to detect pure-static eccentricity in multiphase motors.

- In the case of mixed eccentricity detection, the proposed method allows to distinguish between the symptoms due to the static and the dynamic eccentricities. Therefore, this method can be used to differentiate between a rise in the static or dynamic eccentricity.

- Research work included in the dissertation has given rise to one journal paper [5] and two conference papers [10, 21].

4.2 Future Research

There are several interesting topics suggested for further research in VSD current and voltage harmonics analysis in multiphase motors. These topics are described in the following.

- The proposed current and voltage harmonics mapping method should be extended to multiphase motors with an asymmetrical arrangement of phases.

- The study about current and voltage components produced by time and spatial harmonics in multiphase motors should be extended to other types of machines, such as synchronous, permanent magnet or doubly-fed motors.

- The proposed VSD MCSA eccentricity detection method should be completed with a broader study, including more accurate measures of the eccentricity degree and validated by using a larger variety of multiphase motors.

- The VSD MCSA method can be extended for the detection of other common motor faults, such as open- or short-circuit stator phase or bearing faults.

- A similar monitoring method, based on the VSD, should be developed for motor voltage or power signature analysis and a VSD method that can detect faults in current controlled multiphase drivers should be studied.

References

[1] F. D. Freijedo, A. Vidal, A. G. Yepes, J. M. Guerrero, O. Lopez, J. Malvar, and J. Doval-Gandoy, "Tuning of synchronous-frame PI current controllers in grid-connected converters operating at a low sampling rate by MIMO root locus," *IEEE Trans. Ind. Electron.*, vol. 62, no. 8, pp. 5006–5017, Aug. 2015.

[2] A. Vidal, A. G. Yepes, F. D. Freijedo, O. Lopez, J. Malvar, F. Baneira, and J. Doval-Gandoy, "A method for identification of the equivalent inductance and resistance in the plant model of current-controlled grid-tied converters," *IEEE Trans. Power Electron.*, 2015, early Access.

[3] A. Vidal, A. G. Yepes, F. D. Freijedo, J. Malvar, O. Lopez, and J. Doval-Gandoy, "A technique to estimate the equivalent loss resistance of grid-tied converters for current control analysis and design," *IEEE Trans. Power Electron.*, vol. 30, no. 3, pp. 1747–1761, Mar. 2015.

[4] A. G. Yepes, J. Malvar, A. Vidal, O. Lopez, and J. Doval-Gandoy, "Current harmonics compensation based on multiresonant control in synchronous frames for symmetrical n -phase machines," *IEEE Trans. Ind. Electron.*, vol. 62, no. 5, pp. 2708–2720, May 2015.

[5] J. Malvar, O. Lopez, A. G. Yepes, A. Vidal, F. D. Freijedo, P. Fernandez-Comesana, and J. Doval-Gandoy, "Graphical diagram for subspace and sequence identification of time harmonics in symmetrical multiphase machines," *IEEE Trans. Ind. Electron.*, vol. 61, no. 1, pp. 29–42, Jan. 2014.

[6] A. Vidal, F. D. Freijedo, A. G. Yepes, J. Malvar, O. Lopez, and J. Doval-Gandoy, "Transient response evaluation of stationary-frame resonant current controllers for grid-connected applications," *IEEE Trans. Power Electron.*, vol. 7, no. 7, pp. 1714–1724, Jul. 2014.

[7] A. Vidal, A. G. Yepes, J. Malvar, O. Lopez, J. Doval-Gandoy, and F. D. Freijedo, "Estimation of the plant time constant of current-controlled voltage source converters," in *Proc. ECCE*, Sep. 2014, pp. 5008–5015.

[8] A. G. Yepes, A. Vidal, J. Malvar, O. Lopez, and J. Doval-Gandoy, "Tuning method aimed at optimized settling time and overshoot for synchronous proportional-integral current control in electric machines," *IEEE Trans. Power Electron.*, vol. 29, no. 6, pp. 3041–3054, Jun. 2014.

[9] F. D. Freijedo, A. Vidal, A. G. Yepes, J. Malvar, O. Lopez, and J. Doval-Gandoy, "Assessment of synchronous-frame PI current control dynamics by means of multivariable analysis with time-delays consideration," in *Proc. ECCE*, Sep. 2013, pp. 4104–4111.

[10] J. Malvar, O. Lopez, A. G. Yepes, A. Vidal, and J. Doval-Gandoy, "Interactions between time and spatial harmonics in a series-connected five-phase two-motor drive," in *Proc. IECON*, Nov. 2013, pp. 5197–5202.

[11] A. Vidal, F. D. Freijedo, A. G. Yepes, P. Fernandez-Comesana, J. Malvar, O. Lopez, and J. Doval-Gandoy, "Assessment and optimization of the transient response of proportional-resonant current controllers for distributed power generation systems," *IEEE Trans. Ind. Electron.*, vol. 60, no. 4, pp. 1367–1383, Apr. 2013.

[12] A. Vidal, A. G. Yepes, J. Malvar, O. Lopez, J. Doval-Gandoy, and F. D. Freijedo, "A method to identify the equivalent loss resistance of voltage source converters for current control design," in *Proc. ECCE*, Sep. 2013, pp. 4133–4140.

[13] A. G. Yepes, A. Vidal, F. D. Freijedo, J. Malvar, O. Lopez, and J. Doval-Gandoy, "Assessment of cross-coupling decoupling between orthogonal axes in double synchronous reference frame current control structures," in *Proc. SAAEI*, Jul. 2013, pp. 471–478.

[14] J. Malvar, A. G. Yepes, A. Vidal, O. Lopez, and J. Doval-Gandoy, "Experimental evaluation of harmonic mapping in a multimotor drive," in *Proc. SAAEI*, Jul. 2013, pp. 471–478.

[15] A. G. Yepes, J. Malvar, A. Vidal, O. Lopez, and J. Doval-Gandoy, "Current harmonic compensation in symmetrical multiphase machines by resonant controllers in synchronous reference frames - Part 2: Computational load," in *Proc. IECON*, Nov. 2013, pp. 5161–5166.

[16] ——, "Optimized harmonic current control strategy for nonlinearities compensation in multiphase ac drives," in *Proc. ECCE*, Sep. 2013, pp. 1458–1464.

[17] A. G. Yepes, A. Vidal, F. D. Freijedo, J. Malvar, O. Lopez, and J. Doval-Gandoy, "A simple tuning method aimed at optimal settling time and overshoot for synchronous PI current control in electric machines," in *Proc. ECCE*, Sep. 2013, pp. 1465–1472.

[18] A. G. Yepes, A. Vidal, J. Malvar, O. Lopez, J. Doval-Gandoy, and F. D. Freijedo, "Ineffectiveness of orthogonal axes cross-coupling decoupling technique in dual sequence current control," in *Proc. ECCE*, Sep. 2013, pp. 1047–1053.

[19] A. G. Yepes, J. Malvar, A. Vidal, O. Lopez, and J. Doval-Gandoy, "Optimized harmonic current control strategy for nonlinearities compensation in multiphase AC drives," in *Proc. ECCE*, Sep. 2013, pp. 1458–1464.

[20] O. Lopez, J. Alvarez, J. Malvar, A. G. Yepes, A. Vidal, P. Fernandez-Comesana, F. D. Freijedo, and J. Doval-Gandoy, "Multiphase space vector control modulation technique for voltage source converters," in *Proc. IECON*, Oct. 2012, pp. 3635–3640.

[21] J. Malvar, A. G. Yepes, A. Vidal, P. Fernandez-Comesana, F. D. Freijedo, O. Lopez, and J. Doval-Gandoy, "Harmonic subspace and sequence mapping in a series-connected six-phase two-motor drive," in *Proc. IECON*, Oct. 2012, pp. 3622–3627.

[22] A. Vidal, F. D. Freijedo, A. G. Yepes, J. Malvar, O. Lopez, and J. Doval-Gandoy, "Transient response assessment of vector pi current controllers in renewable energy applications," in *Proc. IECON*, Oct. 2012, pp. 5259–5264.

[23] A. G. Yepes, A. Vidal, F. D. Freijedo, J. Malvar, O. Lopez, and J. Doval-Gandoy, "Transient response evaluation of resonant controllers for AC drives," in *Proc. ECCE*, Sep. 2012, pp. 471–478.

[24] A. G. Yepes, F. D. Freijedo, J. Doval-Gandoy, O. Lopez, J. Malvar, and P. Fernandez-Comesana, "Correction to "effects of discretization methods on the performance of resonant controllers"," *IEEE Trans. Power Electron.*, vol. 27, no. 12, pp. 4976–4976, Dec. 2012.

[25] P. Fernandez-Comesana, F. D. Freijedo, J. Doval-Gandoy, O. Lopez, A. G. Yepes, and J. Malvar, "Mitigation of voltage sags, imbalances and harmonics in sensitive industrial loads by means of a series power line conditioner," *Electr. Power Sys. Research*, vol. 84, no. 1, pp. 20 – 30, Mar. 2012.

[26] F. D. Freijedo, A. G. Yepes, J. Malvar, O. Lopez, P. Fernandez-Comesana, A. Vidal, and J. Doval-Gandoy, "Frequency tracking of digital resonant filters for control of power converters connected to public distribution systems," *IEEE Trans. Power Electron.*, vol. 4, no. 4, pp. 454–462, Apr. 2011.

[27] F. D. Freijedo, A. Vidal, A. G. Yepes, P. Fernandez-Comesana, J. Malvar, O. Lopez, A. Nogueiras, and J. Doval-Gandoy, "WLSE for fast, accurate and robust generation of references in power converter applications," in *Proc. ISIE*, Jul. 2010, pp. 2946–2951.

[28] O. Lopez, J. Alvarez, F. D. Freijedo, A. G. Yepes, J. Malvar, P. Fernandez-Comesana, J. Doval-Gandoy, A. Nogueiras, A. Lago, and C. M. Penalver, "Multilevel multiphase space vector PWM algorithm with switching state redundancy applied to three-phase four-leg converters," in *Proc. IECON*, Nov. 2010, pp. 568–575.

[29] O. Lopez, F. D. Freijedo, A. G. Yepes, P. Fernandez-Comesana, J. Malvar, R. Teodorescu, and J. Doval-Gandoy, "Eliminating ground current in a transformerless photovoltaic application," *IEEE Trans. Energy Convers.*, vol. 25, no. 1, pp. 140–147, Mar. 2010.

[30] A. Vidal, F. D. Freijedo, A. G. Yepes, P. Fernandez-Comesana, J. Malvar, O. Lopez, and J. Doval-Gandoy, "A fast, accurate and robust algorithm to detect fundamental and harmonic sequences," in *Proc. ECCE*, Sep. 2010, pp. 1047–1052.

[31] A. Yepes, F. Francisco, P. Fernandez-Comesana, J. Malvar, O. Lopez, and J. Doval-Gandoy, "Torque ripple minimization in surface-mounted pm drives by means of PI multi-resonant controller in synchronous reference frame," in *Proc. IECON*, Nov. 2010, pp. 1017–1022.

[32] A. G. Yepes, F. D. Freijedo, J. Doval-Gandoy, O. Lopez, J. Malvar, and P. Fernandez-Comesana, "Effects of discretization methods on the performance of resonant controllers," *IEEE Trans. Power Electron.*, vol. 25, no. 7, pp. 1692–1712, Jul. 2010.

[33] A. G. Yepes, F. D. Freijedo, P. Fernandez-Comesana, J. Malvar, O. Lopez, and J. Doval-Gandoy, "Performance enhancement for digital implementations of resonant controllers," in *Proc. ECCE*, Sep. 2010, pp. 2535–2542.

[34] P. Fernandez, F. Freijedo, J. Doval-Gandoy, and J. Malvar, "Control algorithm for a SSSC," in *Proc. CPE*, May 2009, pp. 248–252.

[35] P. Fernandez-Comesana, J. Doval-Gandoy, F. Freijedo, O. Lopez, J. Malvar, A. Yepes, E. Diaz-Dorado, and D. Alvira-Baeza, "Evolutive algorithm for power flow optimization," in *Proc. IECON*, Nov. 2009, pp. 3323–3328.

[36] P. Fernandez-Comesana, F. D. Freijedo, J. Doval-Gandoy, and J. Malvar, "Control algorithm for a SSSC with a predictive synchronization algorithm," in *Proc. ECCE*, Sep. 2009, pp. 2740–2745.

[37] F. D. Freijedo, J. Doval-Gandoy, O. Lopez, C. Martinez-Penalver, A. G. Yepes, P. Fernandez-Comesana, J. Malvar, A. Nogueiras, J. Marcos, and A. Lago, "Grid-synchronization methods for power converters," in *Proc. IECON*, Nov. 2009, pp. 522–529.

[38] O. Lopez, J. Alvarez, F. D. Freijedo, A. G. Yepes, P. Fernandez-Comesana, J. Malvar, J. Doval-Gandoy, A. Nogueiras, A. Lago, and C. M. Penalver, "Multilevel multiphase space vector PWM algorithm with switching state redundancy applied to three-phase converters," in *Proc. IECON*, Nov. 2009, pp. 651–657.

[39] A. G. Yepes, F. D. Freijedo, J. Doval-Gandoy, O. Lopez, P. Fernandez-Comesana, and J. Malvar, "Harmonic detection methods for active power filters based on discrete cosine transform and dithering," in *Proc. IECON*, Nov. 2009, pp. 530–535.

[40] A. G. Yepes, F. D. Freijedo, J. Doval-Gandoy, O. Lopez, J. Malvar, and P. Fernandez-Comesana, "On the discrete-time implementation of resonant controllers for active power filters," in *Proc. IECON*, Nov. 2009, pp. 3686–3691.

[41] D. C. White and H. H. Woodson, *Electromechanical Energy Conversion*, The MIT Press, Ed. New York: John Wiley & Sons, Inc., Nov. 1968.

[42] H. R. Fudeh and C. M. Ong, "Modeling and analysis of induction machines containing space harmonics Part I: Modeling and transformation," *IEEE Trans. Power App. Syst.*, no. 8, pp. 2608–2615, Aug. 1983.

[43] S. Williamson and S. Smith, "Pulsating torque and losses in multiphase induction machines," *IEEE Trans. Ind. Appl.*, vol. 39, no. 4, pp. 986–993, Jul./Aug. 2003.

[44] J. Huang, B. Li, H. Jiang, and M. Kang, "Analysis and control of multiphase permanent-magnet bearingless motor with a single set of half-coiled winding," *IEEE Trans. Ind. Electron.*, vol. 61, no. 7, pp. 3137–3145, Jul. 2014.

[45] H. Guzman, M. Duran, F. Barrero, B. Bogado, and S. Toral, "Speed control of five-phase induction motors with integrated open-phase fault operation using model-based predictive current control techniques," *IEEE Trans. Ind. Electron.*, vol. 61, no. 9, pp. 4474–4484, Sep. 2014.

[46] M. Mengoni, L. Zarri, A. Tani, L. Parsa, G. Serra, and D. Casadei, "High-torque-density control of multiphase induction motor drives operating over a wide speed range," *IEEE Trans. Ind. Electron.*, vol. 62, no. 2, pp. 814–825, Feb. 2015.

[47] E. Levi, "Multiphase electric machines for variable-speed applications," *IEEE Trans. Ind. Electron.*, vol. 55, no. 5, pp. 1893–1909, May 2008.

[48] E. Levi, R. Bojoi, F. Profumo, H. A. Toliyat, and S. Williamson, "Multiphase induction motor drives — A technology status review," *IET Electr. Power Appl.*, vol. 1, no. 4, pp. 489–516, Jul. 2007.

[49] B. Wilamowski and J. Irwin, *Power Electronics and Motor Drives*, ser. Electrical engineering handbook series. CRC Press, 2011.

[50] C. Bruzzese and G. Joksimovic, "Harmonic signatures of static eccentricities in the stator voltages and in the rotor current of no-load salient-pole synchronous generators," *IEEE Trans. Ind. Electron.*, vol. 58, no. 5, pp. 1606–1624, May 2011.

[51] E. Levi, *The Industrial Electronics Handbook, 2nd ed.* CRC Press, 2011, vol. Power Electronics and Motor Drives, ch. Multiphase AC Machines.

[52] J. L. Willems, "Space harmonics in unified electrical-machine theory," *Proc. of the Inst. of Elec. Eng.*, vol. 118, no. 10, pp. 1408–1412, Oct. 1971.

[53] R. Bojoi, M. Lazzari, F. Profumo, and A. Tenconi, "Digital field-oriented control for dual three-phase induction motor drives," *IEEE Trans. Ind. Appl.*, vol. 39, no. 3, pp. 752–760, May/Jun. 2003.

[54] E. Levi, M. Jones, S. N. Vukosavic, and H. A. Toliyat, "Operating principles of a novel multiphase multimotor vector-controlled drive," *IEEE Trans. Energy Convers.*, vol. 19, no. 3, pp. 508–517, Sep. 2004.

[55] S. A. Nasar, "Electromechanical energy conversion in nm-winding double cylindrical structures in presence of space harmonics," *IEEE Trans. Power App. Syst.*, no. 4, pp. 1099–1106, Apr. 1968.

[56] Y. Zhao and T. A. Lipo, "Space vector PWM control of dual three-phase induction machine using vector space decomposition," *IEEE Trans. Ind. Appl.*, vol. 31, no. 5, pp. 1100–1109, Sep./Oct. 1995.

[57] J. Figueroa, J. Cros, and P. Viarouge, "Generalized transformations for polyphase phase-modulation motors," *IEEE Trans. Energy Convers.*, vol. 21, no. 2, pp. 332–341, Jun. 2006.

[58] T. H. Barton and M. Poloujadoff, "A generalized symmetrical component transformation for clyindrical electrical machines," *IEEE Trans. Power App. Syst.*, vol. PAS-91, no. 5, pp. 1781–1786, Sep. 1972.

[59] A. Tessarolo, "On the modeling of poly-phase electric machines through vector-space decomposition: Theoretical considerations," in *Proc. POWERENG*, Mar. 2009, pp. 519–523.

[60] C. Bruzzese, "Analysis and application of particular current signatures (symptoms) for cage monitoring in nonsinusoidally fed motors with high rejection to drive load, inertia, and frequency variations," *IEEE Trans. Ind. Electron.*, vol. 55, no. 12, pp. 4137–4155, Dec. 2008.

[61] Z. Wu and O. Ojo, "Coupled-circuit-model simulation and airgap-field calculation of a dual-stator-winding induction machine," *Elect. Power Appl., IEE Proc.*, vol. 153, no. 3, pp. 387–400, May 2006.

[62] M. A. Abbas, R. Christen, and T. M. Jahns, "Six-phase voltage source inverter driven induction motor," *IEEE Trans. Ind. Appl.*, no. 5, pp. 1251–1259, Sep./Oct. 1984.

[63] D. Dujic, M. Jones, and E. Levi, "Analysis of output current ripple rms in multiphase drives using space vector approach," *IEEE Trans. Power Electron.*, vol. 24, no. 8, pp. 1926–1938, Jul. 2009.

[64] N. Mohan, *Advanced Electric Drives: Analysis, Control, and Modeling Using MATLAB / Simulink*. Wiley, 2014.

[65] M. Jones, S. N. Vukosavic, D. Dujic, and E. Levi, "A synchronous current control scheme for multiphase induction motor drives," *IEEE Trans. Energy Convers.*, vol. 24, no. 4, pp. 860–868, Dec. 2009.

[66] H. S. Che, E. Levi, M. Jones, W.-P. Hew, and N. Rahim, "Current control methods for an asymmetrical six-phase induction motor drive," *IEEE Trans. Power Electron.*, vol. 29, no. 1, pp. 407–417, Jan. 2014.

[67] F. Barrero and M. Duran, "Recent advances in the design, modeling and control of multiphase machines," *IEEE Trans. Ind. Electron.*, 2015, Early Access.

[68] H. Guzman, M. Duran, F. Barrero, L. Zarri, B. Bogado, I. Gonzalez Prieto, and M. Arahal, "Comparative study of predictive and resonant controllers in fault-tolerant five-phase induction motor drives," *IEEE Trans. Ind. Electron.*, 2015, Early Access.

[69] M. Duran, J. Prieto, F. Barrero, and S. Toral, "Predictive current control of dual three-phase drives using restrained search techniques," *IEEE Trans. Ind. Electron.*, vol. 58, no. 8, pp. 3253–3263, Aug. 2011.

[70] F. Barrero, M. Arahal, R. Gregor, S. Toral, and M. Duran, "A proof of concept study of predictive current control for VSI-driven asymmetrical dual three-phase AC machines," *IEEE Trans. Ind. Electron.*, vol. 56, no. 6, pp. 1937–1954, Jun. 2009.

[71] H. Guzman, M. Duran, F. Barrero, B. Bogado, and S. Toral, "Speed control of five-phase induction motors with integrated open-phase fault operation using model-based predictive current control techniques," *IEEE Trans. Ind. Electron.*, vol. 61, no. 9, pp. 4474–4484, Sep. 2014.

[72] M. Duran and F. Barrero, "Recent advances in the design, modeling and control of multiphase machines - part 2," *IEEE Trans. Ind. Electron.*, 2015, Early Access.

[73] I. Gonzalez, M. Duran, H. Che, E. Levi, M. Bermudez, and F. Barrero, "Fault-tolerant operation of six-phase energy conversion systems with parallel machine-side converters," *IEEE Trans. Power Electron.*, 2015, Early Access.

[74] M. Duran, I. Gonzalez, M. Bermudez, F. Barrero, H. Guzman, and M. Arahal, "Optimal fault-tolerant control of six-phase induction motor drives with parallel converters," *IEEE Trans. Ind. Electron.*, 2015, Early Access.

[75] A. S. Abdel-Khalik, M. I. Masoud, and B. W. Williams, "Improved flux pattern with third harmonic injection for multiphase induction machines," *IEEE Trans. Power Electron.*, vol. 27, no. 3, pp. 1563–1578, Mar. 2012.

[76] L. Alberti and N. Bianchi, "Experimental tests of dual three-phase induction motor under faulty operating condition," *IEEE Trans. Ind. Electron.*, vol. 59, no. 5, pp. 2041–2048, May 2012.

[77] E. Levi, M. Jones, S. N. Vukosavic, and H. A. Toliyat, "A novel concept of a multiphase, multimotor vector controlled drive system supplied from a single voltage source inverter," *IEEE Trans. Power Electron.*, vol. 19, no. 2, pp. 320–335, Mar. 2004.

[78] E. Levi, M. Jones, and S. N. Vukosavic, "A series-connected two-motor six-phase drive with induction and permanent magnet machines," *IEEE Trans. Energy Convers.*, vol. 21, no. 1, pp. 121–129, Mar. 2006.

[79] M. Jones, S. N. Vukosavic, E. Levi, and A. Iqbal, "A six-phase series-connected two-motor drive with decoupled dynamic control," *IEEE Trans. Ind. Appl.*, vol. 41, no. 4, pp. 1056–1066, Jul./Aug. 2005.

[80] E. Levi, M. Jones, S. N. Vukosavic, and H. A. Toliyat, "Steady-state modeling of series-connected five-phase and six-phase two-motor drives," *IEEE Trans. Ind. Appl.*, vol. 44, no. 5, pp. 1559–1568, Sep./Oct. 2008.

[81] E. Levi, M. Jones, and S. N. Vukosavic, "Even-phase multi-motor vector controlled drive with single inverter supply and series connection of stator windings," *Elect. Power Appl., IEE Proc.*, vol. 150, no. 5, pp. 580–590, Sep. 2003.

[82] E. Levi, M. Jones, A. Iqbal, S. N. Vukosavic, and H. A. Toliyat, "Induction machine/syn-rel two-motor five-phase series-connected drive," *IEEE Trans. Energy Convers.*, vol. 22, no. 2, pp. 281–289, Jun. 2007.

[83] M. Jones, S. N. Vukosavic, E. Levi, and A. Iqbal, "A novel six-phase series-connected two-motor drive with decoupled dynamic control," in *Proc. IAS*, vol. 1, Oct. 2004, pp. –646.

[84] E. Levi, M. Jones, S. N. Vukosavic, and H. A. Toliyat, "Stator winding design for multiphase two-motor drives with single VSI supply," in *Proc. ICEM*, Sep. 2006.

[85] L. Chen and F. Z. Peng, "Dead-time elimination for voltage source inverters," *IEEE Trans. Power Electron.*, vol. 23, no. 2, pp. 574–580, Mar. 2008.

[86] W. Liang, J. Wang, and W. Fang, "Analytical modeling of sideband current harmonic components in induction machine drive with voltage source inverter by an SVM technique," *IEEE Trans. Power Electron.*, vol. 28, no. 11, pp. 5372–5379, Nov. 2013.

[87] D. Dujic, M. Jones, and E. Levi, "Analysis of output current-ripple rms in multiphase drives using polygon approach," *IEEE Trans. Power Electron.*, vol. 25, no. 7, pp. 1838–1849, Jul. 2010.

[88] L. Schreier, J. Bendl, and M. Chomat, "Influence of space harmonics on properties of six-phase induction machine — Part I. analysis," in *Proc. ICEM*, Sep. 2010, pp. 1–6.

[89] J. A. Riveros, F. Barrero, E. Levi, M. J. Duran, S. Toral, and M. Jones, "Variable-speed five-phase induction motor drive based on predictive torque control," *IEEE Trans. Ind. Electron.*, vol. 60, no. 8, pp. 2957–2968, Aug. 2013.

[90] H. A. Toliyat, T. A. Lipo, and J. C. White, "Analysis of a concentrated winding induction machine for adjustable speed drive applications. I. Motor analysis," *IEEE Trans. Energy Convers.*, vol. 6, no. 4, pp. 679–683, Dec. 1991.

[91] A. S. Abdel-Khalik and S. Ahmed, "Performance evaluation of a five-phase modular winding induction machine," *IEEE Trans. Ind. Electron.*, vol. 59, no. 6, pp. 2654–2669, Jun. 2012.

[92] L. Guo and L. Parsa, "Model reference adaptive control of five-phase IPM motors based on neural network," *IEEE Trans. Ind. Electron.*, vol. 59, no. 3, pp. 1500 –1508, Mar. 2012.

[93] R. Bojoi, F. Farina, G. Griva, F. Profumo, and A. Tenconi, "Direct torque control for dual three-phase induction motor drives," *IEEE Trans. Ind. Appl.*, vol. 41, no. 6, pp. 1627–1636, Nov./Dec. 2005.

[94] E. A. Klingshirn, "Harmonic filters for six-phase and other multiphase motors on voltage source inverters," *IEEE Trans. Ind. Appl.*, vol. IA-21, no. 3, pp. 588–594, May/Jun. 1985.

[95] H.-M. Ryu, J.-H. Kim, and S.-K. Sul, "Analysis of multiphase space vector pulse-width modulation basedon multiple d-q spaces concept," *IEEE Trans. Power Electron.*, vol. 20, no. 6, pp. 1364–1371, Nov. 2005.

[96] S. Xue, X. Wen, and Z. Feng, "A novel multi-dimensional SVPWM strategy of multiphase motor drives," in *Proc. PEMC*, Aug./Sep. 2006, pp. 931–935.

[97] L. Pereira, C. Scharlau, L. Pereira, and S. Haffner, "Influence of saturation on the airgap induction waveform of five-phase induction machines," *IEEE Trans. Energy Convers.*, vol. 27, no. 1, pp. 29–41, Mar. 2012.

[98] S. D. Sudhoff, D. C. Aliprantis, B. T. Kuhn, and P. L. Chapman, "An induction machine model for predicting inverter-machine interaction," *IEEE Trans. Energy Convers.*, vol. 17, no. 2, pp. 203–210, Jun. 2002.

[99] E. Fornasiero, N. Bianchi, and S. Bolognani, "Slot harmonic impact on rotor losses in fractional-slot permanent-magnet machines," *IEEE Trans. Ind. Electron.*, vol. 59, no. 6, pp. 2557–2564, Jun. 2012.

[100] M. Muteba, A. Jimoh, and D. Nicolae, "Torque ripple analysis of three-phase induction machines with non-uniform coil groups distribution," in *Proc. IEMDC*, May 2013, pp. 1358–1363.

[101] M. Valavi, A. Nysveen, R. Nilssen, and T. Rolvag, "Slot harmonic effect on magnetic forces and vibration in low-speed permanent-magnet machine with concentrated windings," *IEEE Trans. Ind. Appl.*, vol. 50, no. 5, pp. 3304–3313, Sep./Oct. 2014.

[102] R. M. Saunders, "Electromechanical energy conversion in double cylindrical structures," *IEEE Trans. Power App. Syst.*, vol. 82, no. 68, pp. 631–638, Oct. 1963.

[103] T. Lipo, *Analysis of Synchronous Machines, Second Edition.* CRC Press, 2012.

[104] H. A. Toliyat, M. M. Rahimian, and T. A. Lipo, "dq modeling of five phase synchronous reluctance machines including third harmonic of air-gap MMF," in *Proc. IAS*, Sep. 1991, pp. 231–237.

[105] A. Abdel-Khalik, M. Daoud, S. Ahmed, A. Elserougi, and A. Massoud, "Parameter identification of five-phase induction machines with single layer windings," *IEEE Trans. Ind. Electron.*, vol. 61, no. 10, pp. 5139–5154, Oct. 2014.

[106] P. Krause, O. Wasynczuk, S. Sudhoff, and I. P. E. Society, *Analysis of electric machinery and drive systems.* IEEE Press, 2002.

[107] J. Pyrhonen, T. Jokinen, and V. Hrabovcova, *Design of Rotating Electrical Machines.* Wiley, 2009.

[108] C. Boccaletti, C. Bruzzese, O. Honorati, and E. Santini, "Rotor bars breakage in railway traction squirrel cage induction motors and diagnosis by MCSA technique part II : Theoretical arrangements for fault-related current sidebands," in *Proc. SDEMPED*, Sep. 2005, pp. 1–6.

[109] H. A. Toliyat, T. A. Lipo, and J. C. White, "Analysis of a concentrated winding induction machine for adjustable speed drive applications. II. Motor design and performance," *IEEE Trans. Energy Convers.*, vol. 6, no. 4, pp. 684–692, Dec. 1991.

[110] M. Ojaghi and S. Nasiri, "Modeling eccentric squirrel-cage induction motors with slotting effect and saturable teeth reluctances," *IEEE Trans. Energy Convers.*, vol. 29, no. 3, pp. 619–627, Sep. 2014.

[111] M. Drif and A. J. M. Cardoso, "Airgap-eccentricity fault diagnosis, in three-phase induction motors, by the complex apparent power signature analysis," *IEEE Trans. Ind. Electron.*, vol. 55, no. 3, pp. 1404–1410, Mar. 2008.

[112] C. Bruzzese, E. Santini, V. Benucci, and A. Millerani, "Model-based eccentricity diagnosis for a ship brushless-generator exploiting the machine voltage signature analysis (MVSA)," in *Proc. SDEMPED*, Aug. 2009, pp. 1–7.

[113] J. Faiz and I. Tabatabaei, "Extension of winding function theory for nonuniform air gap in electric machinery," *IEEE Trans. Magn.*, vol. 38, no. 6, pp. 3654–3657, Nov. 2002.

[114] M. El Hachemi Benbouzid, "A review of induction motors signature analysis as a medium for faults detection," *IEEE Trans. Ind. Electron.*, vol. 47, no. 5, pp. 984–993, Oct. 2000.

[115] G. Joksimovic, J. Riger, T. Wolbank, N. Peric, and M. Vasak, "Stator-current spectrum signature of healthy cage rotor induction machines," *IEEE Trans. Ind. Electron.*, vol. 60, no. 9, pp. 4025–4033, Sep. 2013.

[116] J. Cameron, W. Thomson, and A. Dow, "Vibration and current monitoring for detecting airgap eccentricity in large induction motors," *Elect. Power Appl., IEE Proc. B*, vol. 133, no. 3, pp. 155–163, May 1986.

[117] G. Joksimovic, C. Bruzzese, and E. Santini, "Static eccentricity detection in synchronous generators by field current and stator voltage signature analysis — Part I: Theory," in *Proc. ICEM*, Sep. 2010, pp. 1–6.

[118] J. Gieras, C. Wang, and J. Lai, *Noise of Polyphase Electric Motors.* Taylor & Francis, 2005.

[119] J. Le Besnerais, V. Lanfranchi, M. Hecquet, and P. Brochet, "Optimal slot numbers for magnetic noise reduction in variable-speed induction motors," *IEEE Trans. Magn.*, vol. 45, no. 8, pp. 3131–3136, Aug. 2009.

[120] X. Tu, L.-A. Dessaint, R. Champagne, and K. Al-Haddad, "Transient modeling of squirrel-cage induction machine considering air-gap flux saturation harmonics," *IEEE Trans. Ind. Electron.*, vol. 55, no. 7, pp. 2798–2809, Jul. 2008.

[121] A. Abdel-Khalik, S. Ahmed, and A. Massoud, "A five-phase induction machine model using multiple dq planes considering the effect of magnetic saturation," in *Proc. ECCE*, Sep. 2014, pp. 287–293.

[122] R. Andriamalala, H. Razik, L. Baghli, and F.-M. Sargos, "Eccentricity fault diagnosis of a dual-stator winding induction machine drive considering the slotting effects," *IEEE Trans. Ind. Electron.*, vol. 55, no. 12, pp. 4238–4251, Dec. 2008.

[123] G. Bottiglieri, A. Consoli, and T. Lipo, "Modeling of saturated induction machines with injected high-frequency signals," *IEEE Trans. Energy Convers.*, vol. 22, no. 4, pp. 819–828, Dec. 2007.

[124] A. Abdel-Khalik, S. Ahmed, and A. Massoud, "A five-phase induction machine model using multiple dq planes considering the effect of magnetic saturation," in *Proc. ECCE*, Sep. 2014, pp. 287–293.

[125] G. Joksimovic, "Line current spectrum analysis in saturated three-phase cage induction machines," *Elect. Eng.*, vol. 91, no. 8, pp. 425–437, Mar. 2010.

[126] S. Nandi, S. Ahmed, and H. Toliyat, "Detection of rotor slot and other eccentricity related harmonics in a three phase induction motor with different rotor cages," *IEEE Trans. Energy Convers.*, vol. 16, no. 3, pp. 253–260, Sep. 2001.

[127] S. Nandi, S. Ahmed, H. Toliyat, and R. Mohan Bharadwaj, "Selection criteria of induction machines for speed-sensorless drive applications," *IEEE Trans. Ind. Appl.*, vol. 39, no. 3, pp. 704–712, May/Jun. 2003.

[128] J.-A. Echeverria-Villar, J. Martinez-Roman, and L. Serrano-Iribarnegaray, "Transient harmonic torques in induction machines: measurement and impact on motor performance," *Elect. Eng.*, vol. 94, pp. 67–80, Jun. 2012, 10.1007/s00202-011-0216-4.

[129] W. Thomson and M. Fenger, "Current signature analysis to detect induction motor faults," *IEEE Ind. Appl. Mag.*, vol. 7, no. 4, pp. 26–34, Jul./Aug. 2001.

[130] S. Nandi, H. Toliyat, and X. Li, "Condition monitoring and fault diagnosis of electrical motors-a review," *IEEE Trans. Energy Convers.*, vol. 20, no. 4, pp. 719–729, Dec. 2005.

[131] A. Bellini, F. Filippetti, C. Tassoni, and G.-A. Capolino, "Advances in diagnostic techniques for induction machines," *IEEE Trans. Ind. Electron.*, vol. 55, no. 12, pp. 4109–4126, Dec. 2008.

[132] J. Hong, D. Hyun, S. B. Lee, and C. Kral, "Offline monitoring of airgap eccentricity for inverter-fed induction motors based on the differential inductance," *IEEE Trans. Ind. Appl.*, vol. 49, no. 6, pp. 2533–2542, Nov./Dec. 2013.

[133] D. Morinigo-Sotelo, L. Garcia-Escudero, O. Duque-Perez, and M. Perez-Alonso, "Practical aspects of mixed-eccentricity detection in PWM voltage-source-inverter-fed induction motors," *IEEE Trans. Ind. Electron.*, vol. 57, no. 1, pp. 252–262, Jan. 2010.

[134] D. Dorrell, W. Thomson, and S. Roach, "Analysis of airgap flux, current, and vibration signals as a function of the combination of static and dynamic airgap eccentricity in 3-phase induction motors," *IEEE Trans. Ind. Appl.*, vol. 33, no. 1, pp. 24–34, Jan./Feb. 1997.

[135] S. Williamson and A. Smith, "Steady-state analysis of 3-phase cage motors with rotor-bar and end-ring faults," *Elect. Power Appl., IEE Proc. B*, vol. 129, no. 3, pp. 93–, May 1982.

[136] G. Kliman, R. Koegl, J. Stein, R. Endicott, and M. Madden, "Noninvasive detection of broken rotor bars in operating induction motors," *IEEE Trans. Energy Convers.*, vol. 3, no. 4, pp. 873–879, Dec. 1988.

[137] S. Williamson and K. Mirzoian, "Analysis of cage induction motors with stator winding faults," *IEEE Trans. Power App. Syst.*, vol. PAS-104, no. 7, pp. 1838–1842, Jul. 1985.

[138] R. Schoen, T. Habetler, F. Kamran, and R. Bartfield, "Motor bearing damage detection using stator current monitoring," *IEEE Trans. Ind. Appl.*, vol. 31, no. 6, pp. 1274–1279, Nov./Dec. 1995.

[139] I. Bogiatzidis, A. Safacas, and E. Mitronikas, "Detection of backlash phenomena appearing in a single cement kiln drive using the current and the electromagnetic torque signature," *IEEE Trans. Ind. Electron.*, vol. 60, no. 8, pp. 3441–3453, Aug. 2013.

[140] D. Campos-Delgado, J. Pecina-Saanchez, D. Rivelino Espinoza-Trejo, and E. Roman Arce-Santana, "Diagnosis of open-switch faults in variable speed drives by stator current analysis and pattern recognition," *Elect. Power Appl., IET*, vol. 7, no. 6, pp. 509–522, Jul. 2013.

[141] M. Pineda-Sanchez, R. Puche-Panadero, M. Riera-Guasp, J. Perez-Cruz, J. Roger-Folch, J. Pons-Llinares, V. Climente-Alarcon, and J. Antonino-Daviu, "Application of the Teager Kaiser energy operator to the fault diagnosis of induction motors," *IEEE Trans. Energy Convers.*, vol. 28, no. 4, pp. 1036–1044, Dec. 2013.

[142] A. Soualhi, G. Clerc, and H. Razik, "Detection and diagnosis of faults in induction motor using an improved artificial ant clustering technique," *IEEE Trans. Ind. Electron.*, vol. 60, no. 9, pp. 4053–4062, Sep. 2013.

[143] V. Climente-Alarcon, J. Antonino-Daviu, M. Riera-Guasp, and M. Vlcek, "Induction motor diagnosis by advanced notch fir filters and the Wigner Ville distribution," *IEEE Trans. Ind. Electron.*, vol. 61, no. 8, pp. 4217–4227, Aug. 2014.

[144] Y. Gritli, S. B. Lee, F. Filippetti, and L. Zarri, "Advanced diagnosis of outer cage damage in double-squirrel-cage induction motors under time-varying conditions based on wavelet analysis," *IEEE Trans. Ind. Appl.*, vol. 50, no. 3, pp. 1791–1800, May/Jun. 2014.

[145] C. Pezzani, P. Donolo, G. Bossio, M. Donolo, A. Guzman, and S. Zocholl, "Detecting broken rotor bars with zero-setting protection," *IEEE Trans. Ind. Appl.*, vol. 50, no. 2, pp. 1373–1384, Mar./Apr. 2014.

[146] J. de Jesus Rangel-Magdaleno, H. Peregrina-Barreto, J. Ramirez-Cortes, P. Gomez-Gil, and R. Morales-Caporal, "FPGA-based broken bars detection on induction motors under different load using motor current signature analysis and mathematical morphology," *IEEE Trans. Instrum. Meas.*, vol. 63, no. 5, pp. 1032–1040, May 2014.

[147] S. Das, P. Purkait, C. Koley, and S. Chakravorti, "Performance of a load-immune classifier for robust identification of minor faults in induction motor stator winding," *IEEE Trans. Dielectr. Electr. Insul.*, vol. 21, no. 1, pp. 33–44, Feb. 2014.

[148] E. Fournier, A. Picot, J. Regnier, M. T. Yamdeu, J. Andrejak, and P. Maussion, "Current-based detection of mechanical unbalance in an induction machine using spectral kurtosis with reference," *IEEE Trans. Ind. Electron.*, vol. 62, no. 3, pp. 1879–1887, Mar. 2015.

[149] S. Kia, H. Henao, and G. Capolino, "Gear tooth surface damage fault detection using induction machine stator current space vector analysis," *IEEE Trans. Ind. Electron.*, vol. 62, no. 3, pp. 1866–1878, Mar. 2015.

[150] J. Pons-Llinares, J. Antonino-Daviu, M. Riera-Guasp, S. Bin Lee, T. Kang, and C. Yang, "Advanced induction motor rotor fault diagnosis via continuous and discrete time frequency tools," *IEEE Trans. Ind. Electron.*, vol. 62, no. 3, pp. 1791–1802, Mar. 2015.

[151] A. Giantomassi, F. Ferracuti, S. Iarlori, G. Ippoliti, and S. Longhi, "Electric motor fault detection and diagnosis by kernel density estimation and Kullback-Leibler divergence based on stator current measurements," *IEEE Trans. Ind. Electron.*, vol. 62, no. 3, pp. 1770–1780, Mar. 2015.

[152] C. Yang, T. Kang, S. Lee, J. Yoo, A. Bellini, L. Zarri, and F. Filippetti, "Screening of false induction motor fault alarms produced by axial air ducts based on the space-harmonic-induced current components," *IEEE Trans. Ind. Electron.*, vol. 62, no. 3, pp. 1803–1813, Mar. 2015.

[153] M. Drif and A. J. M. Cardoso, "Discriminating the simultaneous occurrence of three-phase induction motor rotor faults and mechanical load oscillations by the instantaneous active and reactive power media signature analyses," *IEEE Trans. Ind. Electron.*, vol. 59, no. 3, pp. 1630–1639, Mar. 2012.

[154] K. Gyftakis and J. Kappatou, "A novel and effective method of static eccentricity diagnosis in three-phase PSH induction motors," *IEEE Trans. Energy Convers.*, vol. 28, no. 2, pp. 405–412, Jun. 2013.

[155] A. Ceban, R. Pusca, and R. Romary, "Study of rotor faults in induction motors using external magnetic field analysis," *IEEE Trans. Ind. Electron.*, vol. 59, no. 5, pp. 2082–2093, May 2012.

[156] L. Wu, X. Huang, T. Habetler, and R. Harley, "Eliminating load oscillation effects for rotor eccentricity detection in closed-loop drive-connected induction motors," *IEEE Trans. Power Electron.*, vol. 22, no. 4, pp. 1543–1551, Jul. 2007.

[157] L. Wu, T. Habetler, and R. Harley, "A review of separating mechanical load effects from rotor faults detection in induction motors," in *Proc. SDEMPED*, Sep. 2007, pp. 221–225.

[158] B. Akin, S. Choi, U. Orguner, and H. Toliyat, "A simple real-time fault signature monitoring tool for motor-drive-embedded fault diagnosis systems," *IEEE Trans. Ind. Electron.*, vol. 58, no. 5, pp. 1990–2001, May 2011.

[159] L. Zarri, M. Mengoni, Y. Gritli, A. Tani, F. Filippetti, G. Serra, and D. Casadei, "Behavior of multiphase induction machines with unbalanced stator windings," in *Proc. SDEMPED*, Sep. 2011, pp. 84–91.

[160] T. Kato, K. Inoue, and D. Okuda, "Diagnosis of multi-phase turn faults of induction motor stator windings," in *Proc. PEDS*, Nov. 2009, pp. 144–149.

[161] J. Apsley and S. Williamson, "Analysis of multiphase induction machines with winding faults," *IEEE Trans. Ind. Appl.*, vol. 42, no. 2, pp. 465–472, Mar./Apr. 2006.

[162] L. Zarri, M. Mengoni, Y. Gritli, A. Tani, F. Filippetti, G. Serra, and D. Casadei, "Detection and localization of stator resistance dissymmetry based on multiple reference frame controllers in multiphase induction motor drives," *IEEE Trans. Ind. Electron.*, vol. 60, no. 8, pp. 3506–3518, Aug. 2013.

[163] A. G. Yepes, J. A. Riveros, J. Doval-Gandoy, F. Barrero, O. Lopez, B. Bogado, M. Jones, and E. Levi, "Parameter identification of multiphase induction machines with distributed windings. Part 1: sinusoidal excitation methods," *IEEE Trans. Energy Convers.*, vol. 27, no. 4, pp. 1056–1066, Dec. 2012.

[164] P. Garrett, *Abstract algebra.* Chapman & Hall/CRC Statistics and Mathematics, Sep. 2007.

[165] H. Guzman, F. Barrero, and M. Duran, "IGBT-gating failure effect on a fault-tolerant predictive current-controlled five-phase induction motor drive," *IEEE Trans. Ind. Electron.*, vol. 62, no. 1, pp. 15–20, Jan. 2015.

[166] A. Abdel-Khalik, A. Morsy, S. Ahmed, and A. Massoud, "Effect of stator winding connection on performance of five-phase induction machines," *IEEE Trans. Ind. Electron.*, vol. 61, no. 1, pp. 3–19, Jan. 2014.

[167] M. Jones, D. Dujic, E. Levi, and S. N. Vukosavic, "Dead-time effects in voltage source inverter fed multi-phase ac motor drives and their compensation," in *Proc. EPE-ECCE*, Sep. 2009.

[168] Y. Maouche, M. E. K. Oumaamar, M. Boucherma, and A. Khezzar, "Instantaneous power spectrum analysis for broken bar fault detection in inverter-fed six-phase squirrel cage induction motor," *Int. J. of Elec. Power & Energy Syst.*, vol. 62, pp. 110–117, Nov. 2014.

[169] K. Oberretl, "Losses, torques and magnetic noise in induction motors with static converter supply, taking multiple armature reaction and slot openings into account," *IET Electr. Power Appl.*, vol. 1, no. 4, pp. 517–531, Jul. 2007.

[170] A. Abdel-Khalik, S. Ahmed, A. Elserougi, and A. Massoud, "A voltage-behind-reactance model of five-phase induction machines considering the effect of magnetic saturation," *IEEE Trans. Energy Convers.*, vol. 28, no. 3, pp. 576–592, Sep. 2013.

[171] W. Thomson, D. Rankin, and D. Dorrell, "On-line current monitoring to diagnose airgap eccentricity in large three-phase induction motors - industrial case histories verify the predictions," *IEEE Trans. Energy Convers.*, vol. 14, no. 4, pp. 1372–1378, Dec. 1999.

[172] M. Valavi, A. Nysveen, R. Nilssen, R. Lorenz, and T. Rolvag, "Influence of pole and slot combinations on magnetic forces and vibration in low-speed pm wind generators," *IEEE Trans. Magn.*, vol. 50, no. 5, pp. 1–11, May 2014.

[173] R. Burbidge and M. Fryett, "Synchronous and asynchronous torques in squirrel-cage induction motors," *Proc. of the Inst. of Elect. Eng.*, vol. 114, no. 11, pp. 1665–1673, Nov. 1967.

[174] S. Nandi, "Modeling of induction machines including stator and rotor slot effects," *IEEE Trans. Ind. Appl.*, vol. 40, no. 4, pp. 1058–1065, Jul.-Aug. 2004.

[175] A. Tenhunen, T. Benedetti, T. Holopainen, and A. Arkkio, "Electromagnetic forces in cage induction motors with rotor eccentricity," in *Proc. IEMDC*, vol. 3, Jun. 2003, pp. 1616–1622.